Matter wave scattering on complex potentials

Pierrick Cheiney

▶ **To cite this version:**

Pierrick Cheiney. Matter wave scattering on complex potentials. Quantum Gases [cond-mat.quant-gas]. Université Paul Sabatier - Toulouse III, 2013. English. NNT : . tel-00875153

HAL Id: tel-00875153
https://theses.hal.science/tel-00875153

Submitted on 21 Oct 2013

HAL is a multi-disciplinary open access archive for the deposit and dissemination of scientific research documents, whether they are published or not. The documents may come from teaching and research institutions in France or abroad, or from public or private research centers.

L'archive ouverte pluridisciplinaire **HAL**, est destinée au dépôt et à la diffusion de documents scientifiques de niveau recherche, publiés ou non, émanant des établissements d'enseignement et de recherche français ou étrangers, des laboratoires publics ou privés.

Université de Toulouse

THÈSE

En vue de l'obtention du

DOCTORAT DE L'UNIVERSITÉ DE TOULOUSE

Délivré par :

Université Toulouse 3 Paul Sabatier (UT3 Paul Sabatier)

Présentée et soutenue par :
Pierrick Cheiney

le mardi 4 juin 2013

Titre :

Matter wave scattering on complex potentials

École doctorale et discipline ou spécialité :
ED SDM : Physique - COR 02

Unité de recherche :
Laboratoire Collisions, Agrégats, Réactivité

Directeur(s) de Thèse :

David Guéry-Odelin

Jury :
Christophe Salomon: Rapporteur
Iacopo Carusotto: Rapporteur
Christoph Westbrook: Examinateur
Bruno Laburthe-Tolra: Examinateur
Sylvain Capponi: Examinateur
David Guéry-Odelin: Directeur de thèse

Remerciements

Le travail de thèse présenté ici a été possible grâce à de nombreuses personnes qu'il est temps de remercier.

Je voudrais commencer par remercier les directeurs successifs du laboratoire : Jacques Vigué et Béatrice Chatel ainsi que Jean-Marc L'Hermite pour m'avoir accueilli dans le laboratoire pendant ces trois ans.

Je tiens ensuite à remercier vivement les membres de mon jury de thèse : Christophe Salomon et Iacopo Carusotto en tant que rapporteurs ainsi que Christoph Westbrook, Bruno Laburthe-Tolra et Sylvain Capponi pour leurs remarques très constructives.

Je voudrais remercier très chaleureusement toute l'équipe des atomes froids et en premier lieu mon directeur de thèse David Guéry-Odelin qui m'a accueilli dans l'équipe à partir mon stage de M2. Merci pour ta gentillesse tes conseils et ton optimisme à toute épreuve durant ces trois ans, ainsi que du temps que tu as consacré à la relecture de ce manuscrit. Merci également du soutient sans faille que tu m'as apporté durant cette thèse et pour la suite.

Merci à Renaud Mathevet et Olivier Carraz, avec qui j'ai beaucoup appris en travaillant sur le ralentisseur Zeeman. Dorénavant, chaque nouvelle machine devra comporter au moins un aimant permanent! La vidéo du nain de jardin restera également dans les annales! Thierry Lahaye ensuite, c'était un grand plaisir de travailler avec toi, ta grande connaissance de la physique et ton exigence ont été très précieuses.

Un souvenir tout particulier pour Charlotte Fabre et François Vermersch, d'un an mes aînés dans cette aventure. Charlottes, les (longues) prises de données n'auraient pas été aussi fun sans toi. François, il faut qu'on se fasse la ronde du foie gras un jour! Je vous souhaite bonne chance à tous les deux dans la suite de vos aventures enseignantes. Merci enfin à tous les autres membres de l'équipe avec qui j'ai eu le plaisir de travailler: Gianluca Gattobigio, Stéphane Faure, Gabriel Condon, François Damon, Aéla Fortun, Gabriel Hetet et Juliette Billy, ainsi qu'aux services techniques, aux ateliers d'électronique et de mécaniques. Un grand merci aux secrétaires du département: Christinne Soucasse, Sylvie Boukhari et Marie-France Rolland.

Je tiens également à remercier les chercheurs permanents du laboratoire ainsi que les doctorants avec qui j'ai partagé ces trois ans: Simon, Jessica, Renaud, Hugo, Michael, Steven, Wesley, Jonathan, Muammar, Adrien et tous ceux que j'ai pu oublier. Je n'ai qu'une chose à dire: DUB!

Pour finir sur une note peu originale, mais pourtant bien sincère, merci à tous les autres, qui m'ont soutenu. Il y a ma famille, mes amis et bien sûr Chiara qui m'a soutenu et poussé au cul tout du long et ne s'est jamais moquée de mon anglais

;-) bien sur.
Merci à tous!

Contents

Introduction **3**

1 Design and realization of a permanent magnet Zeeman slower **9**
1.1 Introduction . . . 10
1.2 Theoretical framework . . . 10
1.2.1 Principle . . . 10
1.2.2 Simple model, magnetic field shape . . . 11
1.2.3 The adiabatic following condition . . . 12
1.2.4 Atomic structure . . . 13
1.2.5 Choice of the magnetic field parameters . . . 15
1.2.6 Longitudinal or transverse magnetic field . . . 16
1.3 The dipole configuration . . . 17
1.3.1 Choice and modelization of the permanent magnets . . . 17
1.3.2 Position of the magnets . . . 18
1.3.3 Measured magnetic field . . . 20
1.4 Slowed atomic beam . . . 22
1.4.1 Experimental setup . . . 22
1.4.2 Slowed beam velocity distribution . . . 24
1.4.3 Flux as a function of the detuning . . . 25
1.5 The Halbach configuration . . . 26
1.5.1 The principle . . . 26
1.5.2 Field calculations . . . 26
1.5.3 Magnets layout . . . 27
1.6 Mechanics and field measurements . . . 28
1.6.1 Mechanical design . . . 28
1.6.2 Shielding . . . 28
1.6.3 Field parameters and measurement . . . 30
1.7 Performances . . . 31
1.7.1 Needed laser powers . . . 32
1.7.2 Repumper . . . 33
1.7.3 MOT loading . . . 34
1.8 Conclusion . . . 35

2 All optical production of a Rubidium Bose-Einstein condensate **37**

2.1 Introduction . . . 37
2.2 Condensation in an harmonic trap . . . 40
2.3 Pre-cooled atomic source . . . 41
2.3.1 Oven and Zeeman Slower . . . 41
2.3.2 The 2D-MOT . . . 42
2.4 Imaging system . . . 43
2.4.1 Absorption imaging . . . 43
2.4.2 Setup . . . 43
2.4.3 MOT mode . . . 44
2.4.4 BEC mode . . . 44
2.4.5 Quantitative measurements . . . 45
2.5 The horizontal dipole guide . . . 45
2.5.1 Dipole potential . . . 46
2.5.2 The spatial mode . . . 47
2.5.3 Setting up of the horizontal beam . . . 48
2.5.4 Power issues . . . 49
2.5.5 Experimental sequence . . . 51
2.5.6 Lifetime . . . 52
2.6 Crossed dipole trap and evaporation . . . 53
2.6.1 Evaporation constraints . . . 53
2.6.2 Characteristics of the crossed potential . . . 56
2.6.3 Evaporation trajectory . . . 57
2.6.4 Spin distillation . . . 59
2.7 Conclusion . . . 61

3 Lattice setup and characterization 63
3.1 Introduction . . . 63
3.2 Setup of the optical lattice . . . 64
3.2.1 Potential and notations . . . 64
3.2.2 Experimental setup . . . 65
3.2.3 Method to cross the lattice beams . . . 68
3.3 Calibration . . . 68
3.3.1 Kapitza-Dirac diffraction . . . 69
3.3.2 Experimental realization . . . 70
3.3.3 Beyond the Raman-Nath regime . . . 71
3.4 Robustness against misalignments . . . 72
3.5 Conclusion . . . 73

4 A quantum particle in a periodic potential 75
4.1 Introduction . . . 75
4.2 Bloch band structure . . . 75
4.2.1 Bloch theorem . . . 75

4.2.2 Computation of the band structure . . . 76
4.3 Mathieu equation . . . 78
4.3.1 Stability regions . . . 79
4.3.2 Computation of the characteristic exponent . . . 80
4.4 Interpretation of a scattering experiment . . . 81
4.5 Conclusion . . . 83

5 Bragg reflection on a finite size lattice 85
5.1 Introduction . . . 85
5.2 Effect of the envelope . . . 85
5.2.1 Naive picture . . . 85
5.2.2 Contributions of the Landau-Zener transitions . . . 86
5.3 Preparation of the wavepacket . . . 88
5.3.1 Outcoupling of the condensate . . . 88
5.3.2 Acceleration of the wavepacket . . . 90
5.4 Scattering on the lattice . . . 91
5.5 Experimental sequence . . . 91
5.5.1 Time-resolved scattering . . . 92
5.5.2 Probing of the transmission diagram . . . 92
5.6 Cavity effects . . . 94
5.7 Conclusion . . . 95

6 Realization of tunnel barriers for matter waves using spatial gaps 97
6.1 Introduction . . . 97
6.2 Local band structure model . . . 98
6.2.1 Position-dependent band structure . . . 98
6.2.2 Transmission probabilities . . . 99
6.2.3 Comparison with a repulsive barrier . . . 100
6.3 Experiment . . . 101
6.3.1 Preparation of the initial wavepacket . . . 101
6.3.2 Propagation inside the lattice . . . 102
6.3.3 Properties of the tunneled packets . . . 104
6.4 Dephasing between energy components . . . 105
6.4.1 Semi-classical trajectories . . . 105
6.4.2 Optimization of the envelope shape . . . 107
6.5 Conclusion . . . 109

7 Scattering on an amplitude-modulated lattice 111
7.1 Introduction . . . 111
7.2 The experiment . . . 112
7.2.1 Protocol . . . 112
7.2.2 Control of the intensity . . . 112
7.2.3 Experimental results . . . 113

7.3 Interband transitions in the vanishing depth limit 115
7.4 The Floquet-Bloch framework 118
7.4.1 Principle 118
7.4.2 Computation of the Floquet-Bloch band diagram 119
7.4.3 Reflection on a square envelope lattice 120
7.5 Trajectories in the semi-classical model 121
7.5.1 Validation of the semiclassical model 121
7.5.2 Analysis of the reflection mechanism 123
7.6 Application:velocity filter 125
7.7 Conclusion 126

Conclusion **127**

Résumé de la thèse **131**

Appendices **157**

A Published papers **159**
A.1 Zeeman slowers made simple with permanent magnets in a Halbach configuration 159
A.2 Realization of a distributed Bragg reflector for propagating guided matter waves 159
A.3 Guided atom laser: transverse mode quality and longitudinal momentum distribution 160
A.4 Matter wave scattering on an amplitude-modulated optical lattice . . 160
A.5 Realization of tunnel barriers for matter waves using spatial gaps . . 161

B More on the outcoupling dynamics **163**

C Magnetic material characterization **167**

D Atomic flux from absorption measurements **169**

E Recirculating oven **171**

F Ideal Halbach cylinder **173**

G Development of the Floquet-Bloch band eigenvalue problem **177**

Introduction

Atom optics

The wave-particle duality is one of the keystones of quantum mechanics. While the wave nature of light was recognized already in the 17th century by Huygens,the idea of the wave nature of massive particles was first formulated much later in 1923 by Louis de Broglie [1]. In his thesis, de Broglie proposed that all massive particles also possess wave properties characterized by a wavelength

$$\lambda_{\mathrm{DB}} = \frac{h}{mv} \tag{1}$$

where h is the Planck constant and m and v are the particle mass and velocity.

The wave nature of particles was first confirmed in 1927 by Davisson and Germer [2] with the observation of diffraction of electrons on a Nickel crystal.

Three Years later, the diffraction of Helium atoms from freshly cleaved NaCl and LiF crystals was demonstrated by Immanuel Estermann and Otto Stern [3]. In this experiment, the Helium atoms did not penetrate into the crystal and were diffracted by the periodic structure of the surface. Diffraction was also observed with neutrons in 1947 by Enrico Fermi and Leona Marshall [4].

These experiments set the beginning of atom optics *i.e* the possibility to treat atoms as waves and to perform on atoms experiments that were previously restricted to light, such as diffraction or and interferences.. Numerous experiments directly inspired by optics have then been performed with thermal atomic beams; for example, the diffraction of a thermal beam by a transmission grating in the group of D.R Pritchards in 1988 [5] and the Young double-slit experiment realize with Helium in 1991 by O. Carnal and J. Mlynek [6]. These experiments were technically very difficult due to the lack of appropriate atom-optical elements to manipulate the atomic beams and to the small de Broglie wavelength associated with the atoms. Indeed, at a temperature T, the mean particle momentum is such that the thermal de Broglie wavelength decreases as mass increases: $\lambda_T = h/\sqrt{2\pi m k_{\mathrm{B}} T}$ so λ_T is approximately 0.5 Å for Helium atoms at room temperature.

The field of atom optics experienced a renewal with the development of the laser cooling techniques and the manipulation of atoms through their interaction with laser fields. These developments led to the attribution of the Nobel prize in

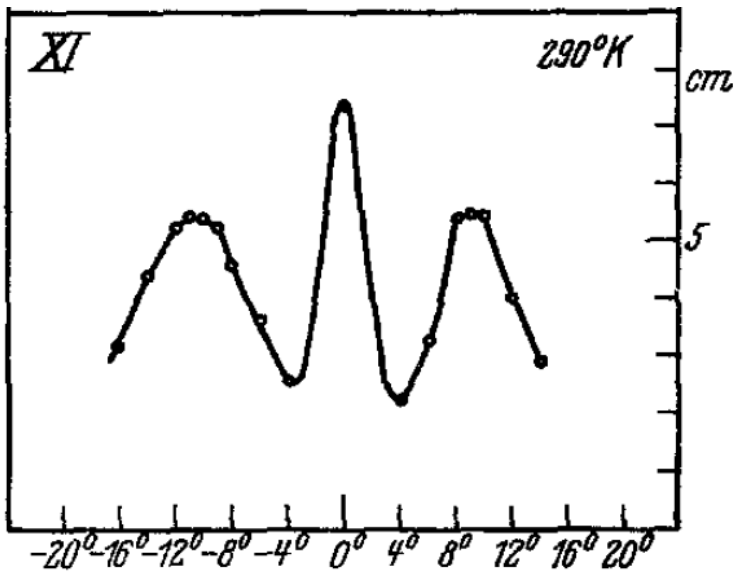

Figure 1: *First evidence of diffraction of He atoms on a NaCl crystal. Figure reproduced from [3].*

1997 awarded to Steven Chu, Claude Cohen-Tannoudji and William D. Phillips "for development of methods to cool and trap atoms with laser light"[7, 8, 9]. By bringing the temperature to the sub microkelvin regime, the de Broglie wavelength raises in the range of 100 nm $-$ 1 μm which makes it relatively easy to observe interferences with atoms. Furthermore, many atom-optical elements have been realized leveraging the use of the interaction between light and matter. Since light is often the most convenient tool to manipulate atoms, the roles of matter and light can be strikingly reversed, and therefore, many atom optics experiments are inspired directly by the analogy with optics. This, in particular will be the case for the work presented in this thesis.

New atomic sources: BEC and atom lasers

Combining laser cooling techniques and evaporative cooling, a new page of atom optics opens up in 1995 with the achievement of the Bose condensation in dilute atomic gases in the groups of E. A. Cornell and C. E. Wiemann with Rubidium and W. Ketterle with Sodium [10, 11]. Based on works of Satyendra Nath Bose, Albert Einstein predicted in 1925 that below a critical temperature, a macroscopic proportion of atoms in a trap condense in the ground state. Within the Bose-Einstein condensate, the individual de Broglie wavelengths of the atoms overlap, thus forming a single coherent matter wave that extends across the system. Soon after the first experimental realization of a Bose-Einstein condensate, these coherence properties were demonstrated by allowing two separated condensates to overlap and interfere [12].

There is an interesting similarity between a Bose-Einstein condensate and a laser in the sense that all particles lie in the same quantum state. The origin of this

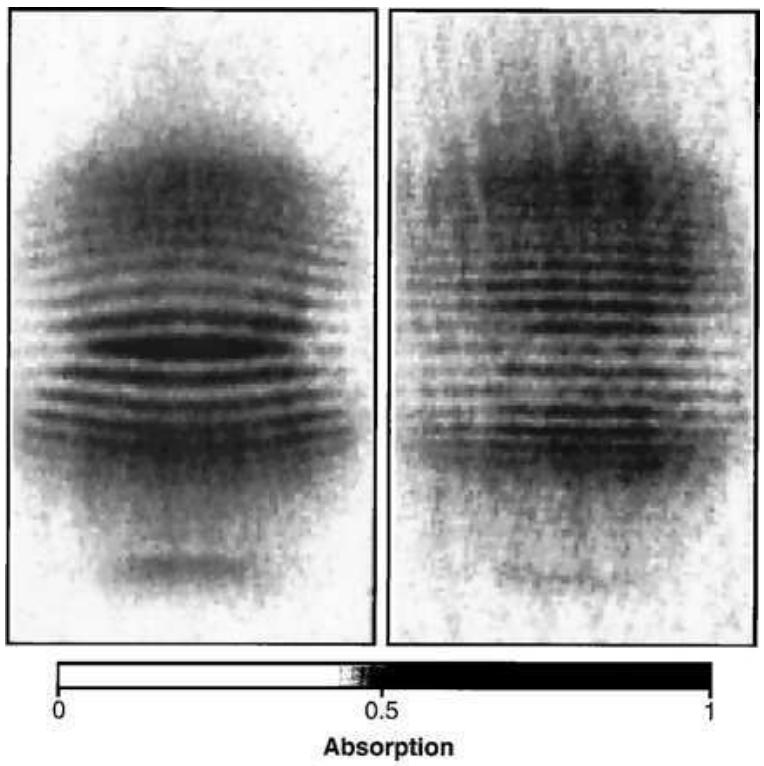

Figure 2: *Interference pattern between two initially separated Bose-Einstein condensate. Figure reproduced from [12]*

phenomenon, however, is quite different: in a laser, the key ingredients are the stimulated emission phenomena and the feedback of light in a cavity, resulting in the amplification of one optical mode of the cavity. The photons, however, do not interact directly with each other and do not reach thermal equilibrium. In a Bose-Einstein condensate the accumulation of particles in the ground state results from the Bose statistics for particle of integer spin at thermal equilibrium. Recently, the analogy was pushed further with the realization of a Bose-Einstein condensate of light [13]. In this experiment, photons thermalized through the interaction with a dye and the photon number was conserved using a micro optical cavity.

Following this analogy, *atom lasers* were developed. The aim was to produce a quasi-continuous coherent matter wave that possesses similar coherence properties as that of a continous optical laser. This is done by extracting atoms coherently from a condensate. Several outcoupling mechanisms have been considered: using a Radio frequency spin flip [14], Raman beams [15], or by lowering progressively the depth of the trapping potential in one direction [16, 17]. Up to now, all atom lasers operate in a pulsed mode limited by the depletion of the condensate. If the extraction from the condensate is coherent, it is possible to produce an atom laser whose temporal coherence is Fourier limited [18]. Strictly speaking, a Bose-Einstein condensate that is simply released by switching off the trap constitutes the simplest atom laser and is analogous to a Q-switch laser.

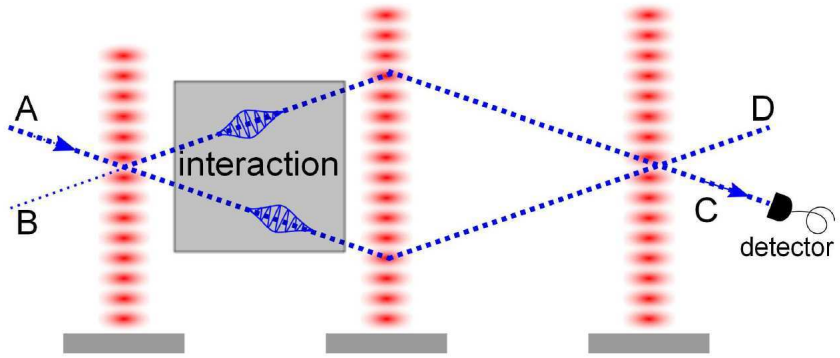

Figure 3: *Sketch of an atomic interferometer with separable arms using Bragg diffraction on an optical lattice. Figure reproduced from [30].*

Atom optics toolbox

To manipulate coherent matter waves, a wide variety of atom-optical elements have been developed. For example, atomic mirrors can be realized using a repulsive potentials produced by an evanescent optical wave [19, 20], a focused laser beam [20] or a magnetic field [19] using the Stern-Gerlach force. An appropriate magnetic field configuration creates an atomic lens [21]. One can also use the diffraction on an optical lattice to realize an atomic lens [22, 23].

In this thesis, we focused on the study of the interaction of matter wave with a periodic potential, which is in close analogy with dielectric optics.

In 1933, Kapitza and Dirac [24] predicted that an electron beam could be diffracted by a standing wave light field. The first experiments were carried out with electrons in 1965 onwards [25, 26] and later in 1983 with neutral atoms in the group of D. E. Pritchard [27]. The use of optical lattices potentials yields many developments in particular in atomic interferometry. In this case, the diffraction is associated with the absorption of a photon in one mode of the field followed by the stimulated emission in an other mode yielding a momentum change: $\Delta p = 2n\hbar k_{\mathrm{L}}$, where λ_{L} is the light wavelength and n the diffraction order. By diffracting atoms in the Bragg regime corresponding to a small lattice depth and a long interaction time [28], it is possible to realize a superposition of only two spatially separated atomic beams. In this regime, the diffraction probability is important if the incoming atomic beam fulfills the Bragg condition [29]

$$2d \sin \Theta = n\lambda_{\mathrm{DB}}, \tag{2}$$

where Θ is the angle between the incoming atomic beam and the lattice (d being the lattice spacing). The weights of the two diffraction orders can be controlled by adjusting the lattice depth. The diffraction on an optical lattice is widely used for example to realize atomic beam-splitters for atomic interferometers with separable

arms [31, 32, 30]. In these setups, the incoming atomic beam impinges on a first optical lattice at the Bragg angle. Two additional lattices first reflect each beam and recombine them to form an Mach-Zehnder interferometer (see FIG. 3). Because the two arms of the interferometers are spatially separated, it is possible to apply a perturbation on only one path of the interferometer.

In such interferometers, it is advantageous to increase the enclosed area and the propagation time in the arms. In this prospect, slow atoms are favorable since the Bragg angle increases as the incident velocity decreases, and because for a given propagation length, atoms can accumulate a phase for a longer time. In order to maximize the interaction time and to prevent the atoms from falling under gravity, is is then necessary to use an atomic waveguide realized by a potential that confines atoms to one direction. This potential can be realized either magnetically [33] or by a red detuned laser, or alternatively using a hollow-core optical fiber guide [34]. A waveguide possesses two advantages: first by confining the atoms to one dimension, it reduces the spreading of the wavepacket with time, which can be useful to propagate a wavepacket for a long time. Second, if the waveguide is horizontal, it compensates for the gravity and prevents the atoms from falling. In this way, as the atoms are not accelerated, λ_{DB} can remain large in the course of the propagation.

Atomic beamsplitters in the guided configuration have been built in a Y and a X configuration with thermal atomic beams [35, 36, 37, 38]. During the past years, our group has also realized a beam splitter for guided atom lasers on a X configuration [39]. During this thesis, we have designed new atom optics tools adapted to the confined geometry. First, we have demonstrated the realization of a Bragg reflector that is the exact analogous of a fiber Bragg grating [40] in optics. In this experiment, the scattering of a matter wave on a finite size lattice realizes in particular different types of velocity filter. Using the same finite size lattice, we studied the transposition of Landau-Zener tunneling to position space. We have shown that this system produces tunnel barrier that are to some extent equivalent to submicronic repulsive barrier. Finally, we have studied the problem of scattering of a matter wave onto a lattice whose depth is modulated with time. Because of this additionnal degree of freedom, this system is very rich and allows to extend the notion of Bragg reflection and to make the Bragg condition tunable. This scattering can be used to realize performant tunable velocity filters in guided environment. Interestingly, this velocity filter does not rely on any specific internal structure and can thus be used with any atom.

Outline

- In the first chapter, I report in detail an experimental development on a separate setup. It consists in the design and realization of a Zeeman Slower whose magnetic field is produced using permanent magnets. I describe two successive magnet configurations and their performances. This work was published

in Review of Scientific Instrument in 2011 [41]. This Zeeman slower is the first step to the realization of a second cold atom experiment in Toulouse. After the realization of this independent project, I moved onto the older setup experiment.

- In the second chapter, I detail the experimental setup that allows us to produce Rubidium Bose-Einstein condensates.

- In the third, I present the setup of the attractive finite size optical lattice that is at the heart of the performed experiments. I also present the characterization of the lattice using Kapitza-Dirac diffraction.

- In the fourth chapter, I present theoretical tools useful to describe the motion of a particle in a periodic potential. I present the well known Bloch band structure, the Bloch states and their extension through the Mathieu equation to the case where the energy lies in a gap of the band structure.

- In the fifth chapter, I present the experimental realization of a Bragg mirror for guided matter wave. A propagating matter-wave impinges on the finite size lattice that acts in certain regions of parameter as a Bragg mirror in confined environment. These results have been published in Physical Review Letters in 2011 [42]

- In the sixth chapter, I present the realization of a Bragg cavity for atoms trapped in the center of the lattice between two Bragg-mirrors. Interestingly, this system allows to realize a tunnel barrier in real space which is to some extent equivalent to a sub micrometric repulsive tunnel barrier. This work has been recently submitted to Physical Review Letters and is available on arXiv [43].

- In the last chapter, I describe a scattering experiment on a time-modulated lattice. In this experiment, we use the modulation with time as a new degree of freedom which allows to perform complex momentum engineering on the impinging wavepacket. One important feature of the method is that it does not imply internal degrees of freedom. As a consequence, it is of very general use and is applicable to any atom. This work was published in Physical Review A in 2013 [44].

- Finally, I present a summary of the thesis in French.

Chapter 1

Design and realization of a permanent magnet Zeeman slower

Contents

1.1 Introduction **10**
1.2 Theoretical framework **10**
1.2.1 Principle 10
1.2.2 Simple model, magnetic field shape 11
1.2.3 The adiabatic following condition 12
1.2.4 Atomic structure 13
1.2.5 Choice of the magnetic field parameters 15
1.2.6 Longitudinal or transverse magnetic field 16
1.3 The dipole configuration **17**
1.3.1 Choice and modelization of the permanent magnets . . . 17
1.3.2 Position of the magnets 18
1.3.3 Measured magnetic field 20
1.4 Slowed atomic beam **22**
1.4.1 Experimental setup 22
1.4.2 Slowed beam velocity distribution 24
1.4.3 Flux as a function of the detuning 25
1.5 The Halbach configuration **26**
1.5.1 The principle 26
1.5.2 Field calculations 26
1.5.3 Magnets layout 27
1.6 Mechanics and field measurements **28**
1.6.1 Mechanical design 28
1.6.2 Shielding 28
1.6.3 Field parameters and measurement 30
1.7 Performances **31**
1.7.1 Needed laser powers 32
1.7.2 Repumper 33
1.7.3 MOT loading 34

1.8 Conclusion 35

1.1 Introduction

Many atomic physics experiments on quantum degenerate gases require a large initial sample of cold atoms, usually captured in a Magneto-Optical Trap (MOT). The MOT can be loaded directly from a hot atomic vapor, however, this technique limits the quality of the vacuum that can be achieved since only the slowest atoms are captured by the MOT. In order to load efficiently a MOT, it is useful to send a slow atomic beam (typically less than a few tenth of m/s) onto the MOT. A wide variety of experimental techniques have been developed for slowing atomic beam such as chirped slowers [45] or 2D-MOTs [46, 47]. In particular, since their first realisation [48], the Zeeman slowers (ZSs) have become very popular for loading MOTs. ZSs require a specific inhomogeneous magnetic field, which is generated in most cases using currents running in wires wound around the atomic beam. Recently, several Zeeman slowers using permanent magnets have been built for Sr atoms by Y. Ovchinnikov [49] and more recently by G. Reinaudi and colleagues [50]. The advantage of this method is to simplify the construction and the functioning of the ZS. In this chapter, we will present two successive realisations of permanent magnets ZSs for ^{87}Rb, the *dipole* and the *Halbach* configuration. Both demonstrated fully satisfactory operation and have important advantages compared to wire-wound setups. We will first present the basics of the theoretical framework and explain the choice of the different parameters. Then, we will present the two designs, the experimental realizations and their performances.

1.2 Theoretical framework

1.2.1 Principle

A Zeeman slower uses the radiation pressure from a resonant laser propagating backward from the atomic beam. Each time a photon is absorbed, the atom velocity along the beam axis decreases by $v_{\mathrm{R}} = \hbar k/m = 5.9$ mm/s for ^{87}Rb (k denotes the laser wavevector and m the atomic mass). The photon is then re-emitted spontaneously in a random direction. The spontaneous emission generates a random walk in the velocity space with a vanishing average and with a finite dispersion. To slow atoms by $\Delta v = 300$ m/s, about $N = m\Delta v/\hbar k \simeq 50000$ absorption-emission cycles are necessary. However, as the atoms are slowed down, the Doppler effect shifts the laser frequency away from the atomic transition, the Doppler shift reads:

$$\delta\omega = -\boldsymbol{k}\cdot\boldsymbol{v}, \tag{1.1}$$

where $\boldsymbol{v}$ is the atom velocity. An atom can then be slowed efficiently by only $\Delta v > \Gamma/k \sim 5$ m/s, (Γ being the transition linewidth), which is largely insufficient. To keep atoms on resonance, the change in the Doppler shift is compensated for by an opposite change of the Zeeman shift induced by a magnetic field B inhomogeneous along the direction of propagation z.

1.2.2 Simple model, magnetic field shape

In a two-level atom, the mean radiation pressure force resulting from the absorption-emission cycles reads:

$$F = \frac{\hbar k \Gamma}{2} \frac{I/I_0}{1 + 4\delta^2/\Gamma^2 + I/I_0}, \tag{1.2}$$

where the detuning δ takes into accounts the Doppler and Zeeman shifts

$$\delta = \omega_{\mathrm{L}} - \omega_{\mathrm{A}} = \delta_0 - \boldsymbol{k} \cdot \boldsymbol{v} - \frac{\mu B}{\hbar}, \tag{1.3}$$

where δ_0 is the shift-free laser detuning from the transition. I_0 and μ are respectively the saturation intensity and the magnetic moment associated with the cooling transition. In practice, one shapes the magnetic field such that the Zeeman shift compensates for the Doppler shift at all times (then δ is constant). To compute the corresponding field, one usually choose first the capture velocity v_{c}. This velocity corresponds to the maximum speed above which an an atom cannot be brought to rest. We now suppose that an atom initially at v_{c} experiences a constant deceleration. We calculate the corresponding trajectory and deduce in a self consistent manner the magnetic field that keeps the transition on resonance.

An atom can experience a maximum acceleration $a_0 = \Gamma\hbar k/(2m) = 1.1 \times 10^5$ m/s^2 reached for a detuning $\delta = 0$ and a saturated transition $s_0 = I/I_0 \gg 1$. To keep a safety margin, the magnetic field is calculated for only a fraction η of a_0 in the ZS design. The atom trajectory thus reads: $v(z) = \sqrt{v_{\mathrm{c}}^2 + 2az}$. Ideally, the atom velocity must be close to zero when the atom leaves the ZS. The apparatus length ℓ is then dictated by the capture velocity and the deceleration: $\ell = v_{\mathrm{c}}^2/(2\eta a_0)$. The condition $\delta = cte$ implies that the magnetic field takes the following form:[1]

$$B(z) = B_{\mathrm{b}} + \Delta B \left(1 - \sqrt{1 - z/\ell}\right). \tag{1.4}$$

The inhomogeneous part compensates for the Doppler shift. In practice, for multi-level atoms, a uniform bias field B_{b} may be superimposed to avoid level crossings as we shall see in Sec. 1.2.4 with the case of ^{87}Rb.

The atomic motion can be elegantly described representing the acceleration in

[1] This shape allows for the most compact ZS, however any field that fulfills the condition 1.8 is valid.

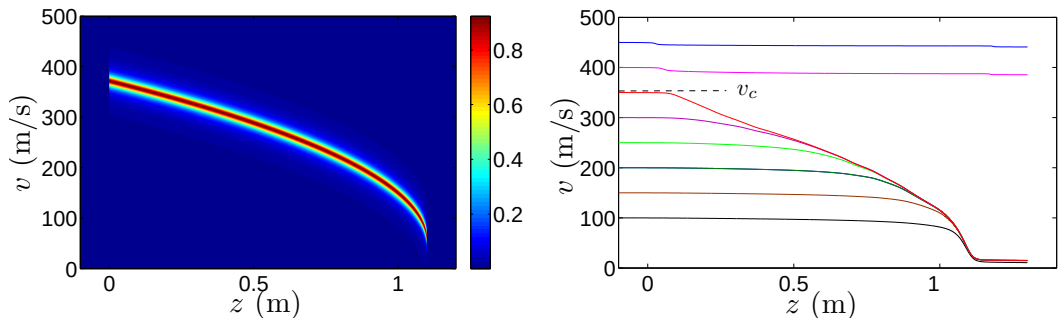

Figure 1.1: *(a) Acceleration divided by the maximum acceleration in phase space. (b) Simulation of a few trajectories. Atoms with an initial velocity $v_\mathrm{i} < v_\mathrm{c}$ are slowed down following the resonance condition.*

the phase space (z, v) (see FIG. 1.1 (a)). We see that in phase space there is a thin line where an atom is slowed that corresponds to the resonance condition. Changing the slowing laser detuning δ_0 shifts this line up and down. Figure 1.1 (b) depicts a few trajectories for various initial velocities. An atom initially out of resonance is not slowed down, therefore, its trajectory is an horizontal straight line. If the atom initial velocity $v_\mathrm{i} < v_\mathrm{c}$, its trajectory reaches the resonance line at a position z inside the slower. The atom then starts to be decelerated. If the magnetic field variation is small enough (see Sec. 1.2.3 for an accurate definition), the trajectory then follows the resonance condition

$$\delta_0 + kv - \frac{\mu B(z)}{\hbar} = cte. \tag{1.5}$$

Atoms with initial velocities $v_\mathrm{i} > v_\mathrm{c}$ are never slowed. At the ZS output, the atoms go abruptly out of resonance and propagate with a constant velocity.

Role of the parameters

Figure 1.2 shows how the slowing process depends on the magnetic field and the laser parameters. The capture velocity is related to the total magnetic field variation through $\Delta B = \hbar k v_c/\mu$. The bias field together with the laser detuning to the transition at rest δ_0 are related to the final output velocity through

$$v_f = -\frac{1}{k}\left(\delta_0 - \frac{\mu B_\mathrm{b}}{\hbar}\right). \tag{1.6}$$

1.2.3 The adiabatic following condition

When an atom reaches the resonance line, the atom trajectory clings to it and the atom is slowed under a specific condition. For a given laser intensity, the maximum acceleration experienced by an atom, reached for $\delta = 0$ reads: $a_\mathrm{max} = a_0/(1 +$

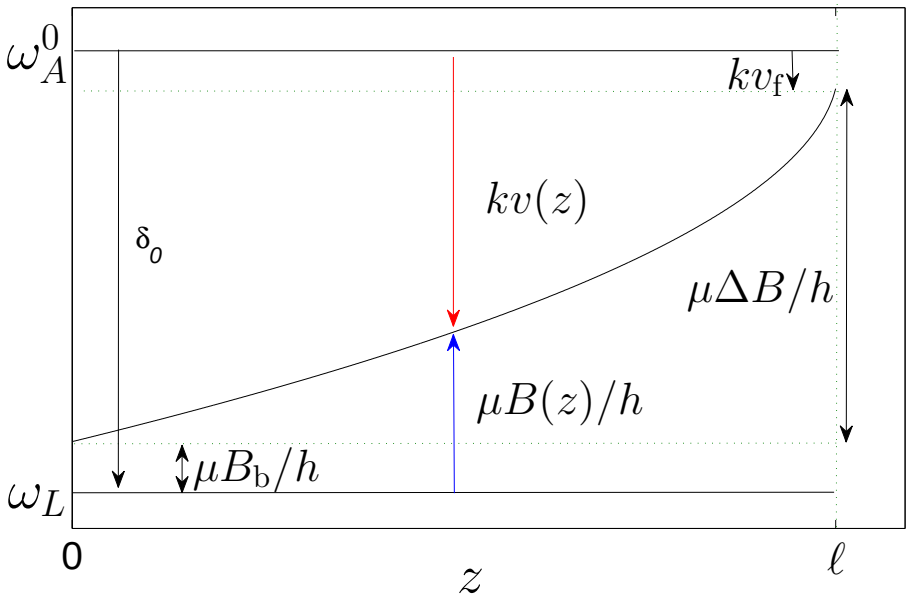

Figure 1.2: *The magnetic field variation ΔB dictates the capture velocity. The detuning at rest δ_0 must almost compensate for the Zeeman shift at the ZS output $\mu B_f = \mu(B_b + \Delta B)$. The difference between the two provides a non-zero output velocity.*

I_0/I). It is necessary that the acceleration chosen to determine the magnetic field parameters is smaller than a_{max}: $a < a_{max}$, which implies the following condition on the laser intensity:[2]

$$I/I_0 > \eta/(1-\eta). \tag{1.7}$$

Besides, by taking the derivative of the resonance condition (1.5), we see that the velocity of an atom that follows the resonance condition must respects $\mathrm{d}v/\mathrm{d}z = (\mu/\hbar k)\mathrm{d}B/\mathrm{d}z$. For a given laser intensity, the acceleration cannot exceed the on-resonance acceleration $a = v\mathrm{d}v/\mathrm{d}z < a_{max}$. This leads to the adiabatic following condition on the magnetic field gradient:

$$\left|\mu\frac{\mathrm{d}B}{\mathrm{d}z}\right| < a_0\frac{\hbar k}{v}\frac{s_0}{1+s_0}, \tag{1.8}$$

that sets a limit on the level of admissible imperfections (that cause sudden variations of B).

1.2.4 Atomic structure

Let us now determine quantitatively the field parameters. First, we need to remind the main lines of interest in the ^{87}Rb atomic structure. The ground state $5S_{1/2}$ is composed of two hyperfine states $F = 1$ and $F = 2$ separated by 6.8 GHz. There

[2] We see here the importance of taking $\eta < 1$.

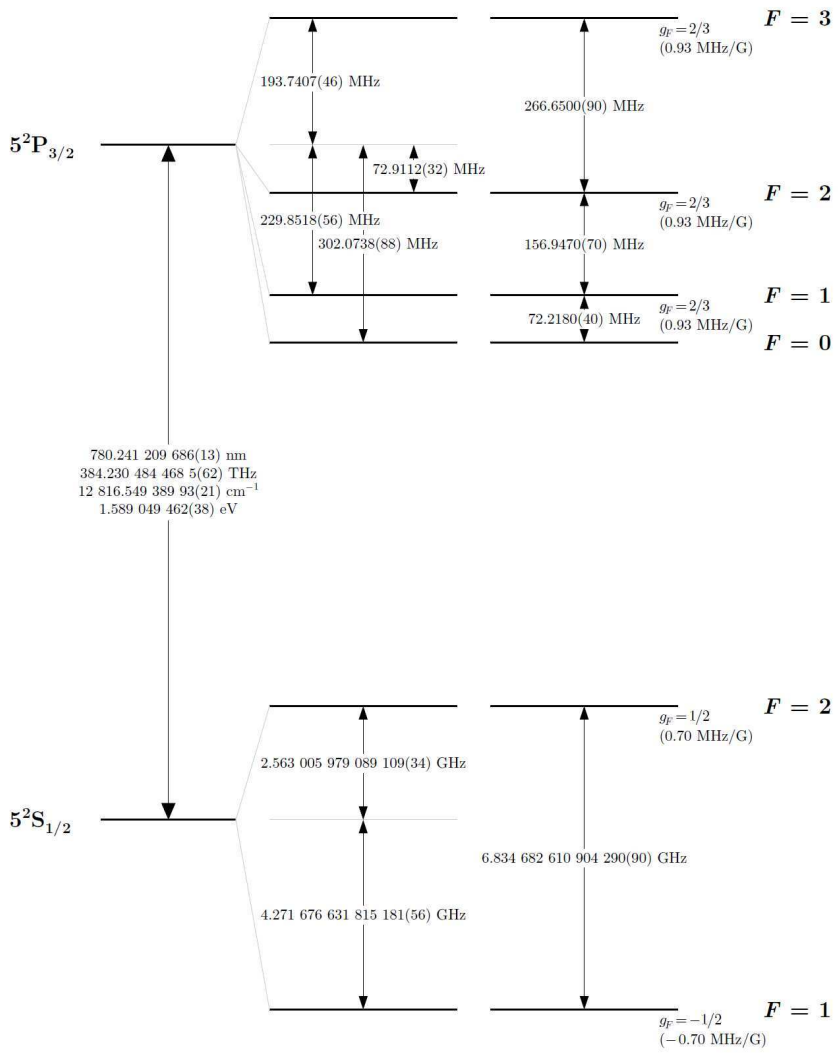

Figure 1.3: *Hyperfine structure of ^{87}Rb. We use the transition $F = 2 \rightarrow F' = 3$ as cooling transition. Figure reproduced from reference [51].*

is a fine structure in the first excited levels $5P_{1/2}$ and $5P_{3/2}$ at 795 and 780 nm respectively. In the following, we are only interested by the $5P_{3/2}$ manifold that comprises four hyperfine states (see FIG. 1.3).

In the presence of an external magnetic field, the different magnetic levels are split and the transitions are shifted by the Zeeman effect (see FIG. 1.4). The cooling transition must be a closed transition so atoms perform a great number of cycles without being pumped into an uncoupled state. In the case of ^{87}Rb, two choices ara available: $m_F = 2 \rightarrow m_{F'} = 3$ and $m_F = -2 \rightarrow m_{F'} = -3$ that are associated respectively with a decreasing or increasing magnetic field.[3] Even though the first ZS used a decreasing field [48], this choice is in general less favorable and makes it hard

[3]These are also the only transitions that have a linear Zeeman shift at all fields.

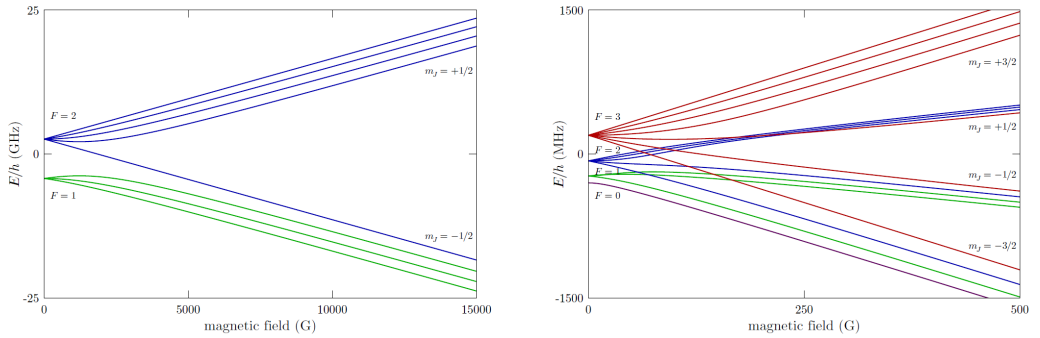

Figure 1.4: *Hyperfine structures in an external magnetic field: ground levels* $5^2S_{1/2}$ *(left pannel) and excited levels* $5^2P_{3/2}$ *(right pannel). We use the transition* $m_F = -2 \to m_{F'} = -3$ *as cooling transition. Figure reproduced from reference [51].*

to obtain low output velocity [52].[4] We thus set the slowing laser on the transition $m_F = -2 \to m_{F'} = -3$ that has a magnetic moment $\mu = -\mu_B$. This transition corresponds to an angular momentum variation $\Delta m = -1$. As a consequence, we need to use σ^- polarized light.

In addition, we observe in FIG. 1.4 that crossings between different hyperfine states occur at about 100 G. These crossings must be avoided to prevent depumping to the $F = 1$ ground state; this is achieved by adding a bias magnetic field B_b.

The following table remind some relevant physical constant for ^{87}Rb.

m	1.44×10^{-25} kg
μ	$-h \cdot 1.4$ MHz/G
Γ	$2\pi \cdot 6.1$ MHz
I_0	1.6 mW/cm^2

1.2.5 Choice of the magnetic field parameters

The magnetic field shape has two free parameters, ΔB and B_b. The field variation is related to the capture velocity through $\Delta B = \hbar k v_c/\mu$. In order to capture an important fraction of the thermal beam, the capture velocity must be on the same order of magnitude as the typical thermal velocity ($v_{th} \sim 300$ m/s for an effusive beam of Rb at 130° C) of the unslowed atomic beam. We thus choose $v_c = 330$ m/s, this implies that $\Delta B = 300$ G. Furthermore, the bias field B_b must be high enough to avoid the level crossings around 100 G. We chose $B_b = 200$ G (the field at the output of the ZS is thus $B_f = 500$ G). The length of the ZS is set at 1 m,

[4] In a decreasing field ZS, the output velocity varies sharply as a function of the detuning for low output velocity. It then becomes difficult to outcouple atoms a velocity small enough to load a MOT.

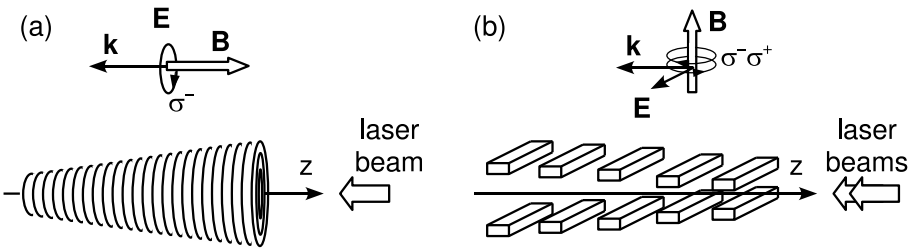

Figure 1.5: *(a) Conventional configuration of a wired wound ZS. The field is longitudinal, and the light polarization is circular. (b) ZS using permanent magnets and a transverse field. In this configuration, the field is transverse. We choose a polarization orthogonal to the quantization axis that can be decomposed into two circular polarization. A repumper beam is then necessary.*

which corresponds to an acceleration about half of the maximum acceleration. The following table presents the different field parameters.

ΔB	300 G
B_b	200 G
ℓ	1 m
v_c	330 m/s
η	0.48

1.2.6 Longitudinal or transverse magnetic field

In the conventional realisation of ZSs, the magnetic field is generated by currents running in a solenoid wrapped around the atomic beam. The magnetic field is then collinear with the light wave vector $\boldsymbol{k}$. In this longitudinal configuration, it is possible to produce light in any polarization state (we define the polarization in regard to the quantization axis fixed by the magnetic field direction). However, as we shall see, in our case, the magnetic field is orthogonal to $\boldsymbol{k}$. Thus, any incoming polarization possesses *a priori* π and $\sigma^\pm$ components: it is not possible to create a pure σ^- polarization state (see FIG. 1.5 and Ref. [53]). As a consequence, even if the light with the wrong polarization is out of resonance, the σ^+ and especially π components excite atoms to the $m_{F'} = -2$ and -1 states respectively. From these states, they can fall into the $F = 1$ ground state. Repumping light is thus necessary between the $F = 1$ and $F = 2$ manifolds.[5] The detrimental effect of the unwanted polarization components is minimized when the incoming polarization is perpendicular to the magnetic field, because there is no π contribution in that case. However, we should emphasize that if the magnetic field is transverse, half of the light necessarily has the wrong polarization and is lost.

[5] In a conventional longitudinal ZS, a repumper is often added to increase the atomic flux but is not mandatory.

1.3 The dipole configuration

We will now present configurations of magnets that produce the desired magnetic field. The first configuration, that we call the *dipole* configuration, is inspired by reference [49].

1.3.1 Choice and modelization of the permanent magnets

Let us first describe the magnetic materials. Since the years 1980, rare earth magnets NdFeB have become progressively compact and cheap and are now of common use in industry for their excellent magnetic properties: a residual magnetic field B_r on the order of 10 kG and a coercive field $H_\mathrm{ci} \simeq 1,1$ kA/mm. Specifically, we used the grade NE35 from HKCM that has a higher maximum operation temperature than other grades. Such rare earth material is very hard from a magnetic point of view so that, despite demagnetizing fields that can be as high as $H_\mathrm{dem} = -0.75$ kA/mm (see Apendix), the magnetization is hardly affected. Therefore, field calculations are particularly simple and reliable because the contributions of each magnet can be added independently.

Modelization of the magnets

It is possible to model the magnets by simple current distributions. Indeed, the vector potential $\boldsymbol{A}(\boldsymbol{x})$ produced by the distribution of magnetization $\boldsymbol{M}(\boldsymbol{x'})$ reads

$$\boldsymbol{A}(\boldsymbol{r}) = \frac{\mu_0}{4\pi}\int_V \frac{\boldsymbol{M}(\boldsymbol{r'}) \times (\boldsymbol{r}-\boldsymbol{r'})}{|\boldsymbol{r}-\boldsymbol{r'}|^3}\mathrm{d}^3r'. \tag{1.9}$$

This can be rewritten as

$$\boldsymbol{A}(\boldsymbol{r}) = \frac{\mu_0}{4\pi}\int_V \nabla \times \left(\frac{\boldsymbol{M}(\boldsymbol{r'})}{|\boldsymbol{r}-\boldsymbol{r'}|}\right) + \frac{\boldsymbol{\nabla} \times \boldsymbol{M}(\boldsymbol{r'})}{|\boldsymbol{r}-\boldsymbol{r'}|}\mathrm{d}^3r'. \tag{1.10}$$

The second term cancels out because the magnetization is homogeneous and the first term can be replaced by the surface integral

$$\boldsymbol{A}(\boldsymbol{r}) = \frac{\mu_0}{4\pi}\int_S \boldsymbol{n} \times \frac{\boldsymbol{M}(\boldsymbol{r'})}{|\boldsymbol{r}-\boldsymbol{r'}|}\mathrm{d}S, \tag{1.11}$$

where we recognize the vector potential produced by a surface current $\boldsymbol{J_s}$ running around the magnet (see FIG. 1.6).

To generate with a single coil the same magnetic field as the one produced by a 5 mm thick magnet, one would need a current as high as 5000 A.

From now on, we will consider the field produced by the equivalent solenoid in the calculations. We use cuboid magnets with the magnetization along the $\boldsymbol{y}$ axis,

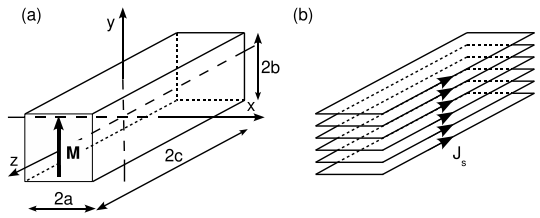

Figure 1.6: *A rectangular magnet is equivalent to a sheet of current orthogonal to the magnetization.*

and note their size $2a \times 2b \times 2c$. Integrating the Biot and Savart's law on one coil and then along the axis $\boldsymbol{y}$, we find for the field produced by a rectangular solenoid:

$$\boldsymbol{B}_{\rm sol}(x,y,z) = \mu_0 J_s \sum_{n,p,q=0}^{1} (-1)^{n+p+q} \boldsymbol{\mathcal{B}}\left(x-(-1)^n a, y-(-1)^p b, z-(-1)^q c\right), \quad (1.12)$$

where $\boldsymbol{\mathcal{B}}$ is a vectorial field whose components reads:

$$\begin{aligned}
\mathcal{B}_x(X,Y,Z) &= \frac{1}{2}\ln\left(\frac{\sqrt{X^2+Y^2+Z^2}-Z}{\sqrt{X^2+Y^2+Z^2}+Z}\right) \\
\mathcal{B}_y(X,Y,Z) &= -\arctan\left(\frac{Y\sqrt{X^2+Y^2+Z^2}}{X\,Z}\right) \\
\mathcal{B}_z(X,Y,Z) &= \mathcal{B}_x(Z,Y,X).
\end{aligned}$$

We used this formula in all the calculations on the dipole configuration.

1.3.2 Position of the magnets

In the proposal from Y. B. Ovchinnikov [49], the magnets are disposed in two rows on each side of the central pipe. The magnetization is directed toward the axis and the size and position of each magnet is adjustable (see FIG. 1.5 (b)). We used a similar geometry in our first prototype with a major improvement. In the Ovchinnikov proposal, the magnets have a cylindrical shape (they can be roughly considered as point-like dipoles) and are close to the atomic beam. As a consequence, the magnetic field varies on a cross section by up to 100 G on a section of CF-16 pipe.

In our configuration, we used elongated magnets ($100\times20\times5$ mm) and we placed them further away from the pipe to guarantee a better transverse homogeneity. However, we then need to use a larger of amount of magnets to compensate for the field decay with the distance from the axis. We fixed a tolerance threshold of 12 G on the transverse homogeneity.[6] In practice, the magnets then have to be placed at

[6] This corresponds to the order of magnitude of the width of the atomic transition.

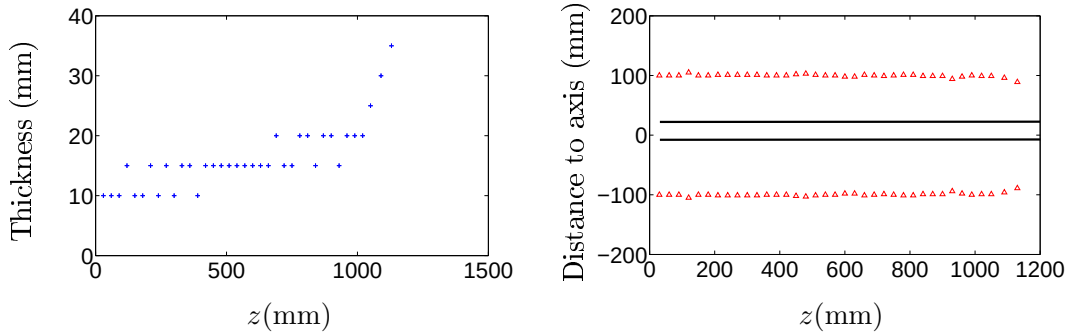

Figure 1.7: *Thickness and position of the magnets in the final configuration. The pipe is depicted as the central black line.*

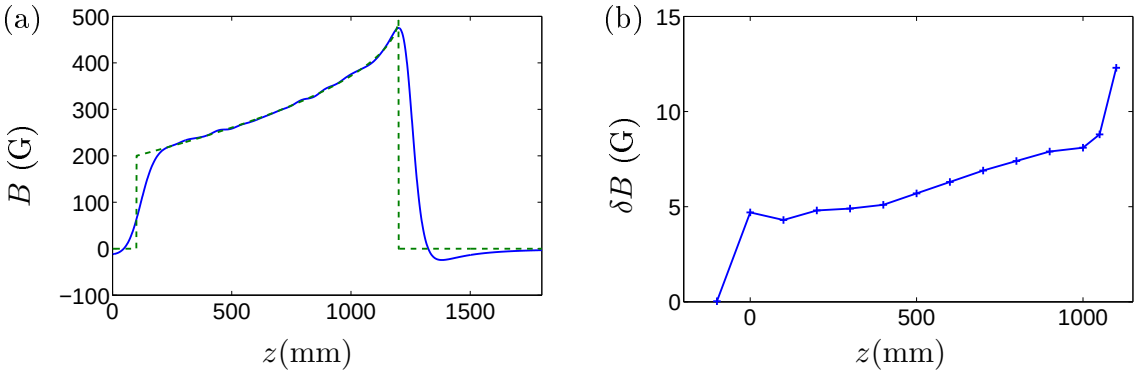

Figure 1.8: *(a) Target and calculated magnetic field (dashed and plain line respectively). The difference between the two is less than 5 G in the region of interest* 200 mm < z < 1200 mm. *(b) Deviation on a transverse section as a function of the longitudinal coordinate.*

about 10 cm from the axis.

In order to keep the machining as simple as possible, we chose a support in one piece, and the magnets were all positioned at about 10 cm from the axes. To obtain the desired longitudinal variation, we varied essentially the magnets thickness (by stacking them) and only changed the distance to axis to obtain a fine adjustment. We used a 3D numerical calculation relying on the Eq. (1.12) to optimize the magnets thicknesses and positions. In the end, we used 240 of our elongated magnets whose positions are given in FIG. 1.7.

Figure 1.8 (a) depicts the ideal and calculated fields on the axis. The transverse inhomogeneity increases near the Slower output. At the end of the ZS, the transverse inhomogeneity is below 12 G (see FIG. 1.8 (b)). To hold the magnets, we built two structures in aluminum in which we drilled gaps every three cm at different depths corresponding to the magnets distances to the axis. The magnets were inserted in the gaps and held by plexiglass protections. The distance to axes can be adjusted

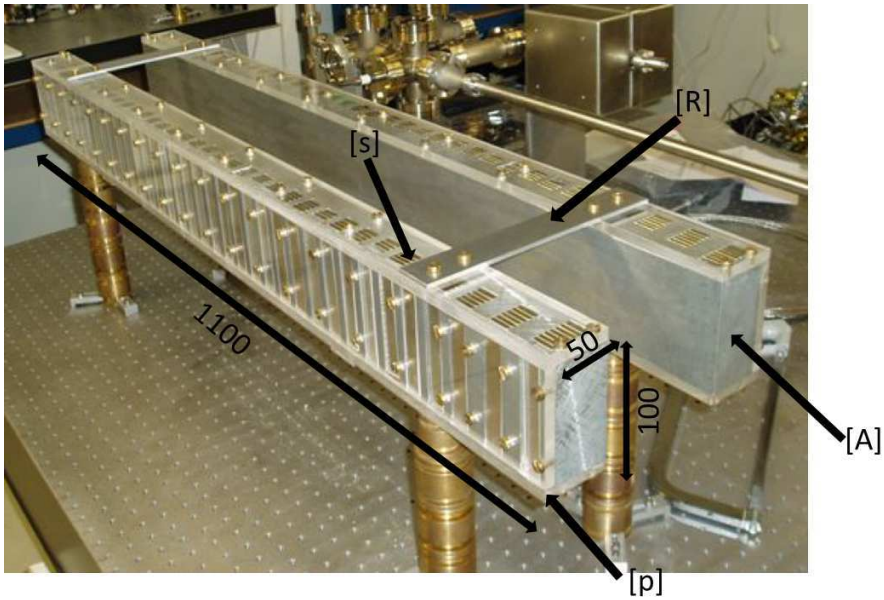

Figure 1.9: *Photo of the dipole configuration ZS: [A] Aluminum structure, [s] gaps with variable depth, [p] plexiglass protections, [R] reinforcing plates. Dimensions are in* mm.

by adding plexiglass slices under the magnets (see FIG. 1.9).

1.3.3 Measured magnetic field

We measured the magnetic field on the axes with a Hall probe and compared it with the calculated field. We found that the actual field is 12 % larger than the simulated one, probably because we underestimated the value of the magnetization in the calculations. The capture velocity is then slightly increased, and it does not cause further problems. Apart from this global factor, the standard deviation to the simulation is 8.4 G, which represents 2.4% of the mean magnetic field (see FIG. 1.10).

Similarly, we measured the field on a transverse section located at 5 cm from the output (see FIG. 1.11). The deviation from the simulation is below 4 G. We thus expect that the slowing process occurs efficiently on the whole section of the Slower.

Magnetic shielding

Since we use an important volume of magnets at a relatively large distance from the axis, the magnetic field decays on $\sim$ 10 cm after the output of the Slower (see FIG. 1.10). This stray magnetic field can perturb the MOT downstream the ZS; to circumvent this limitation, we use a magnetic shielding. As a matter of fact, a magnetic shielding is particularly efficient when it forms a small angle with the field lines. We thus built a soft iron shielding whose shape has been optimized to form an angle of approximately 15° with the field lines (see FIG. 1.12 (a)). To further reduce

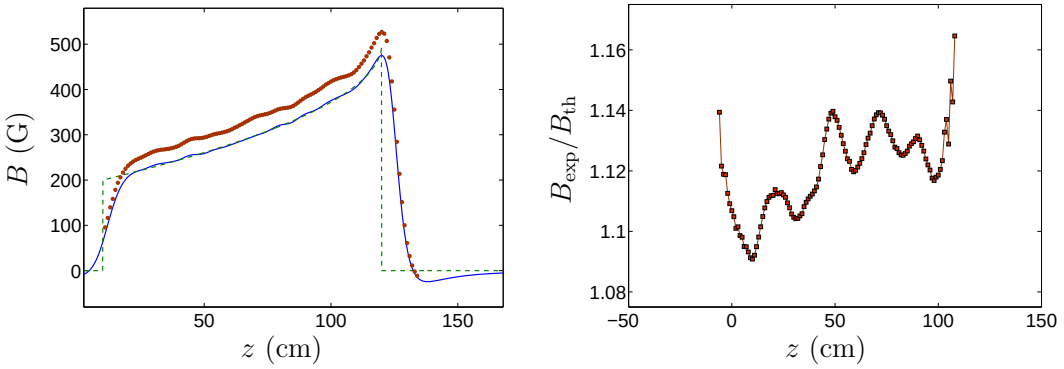

Figure 1.10: *Left: target (dashed line), calculated (plain line) and measured (circles) magnetic field. Right: ratio of the measured to the calculated fields. There is an overall difference of about 12 G.*

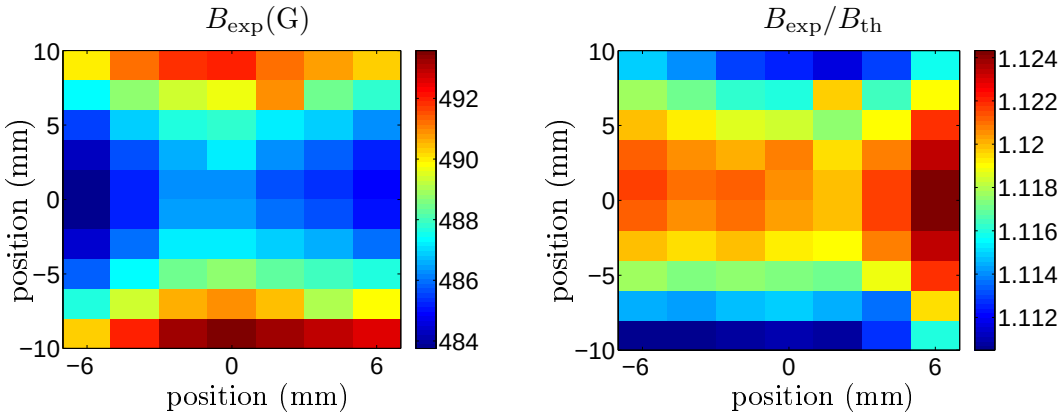

Figure 1.11: *Left: measured field in a transverse section. Right: ratio of the measured to calculated field.*

the stray field on the MOT chamber side, we installed two additional plates with 1 cm between them at the output of the ZS. The residual stray field is the consequence of the unavoidable hole needed for the pipe in the shielding. Thanks to the shielding, we measured an important decrease of the magnetic field at the chamber position that falls at a few G level (see FIG. 1.12 (b)). The shielding also increases the field inside the Slower. This can be simply understood using the method of image charges. For a magnetic shield with an infinite magnetic permeability, the field lines are parallel to the shielding. Such field lines can also be produced by sources of magnetic field symmetric with respect to the shielding. The magnetic field is then the same as the one that would be produced by the ZS itself and its images in every direction. The fields produced by all images add up in the central region.

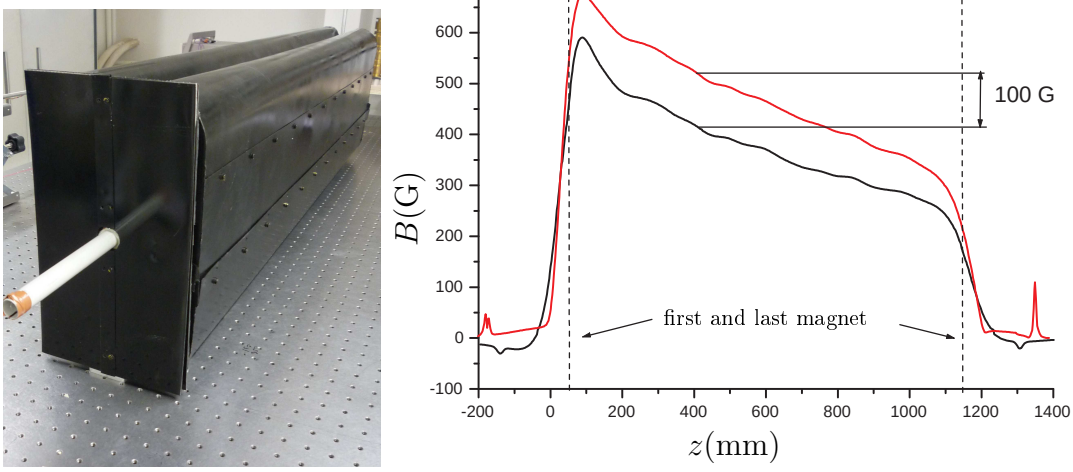

Figure 1.12: *(a) Magnetic shielding conceived to make a small angle with the field lines. (b) Without shielding, the magnetic field is on the 10 G range in the MOT chamber. It falls at the G level with the shielding. Inside of the Slower, the field is reinforced by* ~ 100 G *by the shielding.*

1.4 Slowed atomic beam

In this section, we present the experimental performances obtained with the dipole configuration.

1.4.1 Experimental setup

Vacuum system

Figure 1.13 presents a sketch of the setup. At one end, the MOT chamber is a spherical octagon from Kimball physics (MCF600-SO200800). It has two horizontal CF-100 windows and eight CF-40 ports. It is pumped by a 20 L/s ion pump. One CF-40 port is connected to the 1200 mm-long CF-16 pipe around which the Zeeman slower is set. At the other end, one finds a first six-way cross, used to connect a 40 L/s ion pump, a thermoelectrically cooled cold finger and six-way cross that holds another cold finger, an angle valve for initial evacuation of the chamber and a stepper-motor-actuated beam shutter. Finally, the in-line port holds the recirculating oven (see Appendix E).

Slowing lasers

As outlined in the section 1.2.4, the Zeeman slower operates on the closed transition $\sigma^-, F = 2,\ m_F = -2 \rightarrow F' = 3,\ m_{F'} = -3$. However, as the magnetic field is here perpendicular to the propagation axes, the incoming polarization state possesses

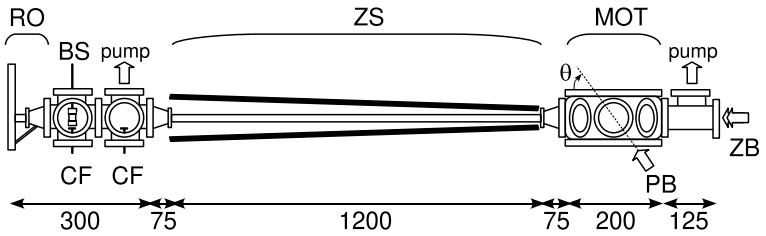

Figure 1.13: *Sketch of the overall experimental setup. [RO] recirculating oven, [BS] beam shutter, [CF] cold finger, [ZS] Zeeman slower, [MOT] MOT chamber, [ZB] Zeeman cycling and repumping beams, [PB]* $\theta = 56°$ *probe beam.* $45°$ *and* $90°$ *probe beams are sent through the horizontal windows depicted on the MOT chamber. Dimensions in* mm, not rigorously to scale.

also a π component that populates the $m_{F'} = -2$ state from which spontaneous emission populates $F = 1$ ground state. Repumping light is thus necessary between the $F = 1$ and $F' = 2$ manifolds. The detuning of the cycling light below the transition corresponding to our field parameters is $\delta_0 \simeq -800$ MHz. Such rather large detunings are realized by sending a master laser through two 200 MHz AOM's in a double pass configuration before locking on a resonance line using saturation spectroscopy. The repumper is simply locked on the red-detuned side of the broad Doppler absorption profile. The two master lasers are free-running diodes with a low ~ 5 MHz linewidth (Sanyo DL7140-201S). Beams are recombined on a cube and pass through a polarizer. Then they are sent with the same polarization into a 1W Tapered Amplifier. A total power of more than 250 mW is available on the atoms after fiber coupling. The beam is expanded to about 23 mm (full width at $1/e^2$) and focused in the vicinity of the oven output aperture for better transverse collimation of the atomic beam.

Probe beam

Probe beams on the $F = 2 \rightarrow F' = 3$ transition can be sent in the chamber through the different windows and absorption is measured in this way at $45°$ or $90°$ from the atomic beam (see FIG. 1.13). Probing the beam with an angle makes the absorption or fluorescence velocity-dependent. Thus, by scanning the detuning to the transition Δ of the probe, we measure the velocity distribution of the atomic beam. The correspondence being

$$v = \frac{\Delta\sqrt{2}}{k}. \tag{1.13}$$

The fluorescence is collected through a CF-40 port by a large aperture condenser lens and focused on a 1 cm^2 PIN photodiode. Photocurrent is measured with a homemade transimpedance amplifier (typically 10 MΩ) and a low noise amplifier

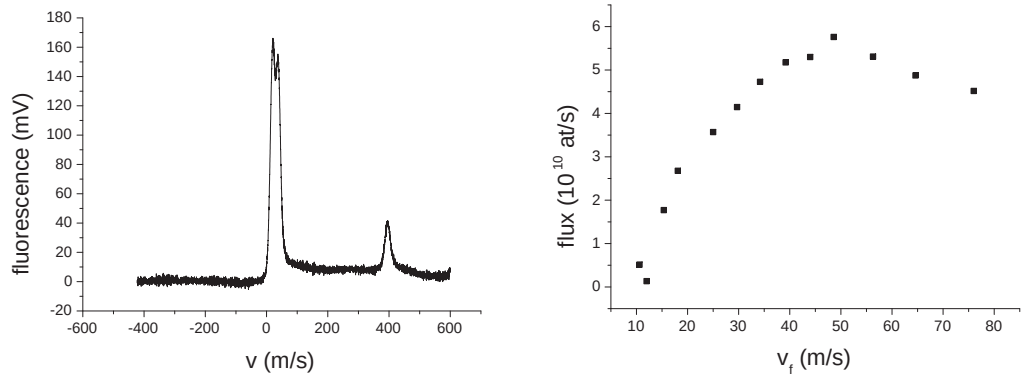

Figure 1.14: *(a) Typical fluorescence signal. The peak corresponding to the slowed atoms is split by Zeeman effect because of the stray field in the chamber. (b) Flux as a function of the output velocity. At* 30 m/s, *the output flux is* $\Phi \sim 4 \times 10^{10}$ at/s.

(Stanford Research Systems SR560) used with a moderate gain ($G = 5$) and a 3 kHz low-pass filter. Absorption is collected on a standard photodiode. A frequency scan without atoms is recorded and subtracted to the absorption signal. The frequency scans are averaged for 8-16 runs. During the measurements, the repumper beam on the $F = 1 \rightarrow F' = 2$ transition may be turned on.

1.4.2 Slowed beam velocity distribution

Figure 1.14 shows a typical fluorescence signal. A narrow peak appears at $v_{\rm m} =$ 30 m/s that has a velocity spread $\delta v = \pm 10$ m/s hardly distinguishable from the natural width of the transition. The smaller peak corresponds to the transition $F = 2 \rightarrow F' = 2$. Note that the main peak is split into two peaks separated by a few MHz. This splitting is due to the stray residual magnetic field from the Slower in the MOT chamber. Adding a compensation coil parallel to the large window of the vacuum chamber, we can merge the two peaks and estimate that the stray field is about 3 G.

In order to extract a quantitative estimate of the atomic flux, we use the absorption signal rather than the fluorescence. In this way we eliminate all geometric errors. From the absorption signal $A(v)$, we extract the maximum absorption $A_{\rm max}$, the mean velocity $\bar{v}$ and velocity spread δv. The atom flux then reads (see Appendix D)

$$\Phi = C \sin\theta \cos\theta D \frac{A_{\rm max} \bar{v} \delta v}{\lambda \Gamma \sigma_0}, \tag{1.14}$$

where C is a geometrical dimensionless parameter close to one and D is the atomic beam diameter.

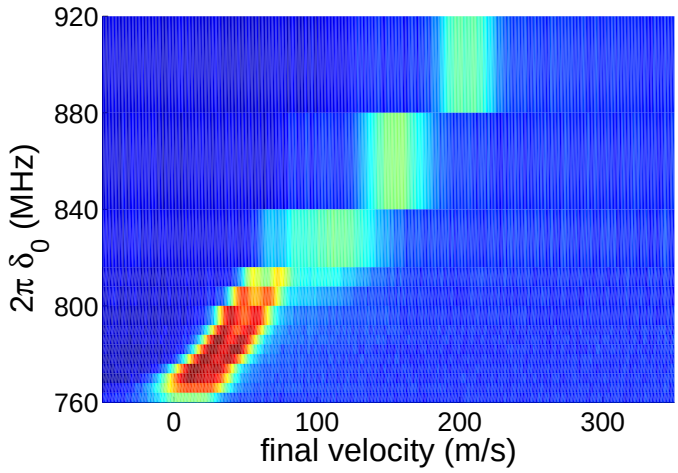

Figure 1.15: *Concatenated fluorescence signals as we vary the detuning of the slowing light δ_0. The output velocity varies linearly with δ_0. Beyond* 100 m/s*, a wider peak appears due to a premature outcoupling.*

1.4.3 Flux as a function of the detuning

We measured the output velocity for different detuning of the cycling light. The output velocity varies roughly linearly with the detuning with a slope $\alpha = 0,95$ m.s^{-1}/MHz (see FIG. 1.15). This slope does not fit with the naive model presented in the first section that predicts a slope $\alpha = 0,75$ m.s^{-1}/MHz. In Appendix B, we present further theoretical work to explain this difference.

For large output velocities, a wider peak appears, this is probably the consequence of the magnetic field imperfections. Indeed equation (1.8) shows that outcoupling can occur because of a bump of the magnetic field and that this effect is amplified at high velocity.

Finally, we calculate the total atomic flux using Eq. (1.14). The flux is roughly constant for output velocity $v_{\text{out}} > 40$ m/s and decreases at low velocity because the beam becomes divergent and atoms make collisions with the walls (see FIG. 1.14 (b)). $\Phi \sim 4 \times 10^{10}$ at/s at 30 m/s which is sufficient to load a MOT very efficiently.

The dipole configuration ZS produces very satisfactory atom flux. In this magnet configuration, a good transverse homogeneity is obtained at the expense of a large distance of the magnets to the axis. Therefore, a large amount of magnets ($V_{\text{mag}} = 2.4\ L$) is necessary which increases the size of the ZS and makes it hard to cancel out the stray magnetic field. In the next section, we thus present a more elegant configuration where the magnetic material is distributed all around the atomic beam.

1.5 The Halbach configuration

1.5.1 The principle

The way to get a homogeneous magnetic field in a transverse cross section is to distribute the magnetic material all around the atomic beam to make a so-called Halbach cylinder. In the context of atom physics, fields with a linear or quadratic dependence have been used to realize refractive atom-optical components [54]. For a ZS, a highly uniform field is required. Following [55], we consider a magnetized rim such that the magnetization $\boldsymbol{M}$ at an angle θ from the y-axis makes an angle 2θ with respect to the same axis (FIG. 1.16 (a)). Using such ideal configuration, the magnetic field is homogeneous inside the rim and cancels out outside. It reads (see Appendix F):

$$\boldsymbol{B}_{\mathrm{Hal}}(\boldsymbol{r}) = \begin{cases} \boldsymbol{0} & \text{for} \quad r > R_{\mathrm{ext}}, \\ B_{\mathrm{R}} \ln\left(\dfrac{R_{\mathrm{ext}}}{R_{\mathrm{int}}}\right) \hat{\boldsymbol{y}} & \text{for} \quad r < R_{\mathrm{int}}, \end{cases}$$

Numerical investigations (see next section) indicate that a 8-pole Halbach-like configuration as depicted in Fig. 1.16 (b) is able to produce fields on the order of 600 G with a homogeneity better than 1 G over a 16 mm cross section. Higher field strength and/or beam diameters are easy to achieve if necessary.

More detailed studies demonstrate that deviations on a typical 600 G magnetic field stay below the ± 1 G limit for ± 0.2 mm mispositioning of the magnets which is a common requirement on machining. Likewise, the same variations are observed for $\pm 2.5\%$ dispersion in the strength of the magnets. A rough statistical analysis on a sample of $20 - 30$ magnets convinced us that it is the right order of magnitude.

1.5.2 Field calculations

Magnets modeling

The whole setup is based on elongated $6 \times 6 \times 148$ mm^3 NdFeB magnets (HKCM, part number: Q148x06x06Zn-30SH) with the magnetization orthogonal to the long axes. Because these magnets have a square cross section ($2a \times 2a$), it is possible to use a dipole approximation. The long magnets can be decomposed in a set of cubic magnets. Then, one easily checks numerically that when the distance to the magnet is larger that twice the side, the field of the associated dipole is an accurate approximation of that of the actual magnet to better than 2%.[7] This approximation makes the calculations very fast on a conventional personal computer.

[7] Convergence can be much slower for cuboids with different aspect ratios. In particular this approximation is not verified for the magnets used in the dipole configuration.

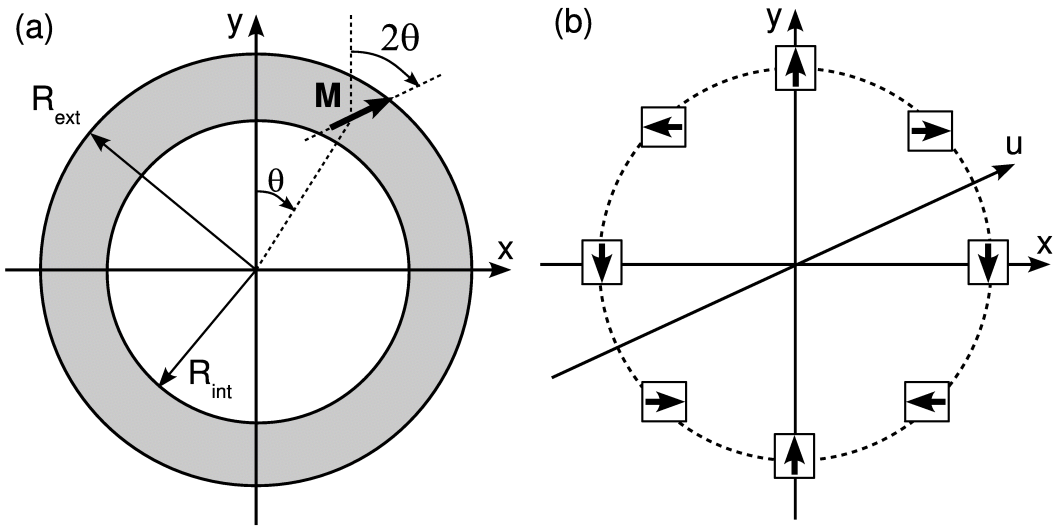

Figure 1.16: *(a) Notations for Halbach cylinder. (b) Transverse cross section showing a 8-pole approximation of the Halbach configuration.*

1.5.3 Magnets layout

In principle, the field magnitude can be adjusted varying the amount, the density and/or the position of the magnetic material. The availability of very elongated magnets ($c/a \approx 25$) directed us toward a simple layout. We vary only the distance to the axis $d(z)$. At first approximation the elongated magnets can be considered as infinite. This is equivalent to an infinite array of magnetic dipoles. The magnetic field strength then decreases as the inverse of the distance to the magnet squared. Thus, to produce the field $B(z)$ a good *ansatz* for $d(z)$ is:

$$d(z) = d(\ell)\sqrt{\frac{B(\ell)}{B(z)}}. \tag{1.15}$$

As a matter of fact, this guess turns out to be both very efficient and close to a linear function. Numerical calculations show (see Fig. 1.17) that a linear approximation of Eq. (1.15) can be optimized to give a field within ± 3 G from the ideal one over the most part of the slower. Such deviations are completely irrelevant concerning the longitudinal motion. Magnets are then positioned on the generatrices of a cone and the mechanics is then straightforward (Sec. 1.6.1).

Naturally, the agreement is not so good at both ends where the ideal profile has sharp edges while the actual field spreads out and vanishes on distances comparable to the diameter on which magnets are distributed. The actual ΔB is reduced which lowers the capture velocity and thus the beam flux. We made additional sections of eight extra cubic magnets in Halbach configuration designed to provide localized

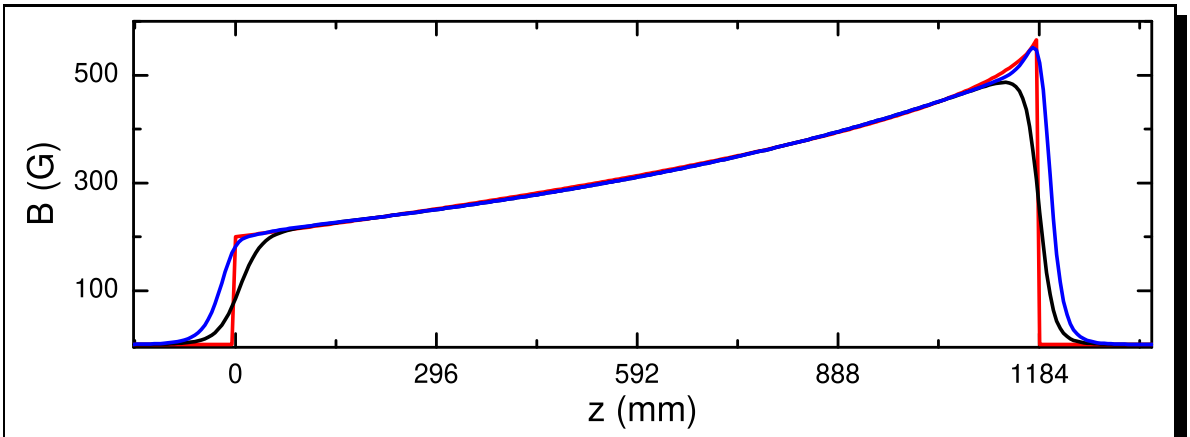

Figure 1.17: *Ideal (red) and calculated profiles, without (black) and with (blue) end caps.*

improvement on the field profile at both ends ('*end caps*'). As seen on Fig. 1.17, matching to the ideal profile is enhanced, especially at the high field side where the ideal profile exhibits a marked increase.

1.6 Mechanics and field measurements

1.6.1 Mechanical design

The Zeeman slower consists in 9 mounts supporting 8 U-shaped aluminum profiles (see Fig. 1.18). The U-shaped profiles go through the mounts by means of square holes evenly spaced on a circle whose diameter decreases from mount to mount according to Eq. (1.4) and Eq. (1.15). Magnets are then inserted one after the other in the U-shaped profiles and clamped by a small plastic wedge. End caps are filled with the suitable block magnets and screwed together with their spacer in the first and last mount. The whole setup is then very rigid and all parts tightly positioned. Indeed, as said before, calculations are very reliable and Zeeman slower operation is known to be robust so there is no need for adjustment. This setup can even be simplified by removing some mounts: the Zeeman slower we use now has only three mounts. Mounts are made of two parts screwed together. The Zeeman slower can then be assembled around the CF-16 pipe without vacuum breaking *e.g.* after baking out the UHV setup.

1.6.2 Shielding

The 8-pole configuration produces very little field outside (see Fig. 1.20 (a)), except of course, at both ends. However, to lower stray fields even further, we have made a rectangular single-layer shield from a 1 mm-thick soft iron sheet wrapped around

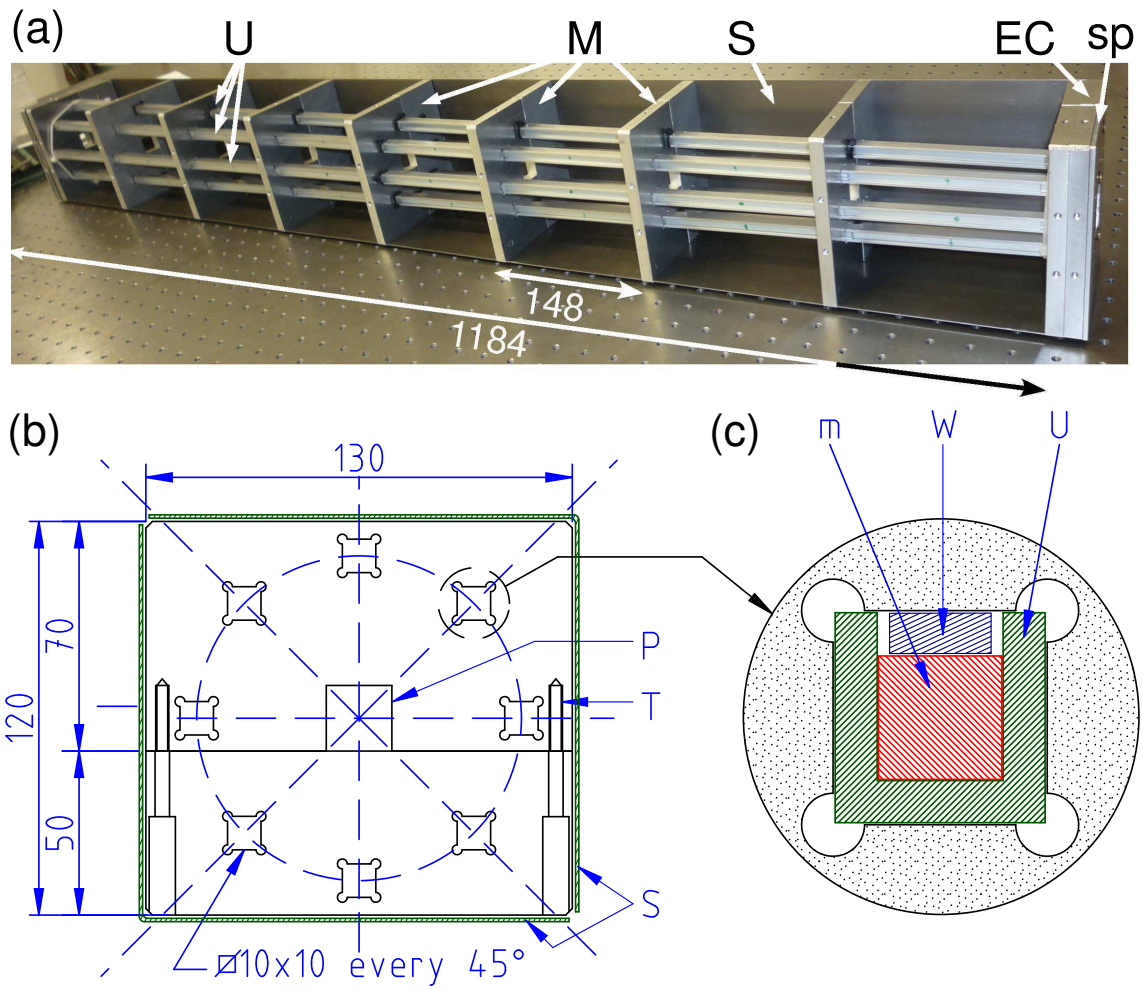

Figure 1.18: *(a) Picture of the Zeeman slower: [M] mounts, [EC] output end cap screwed in last mount, [U] U-shaped profiles, [S] half part of the shield, [sp]* 5 mm *spacer between end cap and shield side. (b) Individual mount; [T] threading to screw the two parts of the mount together, [P] central square milling in which CF-16 pipe goes through. (c) detail of a square hole to show U-shaped profiles insertion, magnets [m] and plastic wedge [W]. Dimensions in mm.*

the mounts. In this way, mechanical properties and protection are improved. As seen on Fig. 1.19 (a), the inner field is almost unaffected. On the contrary, the outer magnetic field falls down much quicker all the more since the plateau around 0.5 G in Fig. 1.19 (b) is probably an artifact associated with the probe. In practice, no disturbance is detected neither on the MOT nor on optical molasses 125 mm downstream.

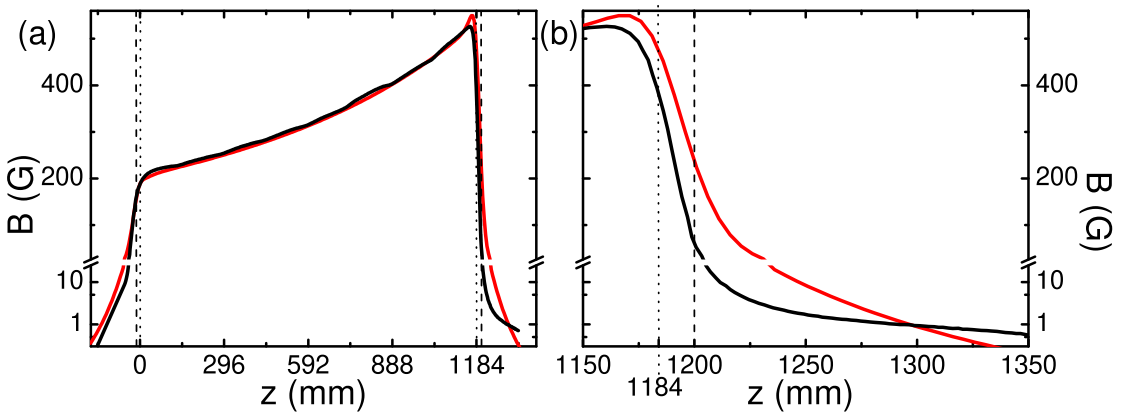

Figure 1.19: *Calculated (red) and measured (black) magnetic field profiles. (a) Scan along the beam axis. (b) Close up of the output region. In the calculation the shield is not taken into account. Dotted and dashed lines indicate the Zeeman slower and the shield physical ends. Log scale below break.*

1.6.3 Field parameters and measurement

The length of the Zeeman slower is $\ell = 1184$ mm corresponding to eight sections of 148 mm-long magnets. The capture velocity is then $v_c \approx 450$ m/s and $\Delta B = 388$ G. A bias field $B_{\text{bias}} = 200$ G is added to avoid low-field level crossings around 120 G. These field parameters together with the magnet size and properties determine the distance and angle to the axis of the magnets. In our case, the best choice was a slope of -15.9 mm/m corresponding to $d(0) = 49.5$ mm and $d(\ell) = 30.7$ mm. Entrance and output end caps are both made of 10 mm-side cubic magnets of N35 grade ($B_R = 11.7$ kG). They are located on circles whose diameters are 94.0 mm and 66.0 mm respectively.

Figure 1.19 displays a longitudinal scan of the magnetic field on the axis of the Zeeman slower with end caps and shield. It can be first noticed that the longitudinal profile is intrinsically very smooth as the magnets make a uniform magnetized medium throughout the Zeeman slower. After calibration of the magnetic material actual remanent field, deviations from the calculated profile are less than a few Gauss. Besides, one usually observes only localized mismatches at the junction between two magnets attributed to the dispersion in the magnetization of the magnets. The shield input and output sides flatten the inner field at both ends. Of course the effect decreases when they get further apart but the Zeeman slower should not be lengthened too much. A 5 mm spacer (tag [sp] in Fig. 1.18) is a good trade off. Then, the actual magnetic field measured parameters are $B_{\text{bias}} = 200$ G and $\Delta B = 350$ G only slightly smaller than the calculated value.

Figure 1.20 depicts a transverse cut of the magnetic field. It is realized along the u-direction of Fig. 1.16 near the middle of the Zeeman slower ($z \sim 460$ mm). The shield was removed to allow the probe to go through. It exhibits the two expected

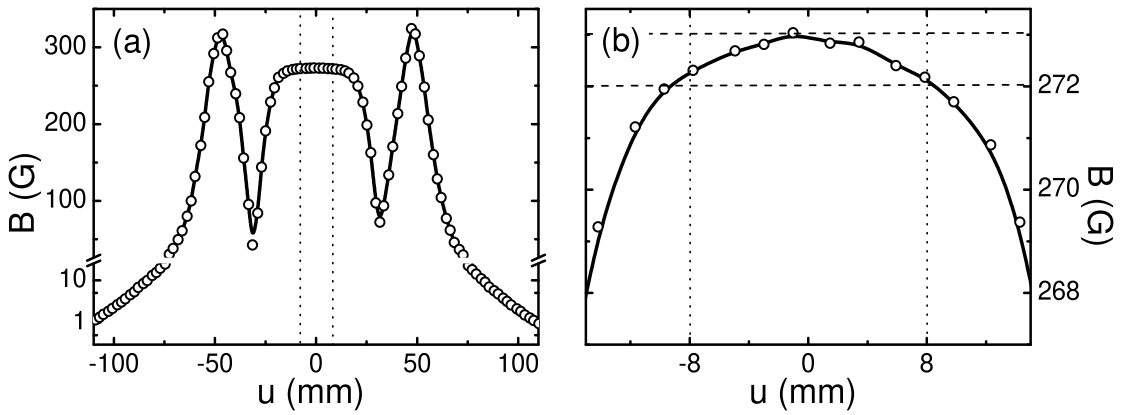

Figure 1.20: *(a) Measured magnetic field without shield across the beam axis at* $z \sim 460$ mm *along the u-direction of Fig. 1.16. (b) Close up of the central region. Dashed lines indicate the atom beam extension and a* 1 G *magnetic field span. Log scale below break. The shield was removed to allow the probe to go through. With the shield, the inner field is almost unaffected and the outer field is below the probe sensitivity.*

features: (i) little outer field (ii) highly homogeneous inner field. In the vicinity of the axis, the measured profile is however less flat than expected. This is mainly due to the finite size of the probe. Anyway, magnetic field deviations stay within a Gauss or so in the region of interest. With the shield, the outer field is below probe sensitivity.

1.7 Performances

The laser system for the slowing and detection is the same as for the dipole configuration. The velocity distribution presents here a simple peak (no splitting) (see FIG. 1.21), which is consistent with the sub-Gauss stray field. We also measure the velocity distribution in the absence of slowing light to observe the thermal distribution. By integrating the thermal and slowed distribution, we determine that the capture rate is 75%. When we vary the detuning, the output velocity vary linearly with δ_0 (see FIG. 1.22 (a)). We find in the same way as in the dipole configuration that the flux is constant for output velocities over 40 m/s (see FIG. 1.22 (b)). We do not observe a broader peak at large output velocity (see FIG. 1.23). This is consistent with the fact that the field homogeneity is better in the Halbach than in the dipole configuration.

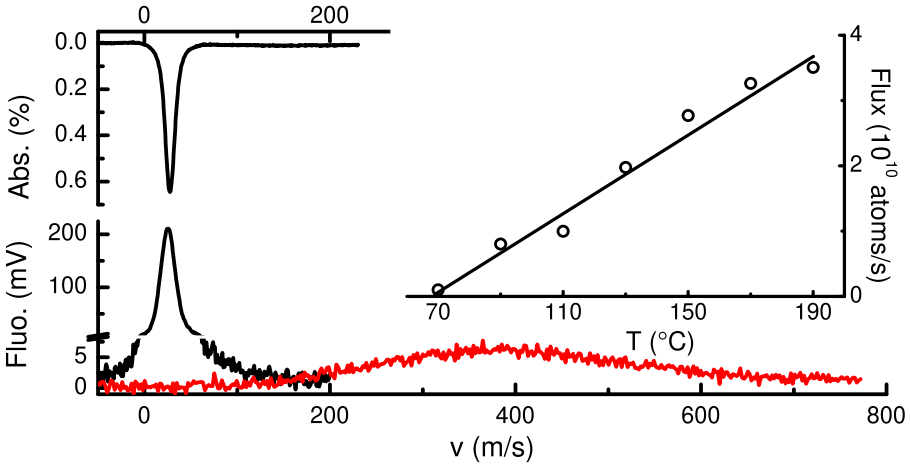

Figure 1.21: *Red: thermal beam fluorescence signal. Black: absorption and fluorescence signals of the slowed beam. Inset: temperature dependence of the atom flux.*

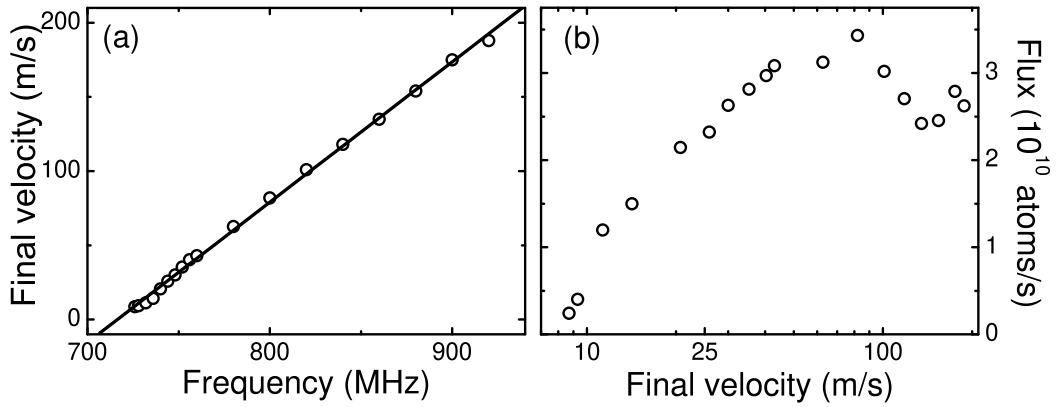

Figure 1.22: *(a) Output velocity as a function of the detuning δ_0, we observe a linear relation with a slope $\alpha = 0,95$ m.s^{-1}/MHz. (b) Atomic flux as a function of the output velocity.*

1.7.1 Needed laser powers

Because we use a tapered amplifier we have a lot of power available in the cycling and repumper beams. Figure 1.24 depicts the output flux as a function of cycling and repumping power. Unexpectedly, it turned out that several tenth of milliwatts of repumping light are necessary to obtain the maximum flux. A total power of 100 mW of cycling and repumper light is necessary to get a non-critical operation of the Zeeman slower at its best flux and a final velocity of 30 m/s. The corresponding intensity, 24 mW/cm^2 is much larger than the saturation intensity of the repumping transition. However, as we shall see now, a lot of power can be saved with more

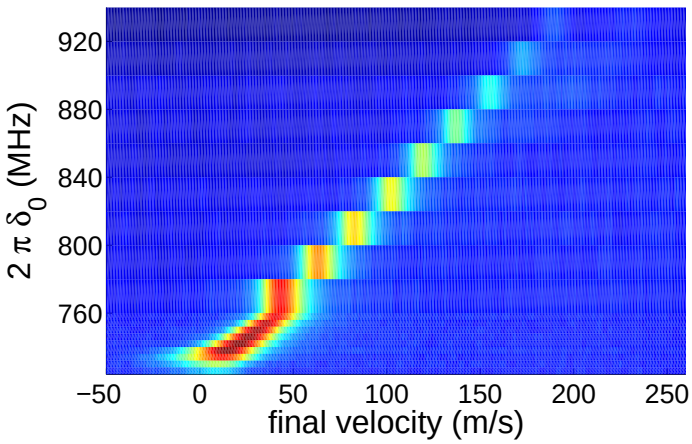

Figure 1.23: *Concatenated fluorescence signals as we vary the detuning of the slowing light δ_0. In contrast with the dipole configuration case, there is no large peak at high velocity (compare with* FIG. *1.15).*

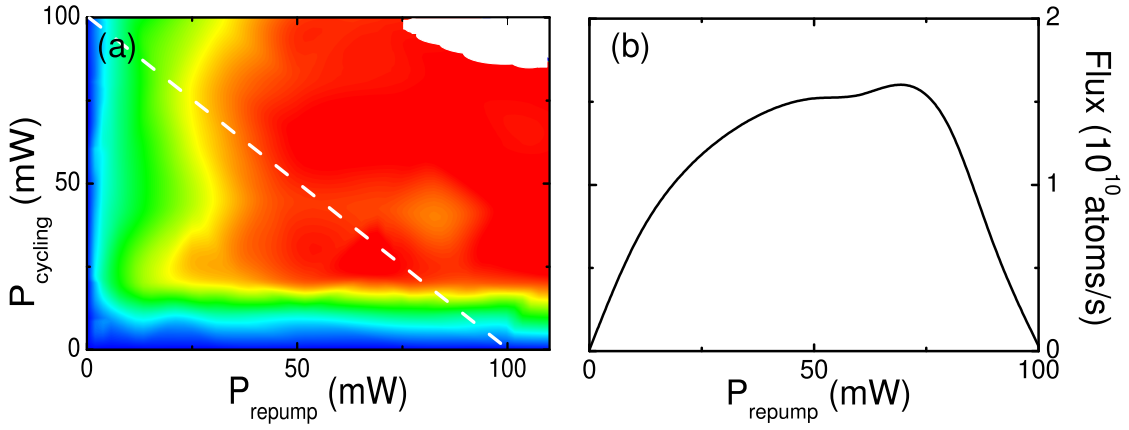

Figure 1.24: *Color online. (a) Atom flux as function of cycling and repumper beams powers. (b) Cross section along the white dotted line corresponding to a total available power of* 100 mW. *Power ratio is measured with a scanning Fabry-Perot interferometer.*

elaborated strategies.

1.7.2 Repumper

To understand why we need so much repumping light, we study the efficiency of the ZS as a function of the repumper frequency and polarization. The polarization can be chosen either parallel (π polarized) or orthogonal to the magnetic field (combination of σ^+ and σ^-). When the repumper frequency is varied as in FIG. 1.25 (a)

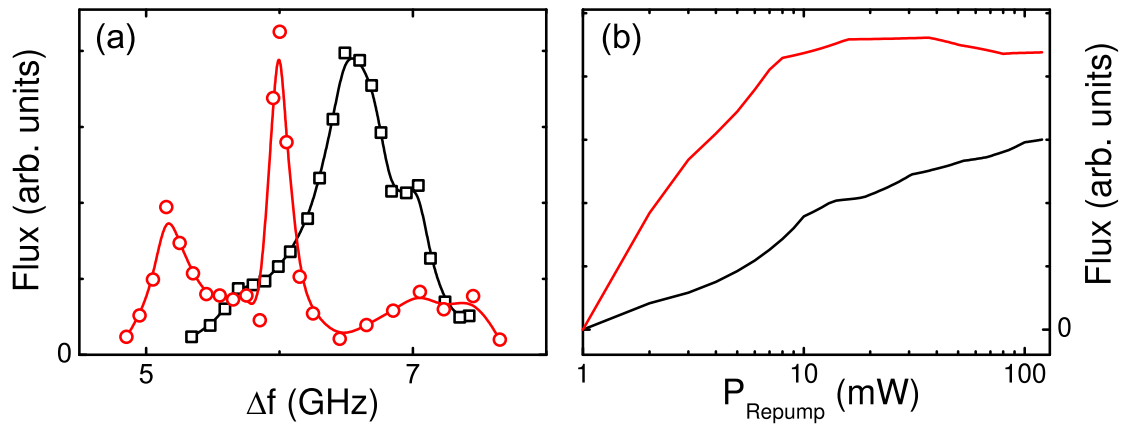

Figure 1.25: *Color online. (a) Atom flux as a function of repumper frequency.* Δf *is the beat note frequency of the repumper with an auxiliary laser locked on the* $F = 2 \rightarrow F' = 3$ *resonance line; red circles/black squares: repumper polarization perpendicular/parallel to the magnetic field. (b) Atom flux as a function of repumper power (log scale) when its frequency is fixed (black) or swept (red) across the full spectrum of left panel.*

very different spectra for the two configurations are observed. Efficient repumping occurs with well defined peaks spread over about 2 GHz and roughly centered around the $F = 1 \rightarrow F' = 2$ transition. This non trivial structure means that several depumping/repumping pathways are involved, probably occurring at localized positions along the Zeeman slower.

It is not easy to get a simple picture of what is happening: a complete *ab-initio* simulation of the internal dynamics is not simple due to the large number of Zeeman sublevels (24 in total), the multiple level crossings occurring in the 50–200 G range, and high light intensities. However, one can overcome this intricate internal dynamics by sweeping quickly (typically around 8 kHz) the repumper frequency over all the observed peaks. With a low-pass filter, the central frequency remains locked on the side of the Doppler profile. Doing so, we get a slightly higher flux for significantly less repumper power, typically 10 mW (see FIG. 1.25 (b)).

1.7.3 MOT loading

A final demonstration of the Zeeman slower efficiency is given by monitoring the loading of a MOT. It is made from 3 retroreflected beams 28 mm in diameter (FW at $1/e^2$). We use $10 - 20$ mW and $1 - 3$ mW of cycling and repumper light per beam and MOT magnetic field gradients on the order 15-20 G/cm. When the Zeeman slower is switched on with a final velocity of 30 m/s, a quasi exponential loading is observed with characteristic time $\tau \sim 320$ ms. After one second or so, the cloud growth is complete. From absorption spectroscopy at a variable detuning

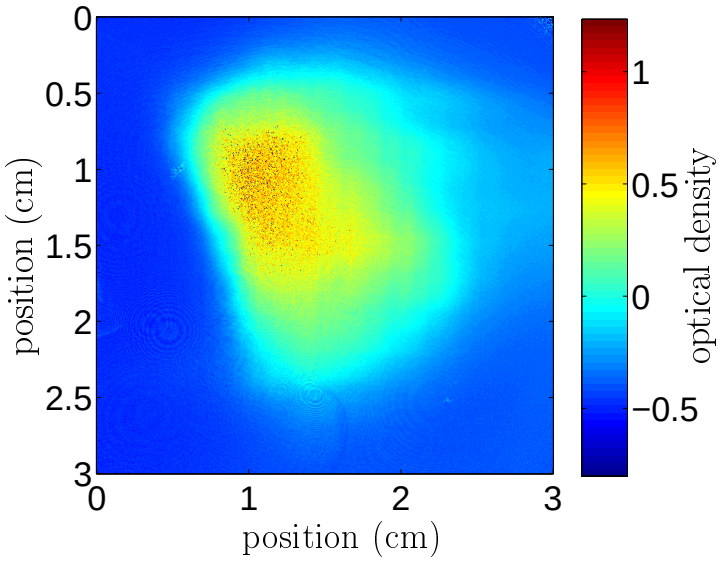

Figure 1.26: *Typical absorption image of the MOT. The frequency of the probe beam is set out of resonance by* 2Γ.

[56], we deduce a density $n = 1.4 \times 10^{10}$ atoms/cm^3. We also perform absorption imaging[8] with a probe set out of resonance by 2Γ so that the optical density is not too important (see FIG. 1.26). The number of atoms is typically $N_{\mathrm{MOT}} \sim 3 \times 10^{10}$ and the temperature measured after a time-of-flight phase $T_{\mathrm{MOT}} = 150$ μK. The temperature is reduced to 15 μK if we perform an optical mollasse by switching the coils off while keeping the cooling lasers for a few milliseconds. These figures are consistent with the above measurements of an atom flux of several 10^{10} atoms/s and nearly unity capture efficiency. As expected, thanks to the high magnetic field in the slower, the Zeeman beams do not disturb the MOT.

1.8 Conclusion

In this chapter, we have presented the realization of two Zeeman Slowers with permanent magnets. Both ZSs offer state of the art performances. We obtain an atomic flux at ~ 30 m/s of up to 5×10^{10} at/s that allows to load a large MOT in less than one second. In contrast to the previous designs by Ovchinnikov, we have paid special attention to the transverse homogeneity of the magnetic field, a problem elegantly solved using the Halbach configuration. In this latter configuration, using a simple magnetic shielding, the stray field is smaller than the earth magnetic field.

Compared to a wired-wound Zeeman Slower, our system provides several interesting advantages:

- no electric power consumption nor water cooling,

[8]The reader not familiar with absorption imaging can find more details in chapter 2.

- easy to assemble and disassemble without vacuum breaking, e.g., for high-temperature baking out,
- simple machining and construction, compact, and light,
- very smooth longitudinal profile and low stray magnetic fields,
- no perturbation associated with the heating of the ZS coils.

Chapter 2

All optical production of a Rubidium Bose-Einstein condensate

Contents

2.1 Introduction **37**
2.2 Condensation in an harmonic trap **40**
2.3 Pre-cooled atomic source **41**
2.3.1 Oven and Zeeman Slower 41
2.3.2 The 2D-MOT 42
2.4 Imaging system **43**
2.4.1 Absorption imaging 43
2.4.2 Setup 43
2.4.3 MOT mode 44
2.4.4 BEC mode 44
2.4.5 Quantitative measurements 45
2.5 The horizontal dipole guide **45**
2.5.1 Dipole potential 46
2.5.2 The spatial mode 47
2.5.3 Setting up of the horizontal beam 48
2.5.4 Power issues 49
2.5.5 Experimental sequence 51
2.5.6 Lifetime 52
2.6 Crossed dipole trap and evaporation **53**
2.6.1 Evaporation constraints 53
2.6.2 Characteristics of the crossed potential 56
2.6.3 Evaporation trajectory 57
2.6.4 Spin distillation 59
2.7 Conclusion **61**

2.1 Introduction

Bose-Einstein condensation was first observed with dilute gases in 1995 for magnetically trapped ^{87}Rb and ^{23}Na [10, 11] and has now been achieved for a wide variety of atomic species. The condensation occurs when the phase space density $\rho = n\lambda_{\mathrm{T}}^3$, where n is the atomic density and $\lambda_{\mathrm{T}} = \hbar(2\pi/mk_{\mathrm{B}}T)^{1/2}$ the thermal de Broglie wavelength, is on the order of 1. To reach the condensation, it is thus necessary to increase the density (while keeping the atoms in a gaseous phase) and decrease the temperature as much as possible. The usual passway to achieve Bose-Einstein condensation is the following:

1. Preparation of a pre-cooled atomic sample in a Magneto-Optical Trap (MOT). A MOT relies on the radiation pressure, *i.e* on a succession of absorption and spontaneous emission cycles. The radiation pressure depends on the atomic velocity via the Doppler shift, which is used to produce a net cooling of the atoms. When adding a gradient of magnetic field, the radiation pressure also depends on the position (Zeeman effect), which is used to trap the atoms.

   The minimum temperature achievable using Doppler cooling is limited as a result of the random nature of the absorption-emission cycles. For a two-level atom, the minimum temperature is $T_{\mathrm{DC}} \sim \hbar\Gamma/2k_{\mathrm{B}}$, where Γ is the cooling transition linewidth. For Rubidium, $T_{\mathrm{DC}} \sim 150\ \mu$K [57]. In practice, sub-Doppler cooling mechanisms due to the multilevel structure of the atomic ground state are at work and lower temperature can be obtained. The temperature in small MOTs is then typically on the order of $50-100\ \mu$K and can be further reduced by an optical molasses phase. The density n in a MOT is typically on the order 10^{10}atoms/cm^3 and thus, the phase space density $\rho \sim 10^{-7}$.

2. Atoms are then transferred in a conservative trap in order to implement the evaporative cooling technique. This trap can be a magnetic trap [58] or can rely on the dipole force exerted by high intensity out of resonance light as in our setup. One can also combine the two techniques. In our setup, we use a direct loading to a crossed dipole trap: the dipole beams are already present during the MOT stage. The density in the trap is increased by two orders of magnitude compared to the density in the MOT. This is important because it increases the phase space density by the same amount but also because an important density is essential to obtain an large collision rate in the evaporative cooling stage.

3. Forced evaporation of the atomic sample. Let us remind the main features: after an elastic collision between two atoms, one of the interacting atoms can get an energy larger than the trap depth. This atom then leaves the trap with an energy larger than the mean energy (related to the temperature), hence reducing the mean energy of the remaining sample. As a result of the

subsequent thermalization, the cloud reaches a new equilibrium state at a lower temperature. As the temperature decreases, fewer atoms get enough energy to leave the trap and the process slows down. In practice, the temperature generally stabilizes at a fraction η of the trap depth U, $\eta = U/T \sim 6 - 8$. It is thus necessary to decrease the trap depth with time to pursue the evaporation.

In our setup (see FIG. 2.1), we use a 2D magneto optical trap (2D-MOT) loaded by a slow atomic beam obtained at the output of a Zeeman Slower (ZS). A dipole trap resulting from the focalisation of a laser beam (the horizontal beam) at 1064 nm in the horizontal plane is present during the MOT loading stage. We call this first trap the horizontal guide in the following. After a *dark* MOT stage (see sect 2.5.5), the atoms are pumped into the $F = 1$ ground state and the MOT is switched off. A fraction of the atoms from the MOT are then captured in the guide. The evaporation is then performed by decreasing the intensity of the horizontal guide beam. If we only use one beam, the trap is very elongated in the direction of propagation of the laser and the trapping frequency in this direction can be as small as a few Herz. The density is then small which results in a slow thermalization. In order to increase the trap frequency in the longitudinal direction, we use a second beam at 1064 nm (called the vertical beam) that crosses the horizontal beam at its waist [59]. The power of this second beam is kept constant in our experiment.

The setup has been relocated from Paris to Toulouse in 2009 and has been reconstructed almost identically. The presentation of the experiment can therefore be found in detail in the thesis of Antoine Couvert and Charlotte Fabre [60, 61]. When I began to work on this setup, most of the setup was installed and we observed the first BECs. One of the dipole beam (the horizontal one) was changed in 2011 and we will present here the last version of the existing setup.

In this chapter, we will first remind some key features on Bose-Einstein condensation. Then, we will detail the MOT, the Zeeman slower and the imaging system. We will then present the loading of the dipole trap, the evaporation and the characterization of the condensates. Finally we will introduce the spin distillation technique, implemented in the course of the evaporation cooling stage, that allows to select the magnetic state of the condensate.

2.2 Condensation in an harmonic trap

We remind here some theoretical results on Bose condensation in an harmonic trap. The Bose-Einstein condensation is a remarkable phase transition because the condensation of a macroscopic number of atoms in the ground state results only from quantum statistical effects. The effect of interactions on the thermodynamical properties yields small corrections because of the diluteness of the sample. We describe the ideal Bose gas in the grand canonical ensemble where the formalism is simple

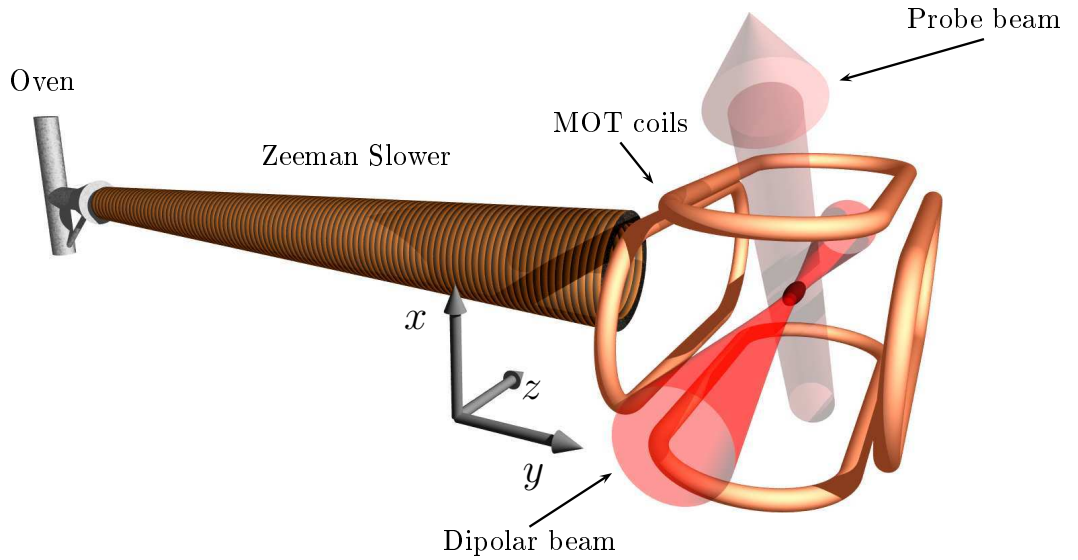

Figure 2.1: *Sketch of the pre-cooled atomic source: Zeeman, MOT and the probe beam.*

(see for example the reference [62]). In the grand canonical ensemble, the number of particle N and the energy E are fluctuants and the chemical potential μ and the temperature T are parameters. The average occupation numbers in a one-particle state i of energy ϵ_i follows the Bose statistics

$$\bar{n}_i(T,\mu) = \frac{1}{\exp\left(\beta(\epsilon_i - \mu)\right) - 1}, \tag{2.1}$$

where $\beta = 1/k_{\mathrm{B}}T$. Only the values of $\mu < \epsilon_0$, where ϵ_0 is the ground state energy have a physical meaning. Let us write the total number of atoms $N = \sum \bar{n}_i$ as

$$N = N_0 + N_T, \tag{2.2}$$

where N_0 is the number of atoms in the ground state and

$$N_T(T,\mu) = \sum_{i \neq 0} \bar{n}_i(T,\mu) \tag{2.3}$$

is the number of particles out of the condensate commonly called thermal component. In 3D,[1] for a fixed temperature, N_{T} is an increasing function of μ which has a maximum for $\mu = \epsilon_0$ $N_{\mathrm{c}}(T) = N_{\mathrm{T}}(T,\epsilon_0)$, and N_0 is always very small except when $\mu \to \epsilon_0$ where it diverges. If $N_{\mathrm{c}}(T)$ is smaller than the total number of atoms N, there is necessarily a macroscopic number of atoms in the condensate in order to satisfy the normalization condition (2.2). The temperature at which $N_{\mathrm{c}}(T) = N$ is

[1] The situation turns out to be very different in lower dimensions.

the critical temperature T_c. If $T < T_c$, N_0 cannot be neglected. In the same time, the thermal component saturates at $N_T = N_c(T)$.

The characteristics of the trap are taken into account in the distribution of energy levels ϵ_i. For an harmonic trapping with angular frequencies $\omega_x, \omega_y, \omega_z$,

$$\epsilon_i = \epsilon_{n_x,n_y,n_z} = \left(n_x + \frac{1}{2}\right)\hbar\omega_x + \left(n_y + \frac{1}{2}\right)\hbar\omega_y + \left(n_z + \frac{1}{2}\right)\hbar\omega_z, \tag{2.4}$$

where n_x, n_y, n_z are positive integers. It is then possible to calculate explicitly the function $N_c(T)$ by replacing the sum in the equation (2.3) by an integral over the different states. This is justified if the occupation numbers vary slowly as a function of the energies ϵ_i, *i.e* if the temperature is much larger than the energy spacing between energy levels. We then find:

$$N_c(T) = \int \mathrm{d}n_x \mathrm{d}n_y \mathrm{d}n_z \frac{1}{\exp\left(\beta\hbar(\omega_x n_x + \omega_y n_y + \omega_z n_z)\right) - 1}. \tag{2.5}$$

Using Eq.(2.5) and the normalisation condition (2.2), one finds the critical temperature:

$$k_B T_c = \hbar\bar{\omega}\left(\frac{N}{\zeta(3)}\right)^{1/3} = 0.94\hbar\bar{\omega}N^{1/3}, \tag{2.6}$$

where $\bar{\omega} = \sqrt{\omega_x\omega_y\omega_z}$ is the geometric average of the trapping frequencies, and $\zeta(n)$ is the Riemann function. We verify that for a macroscopic number of atoms, $k_B T_c \gg \hbar\bar{\omega}$ which is necessary to establish the relation (2.5). The condensation phenomena is thus very different from the trivial effect of freezing of the degrees of motion. We also deduce the condensed fraction when $T < T_c$

$$\frac{N_0}{N} = 1 - \left(\frac{T}{T_c}\right)^3. \tag{2.7}$$

To gain some insight in Eq. (2.6), it is interesting to evaluate the phase space density at T_c. The density of a classical gas at a temperature T in an isotropic trap with trapping frequencies $\bar{\omega}$ is

$$n(x) = \frac{N}{(2\pi)^{3/2}\Delta x^3} e^{-x^2/2\Delta x^2}, \tag{2.8}$$

where x is the distance to the trap center and the size of the cloud is determined by the temperature $\Delta x = (k_B T/\bar{\omega}^2 m)^{1/2}$. Using the definition of the phase space density and the relation (2.6), we find that, at the critical temperature, the phase space density at the center of the trap is equal to one. This means that the size of a wave packet in phase space is on the order of $\hbar$ and becomes Heisenberg-limited.

2.3 Pre-cooled atomic source

2.3.1 Oven and Zeeman Slower

In order to efficiently load the MOT, a slow atomic beam with a typical velocity $v \sim 20-30$ m/s is needed. We produce a hot beam using a recirculating oven heated at 130 °C (see Thierry Lahaye thesis [63] or our more recent publication [41]). At the output of the oven the atoms have a typical thermal velocity of 300 m/s. They are subsequently slowed down to 20 m/s by an increasing field Zeeman Slower (ZS) [48].[2] On our BEC setup, the ZS is a standard wire wound Zeeman Slower with the following parameters (see chapter 1):

ΔB	300 G
B_{b}	200 G
ℓ	1 m
v_{c}	330 m/s

We recall that ΔB is the amplitude of variation of the magnetic field, B_b, the bias field, ℓ the length of the Slower and v_{c} the capture velocity. It delivers an atomic flux of $\sim 2\times 10^{11}$ at/s at 20 m/s. The laser system for the cycling and the repumper light is similar to the one described in chapter 1.

2.3.2 The 2D-MOT

In order to capture as much atoms as possible in the horizontal trap, it is advantageous to optimize the mode matching between the MOT and the dipole guide potential. This is the reason why we have chosen a 2D magnetic configuration to create a six beams 2D-MOT [64]. The magnetic field is generated by four elongated coils (instead of two in a conventional MOT) that produce a 2D quadrupole field with a continuous line of zero field in the vicinity of the z axis (see FIG. 2.1). The field close to the axis reads

$$B_{\mathrm{2D}}(x,y) = b' \begin{pmatrix} -x \\ y \\ 0 \end{pmatrix} \tag{2.9}$$

The six beams are issued from a 2 W tapered amplifier[3] injected by a narrow bandwidth laser diode.[4] The laser diode frequency is actively stabilized using saturated absorptions in a rubidium cell. After the tapered amplifier, the beam is split into four independent beams. Each of them passes through an AOM that controls its

[2] The ZS functioning is described in a slightly different context in chapter 1.
[3] SACHER- S353.
[4] Sanyo DL7140-201S.

power, they are then sent on the main table by mean of four polarization maintaining optical fibers (2 beams are subsequently split on the main table). The power of each beam is locked: after each fiber, a small part of the beam is sent on a photodiode with a beamsplitter. A feedback loop made of a simple electronic integrator acts on a radio frequency attenuator,[5] that control the radio frequency power injected into the AOM until the photodiode signal reaches the consign. The repumper beam, set on the $F = 1 \rightarrow F' = 2$ transition is superimposed with the Zeeman slower beams. The repumper power is not locked. After a loading of 2 s, we obtain a MOT of about 5×10^9 atoms at $T \simeq 120$ μK with a lifetime of ~ 25 s. The typical phase space density in the MOT, $\rho \sim 10^{-7}$ is still far from the Bose-Einstein condensation threshold.

2.4 Imaging system

2.4.1 Absorption imaging

For all measurements on the atomic cloud, we use the absorption imaging technique. The principle is to shine a resonant collimated beam at 780 nm on the atoms. The atoms absorb the probe light very efficiently; the shadow of the atomic cloud is then imaged on a CCD camera. More precisely, consider the case of a collimated beam whose direction of propagation is z and that is absorbed by a cloud of atoms of density $n(x, y, z)$. It is convenient to define the column density $n_c(x, y)$ as the density integrated along the z axis,

$$n_c(x, y) = \int n(x, y, z) \mathrm{d}z. \tag{2.10}$$

The Beer-Lamber law, valid for a low intensity probe, gives the relation between the beam intensities before and after the cloud:

$$I_{\mathrm{out}}(x, y) = I_{\mathrm{in}}(x, y) \mathrm{e}^{-\sigma_0 n_c(x,y)}, \tag{2.11}$$

where σ_0 is the absorption cross section. The optical density is defined by

$$OD(x, y) \equiv \ln \left(\frac{I_{\mathrm{in}}(x, y)}{I_{\mathrm{out}}(x, y)} \right). \tag{2.12}$$

Because the beam intensity is generally not homogeneous (there is some speckle), we take two images: one with the atoms and one once the atoms have fallen and are not in the probe beam anymore (respective intensity noted I_{wat} and I_{woat}) and we deduce the column density from Eq. (2.11). We actually take a third picture in the absence of probe light to substract the background light (intensity I_{bkg}). The

[5] minicircuit PAS-3.

exposure time $t_{\mathrm{snap}} = 80$ μs is chosen so that atoms move of less than one pixel during the snapshot. Finally, we deduce the column density from:

$$\sigma_0 n_{\mathrm{c}} = \ln\left(\frac{I_{\mathrm{wat}}(x,y) - I_{\mathrm{bkg}}(x,y)}{I_{\mathrm{woat}}(x,y) - I_{\mathrm{bkg}}(x,y)}\right), \tag{2.13}$$

2.4.2 Setup

In the experiment, it is necessary to measure two kinds of objects that have a fairly different size: the MOT, which is a few centimeters long and, later, cold atoms and BECs of a few hundred micrometers. To have in both case a good resolution and a good field of view, we alternate between two imaging systems (see FIG. 2.2): the "MOT mode" and the "BEC mode" that have different magnifications. To switch between the two modes, we use magnetic mounts that allow to remove and replace a mirror with a reproducibility on the order of a microradian. In both cases, the probe beam is sent at 45° from the horizontal guide (see FIG. 2.1). This angle makes the imaging a little more complicated to analyze, since the displacements along the guide axis appear with a factor $\sqrt{2}$ on the CCD camera. The CCD camera is a Basler A100f Series that has 1392×1040 square pixels with an edge size $c = 6.45$ μm.

2.4.3 MOT mode

The size of the incoming beam should match the desired field of view. In the MOT mode, it is 3 cm wide. After the chamber, we use a three lenses achromat L_1 that correct for spherical and coma aberrations, and a spherical lens L_2 of respective focal lengths $f_1 = 150$ mm and $f_2 = 50$ mm with a 40 mm spacing between them. The achromat L_1 is also used in BEC mode. This optical system has been chosen to form the image of atoms located 190 mm before L_1 at 46 mm after L_2 with a magnification $\gamma_{\mathrm{MOT}} = 0.26$. One pixel on the camera then corresponds to 25 μm on the atoms. The magnification in this mode is calibrated more precisely by monitoring the free fall of a cold cloud and fit the trajectory by a parabola with known acceleration g. The camera is installed on a translation stage to finely tune the focusing.

2.4.4 BEC mode

In the BEC mode, we take the lens L_2 out, the image of the atoms is then formed at 710 mm from L_1 with a magnification $\gamma_{\mathrm{BEC}} = 3.75$. The calculated pixel size $pix_{\mathrm{BEC}} = 1.7$ μm is measured as before by monitoring the free fall of a cold cloud and later on by analyzing the diffraction pattern produced by a flashed lattice as we shall see in the next chapter. Because the magnification is much larger than in the MOT case (and correlatively, the field of view is much smaller), a lot of the light is actually casted outside of the CCD camera (see FIG. 2.2). This is not an issue for the image formation, however, it reduces the intensity on the camera. In order

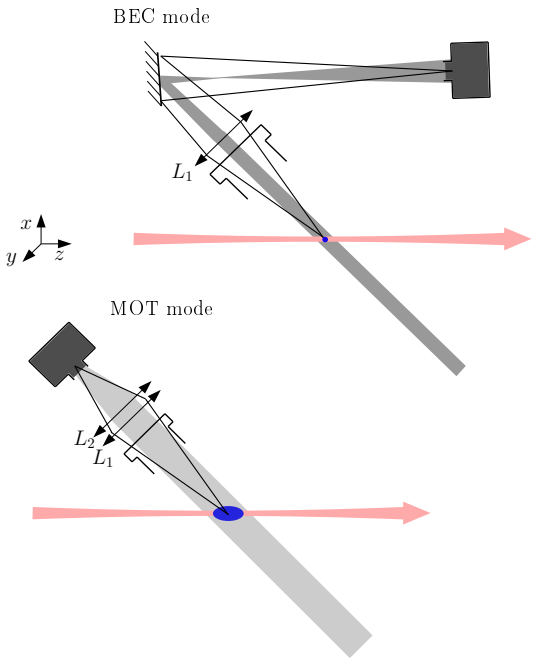

Figure 2.2: *Sketch of the two imaging systems, the magnifications are respectively* $\gamma_{\mathrm{MOT}} = 0.26$ *and* $\gamma_{\mathrm{BEC}} = 3.75$. *We use a 3 cm wide beam in the MOT mode and reduce the size to 3 mm in the BEC mode in order to get more intensity on the camera and remain close to the saturation of the CCD camera.*

to get nonetheless an intensity just below the saturation of the CCD camer (which increases the signal to noise ratio), we use a 3 mm wide beam. We switch between the two beams using a mirror installed on a magnetic mount. As in the MOT mode, the camera is set on a translation stage for the fine tuning of the focusing.

The optical resolution is limited by the optics. In our setup, it is not possible to place lenses very close to the atoms, the lens L_1 is located at 190 mm from the atoms and has a 15 mm radius.

The numerical aperture, limited by the size of L_1 is N.A = 0.07. The Rayleigh criterion for the optical resolution given by

$$R = 0.61\frac{\lambda}{\mathrm{N.A}}, \tag{2.14}$$

yields an optical resolution of about $R = 7$ μm. This was verified by taking an image of a very small object (a BEC before time-of-flight for example).

2.4.5 Quantitative measurements

From the absorption images, it is possible to deduce the number of atoms and the temperature of a cloud of atoms. To measure the total number of atoms, we use the relation (2.13) and integrate it over the plane. In order to be accurate, the optical density must remain moderate (typically O.D < 2). Most of the time, it is necessary to perform a time-of-flight stage of up to 20 ms before taking the imaging to reduce the density. During this stage, all trapping potentials are switched off, atoms fall under gravity and each atom quickly evolves according to a ballistic trajectory

determined by its initial velocity $\boldsymbol{v}_\mathrm{i}$: $x(t) = x_0 + \boldsymbol{v}_\mathrm{i} t_\mathrm{TOF}$. The size of a cloud after a sufficiently long time-of-flight is directly related to the velocity distribution and hence, to the temperature of the cloud. Thanks to the equipartition theorem (not valid for condensates), if the initial size of the cloud is negligible after a given time-of-flight t_TOF, the temperature reads

$$T = \frac{m}{k_\mathrm{B}} \frac{\langle \Delta x^2 \rangle}{t_\mathrm{TOF}}. \tag{2.15}$$

2.5 The horizontal dipole guide

It is necessary, to increase the phase space density, to transfer the atoms from the MOT to a conservative potential and to perform the evaporative cooling.

2.5.1 Dipole potential

In the case of an optical trap, the potential originates from the interaction between the electric field of a far detuned laser beam and the induced electric dipole of the atom. It is also known as the dynamic Stark effect [65]. The dipole potential is proportional to the light intensity $I(\mathbf{r})$:

$$U_\mathrm{dip}(\mathbf{r}) = \zeta I(\mathbf{r}), \tag{2.16}$$

where ζ depends on the polarization and wavelength of the laser and on the atomic structure. In the case of ^{87}Rb:

$$\zeta = \frac{\Gamma_{D_2} \lambda_{D_2}^3}{16\pi^2 c} \left[\left(\frac{1}{\Delta_1} + \frac{1}{\Delta_1 + 2\omega_\mathrm{L}} \right) (1 - q g_F m_F) + \left(\frac{1}{\Delta_2} + \frac{1}{\Delta_2 + 2\omega_\mathrm{L}} \right) (2 + q g_F m_F) \right], \tag{2.17}$$

where Δ_1 (Δ_2) is the detuning from the $D1$ ($D2$) line, q corresponds to the polarization of the light: $q = 0$ for π polarized light and $q = \pm 1$ for $\sigma^{+(-)}$ polarized light. Γ_{D_2} is the lifetime of the $P_{3/2}$ excited state and λ_2 the corresponding transition wavelength. ω_L is the pulsation of the incoming light, g_F is the Lande factor and m_F the magnetic moment.

We can see that far from any resonance, ζ decreases as $1/\Delta$. Beside, when the detuning is negative (red-detuned laser) the potential is attractive whereas it is repulsive for a positive detuning (blue-detuned).
For an atom in the ground state and a linearly polarized light ($q = 0$), we give here the ζ factor for a few common wavelengths:

λ (nm)	ζ (J/(W/m^2))
1064	$-2.10 \cdot 10^{-36}$
840	$-7.71 \cdot 10^{-36}$
785	$-3.98 \cdot 10^{-35}$
532	$8.12 \cdot 10^{-37}$

To perform the evaporation efficiently, the probability to diffuse a photon resonantly must remain low during all the evaporation. When the detuning is important compared to the hyperfine structure, the diffusion rate reads:

$$\Gamma_{\text{diff}} \simeq I \frac{\Gamma_{D_2}^2 \lambda_{D_2}^3}{16\pi^2 c\hbar} \frac{1}{\Delta_{12}^2} \quad \text{with} \quad \frac{1}{\Delta_{12}} \equiv \left(\frac{2}{\Delta_2^2} + \frac{1}{\Delta_1^2} \right). \tag{2.18}$$

After each diffusive event, the energy is modified by up to $mv_{\text{rec}}^2/2$ where $v_{\text{rec}} = \hbar k_{\text{res}}/m \simeq 5.9$ mm/s is the recoil velocity. We can then evaluate the corresponding heating rate

$$\frac{\mathrm{d}T}{\mathrm{d}t} = \Gamma_{\text{diff}} \frac{m v_{\text{rec}}^2}{2k_{\text{B}}} \simeq I \frac{\Gamma_{D_2}^2 \hbar \lambda_{D_2}}{8 c k_{\text{B}} m} \frac{1}{\Delta_{12}^2}. \tag{2.19}$$

The heating rate varies as $1/\Delta_{12}^2$ while the depth of the potential varies as $1/\Delta_{12}$. It is thus possible to get both a deep potential and a negligible heating rate provided that the light is sufficiently out of resonance.

During the evaporation, the potential depth U_0 is generally related to the temperature by : $U_0/k_{\text{B}} \sim \eta T$ where $\eta \sim 6 - 8$. For a laser at 1064 nm the heating rate then reads

$$\frac{\mathrm{d}T}{\mathrm{d}t} \sim T \times 2 \cdot 10^{-2} \text{ s}^{-1}. \tag{2.20}$$

In our setup the evaporation ramps lasts less than 5 s, the heating by photon diffusion is thus negligible.

2.5.2 The spatial mode

Ideally the horizontal guide beam has a Gaussian mode TEM_{00}:

$$I(x, y, z) = \frac{2P}{\pi w^2(z)} \exp\left(-\frac{2(x^2 + y^2)}{w(z)^2} \right), \tag{2.21}$$

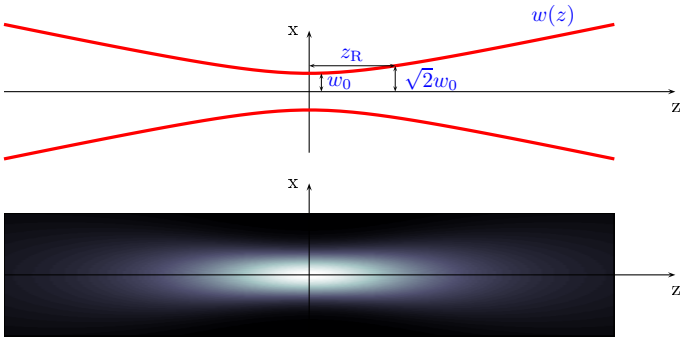

Figure 2.3: *Intensity profile of a TEM_{00} Gaussian beam. The Rayleigh length is defined by $w(z_R) = \sqrt{2}w_0$.*

where P is the power of the laser. The radius at $1/e^2$ depends on the longitudinal coordinate z :

$$w(z) = w_0\sqrt{1 + \left(\frac{z}{z_R}\right)^2}, \tag{2.22}$$

where w_0 is the waist of the beam. The Rayleigh length depends on the waist and the wavelength *via*

$$z_R = \pi\frac{w_0^2}{\lambda}. \tag{2.23}$$

Figure 2.3 shows a typical intensity profile and introduces the different notations.

At 1064 nm and for a waist $w_0 = 50$ μm, the Rayleigh length is $z_R = 7.4$ mm. As a result, the trapping potential is very elongated.

2.5.3 Setting up of the horizontal beam

When I began working on the BEC experiment, the horizontal and vertical beams where issued from the same laser. We used a 300 W fibered laser at 1064 nm from IPG photonics with a large bandwith of a few nm.[6] However, with time the spatial mode at the output of the fiber degraded (see FIG. 2.4). We sent it back to IPG for reparation in October 2010, the origin of the degradation stayed unknown but the spatial mode was fine when the laser came back. Six month later, the spatial mode was degraded again. At some point, this prevented us from reaching the condensation. We thus bought a new 100 W laser with similar spectral characteristics that is used only for the horizontal beam (the waist of the vertical beam being larger, the degradation of the mode is less visible). The setting up of the beams is presented in FIG. 2.5. A telescope adjusts the size of the beam so as

[6]The corresponding coherence length 500 μm smaller than the path difference between the beams so that in principle there is no interference between the two dipole beams. However the spectrum is actually made up of a frequency comb so that each component could interfere. We thus set a detuning of 80 MHz between the two beams.

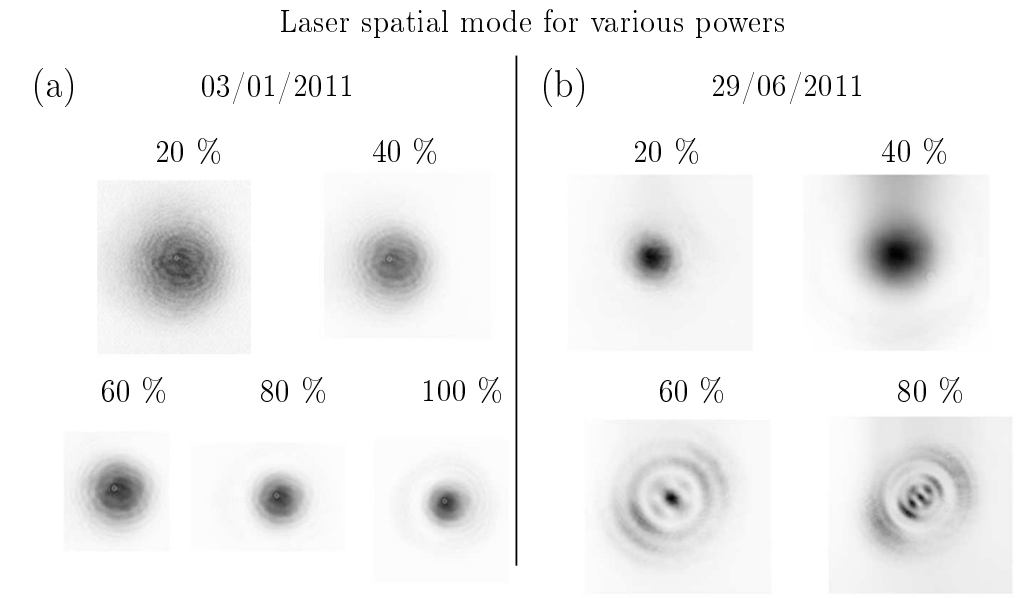

Figure 2.4: *Spatial mode of the 300* W laser for different output power. (As a percentage of the maximum power) after it came back from IPG for reparation and six months later. The degradation is more important for high power but progressively, rings appeared also at low setpoint.

to pass through an AOM that controls the power.[7] The beam is then sent on an upper table, the beam size is adjusted using an other telescope in order to obtain the desired waist on the atoms. Finally a lens with a focal length $f' = 811$ mm focuses the beam into the vacuum chamber. The relation between the waist of the beams before and after a lens of focal length f' is:

$$w_0' = \frac{\lambda f'}{\pi w_0}. \tag{2.24}$$

For a target waist $w_0 = 50$ μm and a focal length $f' = 800$ mm, the beam waist on the lens must be $w_0' = 5.5$ mm. The corresponding Rayleigh length $z_R = 90$ m can then be considered as infinite.

The last lens is set on a servo-controlled translation stage that permits to adjust the waist position. Two mirrors placed after the focusing lens control the beam position and angle.

2.5.4 Power issues

The Ytterbium laser was typically used at an output power $P = 40$ W, this high power implies that we take some precautions when manipulating the beam. We

[7] Diffraction efficiency of 85 %

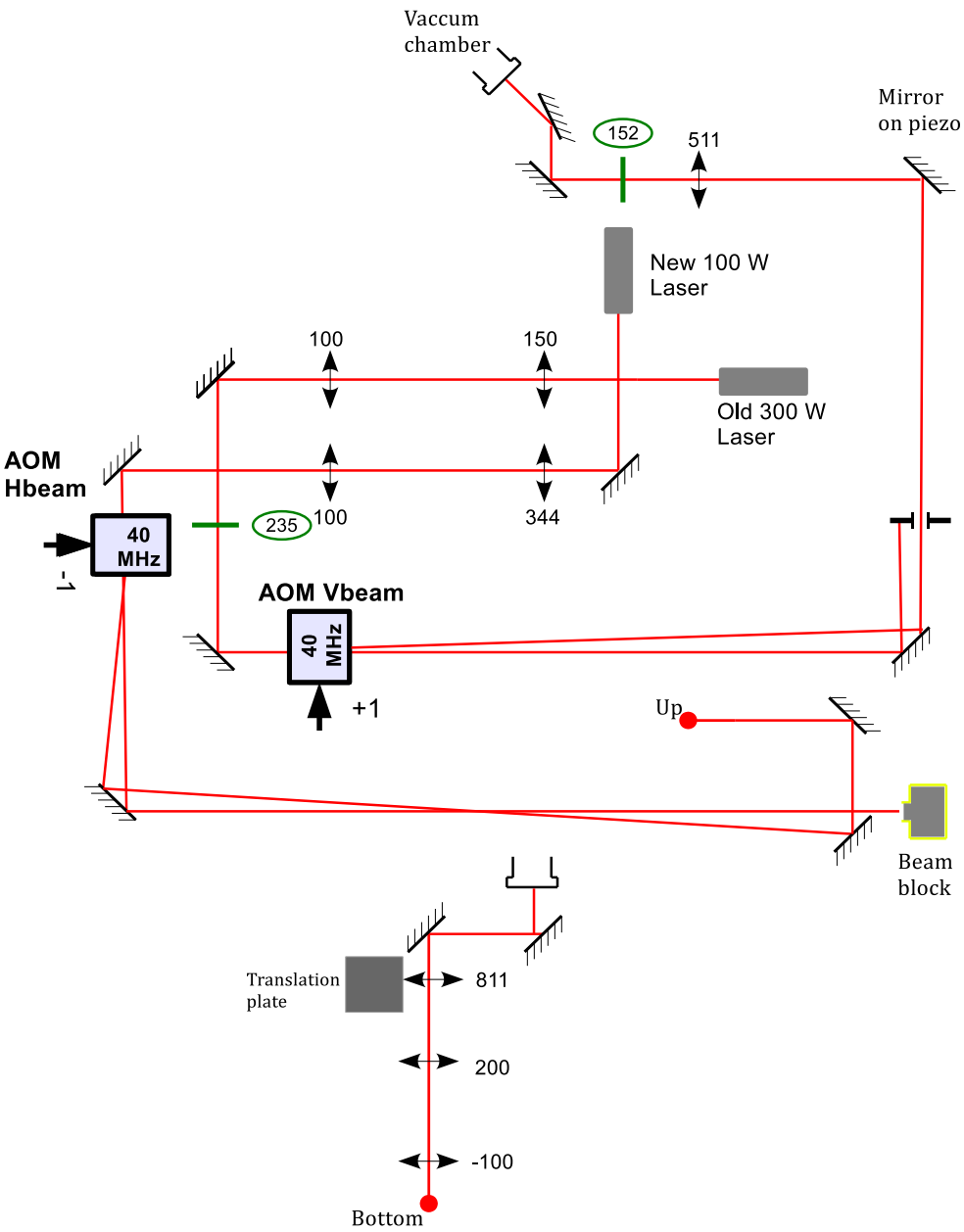

Figure 2.5: *Optical setup to control the power and the size of the two dipole beams. The numbers associated with the lenses are their focal length in mm. The green lines represent $\lambda/2$ waveplates and the numbers their reference angle. The horizontal beam is focused down with a waist $w_h = 50$ μm and the vertical beam with a waist $w_v = 100$ μm.*

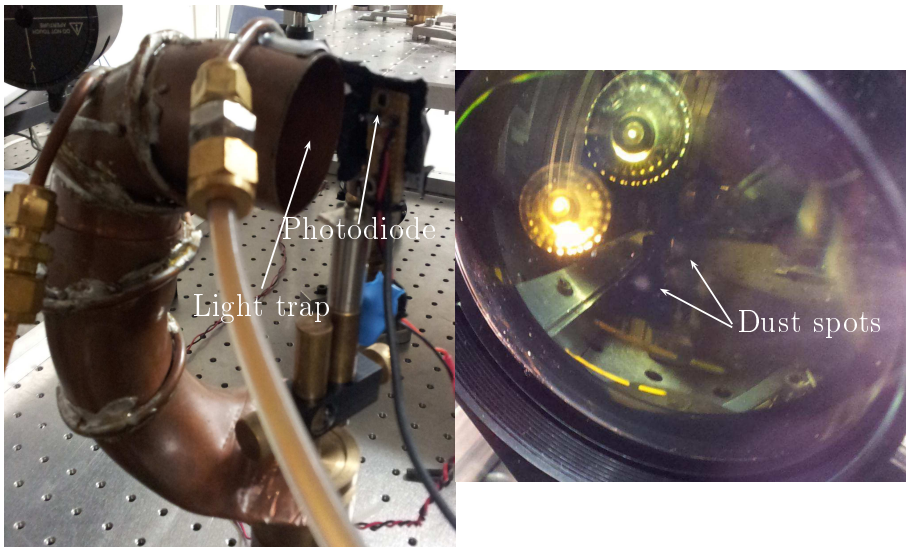

Figure 2.6: *Left: picture of the light trap located after the vacuum chamber on the horizontal beam. The photodiode measures a small fraction of the power of the horizontal beam by gathering the light diffused out of the light trap. Right: Lens before cleaning, spots of dust have appeared at the location of the beam. The spots can degrade the spatial mode, reduce the beam power and eventually absorb enough light to trigger the burning the coating.*

wear protection glasses every time the laser is switched on and security switches have been installed in the room. All optics must be high intensity optics that are generally more expensive. In particular, we have to use silica crystals AOMs that are more resistant to high intensities than TeO_2 crystal. However their compressibility is lower and we need to use 15 W of RF power (instead of typically 2 W). It is then necessary to water-cool the AOM. After each AOM, a water cooled beam block was installed to absorb the zero-th order.

The dipole force which is used for manipulating atoms is actually capable of trapping dust as well. This is visible on each lens, the dust is guided by the dipole beam and deposits on the optics. After some time, spots of dust appear at the exact location of the beam (see FIG. 2.6) and we have to clean them every month. Another problem concerns the power measurement: to measure the total power of a beam, we can use a high intensity power-meter. However, since it relies on thermal effects the response time is on the order of a second. One solution is to use the light that leaks back from a mirror. If the reflectivity is $R \sim 99,9\%$ there are still dozens of milliwatts to be measured. The problem of this technique is that the transmission on Bragg mirrors is highly sensitive to the polarization so that it does not provide a reliable information on the total intensity and is very sensitive to polarization fluctuations. Finally our solution was to use the diffused light from water-cooled light traps[8] (see FIG. 2.6). The power is then actively stabilized using a retroactive

[8]The light traps are water cooled hollow cones. When the light enters in the trap, it is diffused

loop that consists only of an integrator with tunable gain.

2.5.5 Experimental sequence

Figure 2.7 presents the experimental loading sequence:

1. Loading of the 2D-MOT: during this stage, the Zeeman Slower, MOT and repumper lights are on. The magnetic field of the MOT is also switched on. This stage lasts typically 2-3 s.

2. Temporal dark MOT: The MOT dynamics is in a regime where the reabsorption of scattered photon is important. This means that the density is such that when an atom emits a photon, there is an important probability that it get reabsorbed by a neighbor atom, resulting in an effective repulsive force between atoms. This limits the atomic density in the MOT and, following, the number of atoms captured in the guide. In order to increase the density we decrease the repumper intensity producing a commonly-called dark MOT. The atoms then spend more time in the $F = 1$ hyperfine state where they do not scatter any photons, therefore reducing the repulsion between atoms. If we switch off the repumper completely, atoms are no longer trapped and get lost. There is a trade-off for which we can approximatively double the number of captured atoms compared to the sequence without dark MOT stage.

3. Pumping stage: The repumper is completely switched off. The atoms then progressively accumulate the $F = 1$ state. This is necessary to avoid inelastic collisions between atoms in different internal states during the evaporation.

4. Holding time or evaporation: The MOT coils and beams are switched off and only the dipole beams remain. Atoms that are not captured in the dipole trap fall under gravity.

We fix a reference point at a holding time $t_{\mathrm{hold}} = 100$ ms that we use to compare the number of atoms in the guide from day to day. With a total power in the horizontal beam $P = 30$ W, we capture typically 3×10^7 atoms at $T = 120$ μK. This correspond to a parameter $\eta = U_0/k_{\mathrm{B}}T = 8.3$ and a phase space density $\rho = 8 \times 10^{-6}$. If we use a higher power, the cloud is heated up but the number of atoms stays the same. If we use a smaller power, the temperature and the number of atoms decrease.

2.5.6 Lifetime

Once the atom are trapped in the horizontal guide, we study the lifetime for different guide powers by holding the atoms in the guide for a variable time t_{hold} before

a great number of times before leaving the trap in a random direction. The quantity of diffused light is directly proportional to the incoming light and independent of the polarization.

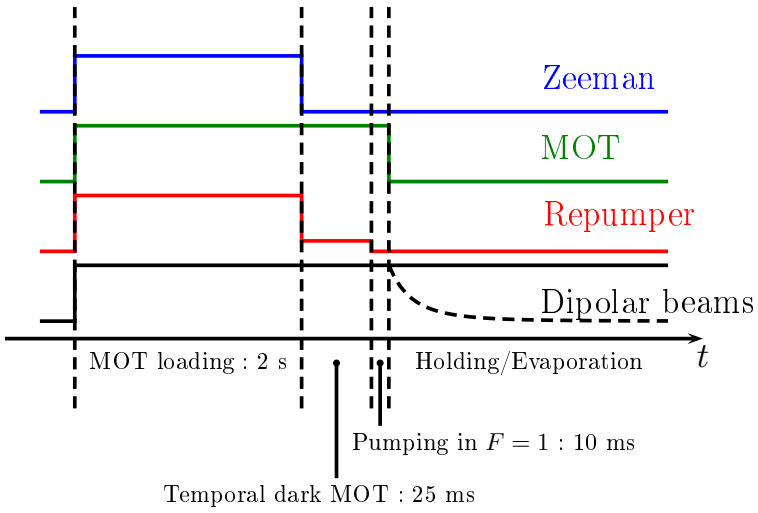

Figure 2.7: *Typical experimental sequence realized to load the atoms in the MOT and transfer them into the $F = 1$ state in the guide, followed by either a holding time or an evaporation.*

measuring the number of remaining atoms. To measure the number of trapped atoms, we need to wait that all the atoms that were not captured in the dipole trap fall by gravity. In practice, it is not possible to measure anything at times prior to 50 ms. We observe (see FIG. 2.8) two distinct characteristic times, the first time is very short and thus hard to measure precisely because atoms of the MOT are still in the image. We think that it corresponds to the initial natural evaporation. The second characteristic time strongly depends on the light intensity. To measure it, we take only the points after 500 ms and we fit the atom number by a decreasing exponential. For $P_{\mathrm{h}} = 14$, 24 and 48 W, the lifetimes are respectively $\tau_{\mathrm{long}} = 2.7, 1.5$ and 1 s. This dependency indicates that the lifetime is not limited by collisions with the background gas but rather by inelastic collisions.

Inelastic collisions between atoms in different ground states can occur if some atoms are still in the $F = 2$ state despite the pumping stage. In the reference [66], where the same kind of spectrally large laser is used, the authors are able to identify a light induced pumping in the $F = 2$ state and explain it by a 2-photons Raman process. This is possible if one remembers that the dipole laser spectrum is made of a frequency comb with frequency components separated by about 200 MHz. Thus, two spectral components can be separated by the hyperfine sructure constant ans can induce a Raman process. This process could explain the losses observed in our trap. Anomalous heating and losses can also be explained by fluctuations of the position or intensity of the trap at the trap frequency or twice the trap frequency respectively. In our setup however, light-induced losses are dominants.

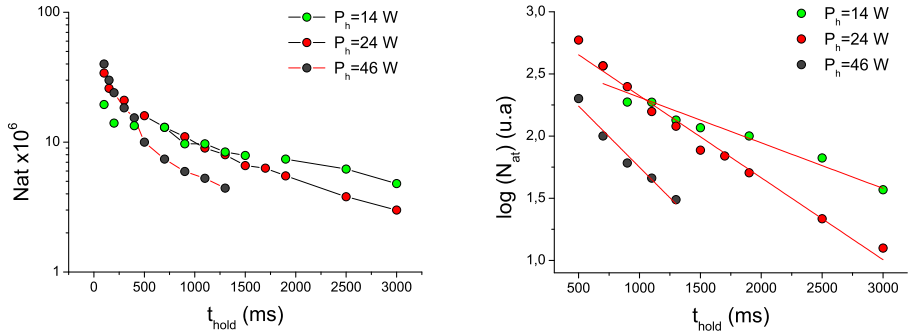

Figure 2.8: *Left: Atom number in the horizontal guide as a function of the holding time. Two typical times are visible, they both depend on the guide intensity. Right: logarithm of the atom number for* $t_{\mathrm{hold}} \geq 500$ ms. *The lifetimes for* $P_{\mathrm{h}} = 14$ W, 24 W *and* 48 W *are* $\tau_{\mathrm{long}} = 2.7$ s, 1.5 s *and* 1 s.

2.6 Crossed dipole trap and evaporation

2.6.1 Evaporation constraints

To perform the evaporation, we decrease the trap depth by lowering the horizontal beam power $P_{\mathrm{h}}(t)$. The typical decreasing time τ_{evap} must ideally satisfy two conditions at all times:

- It must be smaller than the typical time of losses due to inelastic collisions or collisions with the background gas.
- It must remain large compared to the thermalization time. Indeed, in order to cool efficiently while loosing few atoms, only the atoms in the high energy tail of the thermal distribution should leave the trap. In order to replenish the tail of the distribution, the thermalization time must be smaller than the evaporation ramp time. The thermalization time depends on the density, the temperature and the trap frequencies.

If one is able to get few losses and high trap frequencies, it is possible to find an evaporation trajectory $P_{\mathrm{h}}(t)$ that satisfies

$$\tau_{\mathrm{losses}} \gg \tau_{\mathrm{evap}} \gg \tau_{\mathrm{therm}}. \tag{2.25}$$

If we perform the evaporation with the horizontal beam only, the frequency in the longitudinal direction is much smaller than in the other directions. This limits the atomic density and hence, the collision rate. At some point, the thermalization time becomes so important that the temperature does not decrease anymore. To increase the trapping frequency in the longitudinal direction, we add a second beam (the vertical beam) that crosses the horizontal beam at its waist [59].

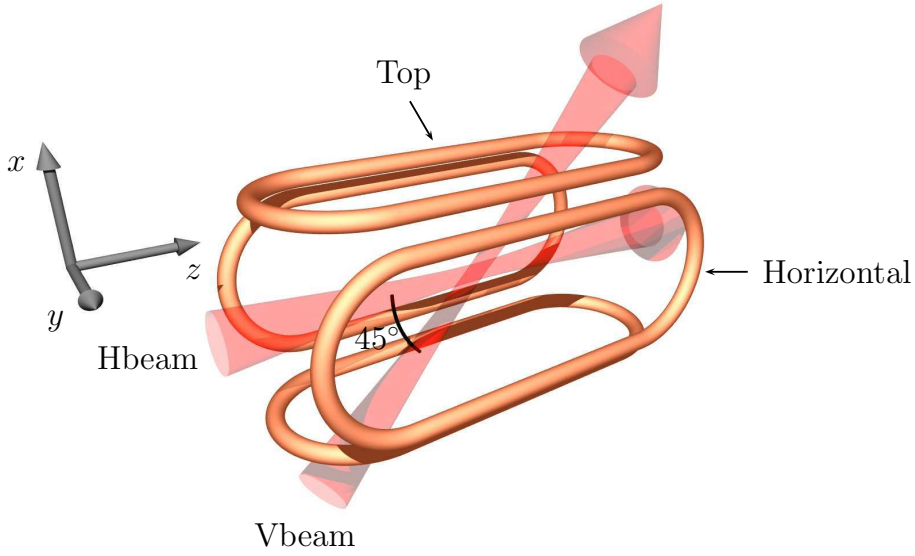

Figure 2.9: *Sketch of the crossed dipole beams and the MOT coils. One of the MOT coil (either the Top or the Horizontal) is also used to perform spin distillation during the evaporation stage*

The vertical beam originates from the "old" 300 W Ytterbium laser. It actually forms an angle 45° with the horizontal beam (see FIG. 2.9). Its waist is $w_v = 100\,\mu$m. The power and beam size are controlled in the same way as for the horizontal guide (see FIG. 2.5). When the two beams originated from the same laser their frequencies where detuned by 80 MHz to avoid interference effects. We kept this in the latter setup. A mirror is set on a three axes piezo-controlled mount to adjust the crossing between the two dipole beams. In practice, crossing the beams can be a delicate operation. We first load the atoms in the guide and begin the evaporation until we reach a temperature of a few μK. If we are far from the crossing, there is no sign of the vertical beam and we have to slowly move it until a dimple appears at the crossing. To optimize the crossing, we then move the vertical beam to get as much atoms as possible in the dimple.

The question of the optimisation of the evaporation ramp has been widely studied (see [67] for example). However, it strongly depends on the parameters of each setup and, in practice, one has to try different trajectories to optimize $P_h(t)$. We use

$$P_h(t) = P_0\,(1 + t/\tau_{evap})^{-4}\,, \tag{2.26}$$

with $\tau_{evap} = 1300$ ms which turns out to be a good choice for us. At the beginning of the evaporation ramp, the intensity is decreased quickly because the losses are important. As the horizontal power decreases, so do the trap frequencies.[9] This is not compensated by an increase of the density (*i.e* we are not in the runaway regime). As a consequence, the thermalization time increases during the evaporation and we

[9]This is to be contrasted with the case of a magnetic trap.

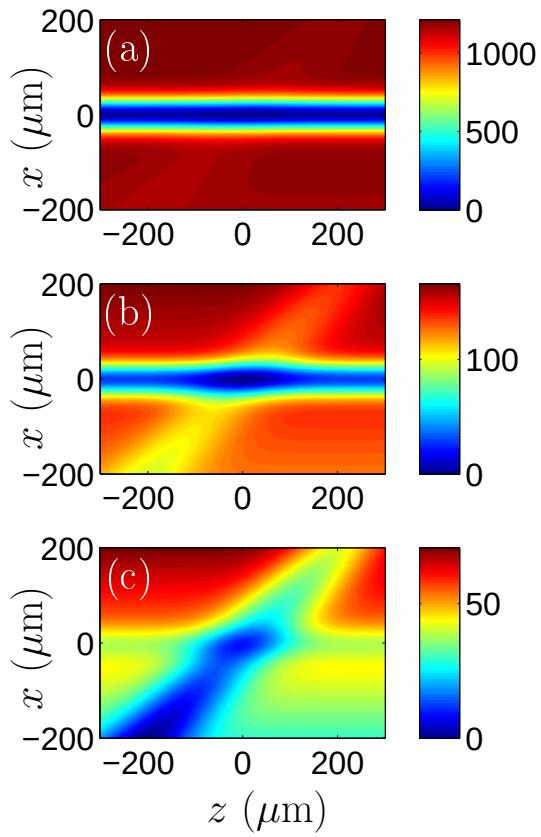

Figure 2.10: *Trapping potential in temperature units $U(x,z)/k_B$ μK at different stages of the evaporation. (a): $P_h = 30$ W, (b): $P_h = 3$ W, (c): $P_h = 300$ mW. At high power, the trap is very elongated and the eigenaxes are along x, y and z. When P_h decreases, the trap becomes more isotropic and the eigenaxes tend to be in the direction of the vertical beam (and orthogonal to it).*

need to decrease the power more slowly as the evaporation progresses. Small changes of τ_{evap} around $\tau_{evap} = 1300$ ms do not alter significantly the result as long as the condition (2.25) is met.

2.6.2 Characteristics of the crossed potential

The power of the vertical beam is constant during the evaporation. If we neglect the variation of the waists in the region of interest, the total potential experienced by the atoms is:

$$U_{cross}(x,y,z) = U_h(x,y,z) + U_v(x,y,z) + mgx \tag{2.27}$$

$$= -U_h \exp\left(-2\frac{x^2+y^2}{w_h^2}\right) - U_v \exp\left(-2\frac{y^2+(x-z)^2/2}{w_v^2}\right) + mgx. \tag{2.28}$$

A theoretical study of the eigenfrequencies and eigenaxes of the crossed trap can be found in Antoine Couvert thesis [60]. We will only recall here the main features with our parameters (see FIG. 2.10). It is always possible to calculate the eigenfrequencies and eigenaxes of the trap during the evaporation (see FIG. 2.11). We typically begin the evaporation at $P_h = 30$ W and $P_v = 3$ W. At the beginning of the evaporation, the potential induced by the vertical beam is negligible and

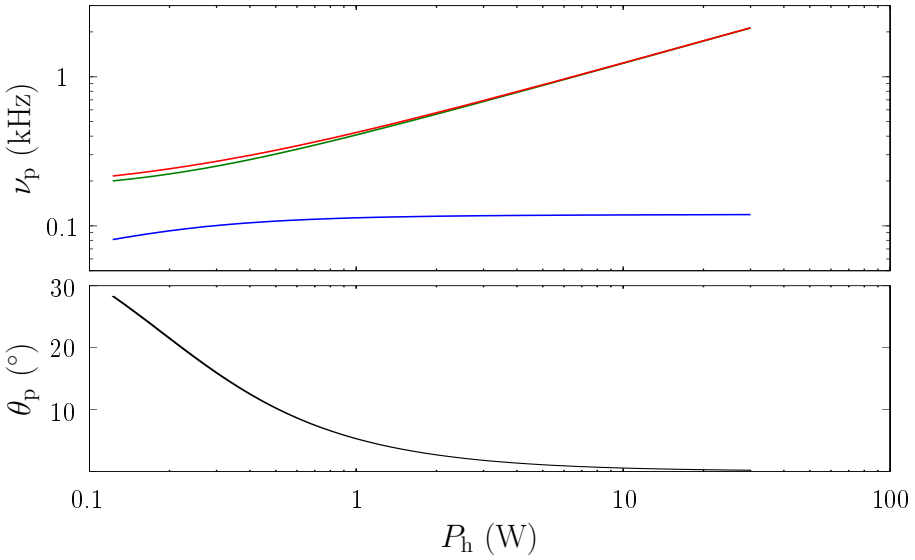

Figure 2.11: *Upper panel: Eigenfrequencies of the trap. Even in the presence of the vertical beam, the frequencies along x and y axes are generally much larger than the frequency in the z direction. Lower panel: angle θ between the eigenaxes and the x, z directions. At the beginning of the evaporation, the trap axes are aligned with the horizontal beam. They tend to align with the vertical beam at the end of the evaporation ramp.*

the trap is very elongated. In this configuration, the trap depth and frequencies along the axes x and y are approximatively the same and are much larger than the frequency along the z-axis, $\nu_x \simeq \nu_y \gg \nu_z$. When the temperature reaches a few μK, the atoms get localized mainly in the dimple. At this point, the eigenaxes also begin to change and tend to be at 45° from the original directions. The trap depth is then much smaller in the direction of the vertical beam, and the atoms evaporate in the vertical beam under the effect of gravity (see FIG. 2.10).

2.6.3 Evaporation trajectory

We can see in FIG. 2.12 a typical evaporation trajectory measured at the beginning of my Ph.D representing the number of atoms as a function of the temperature during the evaporation. We take 4 points every 100 ms until 2700 ms. During the evaporation, the number of atoms decreases by 2 orders of magnitude, the temperature by 3 orders of magnitude and the mean trapping frequency by less than one order of magnitude. Since the phase space density scales as $N\bar{\omega}/T^3$, it is increased by 6 orders of magnitudes during the evaporation. The last points thus correspond to condensed clouds.

There are two signatures of the Bose-Einstein transition:

- Because a macroscopic number of atoms are in the ground state of the trap which has the lowest momentum dispersion, after a time-of-flight, the cloud

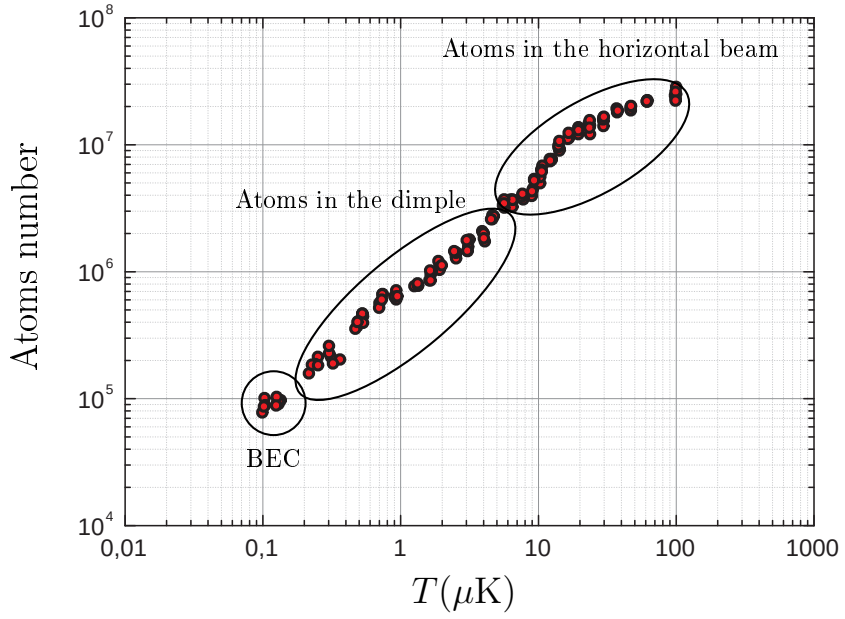

Figure 2.12: *Evaporation trajectory $N(T)$, the evaporation can be roughly divided into two phases. At the beginning of the evaporation, atoms are mainly localized in the horizontal guide. Between 1 and 10 μK, the atoms progressively localize in the dimple. The last points correspond to condensed clouds.*

profile exhibits two components (see FIG. 7.15): the condensed part, which is very sharp, and a larger thermal cloud. We can determine the condensed fraction and the temperature by fitting the cloud by a bimodal Gaussian.[10] The temperature is inferred from the width of the large thermal cloud while the condensed fraction is calculated by comparing the integrals of the two Gaussians.

- Another clear signature of the transition is the anisotropy of the condensed cloud observed after a long time-of-flight. In a thermal cloud, the momentum spread depends only on the temperature while in the ground state of a trap, it reflects the trap characteristics. If the trap is tighter in one direction, the wave function momentum spread will be larger (Heisenberg principle). As a consequence, if the trap is anisotropic, this will be reflected in the cloud shape after a time-of-flight.

We fit the density by the following bimodal function:

$$B(u) = A_{\mathrm{c}} \exp\left(-\frac{(u-u_0)^2}{2\Delta {u_{\mathrm{c}}}^2}\right) + A_{\mathrm{th}} \exp\left(-\frac{(u-u_0)^2}{2\Delta u_{\mathrm{th}}^2}\right), \tag{2.29}$$

[10] The condensate momentum distribution is *a priori* not Gaussian but rather, in the Thomas-Fermi regime, the Fourier transform of an inverse parabola [62]. However this fit is sufficient if one only wants qualitative measurement.

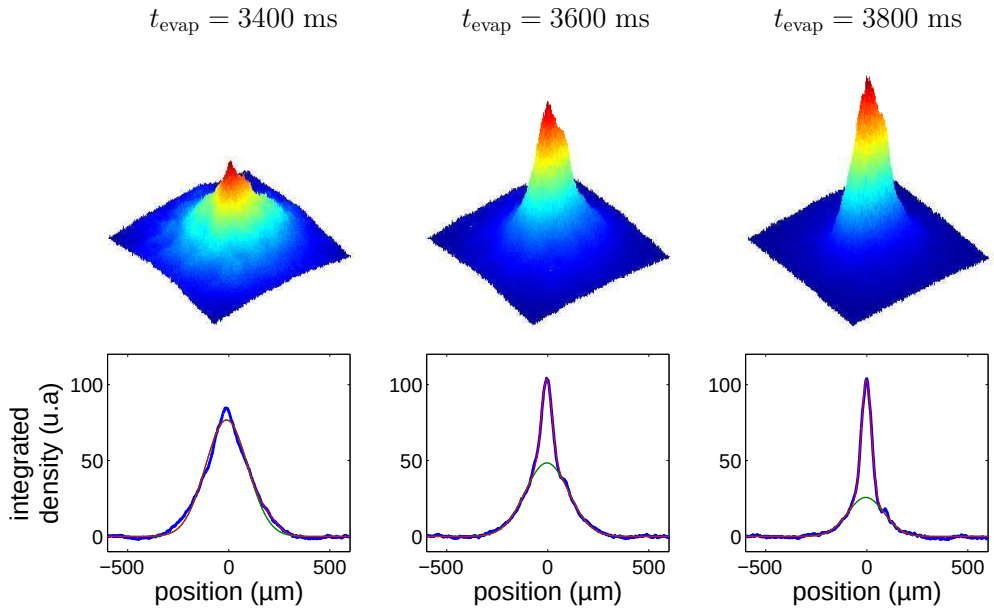

Figure 2.13: *Upper panel: atomic density after 15 ms of time-of-flight for different evaporation time through the Bose-Einstein transition, we see that a sharp peak arises above the thermal cloud. Lower panel: integration of the density along one direction, we fit the column density by a bimodal Gaussian. The spread of the larger Gaussian is related to the temperature of the cloud.*

the condensed fraction is then:

$$\frac{A_c \Delta u_c^2}{A_c \Delta u_c^2 + A_{th} \Delta u_{th}^2}. \tag{2.30}$$

With this method, we can check the relation (2.7) between the condensate fraction and the temperature. It is challeging to measure the thermal fraction and the temperature when the condensed fraction is too important because the thermal part is by definition more dilute than the condensate. In the same way, by fitting by a bimodal Gaussian, the result of the fit always displays a non-zero condensed part even at high temperature. We can nevertheless estimate the critical temperature by fitting with the relation (2.7) (see FIG. 2.14). We find $T_{c,exp} = 165$ nK. Using relation (2.6) and the calculated trap parameters, we estimate $T_{c,th} = 230$ nK

2.6.4 Spin distillation

As outlined before, one advantage of far detuned optical traps is that the dipole potential is the same for all magnetic sublevels.[11] As a consequence, one creates a spinor condensate with equipartition in all Zeeman states. However, in the following experiments, it is necessary to condense in a single state. To measure the number

[11] For a linear polarization.

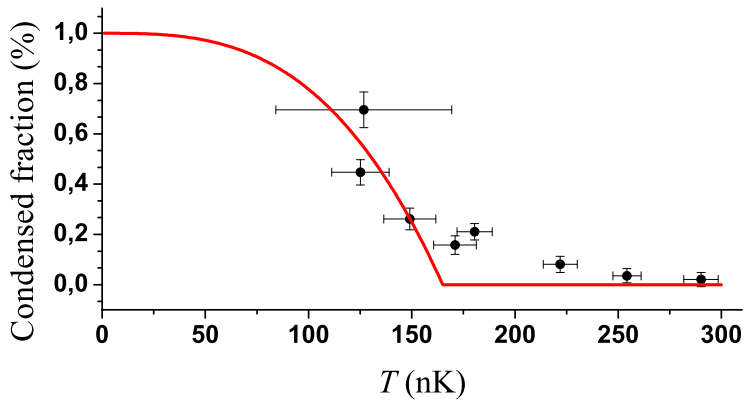

Figure 2.14: *Condensed fraction as a function of the temperature measured by fitting the cloud by a bimodal Gaussian distribution. We fit by the relation (2.6) and estimate* $T_c = 165$ nK.

of atoms in each Zeeman state, we perform a Stern and Gerlach experiment[12] by switching on a MOT coil during the time-of-flight. We use the spin distillation described in [16, 60] to get rid of the non-desired states. The principle is to superimpose a magnetic field gradient during the evaporation so that atoms in different magnetic states do not experience the same trapping potential. For atoms in $F = 1$, the potential is shifted by $m_F|B|\mu_B/2$ for $m_F = \pm 1$ and remains roughly the same for the state $m_F = 0$ since the Zeeman effect is then only quadratic. The trap depth then depends on the magnetic state, some atoms experience a shallower trap and are evaporated preferentially, the magnetic state that experience the deepest trap remain. This technique is not simply a filtering but a combination of evaporation and sympathetic cooling by the species that experience a shallower trap. We obtain comparable total number of atoms using spin distillation or not.

We use two kinds of distillation: the horizontal distillation, to condense atoms in $m_F = 0$ and the vertical distillation to condense in $m_F = +1$. In both cases, we add a current in one of the MOT coils. For the horizontal distillation, we inject typically 160 A in one of the "Horizontal" coil (see FIG. 2.9) that produces near the center of the trap a magnetic field of the form

$$B_{\rm hd} = \begin{pmatrix} -b'x/2 \\ b_0 + b'y \\ -b'z/2 \end{pmatrix} \tag{2.31}$$

Close to the trap center ($x, y, z \ll B_0/b'$), the amplitude of the field simply reads at

[12] We split the time of flight into two phases. A magnetic field gradient of $\Delta B =$ is applied during a first stage of 5 ms to separate the species, and is switched off a few milliseconds before the image is taken so that there is no remanent field when we take the picture.

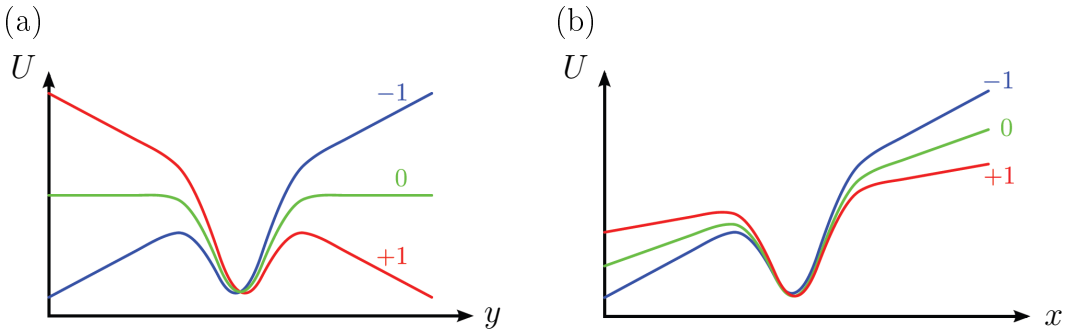

Figure 2.15: *Trapping potential for different Zeeman sublevels. Left: potential along the y axis, the trapping depth in this direction is lowered for the states* $m_F = \pm 1$. *Right: potential along the vertical axis, the magnetic field gradient partially compensates for the gravity for the high field seekers.*

the first order

$$|B_{\mathrm{hd}}| \simeq b_0 + b'y. \tag{2.32}$$

The effect is to bend the potential in the y direction. In FIG. 2.15, we see the modified potentials in the y direction. Because of the magnetic shift, the trap depth is smaller for the $m_F = +1$ state. They get evaporated preferentially and it is possible to end up with only atoms in $m_F = 0$. We also use the horizontal distillation to easily optimize the crossing. As a matter a fact, it is possible to compensate for the magnetic shift by desaligning the vertical beam on one side of the crossing, in this configuration, it is possible to obtain a condensate of atoms in $m_F = +1$ only. This method is not very stable, if one wants to condense into $m_F = +1$, it is better to use the vertical distillation. However, we use this effect as a protocol to optimize the crossing, when the distillation is not complete, the three species can coexist with different weights, by moving the vertical beam it is possible to favor one or another. The crossing is optimized when the populations in $m_F = -1$ and $m_F = 1$ are equal.

For the vertical distillation, we use the Top coil (see FIG. 2.9), the field produced near the center reads

$$B_{\mathrm{hd}} = \begin{pmatrix} -b'x/2 \\ -b'y/2 \\ b_0 + b'z/2 \end{pmatrix} \tag{2.33}$$

and at the first order in x, y, z

$$|B_{\mathrm{hd}}| \simeq b_0 + b'z. \tag{2.34}$$

This introduces a distortion along z that partially compensates for the gravity for high field seekers (see FIG. 2.15). The other species experience a much lower trap depth and evaporate before the $m_F = +1$ specie. It is important to outline here that the distillation in a magnetic state is here only possible because of gravity.

2.7 Conclusion

In this chapter, we have presented our setup to produce rubidium Bose-Einstein condensates using evaporative cooling in a dipole trap. The production of BECs by mean of only optical traps offer some advantages compared to magnetic traps [68]:

- the possibility to decrease the depth of the trap very easily,
- a generally shorter cycle time,
- the possibility to condense in any magnetic state (or a superposition),
- the possibility to condense atoms without magnetic structure, which is particularly interesting for metrology,

and also some drawbacks:

- generally smaller BEC,
- more day to day work to align the beams, clean the optics and so on.

In our case it also offer the important advantage of providing the waveguide used in the scattering experiments.

Chapter 3

Lattice setup and characterization

Contents

3.1 Introduction **63**
3.2 Setup of the optical lattice **64**
3.2.1 Potential and notations 64
3.2.2 Experimental setup 65
3.2.3 Method to cross the lattice beams 68
3.3 Calibration **68**
3.3.1 Kapitza-Dirac diffraction 69
3.3.2 Experimental realization 70
3.3.3 Beyond the Raman-Nath regime 71
3.4 Robustness against misalignments **72**
3.5 Conclusion **73**

3.1 Introduction

By crossing two coherent beams in a region of space, one creates a standing wave pattern. If the laser light is detuned from the atomic transition, the standing wave results in a periodic dipole potential varying on a fraction of the optical wavelength. These commonly-called optical lattices have a wide range of applications in the field of cold atoms due to their great flexibility:

- In terms of dimensionality: by adding standing waves along orthogonal directions, one can produce a periodic potential in 1, 2 or 3 dimensions. If the trap is deep enough in one direction, it is then possible to reduce the dimensionality of the atomic motion.

- The geometry can be tuned by engineering for example the directions, intensities or phases of the lasers or by superimposing two lattices with different spacings [69, 70]

- The potential properties can be easily tuned in time.

These nice properties have been extensively used to study many-body physics and quantum phase transitions. Indeed, there is a strong analogy with condensed matter problems where atoms play the role of the electrons in a solid while the lattice potential plays the role of the potential produced by the static ions. The tunability of the lattice parameters and atomic interactions have allowed for example to study the Mott insulator-superfluid transition [71] and problems of quantum magnetism [72, 73].

Optical lattice can also be used to study one-body physics. Moving molasses realized by introducing a frequency difference between the two beams are used for instance in atomic clocks [74]. Diffraction in the regime of shallow lattice *i.e* Bragg diffraction is commonly used as a beam splitter in atomic interferometers. Moreover, fundamental quantum transport questions such as the Anderson localisation [75, 76], the study of atomic ratchets [77] or dynamical tunneling [78] can also be addressed.

In this chapter, we present the setup of our 1D lattice and the calibration of its depth. To calibrate the lattice depth, we perform Kapitza-Dirac diffraction on a condensate. The basic idea is that atoms can redistribute photons between the two interfering laser beams. In this process, the momentum of the atom is modified by a quantified quantity. After a time-of-flight, the different momentum components separate and produce a diffraction pattern from which one can infer the lattice depth. We will first describe the experimental setup, then we will detail the calibration of the lattice depth.

3.2 Setup of the optical lattice

3.2.1 Potential and notations

To perform the scattering experiments, we need to produce a periodic potential with a finite size envelope. This is realized by intersecting two laser beams of finite extent at a non-zero angle. We use two identical Gaussian laser beams at 850 nm (red-detuned from the transitions) focused to the same waist $w = 110$ μm. The two beams cross at their waist positions with an angle $\theta = 81°$. The beams are both polarized in the vertical direction $\boldsymbol{y}$. Because the Rayleigh length is very large ($z_{\mathrm{R}} = 4.5$ cm), we can neglect the variation of the radius of curvature and of the Gouy phase in the calculation of the electric field. The field produced by one laser then reads:

$$E_{1,2} = E_0 \exp\left(i\boldsymbol{k_{1,2}}\boldsymbol{r} - \frac{d_{1,2}^2}{2w^2}\right)\boldsymbol{y}, \tag{3.1}$$

where $\boldsymbol{k_{1,2}}$ are the wave vectors of the two beams, $d_{1,2}$ the radial distances to the beams axis and E_0 the maximum amplitude. The electric field can be expanded on

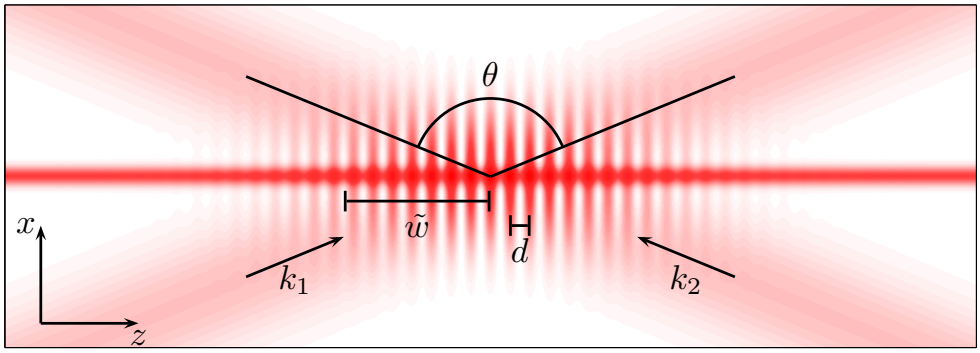

Figure 3.1: *Sketch of the lattice potential and notations.*

the axes related to the horizontal guide ($\boldsymbol{z}$ being the direction of the guide):

$$E_{1,2} = E_0 \exp\left(-\frac{2(\sin(\theta/2)x \pm \cos(\theta/2)z)^2}{w^2}\right) \exp\left(ik(\pm\sin(\theta/2)z + \cos(\theta/2)x)\right)\boldsymbol{y}. \tag{3.2}$$

Close to the guide axis, $(x, y \ll w)$, the potential produced by the two interfering beams thus reads

$$U = \zeta|E_1 + E_2|^2 = \zeta 2I_0 \exp\left(\frac{z^2}{2\tilde{w}^2}\right)(1 + \cos(k_{\mathrm{L}}z)), \tag{3.3}$$

where $\zeta = -7.7 \cdot 10^{-36}$ J.W^{-1}.m^{-2} is the light shift coefficient at 850 nm, $\tilde{w} = w/\cos^2(\theta/2)$, the waist of the lattice envelope in the guide direction, I_0, the maximum intensity of one beam and $k_{\mathrm{L}} = 2k\sin(\theta/2)$, the wave vector associated with the lattice periodicity. The lattice spacing is then $d = 2\pi/k_{\mathrm{L}} = 650$ nm. We also define a velocity scale $v_{\mathrm{L}} = h/md = \hbar k_{\mathrm{L}}/m$ associated with the periodicity, an energy scale[1] $E_{\mathrm{L}} = \hbar^2 k_{\mathrm{L}}^2/2m = mv_{\mathrm{L}}^2/2$ and a frequency scale $\nu_{\mathrm{L}} = E_{\mathrm{L}}/h$. Figure. 3.1 shows a sketch of the potential experienced by the atoms along with the notations. The trapping frequency at the bottom of one lattice site scales as the square root of the lattice depth U_0: $\nu_s = \nu_{\mathrm{L}}\sqrt{U_0/E_{\mathrm{L}}}$

d	650 nm
v_{L}	7.1 mm/s
E_{L}	$3.6 \cdot 10^{-30}$ J $k_{\mathrm{B}} \cdot 262$ nK $h \cdot 5.4$ kHz

[1]Note that we use here a notation different from the one more commonly used $E_{\mathrm{R}} = \hbar^2 k^2/2m$ that represents the recoil energy transferred when an atom absorbs a photon of wavevector k

3.2.2 Experimental setup

The 850 nm laser along with an AOM that permits to control the intensity of the lattice beams are set on an independent table, the laser is then transferred to the main table by means of a polarization maintaining fiber. The separation and the shaping of the beams are managed on the main table (see FIG. 3.2).

We use a 850 nm single mode laser from Toptica Photonics. A master laser in a cavity injects a tapered amplifier followed by an integrated optical isolator. At the output, we get a typical power of 550 mW. We check the monochromaticity and the frequency of the laser by sending a small portion of the master oscillator into a Fabry-Pérot cavity and a commercial lambdameter. The frequency is quite stable and we do not need to lock it. The laser is then sent through a 100 MHz AOM with a 72% efficiency in the first order that allows us to control the intensity. The power of one of the lattice beam is monitored on a 100 MHz bandwidth photodiode placed after the vacuum chamber. The power is actively stabilized using an integrator feedback loop. On the main table, a telescope adjusts the beam size in order to get the desired waist on the atoms $w = 110$ μm, the beam is then split into two arms with equal intensities using a $\lambda/2$ waveplate and a polarizing beamsplitter. We focus the two beams at the center of the vacuum chamber using two additional 1000 mm focal length lenses. Typically, we obtain a maximum power of 50 mW per arm on the atoms. The corresponding potential (non interfering) has a depth $U_{arm}/k_{\mathrm{B}} = 1.5$ μK per arm. The beams are polarized vertically using $\lambda/2$ waveplates and a polarizers in order to obtain a 100% contrast interference pattern.

The crossing of the two beams is critical in the experiments. However, our limited optical access forced us to set the last mirror quite far from the vacuum chamber at about 1 m. When changing the angle of the mirror, the spot position changes with a sensitivity of ~ 2 cm per degree. To move a lattice beam from less than its waist, we thus need a precision better than 100 μrad. In practice, we are limited by the mechanical hysteresis of the optical mount screws. In order to benefit from a more accurate control over the beam positions, we add on each arm thick glass plates that deflect the beams after the focusing lenses.

A plane wave incoming on a plate of thickness e and index n with a relative angle i (see FIG. 3.3 (a)) is displaced by a distance

$$l(i) = e\frac{\cos(i-r)}{\cos r} = e\frac{\sin(i - \arcsin[\sin(i)/n])}{\cos(\arcsin[\sin(i)/n])}. \tag{3.4}$$

Figure 3.3 (b) shows the resulting displacement sensitivity when changing the angle i. Compared to changing the mirror angle, the sensitivity is reduced by two orders of magnitudes. In practice, we first use the mirror to cross approximately the lattice beams then we use the thick plates to accurately tune the spot positions. Our thick waveplates are cheaper and less cumbersome than piezomounted mirrors. However, with this choice, we do not have the possibility to actively stabilize the lattice beam

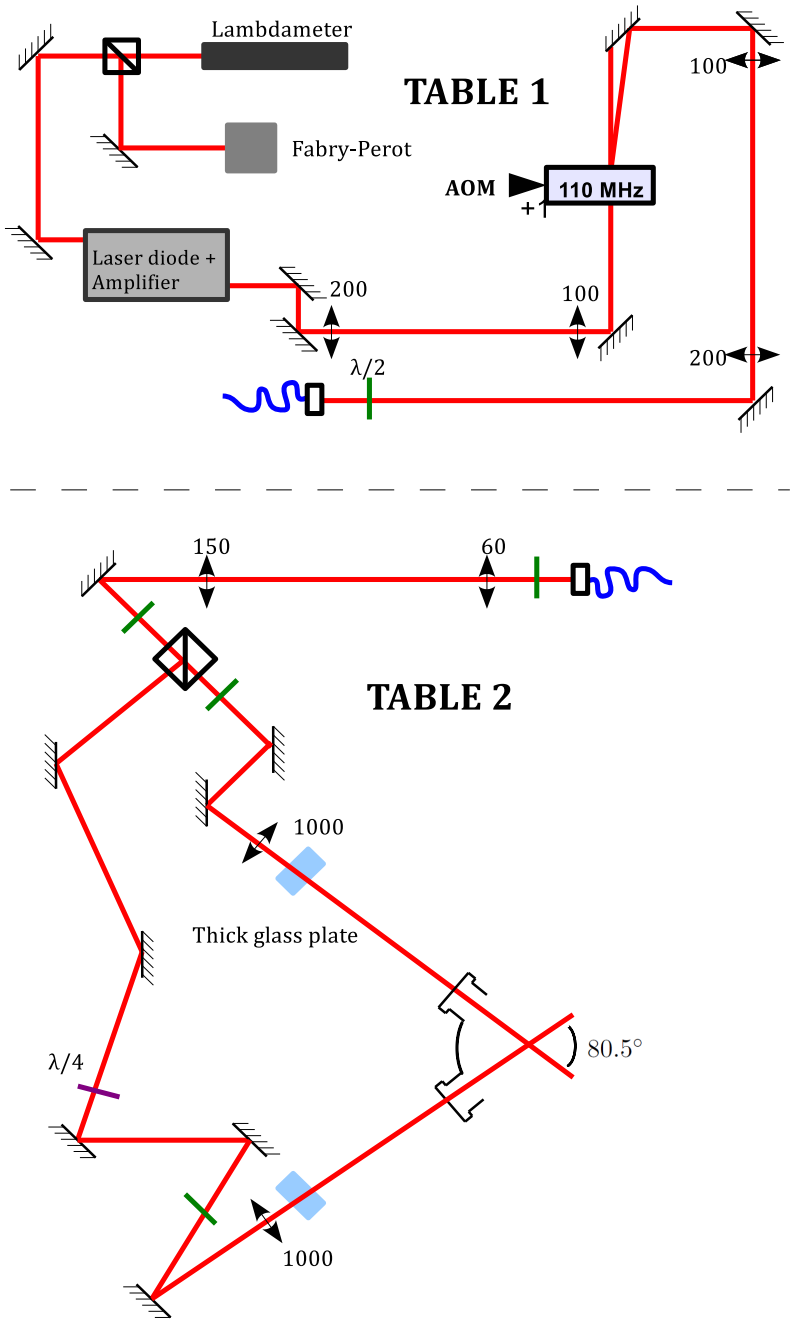

Figure 3.2: *Sketch of the setup of the lattice beams. Table 1 contains the laser and the power control. The splitting of the beam and the shaping are performed on the main table.*

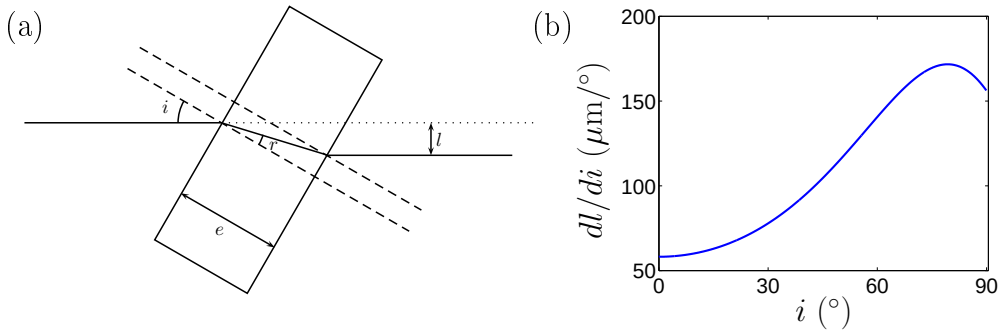

Figure 3.3: *(a) Sketch of the deviating beam device. (b) Sensitivity of the light deviation l.*

positions.

3.2.3 Method to cross the lattice beams

Obviously, the power of the lattice beams is limited, in particular, we do not dispose of enough power to capture directly atoms from the MOT into one of the lattice beam. Consequently, it is not possible to image in situ the positions of the lattice beams. In order to cross them, we first temporarily replace the fiber of the 850 nm laser by one issued from a laser at 780 nm set on the depumping transition $F = 2 \rightarrow F' = 2$. We then start a typical experimental sequence with a different imaging sequence. First, the repumping beam is turned on during 1 ms to repump all atoms in $F = 2$. We then shine the depumping beam which is superimposed to the lattice beams for another ms. Atoms located at the lattice beam positions are locally pumped into the $F = 1$ state. We do not use the repumper during the snapshot to image only atoms in $F = 2$. In this way, the lattice beams appear as holes in the dipole trap. Figure 3.4 shows the holes produced by the two lattice beams (not crossed here) on the horizontal guide. Once the lattice beams are roughly crossed, we go back to the 850 nm laser. As outlined before, the maximum depth we can achieve with all the power in one arm is about $U_{\text{lat}} \sim 3$ μK. In order to accumulate atoms in the dimple produced by the intersection of the horizontal guide and one of the lattice beams, the temperature has to be decreased first using evaporative cooling in the guide only. We optimize the crossing by maximizing the number of atoms in the dimple produced by the crossing of the guide and one arm of the lattice.

3.3 Calibration

The actual depth of the optical lattice is very sensitive to different defects of the experimental setup, among them are: a defect in polarization, a different size of the beam waists or an imperfect crossing. Therefore, it is essential to calibrate the depth

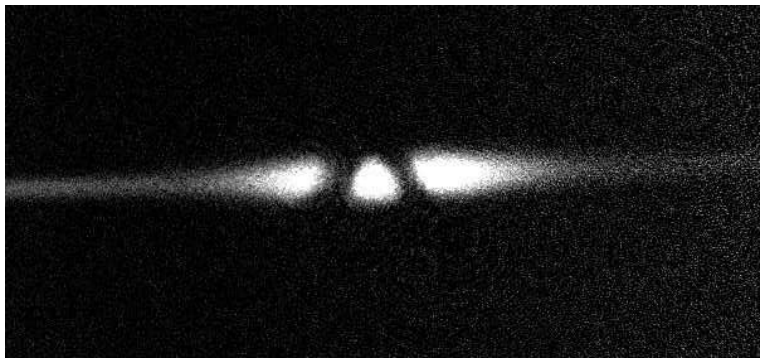

Figure 3.4: *Absorption image of atoms in the horizontal traps. Before taking the image, we shine during 1 ms a resonant depumping laser superimposed with the lattice beams. We do not use a repumper during the imaging so that atoms that have been locally pumped into the $F = 1$ ground state are not visible. Here the two lattice beams are not yet crossed in the final position.*

of the lattice *in situ* with a measurement on the atoms. There are different methods of calibration, the most commonly used rely either on Landau-Zener transitions or on Kapitza-Dirac diffraction; we use the latter method. It consists in shining the optical lattice for a brief amount of time τ on the condensate and observe the resulting diffraction pattern after a time-of-flight.

3.3.1 Kapitza-Dirac diffraction

To begin with, let us consider the Raman-Nath limit of small interaction times [79]. If the interaction time is much smaller than the inverse of the trapping frequency $\nu_s = \nu_{\mathrm{L}}\sqrt{U_0/E_{\mathrm{L}}}$, we can consider that atoms do not have enough time to move during the interaction with the lattice, which amounts to neglecting the kinetic energy term in the Hamiltonian. The resolution of the dynamics is then straightforward using the evolution operator. The BEC wavefunction at a time τ reads:

$$\psi(z,\tau) = e^{-iH\tau/\hbar}\psi(z,0) \simeq e^{-iU(z)\tau/\hbar}\psi(z,0). \tag{3.5}$$

In this limit, the application of the optical lattice potential amounts to a phase imprinting. The phase of the wavefunction is modulated at the period d. Quantitatively, the evolution operator can be expanded as a sum of Bessel functions:

$$e^{-iU_0[1+cos(k_{\mathrm{L}}z)]\tau/2\hbar} = e^{-iU_0\tau/2\hbar}\sum_{n=-\infty}^{n=+\infty}(-1)^n J_n\left(\frac{U_0\tau}{2\hbar}\right)e^{ink_{\mathrm{L}}z}, \tag{3.6}$$

where J_n is the n-th order Bessel function. The global phase term in front of the sum is irrelevant and we will forget about it. The wave function at the time τ now

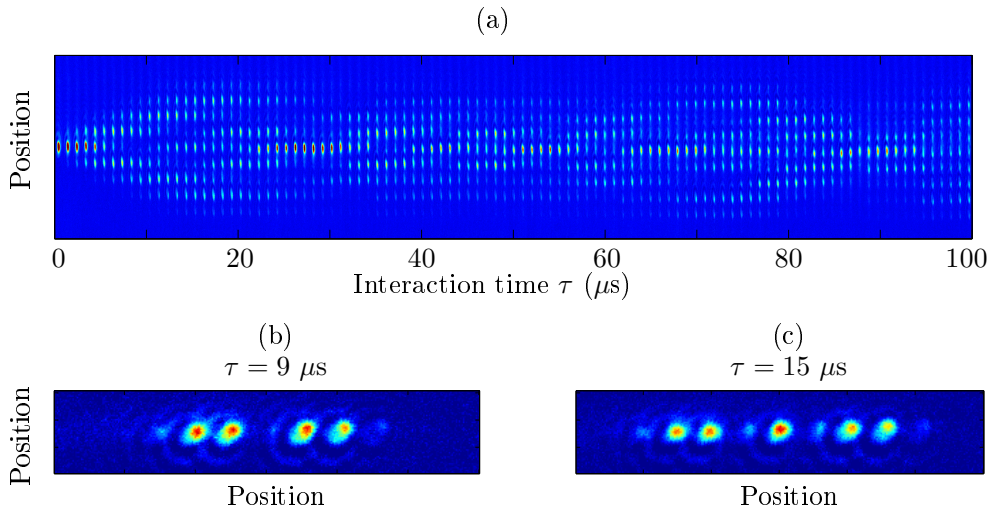

Figure 3.5: *Diffraction patterns with 48 mW per lattice arm. (a) Concatenated patterns for a variable interaction time τ. (b) and (c) Diffraction patterns at $\tau = 9$ and 15 μs respectively.*

reads:

$$\psi(z,\tau) = \sum_{n=-\infty}^{n=+\infty} (-1)^n J_n\left(\frac{U_0\tau}{2\hbar}\right) e^{ink_{\mathrm{L}}z}\psi(z,0). \tag{3.7}$$

Let us take the fourier transform of ψ to calculate the wavefunction in momentum space φ:

$$\varphi(\kappa,\tau) = \sum_{n=-\infty}^{n=+\infty} (-1)^n J_n\left(\frac{U_0\tau}{2\hbar}\right) \delta(\kappa - nk_{\mathrm{L}}) * \varphi(\kappa,0). \tag{3.8}$$

The wavefunction after interaction is noting but the initial wavefunction convoluted with a comb at the lattice frequency. The weights of the diffraction orders are set by the values of the successive Bessel functions at the time τ. If the initial momentum dispersion is smaller than k_{L}, the diffraction orders can be well separated and measured after a time-of-flight.

3.3.2 Experimental realization

We first produce a condensate using the method described in the previous chapter. At the end of the evaporation, we switch off the trap beams and turn on the lattice beam in less than 150 ns with 48 mW per arm for a variable interaction time τ. We then perform a 10 ms time-of-flight before taking an image. Figure 3.5 shows typical diffraction patterns concatenated for interaction times varying from 0 to 100 μs. We see that the initial condensate is diffracted in several orders separated in impulsion

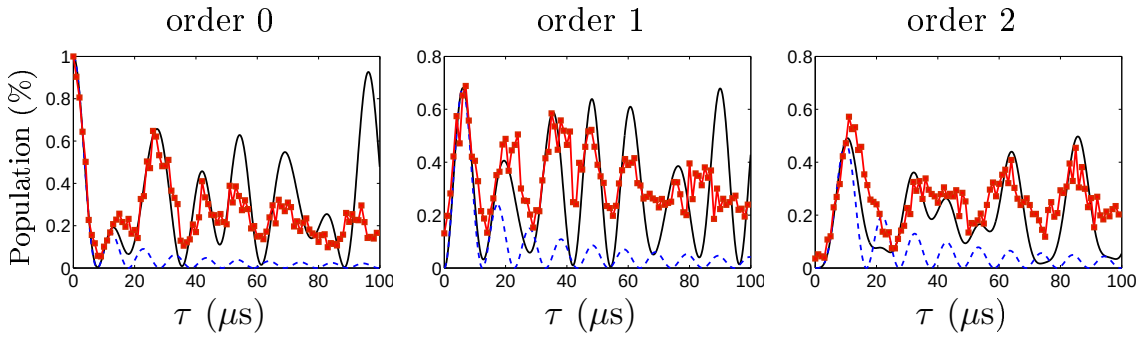

Figure 3.6: *Percentage of the total population in the different orders as a function of τ. Red squares are the experimental data, the green dashed line are the Bessel functions with $U_0 = 17E_L$. The agreement is only good in the Raman-Nath regime i.e at times much shorter than the oscillation period $\sim 44\mu$s. The blue line is the result of the numerical integration of the Schrödinger equation with the same lattice depth. The first cancelation of the zero-th order occurs at $\tau = 9$ μs and the first revival at $\tau = 27$ μs*

space by $\hbar k_L$.[2] From the images, we extract the populations in each order and compare them to the result of the calculations. The calculated maximum depth is $U_0 = 18.4E_L$. Figure 3.6 (red squares) shows the populations in the orders from 0 to 2 as a function of τ. The dashed lines are the result of the Raman-Nath calculation (*i.e* the square of the Bessel functions) with $U_0 = 17E_L$. The agreement is good at small times but is very bad for times $\tau > 15$ μs. This is because we are no longer in the Raman-Nath regime [80]. Indeed, for this lattice depth, $1/\nu_s = 44$ μs. We will see in the next section how we can understand the long interaction time regime. It is interesting to consider the time at which the zero-th order vanishes (with our parameters, we are still in the RN regime). This correspond to the annulation of the first Bessel function, which implies that

$$U_0\tau/2\hbar = 2.405 \tag{3.9}$$

We can then deduce the depth of the lattice potential using only the time of first annulation of the zero-th order τ_{fa}:[3]

$$\frac{U_0}{E_L} = \frac{2.405}{\pi\nu_L\tau_{fa}}. \tag{3.10}$$

We find experimentally $\tau_{fa} = 9$ μs, which implies that $U_0/E_L = 15.7$

[2] We also use the distance between the diffraction peaks to calibrate the magnification of the imaging system.

[3] The rule of the thumb is, for τ_{fa} in μs: $U_0/E_L = 141/\tau_{fa}$

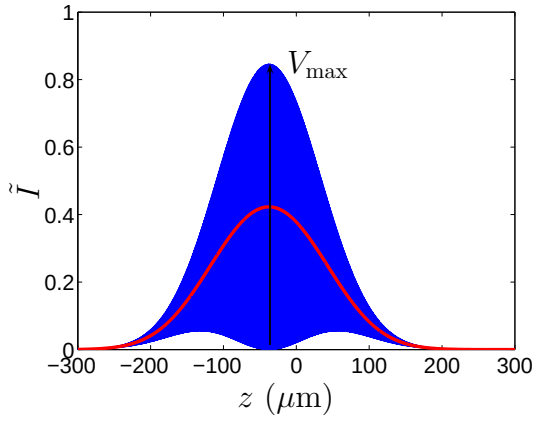

Figure 3.7: *(blue) Interference pattern produced by two beams misaligned by* $\delta z = 75$ μm *normalized by the maximum intensity for a perfect crossing. (red) local mean intensity* $\bar{I}(z)$.

3.3.3 Beyond the Raman-Nath regime

For interacting times that are not small compared to the trapping frequency, there is no simple analytical relation to calculate the diffraction orders weights and it is necessary to solve numerically the Schrödinger equation with the kinetic energy term. However, it is possible to understand some features qualitatively [80, 28]. In particular, we observe revivals of the population in the zero-th order at long time while the first Bessel function quickly vanishes. This phenomena can be understood by projecting the initial wavefunction on the eigenstates of the system. With a deep enough lattice ($U_0/E_\mathrm{L} \gg 1$) and in the harmonic limit, each lattice site yields eigenstates separated in energy by $h\nu_s$, and successively symmetric and antisymmetric. Let us consider an initial state with a zero mean momentum, because the initial wavefunction is symmetric, it has a projection on even parity states only. As a consequence, the populated eigenstates are separated in energy by $2h\nu_s$. This leads to revivals: all states rephase at times $\tau_\mathrm{rev} = 1/(2\nu_s)$. At those particular times, the wavefunction goes back to its original form *i.e* without any diffraction. We observe indeed partial revivals of the zero-th order at 25 and 43 μs, however, the revivals are not complete because of the anharmonicity of the potential. In order to make the most of our measurements, we also use the datas outside of the Raman-Nath regime. We solve numerically the Schrödinger equation with different U_0 and determine the depth for which the simulation provides the best fit of the data. We find $U_0 = 17 \pm 1 E_\mathrm{L}$ which is 7% below the calculated value.

3.4 Robustness against misalignments

Because we cross the lattice beams with a non-zero angle, the crossing procedure is complicated and we expect that, despite our efforts, the two beams can be significantly misaligned. In this case, the interfering patterns can have a complicated shape. As an example, FIG. 3.7 shows the interference pattern if the centers of the two beams are separated by $\delta z = 75$ μm. In this picture, the calibration of the lattice

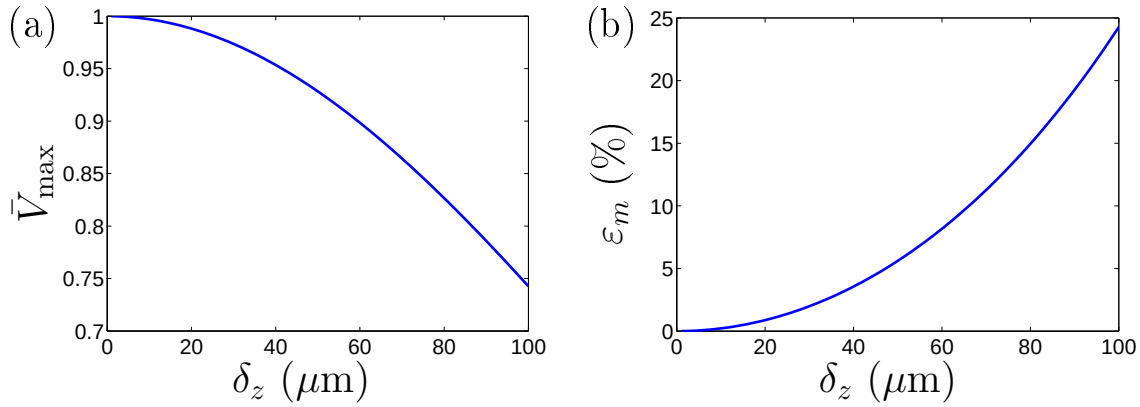

Figure 3.8: *(a) Reduction of the visibility as a function of the misalignment between the two lattice beams. (b) Difference between the real potential and an ideal Gaussian lattice as defined by Eq. (3.11).*

depth by Kapitza-Dirac diffraction is a measurement of the local visibility. Because we optimized the position of the condensate in the lattice, we can consider that we measure the maximum visibility $\bar{V}_{\max}$ of the interference pattern. The question is: how different is the real potential from an ideal lattice with a Gaussian envelope and the measured maximum visibility? To get a quantitative answer, we calculate, for a misaligned potential, the local visibility $\bar{V}(z)$ and local mean intensity $\bar{I}(z)$. For perfectly crossed beams, the potential is such that the visibility is equal to twice the mean intensity everywhere: $\bar{V}(z) = 2\bar{I}(z)$. We thus define the error due to a misalignment by

$$\varepsilon_m(\delta z) = \max(\bar{V}(z)/2 - \bar{I}(z))/\max(\bar{I}(z)). \tag{3.11}$$

Figure 3.8 (a) shows the reduction of the maximum visibility as the two beams are misscrossed. Interestingly, the reduction of visibility remains moderate: the visibility is only reduced by 10% as the centers of the beams are separated by half their waist. Using the ratio between the measured visibility and the calculated one, we thus estimate that in the experiment, the misalignment $\delta_z < 50$ μm. Figure 3.8 (b) shows the error defined by Eq. (3.11) as a function of δ_z, we see that for $\delta_z < 50$ μm, the error is small $\varepsilon_m < 5\%$. This ensures that despite a complicated crossing procedure, the potential experienced by the atoms is very close to a lattice with a Gaussian envelope and a maximum visibility taken equal to the visibility measured by Kapitza-Dirac diffraction

3.5 Conclusion

In this chapter, we have presented our experimental setup to engineer a 1D optical lattice with a finite size envelope. We have described how we calibrate the depth of the lattice *in situ* using Kapitza-Dirac diffraction in the Raman-Nath regime and beyond, and give an argument about the robustness of this method. In the next chapter, we will recall some theoretical tools useful to describe the dynamics of a particle in a periodic potential.

Chapter 4

A quantum particle in a periodic potential

Contents

4.1 Introduction **75**
4.2 Bloch band structure **75**
4.2.1 Bloch theorem 75
4.2.2 Computation of the band structure 76
4.3 Mathieu equation **78**
4.3.1 Stability regions 79
4.3.2 Computation of the characteristic exponent 80
4.4 Interpretation of a scattering experiment **81**
4.5 Conclusion **83**

4.1 Introduction

In this chapter, we recall some theoretical tools of general use when dealing with quantum problems in the presence of a periodic potential. We present the construction of the band energy diagram using Bloch theorem and the closely related solutions of the Mathieu equation. As we will see, these solutions are an extension of Bloch states to the case where the energy lies in a gap of the band structure. They turn out to be very useful when considering scattering problems. We use these solutions to analyze the problem of the scattering of a particle on a semi-infinite lattice.

4.2 Bloch band structure

4.2.1 Bloch theorem

Let us consider a particle in a 1D periodic potential of period d:

$$U(z+d) = U(z). \tag{4.1}$$

The stationary Schrödinger equation that describes the dynamics reads:

$$H\psi(z) = \left(\frac{p^2}{2m} + U(z)\right)\psi(z) = E\psi(z). \tag{4.2}$$

The Bloch theorem then states [81] that the eigenstates of a periodic hamiltonian may be written as the product of a plane wave envelope function with a wavevector k and a function $u_{n,k}(z)$ that has the same periodicity as the potential U:

$$\psi_{n,k}(z) = e^{ikz}u_{n,k}(z) \qquad \text{with} \qquad u_{n,k}(z+d) = u_{n,k}(z). \tag{4.3}$$

n is an integer that denotes the band index. Except for $k = 0$, these Bloch states are propagating states. By injecting this form into Eq. (4.2), we see that the functions $u_{n,k}$ are the eigenstates of a modified Hamiltonian that depends on k:

$$H_k = \frac{(p+\hbar k)^2}{2m} + U(z) \tag{4.4}$$

Using this eigenvalue equation and the boundary condition $u_{n,k}(z) = u_{n,k}(z+d)$, the signification of the band index becomes clear. $E_n(k)$ are the eigenvalues of a modified hamiltonian in a box with periodic boundary conditions. As such, we expect a quantification of the energies that correspond to the discrete band index n. Because of the periodicity of the Bloch functions $u_{n,k}$, we can limit ourselves to the first Brillouin zone, that is to say to $k \in [-k_\mathrm{L}/2, k_\mathrm{L}/2]$ ($k_\mathrm{L} = 2\pi/d$). We can then expand the periodic Bloch functions $u_{n,k}$ as Fourier series.

$$\psi_{n,k}(z) = e^{ikz}u_{n,k}(z) = \sum_l a_l e^{i(k+lk_\mathrm{L})z}. \tag{4.5}$$

For a given k, working out the Bloch state $\psi_{n,k}(z)$ thus amounts to finding the coefficients a_l.

4.2.2 Computation of the band structure

Because the potential U is periodic, we shall expand it as a Fourier serie too:

$$U(z) = \sum_p U_p e^{ipk_\mathrm{L}z}. \tag{4.6}$$

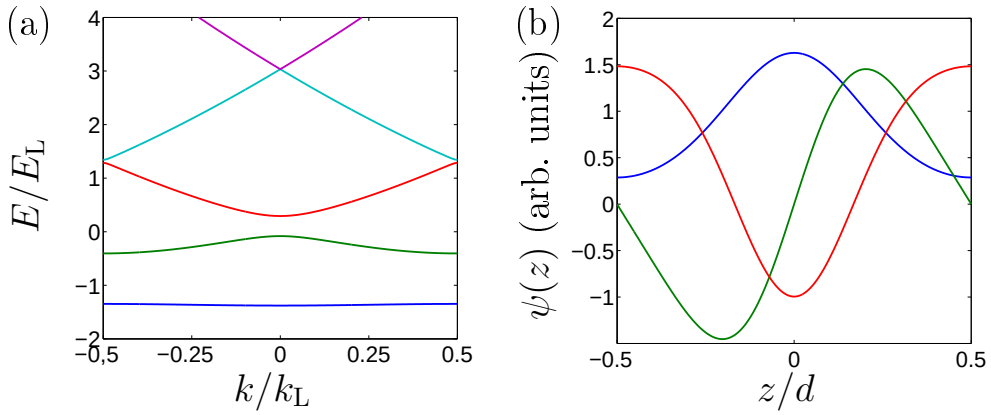

Figure 4.1: *(a) Band structure for $U_0 = -2E_L$. (b) first eigenstates with $k = 0$. n=1: blue, n=2: green, n=3: red. Similarly as for a particle in a symmetric trap, the eigenstates are successively symmetric and antisymmetric.*

By injecting Eq. (4.5) and (4.6) into the Schrödinger equation and identifying each term in $e^{i(k+lk_L)z}$, we obtain a matrix equation that reads:

$$\frac{\hbar^2}{2m}\left(k + lk_L\right)^2 a_l + \sum_p U_p a_{p-l} = E a_l. \tag{4.7}$$

For example, let us take the potential produced by an infinite attractive lattice: $U(z) = -U_0/2(\cos(k_L z) + 1)$, Eq. (4.7) can be represented by:

$$\begin{pmatrix} b_{-N} & u & & & \\ u & b_{-N+1} & u & & \\ & \ddots & \ddots & \ddots & \\ & & u & b_{N-1} & u \\ & & & u & b_N \end{pmatrix} \times \begin{pmatrix} a_{-N} \\ a_{-N+1} \\ \vdots \\ a_{N-1} \\ a_N \end{pmatrix} = E \begin{pmatrix} a_{-N} \\ a_{-N+1} \\ \vdots \\ a_{N-1} \\ a_N \end{pmatrix}, \tag{4.8}$$

where

$$u = \frac{U_0}{4} \quad \text{et} \quad b_l = E_L\left(k/k_L + l\right)^2 - \frac{U_0}{2}. \tag{4.9}$$

For a more complicated potential, as the potential gets more Fourier components, the matrix gets more off-diagonal elements. This system is easily solved using a standard diagonalization algorithm.[1] To describe correctly a Bloch state, it is necessary to consider a large enough number of Fourier components N. The number of relevant Fourier components generally scales as the band index. In the calculations, we choose N equal to three time the maximum considered band index. The different eigenvalues are the energies for a given pseudo-impulsion k but different band index. Figure 4.1 (a) shows the energies $E_n(k)$ for $U_0 = 2E_L$. The energies are grouped in

[1] It is also possible to solve the Schrödinger equation in the position space, however the eigenvalue problem does not display a diagonal matrix so that the computation is much less efficient.

bands separated by gaps. The size of the gap generally decreases as the band index increases. Figure 4.1 (b) shows the corresponding Bloch states with $k = 0$ and a band index $n = 1, 2$ and 3. Just like a particle in a symmetric trap, the eigenstates are successively symmetric and antisymmetric. This is to be related with the tight binding method to construct the band structure. In this method, one starts from states localized in a single well. If the lattice site is symmetric, the eigenstates are always successively symmetric and antisymmetric. One then couple the different lattice sites with a tunneling rate that lifts the degeneracy between the energies associated with each site. The band structure is then reconstructed progressively by coupling an infinite number of lattice sites. Each band is then associated with one state of a single lattice site and this is reflected in the symmetries of the Bloch states.

4.3 Mathieu equation

In the case of scattering experiments on a finite size lattice, the eigenstates are not the only interesting solutions of the time-dependent Schrödinger equation. Let us suppose nonetheless that we can always write the solution of the Schrödinger equation as a function of the position only plus a time-dependent phase of the form:

$$\psi(x,t) = e^{-iEt/\hbar}\phi(x). \tag{4.10}$$

If we inject this form into the Schrödinger equation, one find exactly the time-independent equation. However, E corresponds here to a boundary condition (the energy of the incident particle in a scattering experiment) and is not the solution of an eigenvalue problem. The function ϕ can be diverging so that ψ does not always represent an eigenstate of the Hamiltonian.

The stationary Schrödinger equation can then be set into the form of a Mathieu equation:[2]

$$\frac{\mathrm{d}^2\phi}{\mathrm{d}\tilde{z}^2} + (a - 2q\cos(2\tilde{z}))\,\phi = 0, \tag{4.11}$$

where we introduce $\tilde{z} = \pi z/d$ and make the following correspondence:

$$\begin{cases} a = 4E/E_\mathrm{L} + 2U_0/E_\mathrm{L}, \\ q = U_0/E_\mathrm{L}. \end{cases} \tag{4.12}$$

This equation was originally studied to study the vibrational modes of an elliptic membrane [82] and has been widely studied since. It also appears in trapped ion physics where a Mathieu equation describes the motion of a single ion in a Paul

[2]The Mathieu equation is a restriction of the Hill's equation $\frac{\mathrm{d}^2\phi}{\mathrm{d}z^2} + (a - \mathcal{O}(z))\,\phi = 0$ where $\mathcal{O}$ is a periodic function.

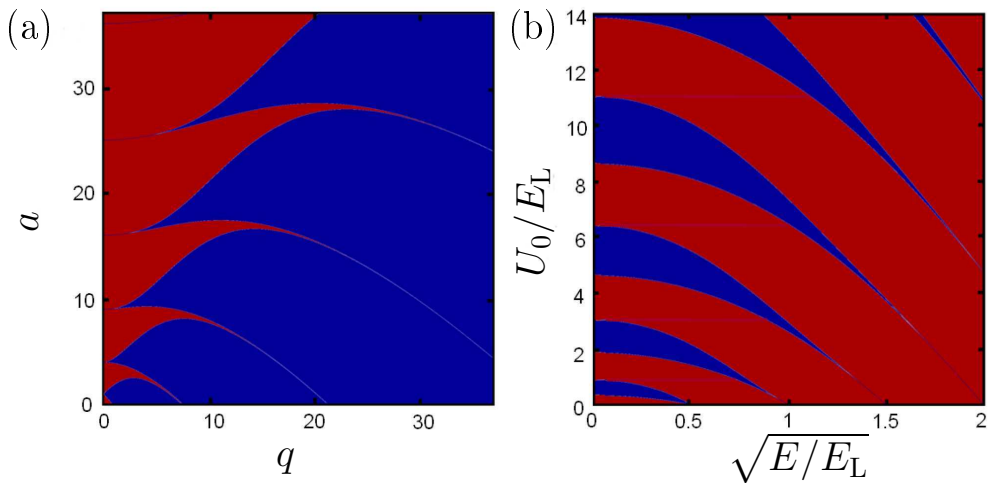

Figure 4.2: *Stability diagram of the Mathieu equation. The stables (unstables) regions are depicted in red (blue). (a) diagram with the parameters of the canonical form of the Mathieu equation. (b) Diagram with the relevant parameters for a particle in a lattice.*

trap.

4.3.1 Stability regions

Floquet theorem states that the solution of the Mathieu equation (4.11) is a linear superposition of two independent functions

$$f_1(z) = e^{ikz} p_1(z) \qquad \text{and} \qquad f_2(z) = e^{-ikz} p_2(z), \tag{4.13}$$

where p_1 and p_2 are periodic functions. In this context, k is also called the Mathieu characteristic exponent. Note that in contrast with the Bloch theorem approach, k is not necessarily real. Depending on the couple of parameters (a, q) or (E, U_0), there are two classes of solutions:

- Solutions with k real: these solutions are bounded and are strictly equivalent to the Bloch states.

- Solutions where k has an imaginary part: in this case, the solution are not bounded and correspond to evanescent waves. The value of the imaginary part of k sets a length scale over which the solution tends to zero.

In the parameter spaces (a, q) or (U_0, E), regions of bounded solution are called stable regions. They correspond to the existence of a Bloch state at the energy E. Regions of unbounded solutions are unstable regions. In this case, the energy lies

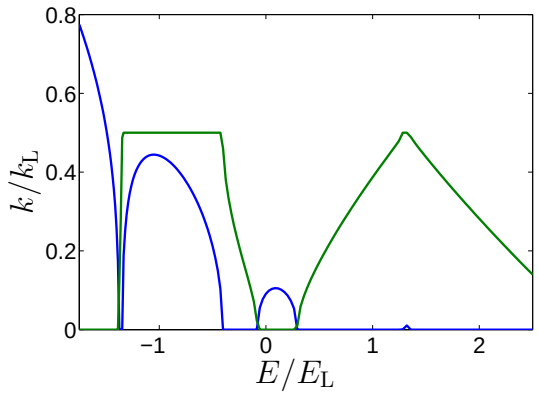

Figure 4.3: *Real (green) and imaginary part (blue) of the Mathieu exponent as a function of the normalized energy* E/E_L.

in a gap of the corresponding band diagram.[3] The frontiers between stable and unstable regions yield two transcendental function, the Mathieu angular functions $a_n(q)$ and $b_n(q)$. They correspond in the set of parameters (U_0, E) respectively to the bottom and top of the Bloch bands. Figure 4.2 shows the different regions as a function of the parameters (a, q) and (U_0, E).

4.3.2 Computation of the characteristic exponent

We will now describe the method to compute the characteristic exponent k. Whittaker was able to found an elegant analytical method to calculate k [83]. We recall here the demonstration, following the references [84, 85] and adapting it to our notations. We start from the Eq. (4.8), we pass the energy term on the left and divide each line by the diagonal term, thus obtaining the system:

$$A(k; E, U_0)\psi = \begin{pmatrix} 1 & \xi_{-N} & & & \\ \xi_{-N+1} & 1 & \xi_{-N+1} & & \\ & \ddots & \ddots & \ddots & \\ & & \xi_{N-1} & 1 & \xi_{N-1} \\ & & & \xi_N & 1 \end{pmatrix} \psi = 0, \tag{4.14}$$

where

$$\xi_l = \frac{U_0/4E_L}{(k/k_L + l)^2 - \kappa} \qquad \text{and} \qquad \kappa = \frac{U_0/2 + E}{E_L}. \tag{4.15}$$

This system has non trivial solutions if $\Delta(k) = \det(A) = 0$. In the limit where $N \to \infty$, it is obvious that $\Delta(k)$ is periodic with period k_L. We can thus restrict ourselves to $0 \leq k \leq k_L$ *i.e* to the first Brillouin zone. Besides, because Δ is a determinant and each one of the $\xi_l(k)$ appear only in one line, Δ is a sum of product of the $\xi_l(k)$. Disregarding their poles, ξ_l are analytical function; Δ is thus analytical except at $k/k_L = \sqrt{\kappa} - l$. Each function ξ_l appears only once in Δ so that all the

[3] In a quadrupole mass spectrometer, the dynamics of a charged particle is governed by a Mathieu equation where a and q correspond respectively to the static and radio-frequency fields. Unstable solutions then correspond to unbounded trajectories. The particle is then rejected.

poles of $\Delta(k)$ at $k/k_{\mathrm{L}} = \sqrt{\kappa} - l$ are simple.

The key ingredient in Whittaker solution is to consider the analytical function

$$D(k) = \frac{1}{\cos(2\pi k/k_{\mathrm{L}}) - \cos(2\pi\sqrt{\kappa})} \tag{4.16}$$

that has exactly the same poles as Δ. It it thus possible to choose a function $C(k)$ such that the function

$$\Theta(k) = \Delta(k) - C(k) \cdot D(k) \tag{4.17}$$

has no singularities. Δ has only one pole in the interval $[0, k_{\mathrm{L}}]$, as a consequence, the function C can be chosen constant and equal to the ratio between the residuals of the functions Δ and D at the unique pole.

Using this proper choosing of C, the function Θ is analytical on the whole complex plane and has no pole. It must then be a constant. Let us now take the limit $k \to +i\infty$. All the off diagonal coefficients of the matrix $A(k; E, U_0)$ vanish so that

$$\lim_{k \to +i\infty} \Delta(k) = 1. \tag{4.18}$$

Besides, $\lim_{k \to +i\infty} D(k) = 0$, hence $\Theta(k) = 1$. It follows that

$$C = \frac{\Delta(k) - 1}{D(k)}. \tag{4.19}$$

In the case $k = 0$, $D(0) = 1/(1 - \cos(\pi\sqrt{\kappa}))$, we can then calculate the value of C

$$C = (\Delta(0) - 1) \cdot (1 - \cos(\pi\sqrt{\kappa})). \tag{4.20}$$

Injecting C in Eq (4.19), and setting $\Delta(k) = 0$ (non-trivial solution), one finds an analytical solution of k:

$$\cos(2\pi k/k_{\mathrm{L}}) = 1 - \Delta(0)(1 - \cos(2\pi\sqrt{\kappa})). \tag{4.21}$$

Figure 4.3 shows the real and imaginary part of k for $U_0 = -2E_{\mathrm{L}}$. In the unstable regions ($\mathrm{Im}(k) \neq 0$), the real part of k/k_{L} is fixed at 0 or 0.5 *i.e* at the center or the edge of the Brillouin zone. Between these regions, $\mathrm{Re}(k)$ varies smoothly while $\mathrm{Im}(k) = 0$.

4.4 Interpretation of a scattering experiment

Let us consider the case of an incoming planewave with energy E that impinges on a semi-infinite optical lattice (see FIG. 4.4). On the left part, the wavefunction is described by an incoming planewave with wave vector k_1 plus a reflected one with a reflection coefficient r. Inside the lattice, the wavefunction is described by the

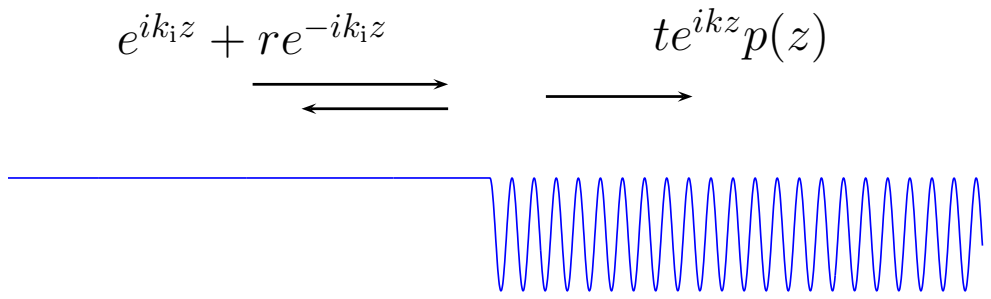

Figure 4.4: *Sketch of the scattering of a planewave on a semi-infinite lattice.*

solution of the Mathieu equation with a characteristic exponent k and a transmission coefficient t. We must now connect the wavefunction at the interface (set at $z = 0$). Because the boundary condition must be valid at all time, the energies in free space and in the lattice are equal. It follows that k is univocally determined by the energy of the incoming planewave. Two cases arise: if the incoming energy falls into a gap of the lattice band structure, k is imaginary. The wavefunction inside the lattice is then an evanescent wave that vanishes over a distance $1/\mathrm{Im}(k)$. In this case, the transmission through the semi-infinite lattice is null and the reflection $R = |r|^2 = 1$. If the incident energy lies in an allowed band, k is real and the solutions of the Mathieu equation correspond to Bloch states. In this case it is possible to compute the function $p(z)$ that appears in Eq. (4.13). The conditions for continuity of the wavefunction and of the atomic flux yield a closed set of equations:

$$\begin{cases} 1 + r = tp(0) \\ 1 - r = t\left(p(0)k/k_\mathrm{i} + p'(0)/ik_\mathrm{i}\right). \end{cases} \tag{4.22}$$

We then deduce the transmission probability:

$$T = |t|^2 = \frac{4}{|p(0)|^2} \frac{1}{|1 + k/k_\mathrm{i} - ip'(0)/(p(0)k_\mathrm{i})|^2}. \tag{4.23}$$

Figure 4.5 shows the transmission T as a function of the incident velocity and the lattice depth. We observe large bands of total reflection that correspond to the unstable regions of the Mathieu equation (compare with FIG. 4.2 (b)). The lower part of this diagram, corresponding to shallow lattices, yields reflection at very precise velocity $v/v_\mathrm{L} = n/2$ with the integer n. This corresponds to the classical Bragg's condition $2d = n\lambda \sin\Theta$, where $\lambda = h/mv$ is the de Broglie wavelength, and $\Theta = \pi/2$, since we consider the case of a normal incidence.

We also observe reflection inside the stable regions at low incoming velocity. These reflection are due to quantum reflection on the firsts wells of the lattice. The shape of the quantum reflection regions is strongly dependent on the phase of the lattice potential at the interface with free space. The quantum reflection is minimized if the interface is set on the edge of a lattice site (the potential has no

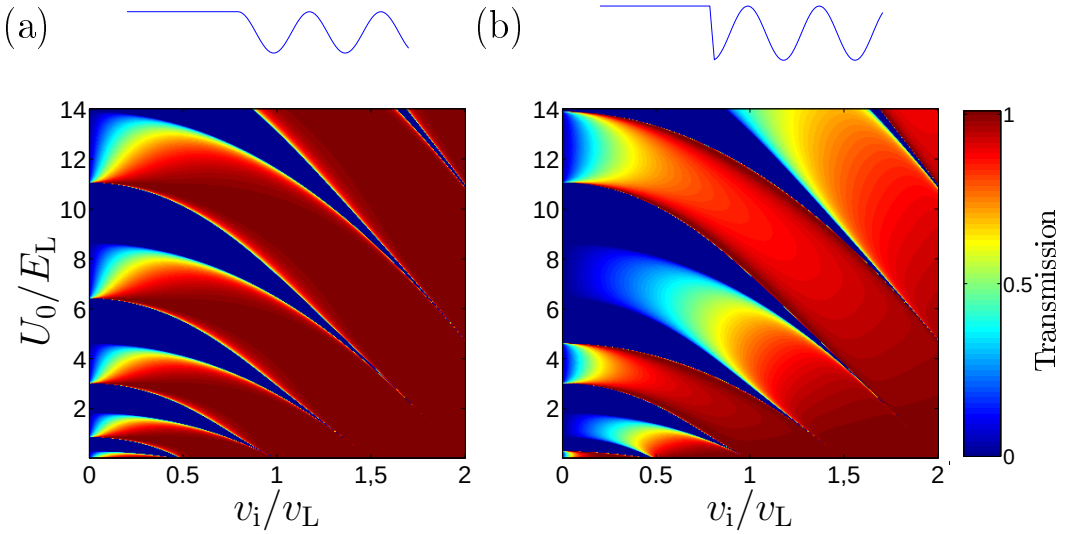

Figure 4.5: *Transmission coefficient T through a semi-infinite lattice as a function of the incident velocity and the lattice depth according to Eq. (4.23). (a) The interface is set on the edge of a lattice site, the potential has no discontinuity. (b) The interface is set at the center of a site so that the discontinuity is maximum. In the latter case, quantum reflection is more important*

discontinuity) and the largest when the interface lies in the middle of a site where the discontinuity is maximal.

4.5 Conclusion

We have presented the energy band structure of the eigenstates in a periodic potential using Bloch theorem and the solutions of the Mathieu equation. Using these solutions, we extend the concept of Bloch waves to cases where the energy lies in a gap of the band structure. We have presented a powerful mathematical method to infer the exponent Mathieu exponent k. In this case, k sets a length scale over which the wave vanishes inside the lattice. By calculating the Bloch state, it is also possible to describe analytically quantum reflection on the first wells.

Chapter 5

Bragg reflection on a finite size lattice

Contents

5.1 Introduction **85**
5.2 Effect of the envelope **85**
5.2.1 Naive picture 85
5.2.2 Contributions of the Landau-Zener transitions 86
5.3 Preparation of the wavepacket **88**
5.3.1 Outcoupling of the condensate 88
5.3.2 Acceleration of the wavepacket 90
5.4 Scattering on the lattice **91**
5.5 Experimental sequence **91**
5.5.1 Time-resolved scattering 92
5.5.2 Probing of the transmission diagram 92
5.6 Cavity effects **94**
5.7 Conclusion **95**

5.1 Introduction

The scattering of light on structures having a periodic refractive index profile is ubiquitous in photonics. Applications range from simple antireflection coatings to the fabrication of dielectric mirrors with ultra-high reflectivities, used for instance in high-finesse cavities, and to semi-conductor laser technology with the example of VCSELs, and DFB or DBR lasers. In the field of guided optics, fiber Bragg gratings [40] are essential components for the telecommunication industry, as well as for the realization of outcoupling mirrors in highpower fiber lasers. In this chapter, we demonstrate, following the proposals of Refs. [86, 87, 88, 89], a Bragg reflector for guided Bose-Einstein condensate propagating in an optical waveguide, i.e. the exact atom-optics counterpart of a photonic fiber Bragg grating. One major difference with

the reflection on a semi-infinite lattice presented in the previous chapter originates from the finite size envelope of the lattice which is more relevant experimentally. In particular, the transmission properties are radically changed by the smooth variation of the lattice depth.

5.2 Effect of the envelope

5.2.1 Naive picture

Using the considerations on the transmission through a semi-infinite lattice presented in the previous chapter, it is possible to understand simply the transmission through a smooth envelope lattice. The basic idea being that for a given incident velocity, the incoming particle can experience all lattice depths from 0 to the depth at the center of the lattice U_0. As the particle penetrates inside the lattice, it will experience an increasing lattice depth. Thus, if at some position inside the lattice, the particle enters into an unstable region of the Mathieu equation, that corresponds to a depth $U_0^{(1)}$, it can get reflected at this particular position. When $U_0 = U_0^{(1)}$ the reflection condition is fulfilled at the center of the lattice *i.e*, at $z = 0$. Then, when U_0 increases, there are some locations $\pm x_{\rm lr}$, on both sides of the lattice center, for which $U(\pm x_{\rm lr}) = U_0^{(1)}$ and where reflection occurs. In this very simple picture, the main effect of the envelope is to extend upwards the regions of reflection of FIG. 5.1 (a). This produces a sawtooth shape transmission diagram (see FIG. 5.1 (b)) where, for a given incident velocity, transmission is only possible below a critical lattice depth. In contrast with the square envelope case, there are no resurgences at high lattice depth.

However, this picture is valid only in the case of a very large envelope where the local depth of the lattice does not change appreciably over a great number of sites.

5.2.2 Contributions of the Landau-Zener transitions

Figure 5.2 (a) shows the transmission coefficient of a plane wave through a square envelope lattice with $N = 800$ sites solved by integrating directly the stationary Schrödinger equation. Expectedly, the transmission looks very much like the one through a semi-infinite lattice presented in the previous chapter (white arrows depict the Bragg condition and quantum reflection is observed at low incoming velocity). Due to the finite size of the lattice, however, the energy bands are not strictly continuous and resolve into N separate states. This gives rise to thin resonances observable at low incoming velocity. Each resonance corresponds to the appearance of a bound state in the lattice (the undersampling gives rise in the figure to the foamy aspect). Figure 5.2 (b) shows the result of the same calculation for a Gaussian envelope lattice with a waist $w = 150$ μm. We recognize the sawtooth structure predicted by our naive approach. Note that in this case, the quantum reflection

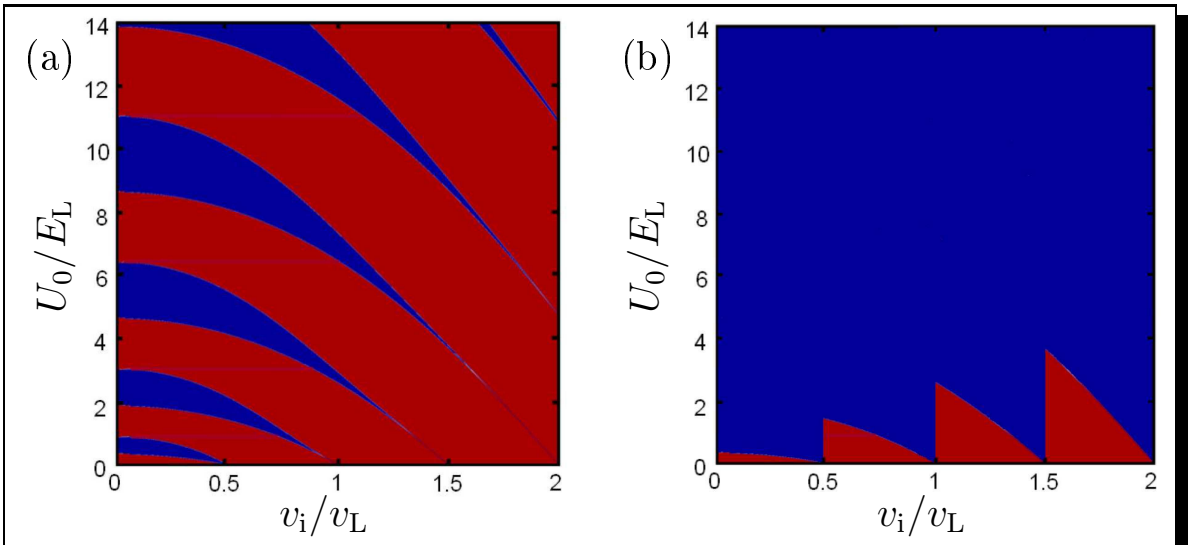

Figure 5.1: *(a) Stable (red) and unstable (blue) regions of the Mathieu equation. Naive extension of the stability regions in the case of a large, smooth envelope lattice.*

regions are no longer distinguishable from the local Bragg-type reflections so that the second effect dominates. However, large regions of transmission that are washed out in the naive model subsist.

To understand the increase of the transmission regions, we use the slowly varying envelope approximation $d \ll w$ and the solutions of the Mathieu equation. Because we can define a local depth in the lattice, it is possible to work out locally the Mathieu exponent (k being imaginary when the incident energy lies in a gap). Here, because of the smooth envelope, the band gaps become position-dependent and have a finite extent. In this case, the gaps of the system are called spatial gaps. If the solution of the Mathieu equation does not decrease significantly over the extent of the spatial gap, a particle can then tunnel through it and get transmitted. This corresponds to a Landau-Zener tunneling to a different band [90]. In the context of Fig. 5.2, this means that, for a given incoming velocity, the thinnest reflection lines should not be expanded upwards because a particle can tunnel through the gap. Quantitatively, in the slowly varying envelope approximation regime ($d \ll w$), the probability of transmission through a spatial gap reads [91]:

$$T(E) = \exp\left(\int -2\mathrm{Im}[k(z,E)]\mathrm{d}z\right). \tag{5.1}$$

Using this formula, we compute the transmission through the Gaussian envelope lattice (see FIG. 5.3). We see that it reproduces very well the figure 5.2 (b) except for large lattice depths where the slowly varying envelope approximation is poorly verified. Indeed, we see in FIG. 5.2 (a) that for a maximum lattice depth $U_0 \sim 10E_L$ a particle with a velocity $v \sim 1.5-2v_L$ must cross several very small spatial gaps whose spatial extent is on the order of the lattice spacing. Besides, the small resonances

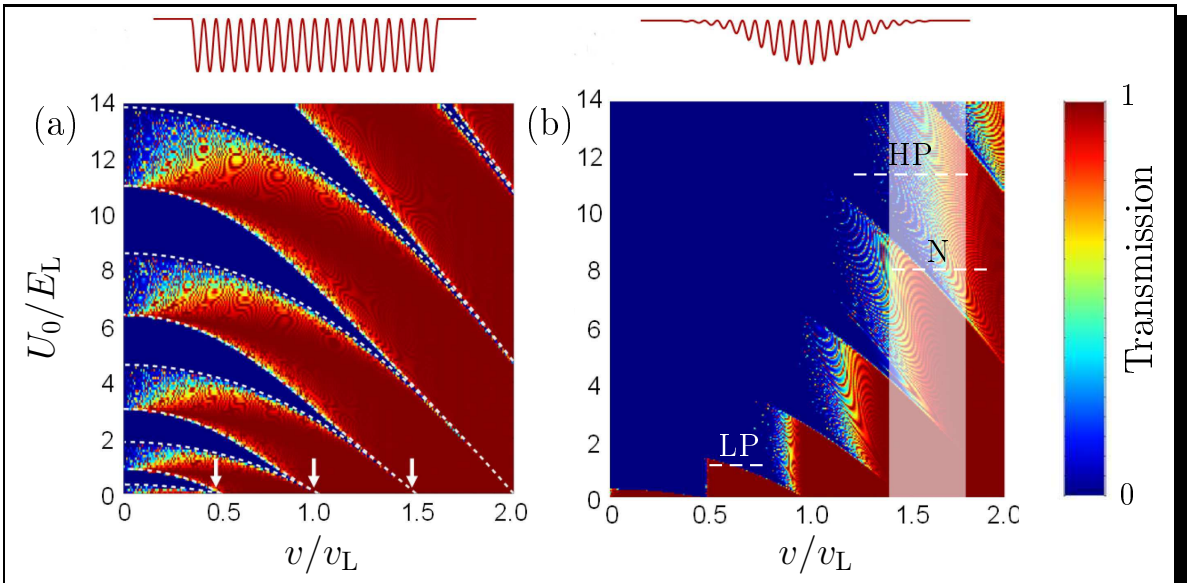

Figure 5.2: *Transmission coefficient of a plane matter wave impinging on an optical lattice as a function of the incident velocity and the lattice depth computed by solving the stationary Schrödinger equation. (a) Square envelope lattice case. (b) Gaussian envelope case, U_0 denotes here the maximum depth of the lattice. LP, HP and N denote the regions of parameters for which the lattice acts respectively as a low-pass, high-pass or notch filter.*

of the Fabry-Perot type resulting from the finite size effects cannot be reproduced with this model.[1]

5.3 Preparation of the wavepacket

We will now describe the scattering experiment itself. In order to probe the transmission across the lattice, it is advantageous to start with a source that contains as much atoms as possible per velocity class.

5.3.1 Outcoupling of the condensate

To optimize the brilliance, we start from a condensate trapped at the crossing of the two dipole beams, we then turn off the vertical beam in two steps. In the first step, we reduce its power adiabatically in order to reduce as much as possible the chemical potential. We then switch off suddenly the vertical beam to release the condensate in the horizontal guide.

At the end of the evaporation ramp, our condensate is well in the Thomas-Fermi regime, that is to say that the kinetic energy is negligible compared to the interaction energy. If we switch off suddenly the confinement along the guide direction, the

[1] The phase of the incoming wavepacket is not taken into account in Eq. (5.1).

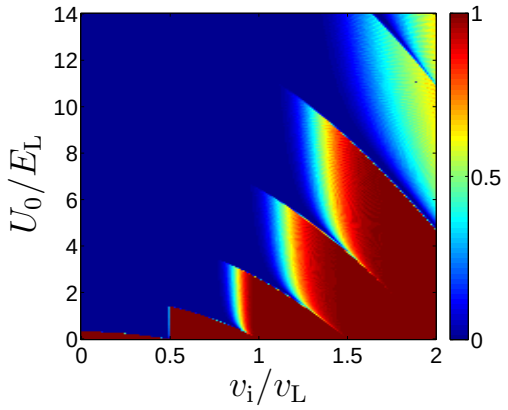

Figure 5.3: *Transmission coefficient of a plane matter wave computed by using the local solutions of Mathieu equation and Eq. (5.1). This model is in good agreement with* FIG. *5.2 (b) except at large depths for which the slowly varying envelope approximation is poorly verified.*

interaction energy is transferred into kinetic energy, so that the interactions set the velocity dispersion of the wavepacket after the outcoupling [92]. In the Thomas-Fermi limit, the chemical potential of the trapped condensate reads: [62]

$$\mu_{\mathrm{TF}} = \frac{\hbar}{2}\bar{\omega}^{6/5}\left(15Na\sqrt{\frac{m}{\hbar}}\right)^{2/5}, \tag{5.2}$$

where a is the scattering length, N the total number of atoms and $\bar{\omega} = (\omega_x\omega_y\omega_z)^{1/3}$, the geometric average of the trapping angular frequencies. Because $\mu_{\mathrm{TF}} \sim \bar{\omega}^{6/5}$, it is possible to reduce the chemical potential without loosing atoms by decreasing the trap frequencies. In our experiment, we reduce the trapping frequencies by decreasing the power of the vertical beam only, which reduces essentially the confinement in the longitudinal direction z. The chemical potential then scales as $\mu_{\mathrm{TF}} \sim \omega_z^{2/5}$.

In order to decrease the trap frequency while keeping the occupancies of the quantum states, the process must be slow enough to be adiabatic. The adiabaticity condition reads here:

$$\frac{\mathrm{d}\omega_z}{\mathrm{d}t}\frac{1}{\omega_z^2} = -C_{\mathrm{ad}} \ll 1. \tag{5.3}$$

We chose to decrease the power of the vertical beam so as to keep the adiabaticity criterium constant and equal to $C_{\mathrm{ad}} = 0.1$. This leads to a power that decreases as

$$P(t) = \frac{P_{\mathrm{i}}}{\left(1 + C'\sqrt{P_{\mathrm{i}}}t\right)^2}, \tag{5.4}$$

where P_{i} is the power at the end of the evaporation ramp and C' depends on C and the initial longitudinal trapping frequency. Following Eq. (5.4), we decrease the power of the vertical beam by a factor 20 in 78 ms. This leads to a moderate reduction of the chemical potential by a factor 1.8. At the end, the longitudinal angular frequency $\omega_z \sim 8$ Hz is very small. As a consequence, if we try to further decompress the trap, some atoms are outcouled in the guide. This sets an experimental limit to our decompression.

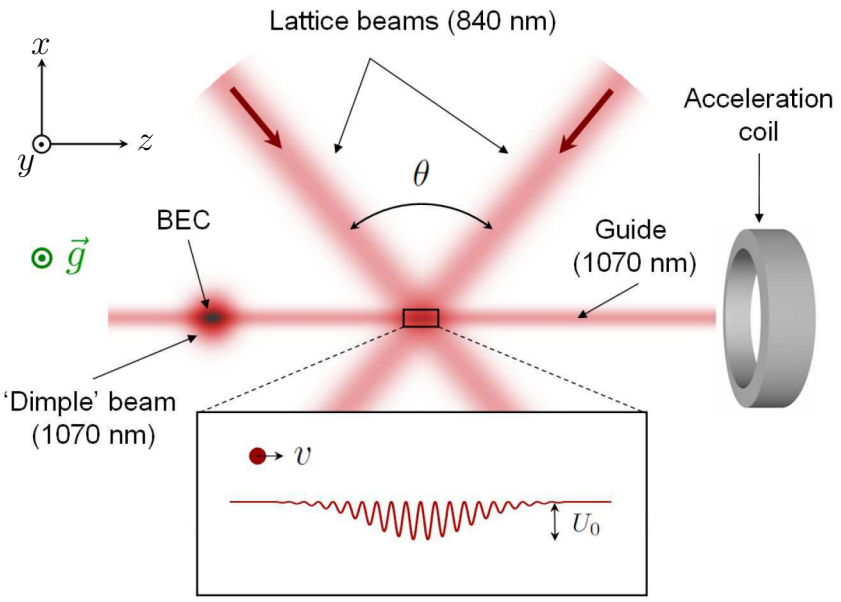

Figure 5.4: *Sketch of the experimental setup.*

At this point, we switch off suddenly the vertical beam and let the resulting wavepacket propagate freely in the guide. To measure the velocity distribution of the wavepacket, we let it propagate for a variable time in the guide. From linear fits of the mean position and position width as a function of the propagation time, we deduce the mean velocity $\bar{v}$ and the velocity spread Δv. At the end, we obtain typically velocity spreads $\Delta v \sim 1.3 - 1.7$ mm/s. We also measure, with a second order polynomial fit, the residual acceleration (that could be caused by a tilting of the horizontal beam, or a residual magnetic field). The residual acceleration is compatible with zero with an upper bound of $g/1000$. It can thus be forgotten in the analysis.

5.3.2 Acceleration of the wavepacket

Up to now, the mean velocity $\bar{v}$ is close to zero.[2] In order to study the scattering on the optical lattice, we accelerate the wavepacket to velocities on the order of the velocity scale $v_{\mathrm{L}} = h/md = 7.1$ mm/s associated with the lattice periodicity. This is done by using a magnetic field gradient pulse. To realize this gradient we use an additional acceleration coil set in the guide axis (see FIG. 5.4). The coil produces a field at the center of the chamber:

$$B(0) = 0.35 \text{ G/A} \qquad \text{and} \qquad \left|\frac{\mathrm{d}B}{\mathrm{d}z}\right| = 0.1 \text{ G.A}^{-1}/\text{cm}. \tag{5.5}$$

[2] A small residual mean velocity on the order of 0.1 mm/s can result from the outcoupling process.

In this experiment, we used the horizontal spin distillation technique (see chapter 2) that produces a condensate in the state $m_F = 0$. Atoms in $m_F = 0$ are high field seeker at the second order in B, the Zeeman shit in this state reads:

$$\Delta E = -\frac{\mu_{\mathrm{B}}^2 B^2}{\Delta E_{\mathrm{hfs}}}, \tag{5.6}$$

where ΔE_{hfs} is the separation between the hyperfine states. The atoms are thus set into motion towards the acceleration coil with an acceleration

$$a_{m_{\mathrm{F}}=0} = \frac{2\mu_{\mathrm{B}}^2 B}{m\Delta E_{\mathrm{hfs}}} \frac{\mathrm{d}B}{\mathrm{d}z} \tag{5.7}$$

Because atoms in $m_F = 0$ are only sensitive to the magnetic field at the second order, it is necessary to realize strong magnetic fields. We use two current generators in parallel to inject currents up to 400 A. In the experiment, we chose to switch on the acceleration coil with 320 A during 15 ms to reach the desired velocity. The theoretical final velocity is then $v_{\mathrm{th}} = 14$ mm/s. Experimentally, we measure a smaller velocity $\bar{v} \simeq 11$ mm/s. This discrepancy is explained by the finite ramping time of the current in the coils as was checked by measuring the actual current with a clamp meter. Finally, we obtain a wavepacket whose characteristics are:

$$\bar{v} = 1.5 v_{\mathrm{L}} = 11 \text{ mm/s} \qquad \text{and} \qquad \Delta v = 1.3 \text{ mm/s}. \tag{5.8}$$

The characteristics of the wavepacket are depicted by the shaded area in FIG. 5.2 (b)

5.4 Scattering on the lattice

5.5 Experimental sequence

Figure 5.4 shows a sketch of the experiment. First, we have to calibrate the lattice depth by Kapitza-Dirac diffraction. To do so, we move the BEC (by moving the vertical beam) to superimpose it with the lattice. Because, the lattice beams can slightly move from day to day, it is important to carry out the calibration the same day as the experiment. Once the calibration has been done, we move the condensate 350 μm away from the lattice. During the next sequences, we outcouple the condensate, accelerate it towards the lattice, and then let the wavepacket propagate and interact with the lattice for a time t_{prop} before taking an image.

5.5.1 Time-resolved scattering

In the first set of experiments, we set the lattice depth at $U_0 = 11 E_{\mathrm{L}}$ and let the wavepacket propagate for a variable time. The atomic density is then measured after a 10 ms time-of-flight. As the wavepacket spreads during the propagation,

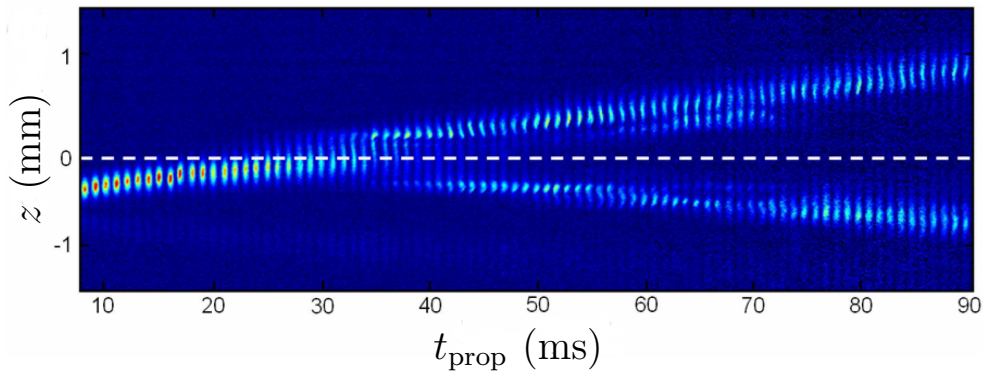

Figure 5.5: *Atomic density as a function of the position and the propagation time for a lattice depth $U_0 = 11E_{\mathrm{L}}$. The white dashed line depicts the lattice center.*

it becomes quickly very diluted. As a consequence, the interatomic interactions no longer play a role in the dynamics. Figure 5.5 shows the atomic density as a function of the propagation time. During the first 20 ms, the wavepacket propagates towards the lattice. The interaction with the lattice occurs mainly for propagation times $20 < t_{\mathrm{prop}} < 40$ ms. After the interaction, the wavepacket is split into a transmitted and a reflected part. This is in agreement with the numerical simulations of FIG. 5.2 where we see that for $U_0 = 11E_{\mathrm{L}}$ and the incident velocity distribution, the fastest atoms are transmitted and the slowest are reflected. The reflection of the low velocity component is exactly the analogue of Bragg reflection on dielectric mirrors in optics.

We observe some additional effects:

- After the interaction with the lattice, at $t_{\mathrm{prop}} > 40$ ms, the wavepacket presents slight oscillations. This is due to the excitation of transverse modes of the guide. The excitation of the transverse modes could be due to an imperfect crossing of one of the lattice beams that breaks the symmetry of the potential and couple the longitudinal and transverse degrees of freedom [93].

- For $65 < t_{\mathrm{prop}} < 75$ ms, a second packet appears in the transmitted part behind the main part. For $U_0 = 11E_{\mathrm{L}}$, this was not predicted by the theory. However, this kind of structure is expected for slightly smaller lattice depth as we will see in detail in the next section. We thus believe that thermal fluctuations in the room induced a variation of the crossing of the lattice beams. The depth of the lattice would thus be reduced compared to the depth calibrated by Kapitza-Dirac diffraction in the preliminary experiment.

5.5.2 Probing of the transmission diagram

In this section, we describe how we probe the transmission diagram. We now let the atoms propagate for a long propagation time $t_{\mathrm{prop}} = 100$ ms, all atoms have then left

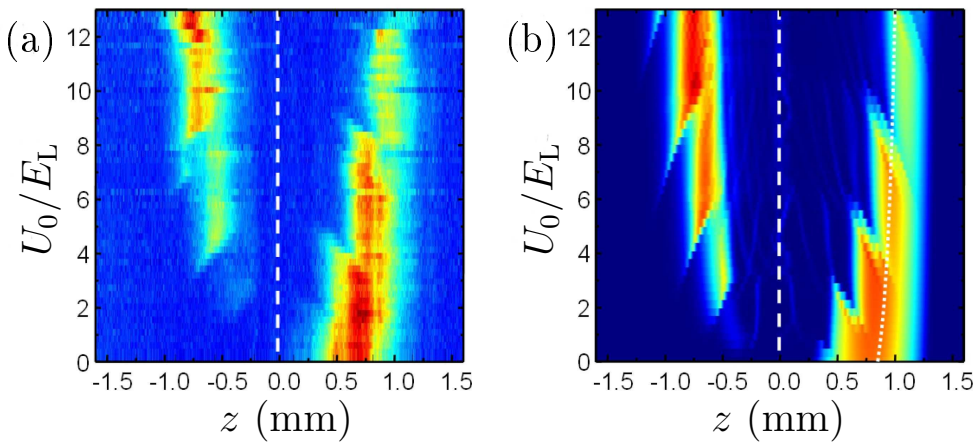

Figure 5.6: *(a) Experiment and (b) Numerical simulation of the atomic density as a function of position and lattice depth for a propagation time of* 100 ms. *Each horizontal line is the average of eight shots integrated in the transverse direction. The white dashed line depicts the lattice center.*

the region of interaction with the lattice. The depth of the lattice is varied from 0 to $13E_L$. For each lattice depth, we integrate the images in the transverse direction, repeat the experiment 8 times and take the average of the experimental runs to reduce the noise by a factor of approximately 3. Figure 5.6 (a) shows the result of these measures, each of the 55 horizontal line corresponds to a given lattice depth. The wavepacket initially propagates towards the right side of this plot. The white dashed line depicts the position of the lattice center, the right part of the plot thus corresponds to transmitted atoms, while the left part corresponds to reflected ones. For sake of comparison, FIG. 5.6 (b) shows the result of a simulation that solves the Schrödinger equation using the split Fourier method [94] with the experimentally measured lattice and wavepacket characteristics. It is in very good agreement with the experiment.

Let us concentrate on the transmitted part of the wavepacket. If there were no lattice, the propagation time is long enough so that the initial size of the wavepacket is negligible with respect to its size after propagation. The spatial distribution of the wavepacket would then be a direct mapping of its initial velocity distribution $f(v)$: $n(z, t_{\text{prop}}) = f[(z - z_0)/t_{\text{prop}}]$. If we suppose that the delays induced by the interaction with the lattice are negligible, then, the density in the transmitted part is nothing but the transmission diagram of the FIG. 5.2 integrated over the initial velocity distribution (shaded area). This explains why we observe the same sawtooth appearance which is a fingerprint of the band structure. Noticeably, for $U_0/E_L \simeq 9.5$, the density distribution presents a hole in the transmitted part that corresponds to the reflection of a narrow class of velocity between two transmitted classes of velocity and was observed incidentally in the time-resolved experiment. The reflected part propagates backwards and is thus located at a symmetric position, it is then the

complementary part of the transmitted packet.

The effect of the lattice potential is not limited to its sinusoidal component. The averaged part of the potential also accelerates transiently the atoms during the propagation. This is observable by looking closely at the front of the wavepacket. We can see that it is in advance for the larger lattice depths because the transient acceleration is then more important. The white dotted line in FIG. 5.6 (b) shows the final position of a classical particle starting with the velocity $\bar{v}$ and interacting with the spatially averaged lattice. It reproduces well the curvature of the front of the wavepacket.

Beside being used as a mirror, this experiment shows that this system can be used for more complex momentum engineering. Indeed, depending on the lattice depth and on the incoming velocity distribution, this system realizes a high pass filter, a notch filter and even at low velocity and small lattice depth a low pass filter (see FIG. 5.2). In this prospect, this system offers more flexibility than a repulsive barrier that can only act as a high-pass filter. In the chapter 7, we will show how we can further add some tunability to this momentum engineering.

5.6 Cavity effects

In the local reflection picture presented, here, the reflection condition is always met at two symmetric positions around the lattice center. The main features of the transmission diagram can be interpreted considering the reflection on the first Bragg mirror only. Yet, the presence of two mirrors yields cavity effects. The narrow resonances observed in the simulation can be interpreted as Fabry-Perot resonances in the cavity produced by the two Bragg mirrors. These resonances are far too narrow to be observed in our experiment,[3] it should be possible nonetheless to observe some oscillations inside this Bragg cavity. Figure 5.7 shows a simulation corresponding to our time-resolved experiment with increased contrast. We observe that a small number of atoms perform oscillations between two symmetric positions around the lattice center. Each time the atoms reach one of these positions, a small proportion of the atoms leaks out of the cavity. These effects could not be observed in the scattering experiment described in this chapter because of the low number of involved atoms. We will see in the next chapter how it is possible to observe these cavity effects with a similar setup.

5.7 Conclusion

In this chapter, we have presented the scattering of a Bose-Einstein condensate on a Gaussian envelope lattice. The scattering can be considered as a way to probe a

[3]The free spectral range between two resonances is on the order of $\Delta v_{\mathrm{FSR}} \sim v_{\mathrm{L}} d/L$ where $L \sim 100$ μm is the length of the cavity. Thus $\Delta v_{\mathrm{FSR}} \sim v_{\mathrm{L}}/800$.

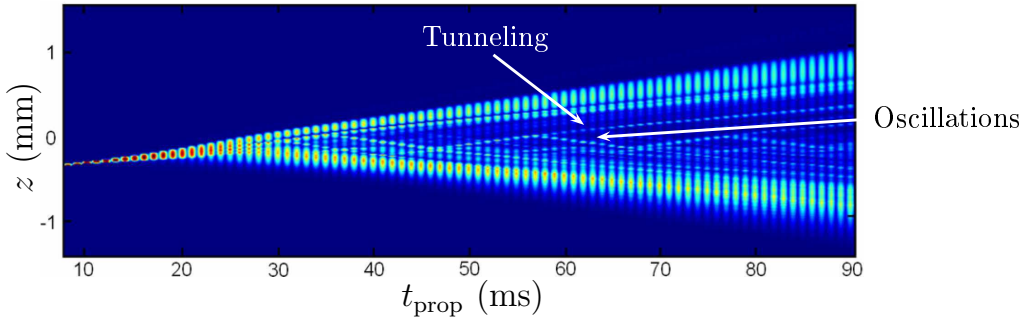

Figure 5.7: *Numerical integration of the atomic density as a function of position and propagation time for a lattice depth $U_0 = 11E_{\mathrm{L}}$. The saturation as been greatly increased to observe oscillations between two symmetric positions.*

system. In our case, we probe directly the band structure of the lattice. There are few experiments where a matter wave is used as a probe. An example is provided by reference [95] where cold atoms are scattered by target atoms confined in an optical lattice in a Mott insulator phase.

This system can be used to engineer the momentum distribution of the incoming wavepacket. The interaction with the lattice can be used as a low-pass, high-pass or notch filter depending on the explored region of parameters. In chapter 7, we will show how we can improve the characteristics of this filter using an amplitude-modulated lattice.

One open question that is currently under investigation is the effect of interatomic interaction. With repulsive interaction, in this kind of scattering experiment, the sample gets quickly too diluted. However, with attractive interaction (or with a negative effective mass [96]), one can produce a solitary matter wave that does not spreads over time. The scattering properties of these object are highly non trivial (there is a possibility to produce mesoscopics Schrödinger cats [97]) and attract recently much interest both theoretically and experimentally [98, 99].

Chapter 6

Realization of tunnel barriers for matter waves using spatial gaps

6.1 Introduction

The tunneling effect is a cornerstone of quantum mechanics according to which a particle can penetrate and even pass through a classically impenetrable barrier. This behavior results from the wave nature of particles and is at work in many domains of physics including nuclear desintegration [100, 101], quantum electronics [102, 103], scanning tunneling microscope [104], tunnel ionization [105, 106] and in various superconducting devices [107, 108].

In the cold atom field, realizing a thin enough single barrier enabling one to investigate the dynamics induced by the atomic tunneling through it remains very challenging. This has been realized so far in at least three different ways to study, for instance, the ac and dc atomic Josephson effect using (i) the combination of an optical lattice and a harmonic potential [109], (ii) a strongly focussed far-off resonance blue-detuned laser [110] and (iii) RF-dressed potentials [111].

The concept of the tunnel effect has also been generalized to other kinds of space. The Landau-Zener transition between the energy bands of a lattice can be seen as a tunnel effect in quasi-momentum space [112], and dynamical tunneling has been introduced to describe the tunneling between classically trapped region in a regular phase space [113].

In this chapter, we study the Bragg cavity briefly presented in the previous chapter and resulting from the smooth envelope of the optical lattice [114, 115, 88, 91]. By loading atoms at the center of the lattice, we are able to directly observe oscillations of a wavepacket along with single tunneling events whenever the packet bounces off one of these effective mirrors. The outcoupling of matter wave through a tunnel event is especially interesting since it provides a novel type of tunnel barrier in real space.

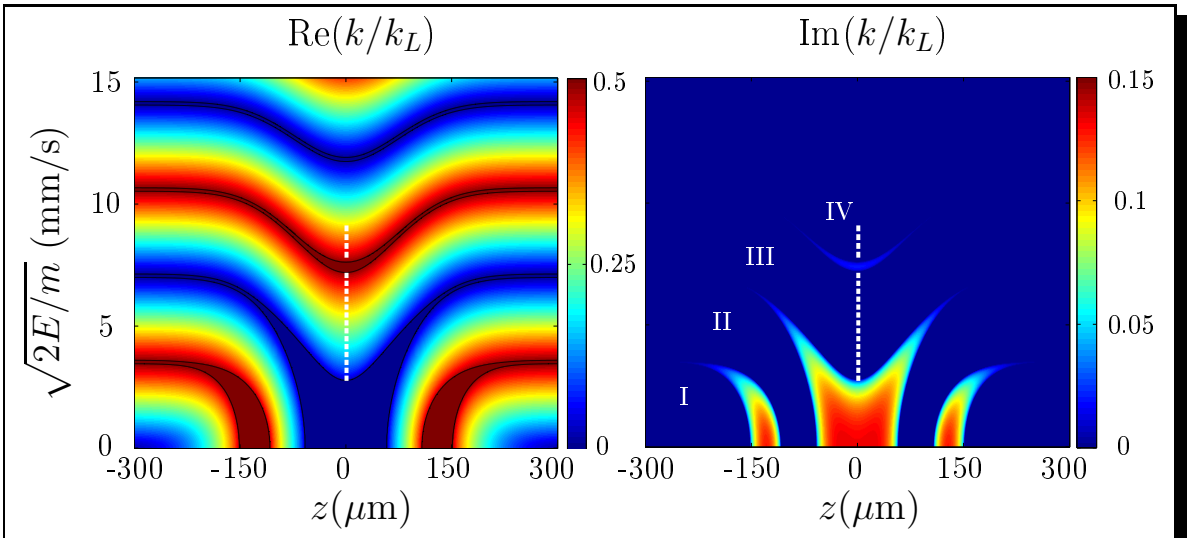

Figure 6.1: *Real and imaginary part of the Mathieu exponent k with $U_0/E_L = 2.5$. Regions where $\mathrm{Im}(k) \neq 0$ are spatial gaps corresponding to evanescent waves. The roman numbers indicate the band index. The white dashed line depicts the initial energy distribution (95 % of the atoms).*

6.2 Local band structure model

In this section, we present a simple local band structure model that allows to understand very simply the dynamics of the atoms in the Bragg cavity as well as the tunneling out.

6.2.1 Position-dependent band structure

We place ourselves in the slowly varying envelope approximation $d \ll w$. In this case, we can associate with each position an equivalent infinite potential with a depth:

$$U_0(z) = U_0 \exp(-2z^2/w^2). \tag{6.1}$$

We then work out the corresponding Mathieu exponent as a function of position and energy. Figure 6.1 shows such local band structure with a maximum lattice depth $U_0 = 2.5E_L$. It corresponds to an extended position-dependent band structure of the lattice. We choose to represent this plot as a function of the square root of the energy so that far from the lattice, we simply represent k as a function of the velocity. The regions where $\mathrm{Im}(k) \neq 0$ are the spatial gaps that separate different allowed bands. If the width of the spatial gap is small enough, a particle can tunnel through it and get outcoupled from the cavity. According to this picture, the reflection on a gap corresponds to a Bragg reflection, while tunneling through the barrier is analogous to a Landau-Zener transition to a different band transposed into the position space.

The symmetry of the band structure originates from the symmetry of the Gaussian envelope. Note that we have represented the band structure for positive energies only (relatively to the continuum) so that any reflection in this context has no classical counterpart. In the spatial gaps, the real part of k is set at one of the band edges. Note that far from the lattice center, the spatial gaps are located at energies fulfilling the Bragg condition $\sqrt{2E/m} = nv_{\mathrm{L}}/2$,[1] where n is an integer.

We see that for these lattice parameters, there is a region in the center of the lattice that is surrounded by two spatial gaps that define a Bragg cavity. In order to observe the cavity effects with a maximum number of atoms, we should start with an atomic wavepacket in this particular region, that corresponds to the third and fourth band.

6.2.2 Transmission probabilities

As described in the previous chapter, the transmission of a monochromatic wave with energy E through a single spatial gap can be readily calculated by integrating the imaginary part of k over the forbidden region:

$$T(E) = \exp\left(\int -2\mathrm{Im}[k(z,E)]\mathrm{d}z\right). \tag{6.2}$$

In FIG. 6.2 (b), the blue solid line represents this transmission probability through half of the lattice for the same lattice depth as in FIG. 6.1 $U_0 = 2.5E_{\mathrm{L}}$. At low velocity, where the spatial gaps are wide, the transmission vanishes. As the energy increases, the barrier becomes thinner and the transmission increases. It saturates to $T = 1$ at energies $\sqrt{2E/m} \sim 7$ mm/s where there is no gap at all. The presence of the spatial gap between the third and the fourth band yields an other drop of transmission for $7.2 < \sqrt{2E/m} < 8.5$ mm/s. At higher velocities, there are no more significant band gaps. In the experiment, we initially load the atoms at the center of the lattice with an energy distribution that spreads over the third and fourth bands. By energy conservation, the "trajectory" of an atom with a given energy remains an horizontal line in the diagram of FIG. 6.1 and may be split on the spatial gaps as a consequence of a partial tunneling.

Atoms at the bottom of the third band experience wide gaps and are reflected with a probability close to one. We expect them to bounce back and forth quasi-indefinitely. Atoms loaded at the top of the band see essentially no gap and leave immediately the lattice. Between these two extreme cases, atoms have an intermediate tunneling rate and can leave the trap after one or several oscillations. The green dashed line of FIG. 6.2 (b) thus represents the probability $T_2 = T(E)(1 - T(E))$ to bounce back on the first spatial gap then tunnel out of the cavity at the symmetric position (see FIG. 6.2 (a)). Expectedly, it presents peaks denoted α and β at energies corresponding to simple tunneling probabilities $T \sim 0.5$ and saturates at

[1] $v_{\mathrm{L}} = h/md$

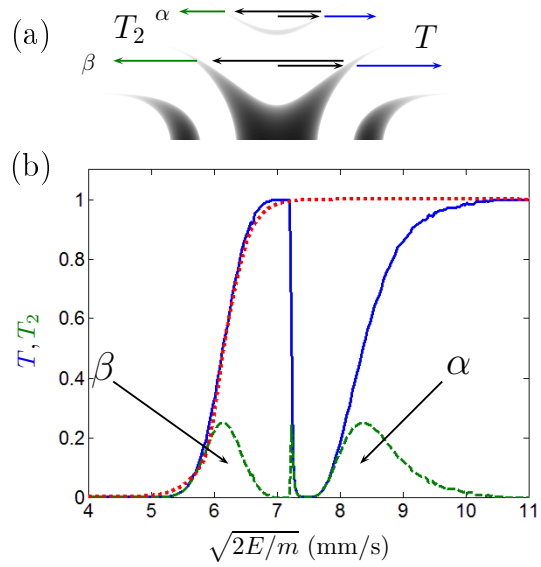

Figure 6.2: *(a) Schematic of the evolution of the wavepacket inside the lattice and definition of T and T_2. (b) Transmission probabilities. Solid blue line: Transmission through half of the lattice, the regions of reflection correspond to wide band gaps. Red dotted line: Transmission probability through a repulsive Gaussian barrier of variance $\sigma =$ 387 nm. Green dashed line: probability to tunnel out of the lattice after one oscillation.*

$T_2 = 0.25$. Because the concerned classes of energy have been reflected once, we can attribute unambiguously the outcoupling at the symmetric position as a tunneling event. Moreover, because the atoms that do not see any gap leave the lattice region on the other side, those that have performed one oscillation are spatially separated.

6.2.3 Comparison with a repulsive barrier

The projection of the band gaps into position space realizes a novel type of tunnel barrier in real space. It is instructive to compare it with a repulsive tunnel barrier. One way to characterize a tunnel barrier is to consider the transmission as a function of the incident energy. In the classic regime corresponding to a very wide repulsive barrier, it presents a sharp step at an energy equal to the barrier height. As the barrier gets thinner, the step widens; the region where it passes from 0 to 1 corresponds to tunneling and quantum reflection. The width of the steps-like transmission is thus a characteristic of the tunnel barrier, the larger the step the easier it is to observe tunneling. The transmission curve in out case is more complicated but also presents a step-like structure. In FIG. 6.2 (red dotted line), we fit the first step (corresponding to the spatial gap β) by the transmission probability obtained from a repulsive Gaussian barrier with adjustable width. We find the best agreement for a standard deviation of the repulsive barrier $\sigma = 387$ nm. It would be quite challenging to realize such a barrier by optical means since it requires a blue-detuned laser of waist $w = 2\sigma = 775$ nm close to its diffraction limit.[2] The tunnel barrier realized by a spatial gap can thus provide a good alternative to repulsive barriers.

[2]For example with a laser at 532 nm, this would require a numerical aperture N.A ~ 0.5

6.3 Experiment

We now present the experiment itself. The setup is essentially the same as in the previous chapter.

6.3.1 Preparation of the initial wavepacket

In contrast with the scattering experiment presented in the previous chapter, in this case we need to prepare the Bose-Einstein condensate at the same position as the lattice. We then outcouple the condensate into the guide using the decompression technique. The next step is to load adiabatically the wavepacket into the third and fourth band. The adiabatic loading of atoms in an optical lattice is ubiquitous in the cold atoms community but is usually realized with atoms at rest that are thus loaded into the first band of the lattice. The principle of any adiabatic loading is that during the process, the quantum state occupancies are conserved. In the case of the loading into a lattice, it corresponds to the conservation of the band index and the pseudo-momentum. To load the atoms in the third and fourth band of the lattice with $U_0/E_\mathrm{L} = 2.5$, we thus need to start with a wavepacket that spreads over the third and fourth bands in the energy diagram of a lattice with vanishing depth. In this case, the band diagram is nothing but a wrapped parabola, the n-th band spreads over velocities:

$$(n-1)/2 < v/v_\mathrm{L} < n/2. \tag{6.3}$$

In contrast with the scattering experiments (see chapter 5 and 7), it is very important that the wavepacket do not spread significantly compared to the size of the lattice envelope during the acceleration stage. This is why we use this time atoms in the $m_F = +1$ state that are sensitive to a magnetic field gradient to the first order so that we can accelerate them in a smaller amount of time. To produce a condensate in this state, we used the vertical spin distillation presented in chapter 2. In the $m_F = +1$ state, the Zeeman shift reads:

$$\Delta E = -\frac{\mu_\mathrm{B}}{2} B. \tag{6.4}$$

For our acceleration coil, this Zeeman shift yields an acceleration:

$$a_{m_F=+1} = -\frac{\mu_\mathrm{B}}{2m}\frac{\mathrm{d}B}{\mathrm{d}z} = 3.2 \cdot 10^{-2}\ \mathrm{m.s^{-2}/A}. \tag{6.5}$$

Experimentally, we choose to accelerate the wavepacket during 4 ms to the final mean velocity $\bar{v} = 9.4$ mm/s using the magnetic gradient produced by the acceleration coil. This choice corresponds to a mean[3] magnetic gradient of 7.5 G/cm. The relatively small acceleration time ensures that the wavepacket spreads by less than 10 μm

[3]Because of the final ramping time of the current in the acceleration coil, the acceleration is not constant.

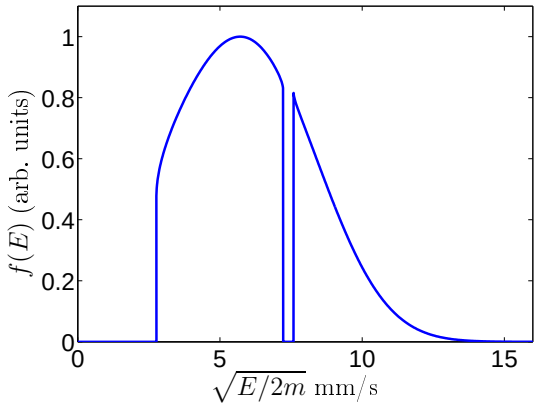

Figure 6.3: *Initial energy distribution after the adiabatic loading. The distribution is calculated by assuming the conservation of the band index and pseudo-momentum during the loading into the lattice. The energy distribution spreads over the third and fourth band essentially. This corresponds to the white dashed line in* FIG. *6.1*

during this stage which is much smaller than the width of the lattice envelope. We can then consider that the atoms still start at the center of the lattice. After the acceleration stage, we immediately ramp up the lattice intensity adiabatically, *i.e* such that [116, 117].

$$\frac{\mathrm{d}U_0}{\mathrm{d}t} \ll \frac{E_\mathrm{L}}{\hbar}\Delta E_k^2/E_L^2, \tag{6.6}$$

where ΔE_k is the energy difference between the initial state $|n,k\rangle$ and the first excitable state $|n',k\rangle$ on the adjacent band. Because $E_\mathrm{L}/\hbar = 2\pi \cdot 5.4$ kHz, the adiabaticity condition is easily fulfilled on submillisecond timescales except at the band edges where ΔE_k vanishes.

We chose to ramp up the lattice linearly in 1 ms to the final lattice depth $U_0/E_\mathrm{L} = 2.5$. We checked experimentally that the process is indeed adiabatic by ramping up and down the lattice. The wavepacket after this procedure is unchanged which is a good indication of the adiabaticity.

Finally, the whole procedure produces a wavepacket whose energy distribution and initial position correspond to the dashed white line in FIG. 6.1 (95 % of the atoms). The theoretical energy distribution (see FIG. 6.3) is not trivial and result from the adiabatic loading into the lattice. To work it out, we start from the experimentally measured initial distribution in free space and assume the conservation of the band index and pseudo-momentum.

6.3.2 Propagation inside the lattice

We now let the wavepacket propagate for a variable time t_prop before imaging the atoms *in situ*. Figure 6.4 (a) shows the measured atomic density along the guide during the propagation. Each horizontal line is the average of four images integrated along the transverse direction. For sake of comparison, FIG. 6.4 (b) is the result of the numerical integration of the Schrödinger equation with a wavepacket whose characteristics match the experimental ones without any adjustable parameters. In this experiment, all atoms are initially launched toward the right side of the lattice.

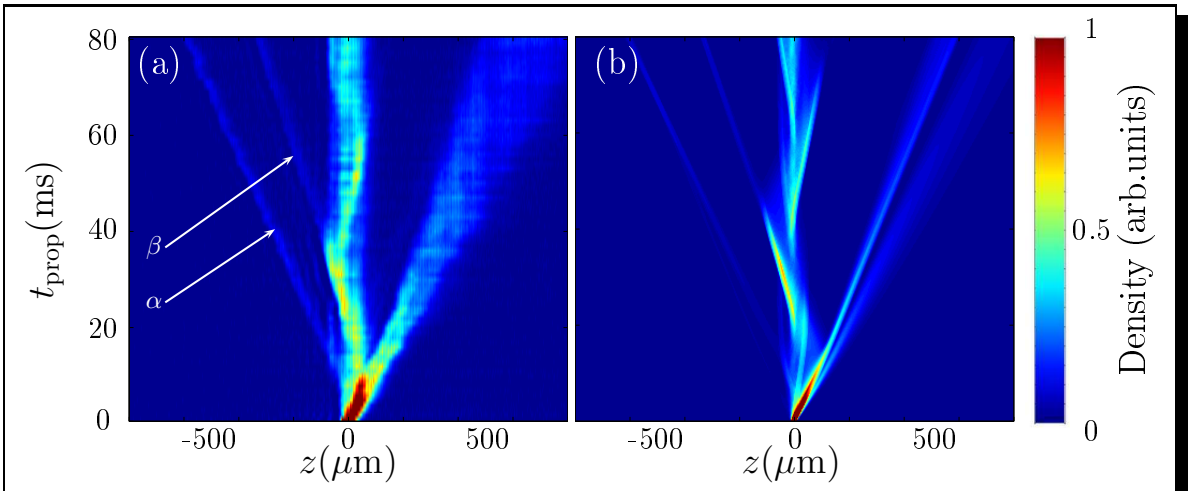

Figure 6.4: *(a) Measured density distribution of the wavepacket for different propagation time. Each horizontal line is the average of 4 images integrated along the transverse direction. (b) Direct numerical integration of the Schrödinger equation for a wavepacket whose velocity distribution matches the experimental one.*

Three effects can be noticed:

- A part of the wavepacket immediately leaves the lattice, it corresponds to velocity classes ($6.7 \lesssim v \lesssim 7.2$ and $v \gtrsim 9.5$ mm/s) that do not encounter a significant band gap.

- A periodic oscillations inside the lattice can be clearly observed. The oscillations have a spine shape that corresponds to caustics resulting from the addition in these regions of the trajectories associated with different velocities. They have a period of approximatively 50 ms and are washed out after a few oscillations, once again as a result of the dephasing between the different energy components. We will describe these effects in detail in the section 6.4.

- In the direction opposite to the initial velocity we observe the emission from the left side of the lattice of two atomic packets α and β. They leave the lattice by tunneling through a spatial gap, and then propagate freely. These packets are nothing but the atoms that have bounced back on the first spatial gap and tunneled out of the cavity at the symmetric position. Their transmission probabilities have been represented in FIG. 6.2(b). In FIG. 6.5, we also plot the measured and theoretical proportion of atoms on the left side of the lattice (at more than 150 μm from the center) as a function of time. It displays two steps well reproduced by the simulation that represent each about 3 % of the total number of atoms and correspond to the two tunneling events.

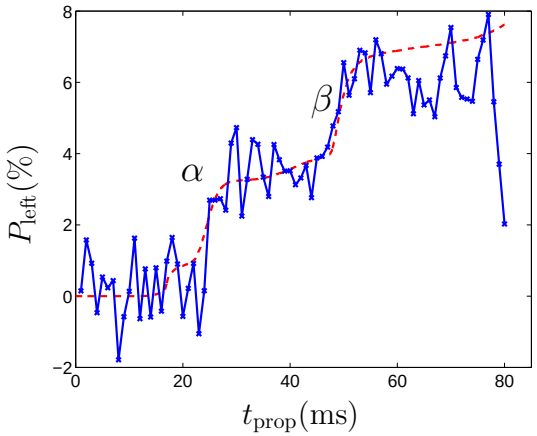

Figure 6.5: *Proportion of atoms on the left side of the lattice. Experimental results (blue solid line) and numerical integration without any adjustable parameters (red dashed line).*

6.3.3 Properties of the tunneled packets

Let us now focus on the properties of the two packets that tunnel out on the left side of the lattice.

Mean velocities and interpretation

Using the data presented in FIG. 6.4 (a), we measure the mean position of the two tunneled packets as a function of the propagation time to determine the mean velocity (see FIG. 6.6 (b)). We find:

$$\bar{v}_\alpha = 7.9 \pm 0.1 \text{ mm/s} \qquad \text{and} \qquad \bar{v}_\beta = 5.9 \pm 0.1 \text{ mm/s}. \tag{6.7}$$

Figure 6.6 (a) presents the theoretical velocity distribution of the emitted packets determined in two ways:

- By integrating the probability $T_2(E)$ over the initial energy distribution depicted in FIG. 6.3.
- By using the full resolution of the Schrödinger equation corresponding to FIG. 6.4 (b).

The two methods yield similar results and predict two peaks centered at 5.9 and 8.3 mm/s using the band model calculation and 6.1 and 8.1 mm/s using the numerical integration, in good agreement with the measured values. We can thus attribute the first packet (α) to a short oscillation of atoms initially on the fourth band, and the second packet (β) to a longer oscillation of atoms initially on the third band.

Velocity dispersion

From the local-band model 6.3.3, we expect these packets to have a velocity dispersion on the order of $\Delta v \sim 250$ μm/s. This selectivity is as high as the one provided by velocity-selective Raman transitions [118, 119] and does not requires any specific

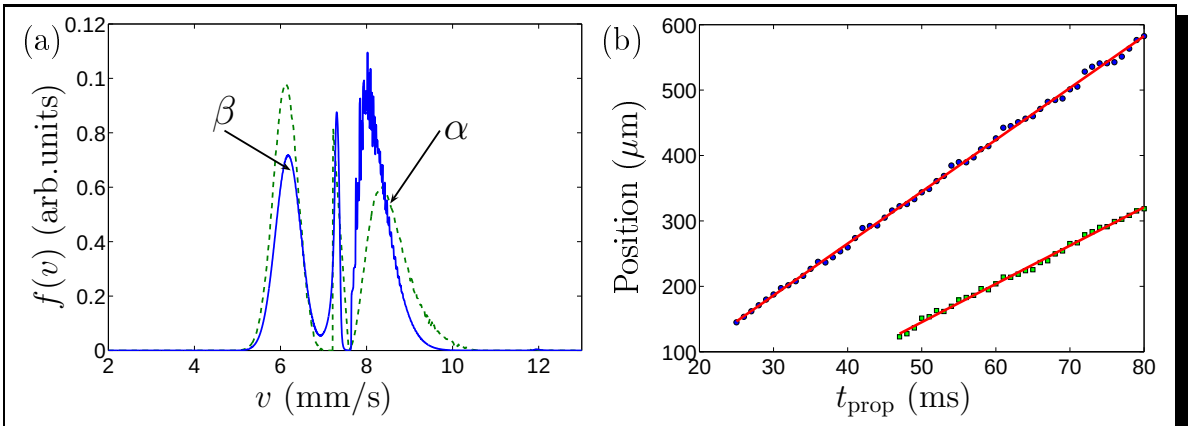

Figure 6.6: *(a) Calculated velocity distribution of atoms that leave the lattice after one oscillation using the local band model (green dashed line) and the full numerical integration (blue solid line). (b) Experimental measure of the positions od the tunneled packets as a function of* t_{prop}*. Linear fits result in measured mean velocities* $\bar{v}_\alpha = 7.9 \pm 0.1$ *and* $\bar{v}_\beta = 5.9 \pm 0.1$ mm/s.

internal state configuration. The maximum transmission probability of T_2 being, however, smaller than 1.

Surprisingly, the two packets do not seem to expand over several tenth of ms while after 50 ms of propagation, while according to their velocity dispersion, we could naively expect an increase of the width by more than 10 μm which should be visible. Actually, the simulation indicates that the wavepackets are focused at a finite time (at $t_{\mathrm{prop}} \simeq 70$ ms for the packet α). This is a consequence of the fact that different velocity classes are outcoupled at different times. The most energetic atoms travel faster in the cavity, however, they see a larger effective cavity (see Fig. 6.1). As we will see, it turns out that the second effect is more important so that the oscillation period increases with the energy. Concerning the tunneled packet, this results in an chirped pulse with the high frequencies at the back. High velocities then catch up with the slow ones at a finite time. This effect hinders a direct measurement of the velocity dispersion.

6.4 Dephasing between energy components

In this section, we describe more precisely the dephasing between the different energy components and propose a way to cancel it.

6.4.1 Semi-classical trajectories

To understand quantitatively the effect of dispersion between the different energy components, we developed a semi-classical simulation that enables one to isolate the dynamics of the different energy components. It contains two ingredients. The

first one is the description of the particle motion on a given Bloch band n through the combined evolution of the wavepacket position and mean pseudo-momentum k (in this sense it is a semi-classical simulation). The corresponding set of coupled equation reads

$$\dot{z} = \frac{1}{\hbar}\frac{\partial E_n}{\partial k} \qquad \text{and} \qquad \dot{k} = -\frac{1}{\hbar}\frac{\partial E_n}{\partial z}. \tag{6.8}$$

The first equation defines the group velocity of the wavepacket associated with the slope of the Bloch band, while the second results from the energy conservation condition $\mathrm{d}E_n(k,z)/\mathrm{d}t = 0$ [81].

The second ingredient consists in taking into account the possibility for a particle to undergo a Landau-Zener transition to an other band when it reaches the edge or the center of the Brillouin zone where it reaches a gap. In our case, the approximation of a local two-level situation is valid and therefore, the probability to change the band index is $P = e^{-2\pi\gamma}$ with

$$\gamma = \frac{\Delta E^2}{4\hbar}\left|\frac{\mathrm{d}}{\mathrm{d}t}(E_n - E_{n\pm1})\right|^{-1} \tag{6.9}$$

where ΔE is the size of the gap [90].

In practice, we evolve the particle according to Eqs. (6.8) and we evaluate the energy difference to lower or upper bands at each time step. When this quantity reaches a minimum (at the center of the edge of the Brillouin zone), we compute the corresponding Landau-Zener probability and transfer or not the particle to the next band according to this probability.

In order to validate this semi-classical trajectory method, we compare it with the full resolution of the corresponding 1D Schrödinger equation. To perform this comparison, we have simulated the semi-classical trajectories of 1200 incoming velocities about the mean velocity of the packet in the following range $5.6 < v < 13.2$ mm/s. In this way, we sample 95 % of the initial distribution (see FIG. 6.3). Furthermore, we perform 8 shots for each incoming velocity to improve the statistics of our Monte Carlo simulation. For each velocity class, we get the density from the positions of the different shots weighted by the initial wavepacket velocity distribution density. Figure 6.7 (a) shows the result of such simulation with the same parameters as in the experiment. We find a good agreement with FIG. 6.4 which validates the semi-classical simulation.

The interest of this simulation lies in the possibility to isolate different trajectories. In FIG. 6.7 (b), we have selected some trajectories for particles initially on the third band. We see that the spine structure observed in the experiments corresponds to the caustics indicated by the arrows. We also observe the increase of the oscillation period with the energy, indeed, the trajectories that travel the furthest away from the center (that correspond to more energetic atoms) bounce back at a larger time. This results here in the chirp of the tunneled wavepacket β which is visible in the fact that the two trajectories associated with the tunneled packet move

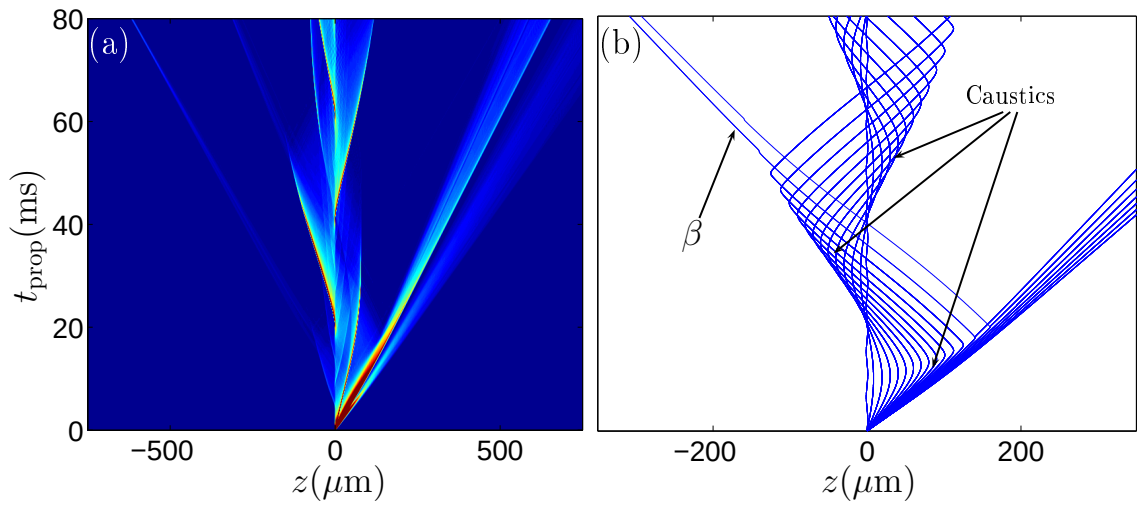

Figure 6.7: *(a) Density distribution for different propagation time reconstructed by simulating the semi-classical trajectories for the whole initial velocity distribution. (b) Examples of trajectories of particles initially on the third band. We observe the building up of the caustics and the dependency of the oscillation period with energy.*

towards each other.

6.4.2 Optimization of the envelope shape

The dephasing of the different energy components may appear as a limitation of the Bragg cavity device, it enlarges the initial width of the tunnel packet which increases the width of the steps observed in FIG. 6.5 and reduces the number of visible oscillations. Nevertheless, it is possible to circumvent this limitation by keeping the different energy components in phase with a proper shaping of the envelope.

This shaping consists in adjusting the effective size of the cavity for each velocity class to compensate exactly for the change in group velocity. As outlined before, in the case of a Gaussian envelope, as the energy increases, the corresponding increase of cavity length overcompensate the increase of the group velocity. In order to keep the different energy components in phase, we should thus reduce the dependency of the cavity length as a function of the energy. This means that the "walls" of the cavity as presented in FIG. 6.1 should be steeper. In the following, we demonstrate the optimization of the envelope shape using the simple *ansatz*:

$$U(z) = -U_0 \exp(-2z^2/w^2)\left(1 + \frac{z^2}{D^2}\right), \tag{6.10}$$

where D is a free parameter. Such an envelope could be realized for example by using holographic plates. This *ansatz* keeps the symmetry of the Gaussian envelope

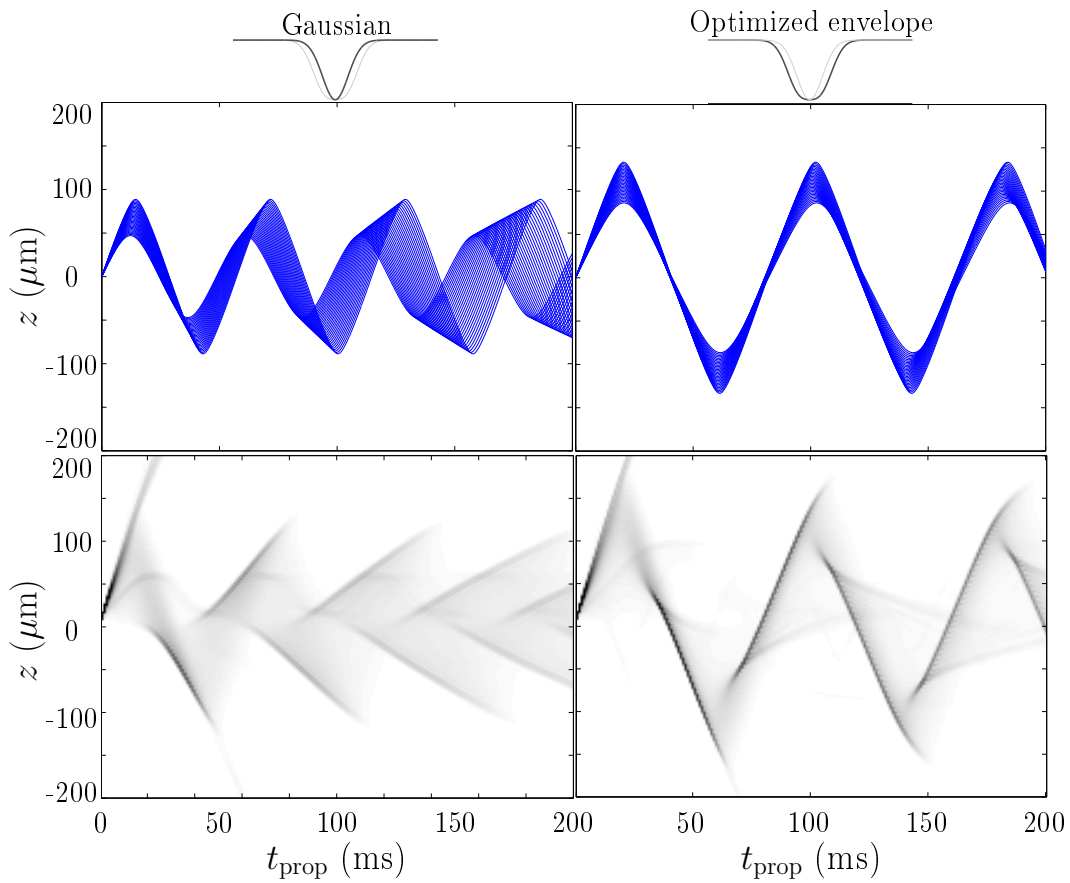

Figure 6.8: *Semi-classical trajectories (upper pannel) and full numerical integration (lower panel) of the wavepacket dynamics in (left) the Gaussian envelope lattice and in (right) the optimized envelope lattice with* $D = 0.75w = 112$ μm.

but has steeper spatial gaps if $D > 0$. The simplicity of the *ansatz* also ensures that the result of the optimization possesses a relatively simple shape.

Because of the caustic effect, it is difficult to define an oscillation period using the full numerical integration. Thereby, we have performed this optimization using the semi-classical model. We simulate the trajectories of particles with nearby energies, measure the variation of the oscillation period and change D in order to cancel out the first order variation of the oscillation period with energy.[4] For our parameters, we find $D = 0.75w = 112$ μm, the new envelope is very smooth and has a flat top. We then check with the full numerical integration that the optimized envelope reduces effectively the dephasing. In FIG. 6.8, we compare the results for a packet of velocity dispersion $\Delta v = 1.2$ mm/s for the semi-classical approach and the full numerical integration with and without the optimization. The blurring of the oscillations is greatly reduced and therefore all velocity components tunnel at the same time generating a train of matter wave pulses with an identical and well-defined velocity dispersion and no chirp.

6.5 Conclusion

We have demonstrated that spatial gaps resulting from an inhomogeneous envelope of a lattice produce barriers with a probability transmission equivalent to thin real barriers of a few hundreds of nm. They open new perspectives for single tunnel barrier physics including time-modulated tunnel barrier, many-body wavefunctions (such as solitons) tunneling [120, 121, 122], Josephson-like experiments [111, 110]. This system is also of interest for multiple barriers configurations including cavity or Anderson localization investigation in real space [123, 75]. It can be readily generalized to higher dimensions and may be used as a test bed for semi-classical approaches of tunneling in 2D [124].

[4] It is possible to extend the *ansatz* to higher order to cancel out the second derivative of the oscillation period, however the resulting potentials have a much more complicated shape that would not be relevant experimentally.

Chapter 7

Scattering on an amplitude-modulated lattice

Contents

7.1 Introduction **111**
7.2 The experiment **112**
7.2.1 Protocol 112
7.2.2 Control of the intensity 112
7.2.3 Experimental results 113
7.3 Interband transitions in the vanishing depth limit **115**
7.4 The Floquet-Bloch framework **118**
7.4.1 Principle 118
7.4.2 Computation of the Floquet-Bloch band diagram 119
7.4.3 Reflection on a square envelope lattice 120
7.5 Trajectories in the semi-classical model **121**
7.5.1 Validation of the semiclassical model 121
7.5.2 Analysis of the reflection mechanism 123
7.6 Application:velocity filter **125**
7.7 Conclusion **126**

7.1 Introduction

Cold atoms interacting with time-modulated optical lattices display a wide variety of quantum and classical dynamics. These include the observations of dynamical localization [125, 126], chaos-assisted tunneling [78, 119], the Anderson metal-insulator transition in momentum space [127], dynamically controlled tunneling [128, 129, 130] and matter wave engineering [131, 132, 133, 134]. In this chapter, we study the problem of matter wave scattering on a time-modulated lattice.

In chapter 5, we have demonstrated the possibility to perform momentum engineering using the scattering of a matter-wave on a static lattice. However, in this

case, the Bragg reflection condition is directly related to the lattice spacing and therefore, cannot be easily tuned over a large range. In contrast with a scattering experiment in optics, we are able to control easily the potential strength in time which offers a new degree of freedom. As we shall see, the interaction of the matter wave with an amplitude-modulated lattice yields new reflection conditions that offer much more flexibility and render possible the realization of a tunable Bragg reflector in confined geometry.

In this chapter, we first present the experimental protocol and the results of the scattering experiment. We then analyze these results using a very simple approach based on interband transitions. Next, we propose an analysis relying on the semi-classical model presented in chapter 6 in combination with the Floquet-Bloch framework. This allows to get a deep insight into the physics at play in this system.

7.2 The experiment

7.2.1 Protocol

The protocol of this experiment is very similar to the one presented in chapter 5. We start with a cooled atomic packet at 500 μm from the lattice center. Here we do not use a Bose-Einstein condensate but rather a thermal cloud of typically 10^5 atoms at 500 nK in order to probe the modulated lattice for a wide range of incoming velocity in a single shot. The atoms are prepared in the state $m_{\mathrm{F}} = 0$ using the horizontal spin distillation. We then switch off the dimple beam (without decompression) and release a packet of resulting longitudinal velocity dispersion $\Delta v \simeq 6$ mm/s. Atoms are subsequently accelerated in $t_{\mathrm{acc}} = 15$ ms to a mean velocity $\bar{v} = 10$ mm/s by an inhomogeneous magnetic field pulse. The atoms then propagate towards the modulated lattice and interact with it for a time t_{prop} before imaging.

The lattice amplitude is modulated at a frequency ν in the kHz range, the time-dependent potential experienced by the atoms reads:

$$U(z,t) = -U_0(t)e^{-2z^2/w^2}(1+\cos(k_{\mathrm{L}}z)), \tag{7.1}$$

with

$$U_0(t) = U_0(1+\eta\cos(2\pi\nu t)), \tag{7.2}$$

where η is the modulation amplitude. η can be quite large in the experiment and is often taken equal to 30%. In the following experiments, the mean lattice depth and modulation amplitude are kept constant and we vary the modulation frequency.

7.2.2 Control of the intensity

In order to accurately control the mean depth U_0 and the modulation amplitude η, we use a "double" feedback scheme whose principle is diagrammatically represented

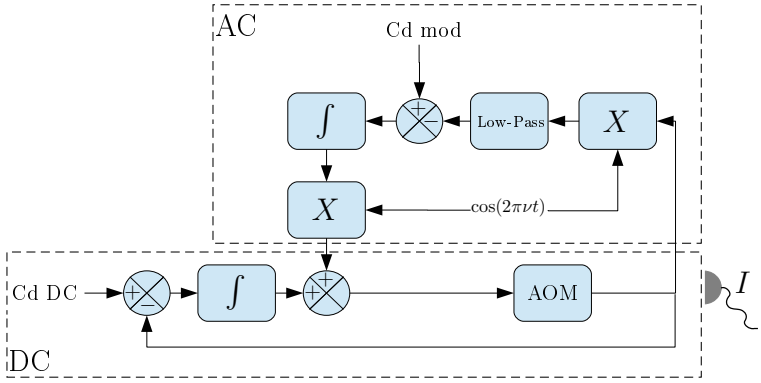

Figure 7.1: *Sketch of the feedback system to lock both the DC and AC component of the lattice beams intensity. The amplitude of the AC component is measured using a lock-in amplifier. Symbols: X: multiplier (AD633),* $\int$ *ideal integrator with adjustable gain, Cd: electronic command of the lattice depth or modulation amplitude, Low-Pass: 100* Hz low-pass filter.

in FIG. 7.1. The power in the lattice beams is controlled via a single AOM prior to the beam separation. A photodiode with a 100 MHz bandwidth measures the intensity of the lattice beams and is set on one arm after the vacuum chamber. The lower part of the diagram 7.1 concerns the DC component and is simply made of a pure integrator. The timescale of this integrator is such that it averages the AC component. The AC modulation is injected after the integrator, its amplitude is locked using the upper part of the diagram. In the upper part, the photodiode signal is multiplied by a signal at the modulation frequency and subsequently filtered to realize a lock-in amplifier. The error signal resulting from the substraction of the command is then multiplied with the reference modulation and injected to the command of the AOM.

7.2.3 Experimental results

Figure 7.2 (b) shows the atomic density after a propagation time $t_{\mathrm{prop}} = 78$ ms as a function of the modulation frequency ν with a mean lattice depth $U_0 = 2E_{\mathrm{L}}$ and a modulation amplitude $\eta = 30$ %. Each horizontal line is obtained by averaging 8 images integrated along the transverse direction to improve the signal to noise ratio. Atoms are launched at $z = 0$ towards the lattice, located 500 μm downwards and depicted by the dashed line. Atoms on the right side of the plot ($z > 500$ μm) are transmitted. In this complicated transmitted part, we observe two kinds of density dips:

- dips whose positions do not depend on the modulation frequency (vertical depletion lines) and that correspond to velocity classes fulfilling the Bragg reflection condition on the *static* lattice as presented in chapter 5.

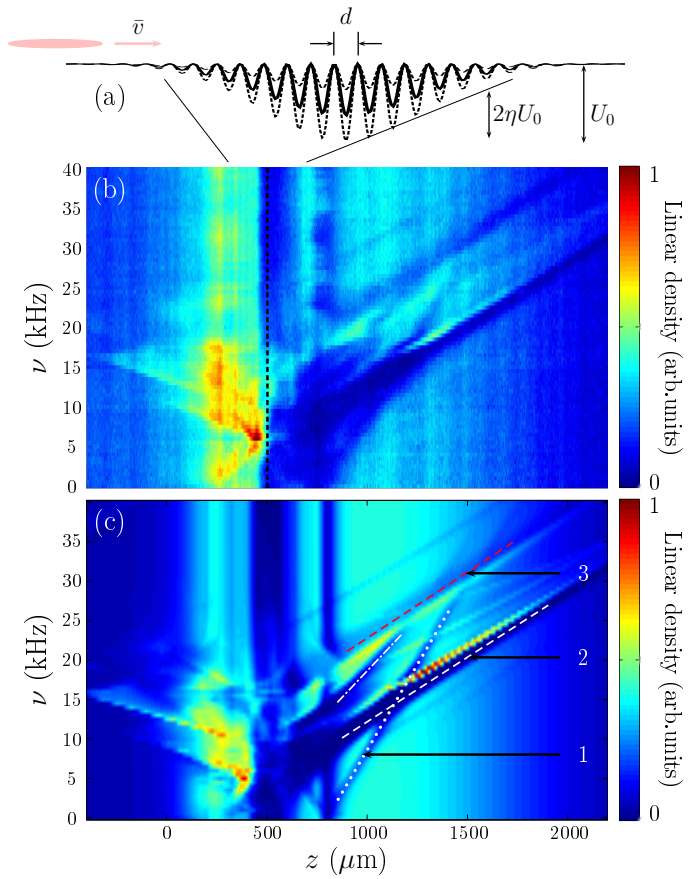

Figure 7.2: *(a) Sketch of a propagating atomic packet impinging onto an optical lattice whose amplitude is modulated. (b) Measured longitudinal density* $n(z, t_{\mathrm{acc}} + t_{\mathrm{prop}})$ *after a propagation time* $t_{\mathrm{prop}} = 78$ ms *for a variable lattice modulation frequency* ν *(lattice depth* $U_0 = 2E_L$*. The modulation depth is* $\eta = 30\%$*, and the lattice position is depicted by the dotted line. (c) Numerical simulations convoluted with a* 10 μm *wide Gaussian to match the experimental resolution. Frequency-dependent dips are observed in the transmitted distribution. Dotted, dot-dashed and dashed lines in (c) show the linear dependence of the dip position with* ν*.*

- Dips whose positions depend on the frequency. As we shall discuss below, some dips of the latter category have their counterpart in the reflected packet and correspond to reflected class of velocity while others are due to slowing down or acceleration effects.

For sake of comparison, FIG. 7.2 (c) is the result of a numerical simulation of the atomic packet dynamics using the one-dimensional Schrödinger equation with a wave packet whose initial momentum and position distributions match the measured experimental values. We find a very nice agreement between simulations and experiment. However, the elementary mechanisms at work cannot be inferred from such an approach.

Except for the zones very close to the depletion lines in the transmitted part in Fig. 7.2, each position downward the lattice can be mapped onto a well defined class of incident velocity $z \simeq v_0(t_{\rm acc} + t_{\rm prop}) + K$ where K is a constant.[1]

Let us characterize the different depletion lines. Using the correspondence between x and v_0: the main depletion line (white dashed line) in Fig. 7.2 (c) has a slope $\mathrm{d}\nu/\mathrm{d}v_0 = (660\ \mathrm{nm})^{-1} \simeq 1/d$. We also observe directly the corresponding reflected atoms in the region $x < 0$. The red upper dashed line of depleted atoms is parallel to the main line but has no counterpart in the reflected region. The white dot-dashed and dotted lines, have slopes respectively twice and three times as large as the one of the dashed white and red depletion lines. In this experiment, the lattice spacing d is one of the two relevant distances (the other one being the envelope waist). It is thus not surprising to find that the slopes of the depletion lines have simple relations with d. However, the absence of numerical factor in the relation of the type $\mathrm{d}\nu/\mathrm{d}v_0 = n/d$ with n integer may seem astonishing.

7.3 Interband transitions in the vanishing depth limit

In this section, we present a very simple model based on interband transitions that allows to reproduce the slopes and relative positions of the depletion lines.

Let us consider the case of a vanishing depth lattice and consider an incident quasi-monochromatic wave packet of velocity v_0. In the vanishing depth limit, the band structure is constructed by the superposition of parabolic energy spectra centered around all reciprocal points $E_n(k) = \hbar^2(k - nk_L)^2/2m$, where n is an integer. For instance, bands 2 and 3 are constructed from the parabolas centered at $\pm\hbar k_L$ (see FIG. 7.3). The incoming velocity v_0 dictates the band in which the incoming atom enters. For instance, if $3v_{\rm L}/2 < v_0 < 2v_{\rm L}$ the atom will be on band 4. According to this figure, there are two possibilities symmetric around $k = 0$. We always choose the side where the group velocity of the wavepacket is positive, that corresponds to a positive slope of the band diagram.

[1] If a denotes the acceleration experienced by the atoms during the magnetic pulse, one finds $K = at_{\rm acc}(t_{\rm acc}/2 - t_{\rm prop})$.

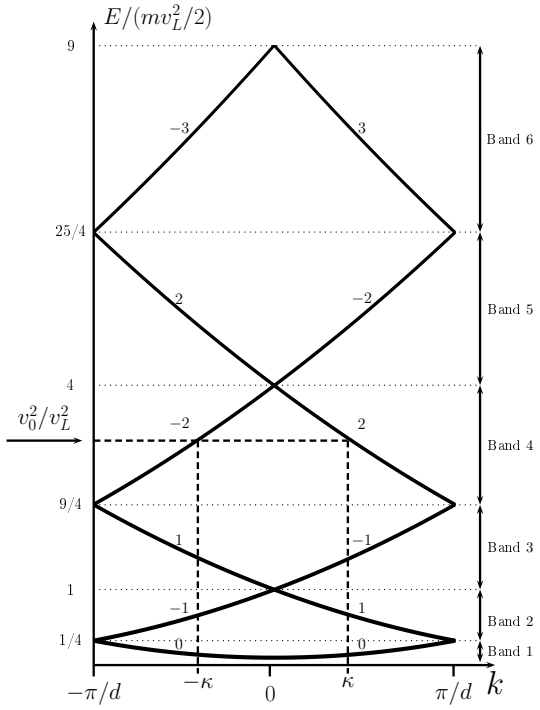

Figure 7.3: *The band diagram at vanishing depth is constructed by the superposition of parabolic energy spectra centered around all reciprocal points* $E_n(k) = \hbar^2(k - nk_L)^2/2m$. *For each band we have indicated the index* n *of the parabola from which the corresponding branches have been constructed.*

Let us now assume that the modulation of the lattice can drive interband transition between two distinct parabolas n and n'. The time-dependent coupling potential possesses the simple form $V \sim \cos(k_{\mathrm{L}} z)$. The probability of transmission from a Bloch state $\psi_{p,k}$ to a state on a different band $\psi_{p',k'}$ is then be proportional to

$$|\langle \psi_{p',k'}|V|\psi_{p,k}\rangle|^2 = \int e^{2i(k-k')z} \cos(k_{\mathrm{L}} z) u^*_{p',k'}(z) u_{p,k}(z) \mathrm{d}z. \tag{7.3}$$

This matrix element vanishes as soon as $k \neq k'$, because of the symmetry of the modulation potential and the periodicity of the Bloch functions $u_{p,k}(z)$. The modulation can thus only drive vertical transitions that leave the pseudo-momentum unchanged.

The interband transition frequency that promote an atom from a band p corresponding to the n-th parabola to a band p' (n'-th parabola) are given by:

$$\pm\nu_{n\to n'} = (E_n - E_{n'})/h. \tag{7.4}$$

The sign + (−) corresponds to a transition to a lower (upper) band. By energy conservation, we have

$$\frac{1}{2} m v_0^2 = E_n(\kappa). \tag{7.5}$$

Combining Eqs. (7.4) and (7.5), we get

$$\pm\nu_{n\to n'} = \frac{E_n - E_{n'}}{h} = -(n - n')^2 \nu_{\mathrm{L}} + \frac{n' - n}{d} v_0, \tag{7.6}$$

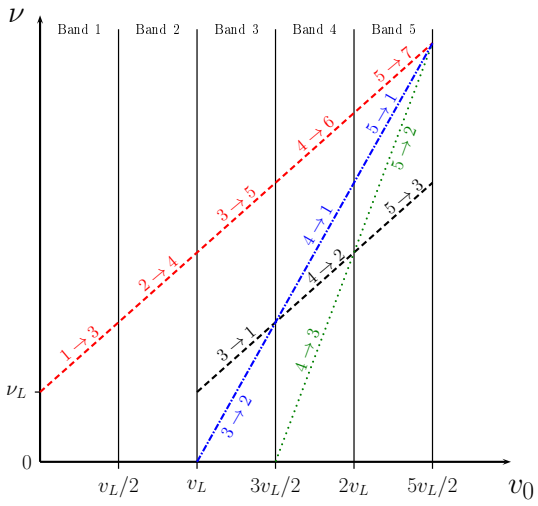

Figure 7.4: *Interband transition resonance frequency for various couples of initial and final parabolas. The lines associated with the interband transitions match the depletion lines observed in the experiment (see* FIG. *7.2). Depending on the incident velocity, a transition between different parabolas correspond to differents interband transitions.*

where we remind that $\nu_\mathrm{L} = E_\mathrm{L}/h$. According to Eq. (7.6), the interband transition resonance frequency varies linearly with the incident velocity with a slope $(n'-n)/d$, where $n'-n$ is an integer. It is thus very tempting to associate each depletion line with an interband transition. Let us precise this correspondence.

In FIG. 7.4, we have represented different resonance frequency associated with the transitions from the initial parabola n to the parabola n' using Eq. 7.6 as a function of the incident velocity. For each line, we have also indicated two numbers: the first corresponds to the band on which atoms initially lie according to their incident energy $E = mv_0^2/2$ while the second corresponds to the band on which atoms are resonantly transferred by the modulation. As an example, let us consider the green dotted depletion line in FIG. 7.4. In the incident velocity domain $3v_\mathrm{L}/2 < v_0 < 2v_\mathrm{L}$, it corresponds to a resonant transition between bands 4 and 3. In the domain $2v_\mathrm{L} < v_0 < 5v_\mathrm{L}/2$, it corresponds to a transition between the band 5 and 2 (see FIG. 7.5). Figure 7.5 shows the correspondance between interband transitions and transitions between different parabolas in the case of the (green) transition $n = -2 \to n' = 1$ and (black) $n = -1 \to n' = 0$. We see that the succession on the same line of different interband transitions is merely due to the folding of the parabolas in the first Brillouin zone.

The following table shows the equations associated with the represented transitions:

red	$n = 0, n' = -1$	$\nu = \nu_\mathrm{L} + v_0/d$
black	$n = -1, n' = 0$	$\nu = -\nu_\mathrm{L} + v_0/d$
blue	$n = -1, n' = 1$	$\nu = -4\nu_\mathrm{L} + 2v_0/d$
darkgreen	$n = -2, n' = 1$	$\nu = -9\nu_\mathrm{L} + 3v_0/d$

The four transitions represented here correspond very accurately to each one of the depletion line in terms of the slopes of the depletion lines but also of their relative positions (The offset between the two parallel dashed lines in the experimental figure

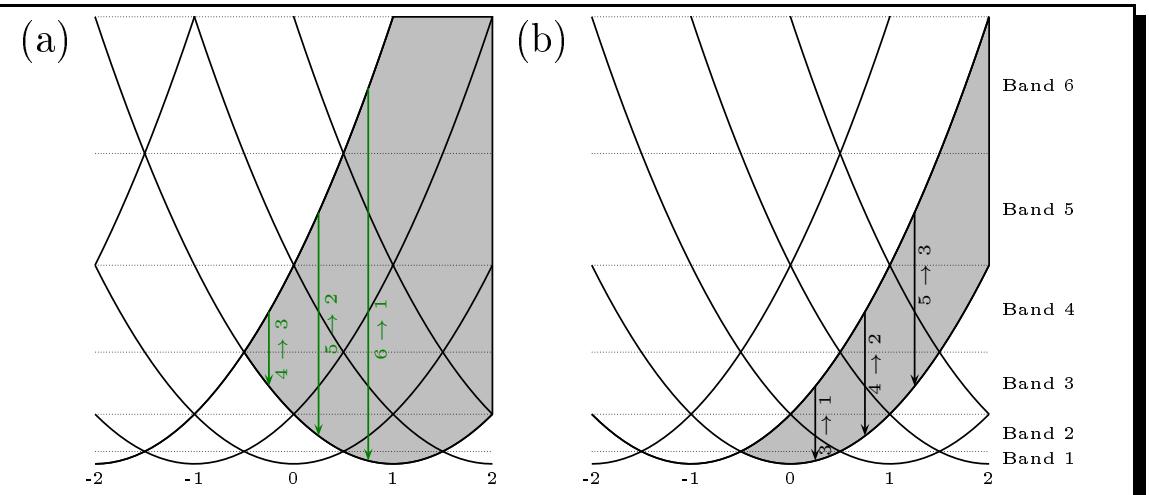

Figure 7.5: *Illustration of the correspondance between a transition from two parabolas and two bands. (a) Transition (green) $n = -2 \rightarrow n' = 1$. (b) Transition (black) $n = -1 \rightarrow n' = 0$.*

7.2 is in particular equal to $2\nu_L \simeq 10.8$ kHz.). The transition $n = 0 \rightarrow n' = -1$ matches the red dashed depletion line, $n = -1 \rightarrow n' = 0$, the main depletion (white dashed line), $n = -1 \rightarrow n' = 1$ and $n = -2 \rightarrow n' = 1$ the dot-dashed and dotted lines respectively. This constitute a very strong evidence that interband transitions are at the heart of the reflection process.

To get a better understanding of the width of the depletion lines, their interpretation in terms of elementary processes, the timescale on which the reflections occur and the role played by the Gaussian envelope of the lattice potential, we introduce now a more elaborated analysis based on the local Floquet-Bloch framework [81, 135].

7.4 The Floquet-Bloch framework

7.4.1 Principle

This approach is not restricted to small modulation depths and is thus well-adapted to analyze the experimental situation. For a potential periodic in both space and time, the Bloch theorem can be extended to the time domain. The solutions of the time-dependent Schrödinger equation then possess the form of a Floquet-Bloch state:

$$\psi_{n,k}(z,t) = e^{i(kz-\varepsilon_n(k)t/\hbar)} u_{n,k}(z,t), \tag{7.7}$$

where $\varepsilon_n(k)$ are the quasi-energies. The functions $u_{n,k}(z,t)$ are biperiodic in space and time and therefore can be Fourier expanded:

$$\begin{aligned} u_{n,k}(z,t) &= u_{n,k}(z+d,t) = u_{n,k}(z,t+T) \\ &= \sum_l \sum_{n_F} \phi^{n_F,l} e^{i(lk_L z - n_F \omega t)}, \end{aligned} \tag{7.8}$$

where $\omega = \nu/2\pi$. In the following, we restrict ourselves to $n_F \in \{-1,0,1\}$ *i.e* to situations in which only one Floquet photon can be absorbed or emitted.[2] As in the static lattice case, we can build a band diagram described by a band index and a pseudo-momentum. At zero modulation depth, the Floquet-Bloch band diagram is nothing but the superposition of static lattice Bloch diagrams shifted by $n_F \hbar\omega$.

7.4.2 Computation of the Floquet-Bloch band diagram

To compute the Floquet-Bloch states and quasi-energies, we insert the developments (7.7) and (7.8) into the Schrödinger equation and expand the potential on the Fourier basis. The details of the development can be found in appendix G. The coefficients $\phi^{n_\mathrm{F},l}$ obey the following eigenvalue equation:

$$\begin{aligned} \left[n_\mathrm{F}\zeta + q/2 + (k/k_\mathrm{L} + l)^2\right] \phi^{n_\mathrm{F},l} + \eta q/4(\phi^{n_\mathrm{F}+1,l} + \phi^{n_\mathrm{F}-1,l}) - q/4(\phi^{n_\mathrm{F},l+1} + \phi^{n_\mathrm{F},l-1}) \\ -q/8(\phi^{n_\mathrm{F}+1,l+1} + \phi^{n_\mathrm{F}+1,l-1} + \phi^{n_\mathrm{F}-1,l+1} + \phi^{n_\mathrm{F}-1,l-1}) = \varepsilon \phi^{n_\mathrm{F},l}, \end{aligned} \tag{7.9}$$

where $q = U_0/E_\mathrm{L}$ and $\zeta = \hbar\omega/E_\mathrm{L}$ are the normalized lattice depth and modulation frequency. This system can be decomposed into a block matrix eigenvalue problem:

$$\begin{pmatrix} A-\zeta & C & 0 \\ C & A & C \\ 0 & C & A+\zeta \end{pmatrix} \times \begin{pmatrix} \phi^{-1} \\ \phi^0 \\ \phi^1 \end{pmatrix} = \frac{\varepsilon}{E_\mathrm{L}} \begin{pmatrix} \phi^{-1} \\ \phi^0 \\ \phi^1 \end{pmatrix} \tag{7.10}$$

where

$$\phi^{n_\mathrm{F}} = \begin{pmatrix} \phi^{nF,-N} \\ \vdots \\ \phi^{nF,N} \end{pmatrix} \tag{7.11}$$

[2] This assumption suffices to capture all observed phenomena on the experiment. The extension to larger Floquet excitations is straightforward.

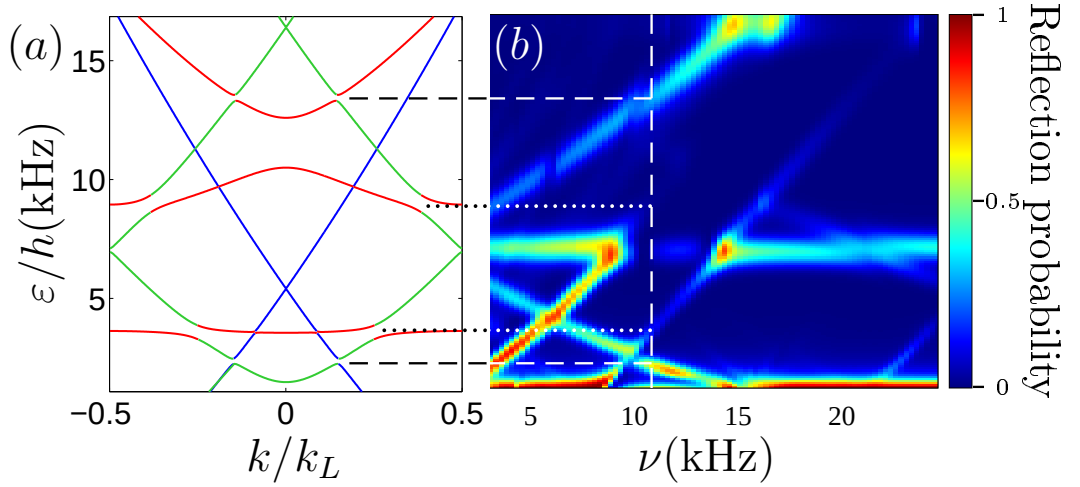

Figure 7.6: *(a) Floquet-Bloch band diagram with a depth* $U_0 = 2E_L$ *and modulation frequency* $\nu = 11$ kHz*. Band color code: green* $-0.5 < \langle n_F \rangle < 0.5$*, red* $\langle n_F \rangle > 0.5$ *and blue* $\langle n_F \rangle < -0.5$*. (b) Probability of reflection obtained from a numerical simulation of a 1D wavepacket with an incident velocity dispersion* $\Delta v = 0.2$ *mm/s with a finite square-envelope lattice as a function of the incident energy and* ν*. The horizontal white dashed line shows the case* $\nu = 11$ kHz *that corresponds to the diagram (a). The horizontal dashed (dotted) lines denotes open gap (degenerate) anticrossings. Only open gap anticrossings yield reflection.*

is the part of the eigenstate with n_F Floquet excitations.

$$A = \begin{pmatrix} b_{-N} & u & & & \\ u & b_{-N+1} & u & & \\ & \ddots & \ddots & \ddots & \\ & & u & b_{N-1} & u \\ & & & u & b_N \end{pmatrix} \tag{7.12}$$

with $u = q/4$ and $b_l = (k/k_\mathrm{L} + l)^2 - q/2$. The matrix A is the same as in the static case. The matrix C that couple the different domains reads:

$$C = \eta q/4 \begin{pmatrix} 1 & -1/2 & & \\ -1/2 & \ddots & \ddots & \\ & \ddots & \ddots & -1/2 \\ & & -1/2 & 1 \end{pmatrix} \tag{7.13}$$

In the absence of modulation, $C = 0$, the problem is separable and the band diagram is simply the superposition of static Bloch diagrams shifted by $n_\mathrm{F}\zeta$. As the modulation increases, the matrix C couples the different diagrams, at each crossing between the initially independent band diagrams, an anticrossing appears.

Figure 7.6 (a) shows such Floquet-Bloch diagram with $U_0 = 2E_L$, $\nu = 11$ kHz and $\eta = 30\%$. The different colors correspond to the mean number of Floquet excitation $\langle n_F \rangle = -|\phi^{-1}|^2 + |\phi^1|^2$ of the corresponding eingenstate.

The band color code is the following: green $-0.5 < \langle n_F \rangle < 0.5$, red $\langle n_F \rangle > 0.5$ and blue $\langle n_F \rangle < -0.5$.

7.4.3 Reflection on a square envelope lattice

In the Floquet-Bloch band diagram, two kinds of anticrossings can be identified: those yielding open gaps (horizontal dashed line in Fig. 7.6) and those without gaps for which two states with the same quasi-energy are available (horizontal dotted line in Fig. 7.6).[3] To identify the role of the different types of anticrossings on the incident matter wave packet, we have performed a 1D simulation that solves the corresponding time-dependent Schrödinger equation in the case of a square envelope lattice with 80 lattice sites, a depth $U_0 = 2E_L$ and a modulation $\eta = 30\%$. Figure 7.6(b) depicts the reflection coefficient as a function of the incident energy E_0 and the modulation frequency ν calculated by simulating the dynamics of wavepackets with a narrow velocity dispersion $\Delta v = 0.2$ mm/s. Two types of reflection can be clearly identified: (i) those due to Bragg reflection onto the static lattice (no dependence on ν) and (ii) those that correspond to open gap anticrossings and whose positions depend on ν. The interpretation is clear: when the incident energy falls in an open gap anticrossing, no propagating state is available and the particle is reflected. The degenerate anticrossings do not induce reflection in the square-envelope case. However, as we discuss below, they turn out to play an important role in the dynamics of the experimentally relevant case in which the lattice has a slowly varying envelope.

7.5 Trajectories in the semi-classical model

In this latter case, the situation turns out to be radically different since the system can follow adiabatically a quasi-energy band during its time evolution. To describe this propagation, we use the semi-classical model presented in the previous chapter and apply it to describe the motion of a fictitious particle in the Floquet-Bloch band diagram. We remind that the semi-classical simulation contains two ingredients. The description of the particle on a given *local* Floquet-Bloch band through the evolution of the wavepacket position and pseudo-momentum via the semi-classical equation:

$$\dot{x} = \frac{1}{\hbar}\frac{\partial \varepsilon_n}{\partial k} \qquad \text{and} \qquad \dot{k} = -\frac{1}{\hbar}\frac{\partial \varepsilon_n}{\partial x}. \tag{7.14}$$

[3] A third state far from the anticrossing and corresponding to a well-defined number of Floquet excitation can be present but do not alter the physics.

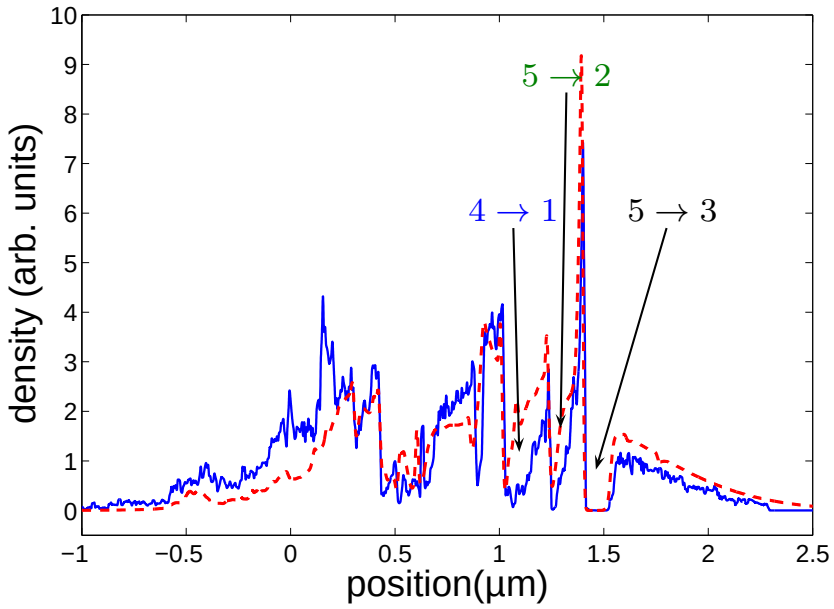

Figure 7.7: *Dashed line: Result of the resolution of the 1D Schrödinger equation with lattice and wavepacket parameters corresponding to the ones of* FIG. *7.2 (b) and a modulation frequency* $\nu = 20$ kHz. *Solid line, result of the semiclassical simulation with random Landau-Zener transition. The arrows indicate the main processes for three depletion lines. The wave packet has a mean velocity* $\bar{v} = 10$ mm/s *and a velocity dispersion* $\Delta v = 6$ mm/s.

The second ingredient consists in taking into account the possibility to undergo a Landau-Zener transition to a different band with the probability $P = e^{-2\pi\gamma}$ with:

$$\gamma = \frac{\Delta E^2}{4\hbar} \left| \frac{\mathrm{d}}{\mathrm{d}t}(\varepsilon_n - \varepsilon_{n\pm1}) \right|^{-1} \tag{7.15}$$

7.5.1 Validation of the semiclassical model

To validate the semiclassical trajectory method in the Floquet-Bloch frame, we compare it with the full resolution of the Schrödinger equation. In this case, we have simulated the semiclassical trajectories of 1700 incoming velocities about the mean velocity of the packet in the following range -4.5 mm/s $< v_0 <$ 24.5 mm/s. In this way, we sample 98 % of the initial distribution. Furthermore, we perform 35 shots for each incoming velocity to improve the statistics of our Monte Carlo simulation.

For each velocity class v_0, we get the density from the final positions of the different shots weighted by the initial wavepacket velocity distibution at v_0. Figure 7.7 provides an example of such a comparison for $\nu = 20$ kHz. The key features are very well captured by the semiclassical simulation and the three depletion lines in the transmission are clearly visible. The arrows indicate the interband transition

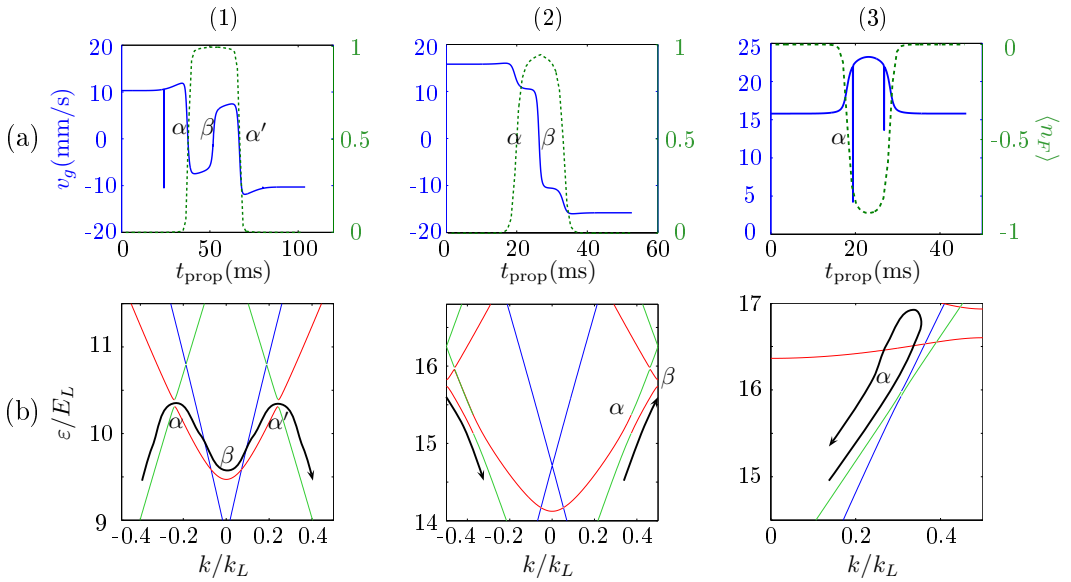

Figure 7.8: *(a) Velocity and mean Floquet excitation number $\langle n_F \rangle$ as a function of the propagating time for parameters corresponding to three different depletion zones shown in* FIG. *7.2. (b) Local Floquet-Bloch diagram. Arrows denote the trajectories followed by the fictitious particles. (1) Reflection on an open gap $v = 10.3$ mm/s, $\nu =$ 8 kHz. (2) Reflection on an anticrossing without gap $v = 15.8$ mm/s, $\nu = 20$ kHz. (3) Transient acceleration $v = 15.8$ mm/s, $\nu = 30.5$ kHz. α (β) denotes absorption or emission of one Floquet photon (reflection).*

associated with each of these depletion. This comparison thus validates the semi-classical approach in this case.

7.5.2 Analysis of the reflection mechanism

We can now use the semiclassical model to analyze the different mechanisms yielding to depletion bands as observed in FIG. 7.2. For this purpose, we follow deterministically the branch for which the Landau-Zener transition probability is above 1/2 at an avoided crossing. This select the most probable trajectory. To illustrate the wide variety of possibilities, we shall choose three generic and different set of parameters (v_i, ν) yielding to dips in the output density distribution (see labels 1, 2 and 3 in Fig. 7.2(c)).

In FIG. 7.8(a), we plot the velocity along with the mean Floquet excitation number for each case and for the main trajectory given by the Monte-Carlo simulation. In FIG. 7.8(b) we show the corresponding Floquet-Bloch diagrams in the region of interest. When a particle is moving toward the center, all quasi energies decrease since the amplitude of the attractive lattice increases. As a result, the particle state moves up relatively to the band diagram. In the same way, if the particle is moving backward, it will go down the hills of the diagram. With these simple pictures in

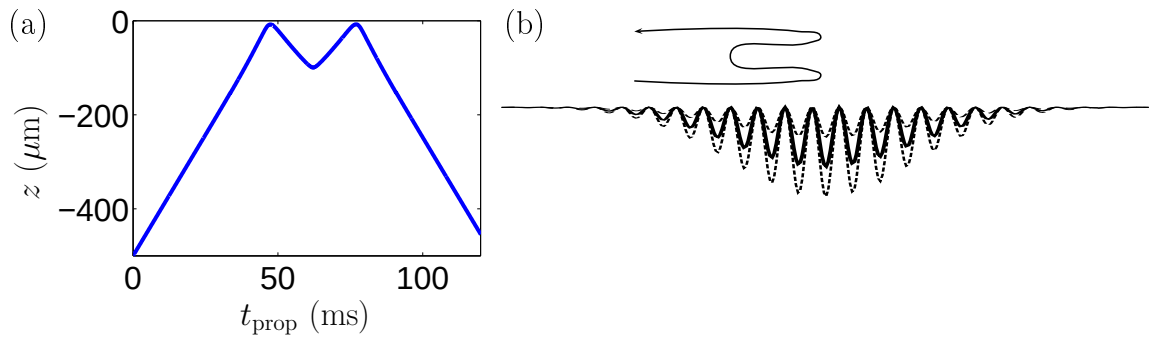

Figure 7.9: *(a) position of the fictitious particle as a function of the propagation time for the trajectory (1) of* FIG. *7.8. (b) Illustration of the particle motion, this particular trajectory is highly non trivial.*

mind trajectories can be readily interpreted.

In each case, the key phenomenon is the absorption or stimulated emission of a Floquet photon by adiabatic following of the Floquet-Bloch band denoted by α in FIG. 7.8.

- In case (1), the particle emits a Floquet photon at $t_{\mathrm{prop}} \simeq 40$ ms, which changes the sign of the group velocity. The particle is thus moving away from the lattice center. It then performs a reflection (denoted β) when reaching the bottom of the band (the sign of the group velocity is switched back again). When reaching the same position as for the first emission α, the particle then absorbs a Floquet photon (α') before leaving the lattice. In position space, the trajectory is thus also highly non-trivial (see FIG. 7.9).

- The case (2) is very similar except that the first emission only slows down the particle which is then Bragg reflected and subsequently accelerated by Floquet photon absorption. Note that in this case the anticrossing is closed (there are always two degenerate states) so that such anticrossing does not induce any reflection in the square envelope case.

- In case (3), the particle is not reflected. It is only transiently accelerated in the lattice by a Floquet photon absorption-emission cycle. For a much longer time, the dip observed in FIG. 7.2 would thus be refiled.

Other features of the experimental and numerical diagrams of FIG. 7.2 can be readily explained thanks to our semiclassical model. For instance, the density bump above the white dashed line corresponds to atoms that have been slowed down.

For a given incident kinetic energy E_0, a large size of the envelope and/or a large modulation depth increases the efficiency of the process since it favors an adiabatic following of the anticrossings. A less intuitive feature concerns the lattice depth. Indeed, a small lattice depth ($U_0 < E_0$) increases the selectivity of the class of

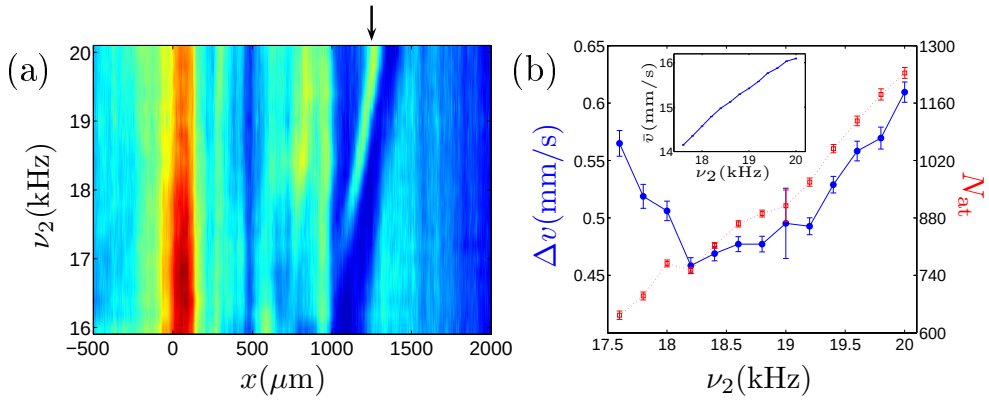

Figure 7.10: *(a) Density distribution for the scattering on a two-frequency modulated optical lattice (same conditions as in* FIG. *7.2) for a fixed frequency* $\nu_1 = 16$ kHz *and a scanned frequency* ν_2*. A narrow slice of transmitted atoms is produced (see arrow). (b) Number of atoms and velocity dispersion associated with these narrow slices of transmitted atoms as a function of* ν_2*. Inset: mean velocity of the slice of atoms as a function of* ν_2*.*

incident velocities that are affected by the modulation. Indeed, the selectivity is determined by the variation of the position of the anticrossing along the lattice. As the depth of the lattice increases, all quasi-energies decrease by a quantity that is roughly equal in a first approximation to the mean potential $U(z)/2$.[4] A particle with an energy larger than the anticrossing energy thus cannot absorb a Floquet photon. A particle with an energy smaller than the anticrossing energy can absorb a Floquet photon if in the course of the propagation, its trajectory reaches the anticrossing which is possible only if the difference of energy is smaller than $U_0/2$. The width of the depletion line thus decreases with a small lattice depth.

7.6 Application:velocity filter

The narrowest velocity filters used in the cold atom community rely on velocity selective Raman transitions on atoms in free space. This technique involves a combined change of internal and external states. The achievable velocity width are in the range of 200-300 μm/s [118, 119, 136]. Using the scattering on amplitude modulated optical lattice we demonstrate hereafter a new technique to realize a velocity filter with a width slightly larger than the state of the art with velocity selective Raman transitions. Our technique uses only the external degrees of freedom and thus does not require any specific internal configuration. In addition it is well adapted for guided matter waves.

We turn our device into a tunable momentum filter by combining different mod-

[4]This is particulary true if the typical kinetic energy is large compared to the lattice depth.

ulation frequencies. We use here the main reflection line (white dashed line in FIG. 7.2) that acts as a notch filter in momentum space. For this purpose, we modulate the lattice with two different frequencies to create a transmitted band between two rejected ones: $U_0(t) = U_0(1 + \eta\cos(2\pi\nu_1 t) + \eta\cos(2\pi\nu_2 t))$. Strictly speaking, the detailed dynamics of a wave packet submitted to this two frequency and non perturbative modulation cannot be inferred directly from the single frequency dynamics. However, the simple picture according to which nearly independent dips can be drilled into the velocity distribution with two frequencies is quite robust. We observe that the reflection spectrum is roughly the product of the two independent spectra (see FIG. 7.10). The mean velocity of the slice of atoms is therefore governed by $d(\nu_1 + \nu_2)/2$ while its width is controlled by the frequency difference $|\nu_2 - \nu_1|$. In our set of experiments, ν_1 is fixed at 16 kHz and ν_2 is varied from 16 to 20 kHz. Between the two reflection lines, atoms in a narrow class of velocity are transmitted (arrow in FIG. 7.10). The slice contains about 1000 atoms and has a mean velocity on the order of 15 mm/s (inset of FIG. 7.10). The minimum velocity dispersion of the velocity filter that we have designed is on the order of 450 μm/s for our parameters

7.7 Conclusion

The matter wave engineering presented here does not have any fundamental limit. It is easily tunable by changing the modulation frequencies and complex transmission spectra can be designed by using a multifrequency modulation. A further improvement of velocity selection could be achieved using a smaller depth lattice which would realize a narrower filter combined with a larger waist size to conserve a maximum reflection probability on the order of 1. One fundamental advantage of this technique over filtering using Raman velocity selection lies int the fact that it does not rely on a specific internat level configuration. This technique can thus be transposed easily to other species. By construction, it is well adapted to 1D geometry and therefore enhances the toolbox of guided atom optics.

Conclusion

In this thesis, we have described two separate studies: the realization of Zeeman Slowers using permanent magnets and the scattering of matter waves on complex potentials provided by an optical lattice with a finite size envelope.

- In the first project we have studied two different configurations: the *dipole* configuration were two arrays of dipole-like magnets are distributed on each side of the atomic beam, and the *Halbach* configuration were the magnets are distributed all around the atomic beam. The magnets configuration then realizes an approximation of the ideal Halbach cylinder which produces highly homogeneous magnetic field. Both slowers offer state of the art performances *i.e* an atomic flux at $\sim$ 30 m/s of $1 - 5 \times 10^{10}$ at/s that allows to load a large MOT in less than 1 s. An important difference compared to wire-wound Zeeman slowers is that in this case the magnetic field is transverse. The main effect being that the addition of a repumping beam is mandatory (while it is optional in a conventional ZS). Permanent magnets based slowers offer several interesting advantages compared to conventional Zeeman slowers: it does not require high currents nor water cooling, is easy to assemble without vacuum breaking, which is useful for high-temperature baking and is very easy to build. We believe that wherever the necessity of an additional repumping beam is not an important issue, this configuration is superior to the common wire-wound Zeeman Slower.

- The second project is about the scattering of a cold atom matter wave on a complex potential realized by a finite size lattice. We have first presented the experimental setup that allows us to produce Bose-Einstein condensate in a crossed dipole trap. We typically obtain rather small condensates of about 5×10^4 atoms in a well defined magnetic state using the spin distillation technique. We then described the setup of the finite size optical lattice and the calibration of its depth using Kapitza-Dirac diffraction. The next chapter presents some theoretical tools useful to describe particles in a periodic potentials and to study the scattering on such potentials. In particular, we introduced the solutions of the Mathieu equation that allow to extend the notion of Bloch state to the case where the energy lies in a gap of the band structure.

  In the next chapter, we presented the experimental study of the scattering of

a guided matterwave on a finite length optical lattice. We have presented the outcoupling of the condensate in the guide in order to minimize the velocity dispersion. Then we described a time-resolved scattering experiment and the measurement of the transmission spectrum by varying the lattice depth. The whole lattice can be seen as a Bragg reflector. The properties of the Bragg mirror are described within the slowly varying envelope limit. Because of the rich structure of the transmission spectra, depending on the lattice and wavepackets parameters, the Bragg reflector can be used as a low-pass, band-pass or high-pass filter.

Next, we have studied in detail the cavity effects associated with the presence at two symmetric positions of two Bragg mirrors. In this experiment, we load initially the atoms at the center of the lattice on a high band of the lattice energy structure (the third band essentially). The atoms then see two semitransparent mirrors with an energy-dependent transmissivity. We let the atoms propagate in the lattice, and observe oscillations of the wavepacket inside the cavity as well as localized tunneling events when the wave packet reaches one of the two Bragg mirrors. We analyze quantitatively the tunneling out of a fraction of the atoms using the notion of finite extent spatial gaps: because of the smooth envelope of the lattice, the band gaps are transposed into position space. This allows us to characterize the transmissivity of the Bragg mirrors. We show that the transmissivity of the mirrors is to some extent equivalent to the one from a repulsive tunnel barrier of submicronic size. Because it is experimentally challenging to realize such a small barrier for example by optical means, our method can provide a good alternative to introduce a tunnel barrier in an experiment.

In the Bragg cavity, all velocity components do not generally keep up with each other, so that the oscillations inside the cavity are washed out after a few oscillations. This constitutes a limitation, both to observe the oscillations and to analyze the tunneled packets. We showed theoretically, however, that it is possible to maintain the different components in phase with an appropriate shaping of the envelope.

It is possible to pursue these studies in several directions. First if one disposes of a of high numerical aperture optics, it would be possible to drastically reduce the length of the envelope and to generate a lattice with only a few sites. One could then tailor almost arbitrarily the matterwave filter response by using for example holographic plates. In a different direction, it would be appealing to study the effect of interatomic interactions on the propagation of the wavepacket and particularly on the dynamics inside the Bragg cavity. This regime could be reached by using much larger transverse frequency or, by using a Feshbach resonance (this would require to work with an other atom). The use of a Feschbach resonance would also render possible the study of the scatter-

ing of a matter wave bright soliton on this periodic structure. The question of the scattering of these objects that possess both quantum and classical properties attracted much attention recently to produce for example mesoscopic Schrödinger cats [99, 137]. This question will be investigated theoretically in Francois Damon thesis.

Finally, we have studied the problem of scattering on a lattice whose depth is modulated. We have studied the transmission spectra when varying the frequency of the modulation. The modulation gives rise to several drops in the transmission whose positions in term of the incident velocity depend directly of the modulation frequency. In this sense, this constitutes a tunable Bragg reflector. We have analyzed the scattering using first a simple model based on interband transitions in the case of a vanishing depth lattice. This model predicts correctly the positions and slopes of the observed depletion lines. We have then analysed the dynamics using a semi-classical model based on the Floquet-Bloch formalism that describes the particles dynamics on a given Bloch band as well as the Landau-Zener tunneling to a different band. This allows to analyze the dynamics in the experimentally relevant case of a finite depth lattice and to get much more insight into the complicated atomic motion. We found that the reflections can be explained by the combination of adiabatic absorption/emissions of Floquet photons and of Bragg reflections on the edge of the Brillouin zone. Finally, we demonstrate the use of this technique with a bichromatic modulation to design a tunable sub-recoil velocity filter. The selectivity of this filter, on the order of 450μm/s is comparable to the one obtained with Raman velocity selection. Interestingly, such a filter can be transposed to all species since it does not rely on a specific internal level configuration. A possible extension of this work would be to combine the Bragg cavity with the modulation of the lattice depth which could act as a controlled outcoupling mechanism.

Résumé de la thèse

Conception et réalisation d'un ralentisseur Zeeman à aimants permanents

Le piège magnéto-optique (PMO) constitue une source d'atomes pre-refroidis utilisée comme point de départ dans la plupart des expériences sur les gaz quantiques dégénérés. Pour charger efficacement un PMO, il est nécessaire de l'alimenter avec un jet d'atomes ralentis à des vitesses de l'ordre de la dizaine de m/s. Le ralentisseur à effet Zeeman constitue l'un des dispositifs les plus utilisés pour fournir une telle source en ralentissant des jets thermiques. Ce type de ralentisseur nécessite la génération d'un champ magnétique inhomogène le long de l'axe de propagation du jet atomique. Le champ magnétique est habituellement produit par un courant circulant dans une bobine d'épaisseur variable qui enserre le jet atomique. Grâce à l'apparition des aimants NdFeB, il est aujourd'hui possible de générer le champ magnétique avec des aimants permanents de faÃ§on à simplifier le dispositif. Ce chapitre décrit la conception et la réalisation de deux ralentisseurs à effet Zeeman utilisant différentes configurations d'aimants.

Principe et caractéristiques du ralentisseur

Un ralentisseur à effet Zeeman utilise la pression de radiation exercée par un faisceau laser contrapropageant dont la fréquence est proche d'une résonance atomique. A résonance, l'accélération subie par un atome peut être très importante $a_{\max} = 1.1 \times 10^5$ m/s pour le ^{87}Rb. Elle permet d'amener au repos sur des distances inférieures au mètre des atomes initialement à des vitesses thermiques. Cependant, à cause de l'effet Doppler, la fréquence apparente de la transition atomique varie à mesure que l'atome est ralenti de sorte que le laser sort rapidement de résonance. Dans un ralentisseur à effet Zeeman, un champ magnétique inhomogène est ajouté de manière à ce que le décalage Zeeman compense partout le décalage Doppler.

Le champ magnétique inhomogène idéal a la forme suivante:

$$B(z) = B_{\mathrm{b}} + \Delta B \left(1 - \sqrt{1 - z/\ell}\right). \tag{7.16}$$

Les atomes dont la vitesse initiale est inférieure à la vitesse de capture $v_{\mathrm{c}} = \mu \Delta B/(\hbar k)$

sont ralentis jusqu'à une vitesse proche de zero. Un champ uniforme B_b peut être rajouté afin d'éviter des croisements de niveaux qui se situent autour de 100 G pour le ^{87}Rb. Nous utilisons pour générer la pression de radiation la transition cyclante $F = 2, m_F = -2 \rightarrow F' = 3, m_{F'} = -3$, qui correspond au choix d'un champ magnétique croissant et d'une lumière polarisée σ^-. Les paramètres du ralentisseur sont récapitulés dans le tableau suivant:

ΔB	300 G
B_b	200 G
ℓ	1 m
v_c	330 m/s

Configuration *dipole*

La première configuration d'aimants dite *dipole* est directement inspirée de la référence [49]. Deux rangées d'aimants dont la magnétisation est orthogonale au jet atomique sont placées symétriquement de part et d'autre du tube du ralentisseur. Contrairement à la proposition d'Ovchninnikov, nous avons pris soin de minimiser la déviation du champ magnétique sur une section transverse du ralentisseur. Pour cela, il est favorable à la fois de ne pas placer les aimants trop près de l'axe du ralentisseur et d'utiliser des aimants allongés dans la direction transverse. En conséquence, nous utilisons des aimants de taille $100 \times 20 \times 5$ mm^3, placés à environs 10 cm de l'axe du ralentisseur. Plusieurs aimants peuvent être empilés afin d'augmenter le volume d'un élément de la rangée. Pour obtenir le profil de champ désiré, le nombre d'aimants empilés augmente progressivement le long du ralentisseur. Les éléments de la rangée sont séparés de 3 cm, le nombre d'aimants empilés étant discret, nous ajustons finement le champ en faisant varier faiblement la distance à l'axe de chaque élément. Une optimisation basée sur des calculs de champ 3D permet de fixer les positions et volumes de chaque élément de faÃ§on à approcher au mieux du champ ideal (7.16). Dans cette configuration, le champ magnétique varie de moins de 12 G sur une section de tube CF16.

D'un point de vue mécanique, nous avons construit une structure en aluminium de $1100 \times 100 \times 50$ mm^3 dans laquelle des sillons de 20 mm de largeur ont été fraisés à des profondeurs correspondant aux distances à l'axe de chaque élément. Les aimants sont insérés un à un dans ces sillons, puis bloqués sur les cotés et le dessus par des plaques de plexiglass vissées dans l'aluminium (voir FIG. 7.11). Afin que le champ magnétique du ralentisseur ne perturbe pas le PMO situé à sa sortie, un blindage magnétique est installé autour du ralentisseur Zeeman. Ce blindage réduit le champ résiduel au niveau du G dans la chambre PMO et augmente également le champ magnétique dans le ralentisseur Zeeman d'environ 100 G.

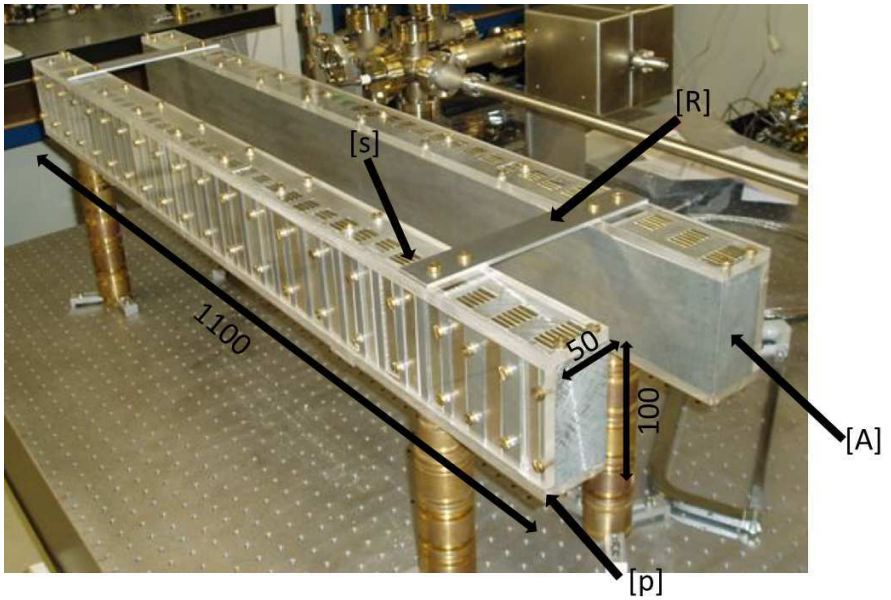

Figure 7.11: *Photo de la configuration dipole: [A] structure en aluminium, [s] sillons de profondeur variable, [p] protections en plexiglass, [R] plaques de renfort. Dimensions en* mm.

Caractérisation du jet atomique ralenti

Le jet atomique de rubidium est issu d'un four à recirculation chauffé à 130° C qui produit un jet effusif. Le jet est ensuite ralenti dans le ralentisseur Zeeman et détecté dans la chambre du PMO. La distribution des vitesses du jet ralenti est mesurée par fluorescence et par absorption à l'aide d'une sonde à 45° C du jet atomique. Grâce à cet angle, l'absorption et la fluorescence dépendent de la vitesse du jet. En balayant la fréquence de la sonde, on obtient ainsi la distribution des vitesses du jet. Dans cette configuration d'aimants, nous obtenons un simple pic dont la vitesse peut être ajustée en variant la fréquence du faisceau ralentisseur. Nous obtenons des flux atomiques $\Phi = 4 \times 10^{10}$ atomes/s à 30 m/s, ce qui est largement suffisant pour charger efficacement un PMO.

Cette configuration d'aimants, satisfaisante en terme de flux atomique présente néanmoins le défaut d'être relativement encombrante. De plus, à cause de la nature transverse du champ magnétique, il est difficile d'annuler totalement le champ de fuite au niveau du PMO. Nous avons donc développé une deuxième configuration plus élégante qui permet d'utiliser un volume d'aimant plus faible.

Configuration *Halbach*

Afin d'obtenir une bonne homogénéité transverse à moindre coÃ»t (sans utiliser des aimants très éloignés de l'axe), nous utilisons une configuration dite de Halbach dans

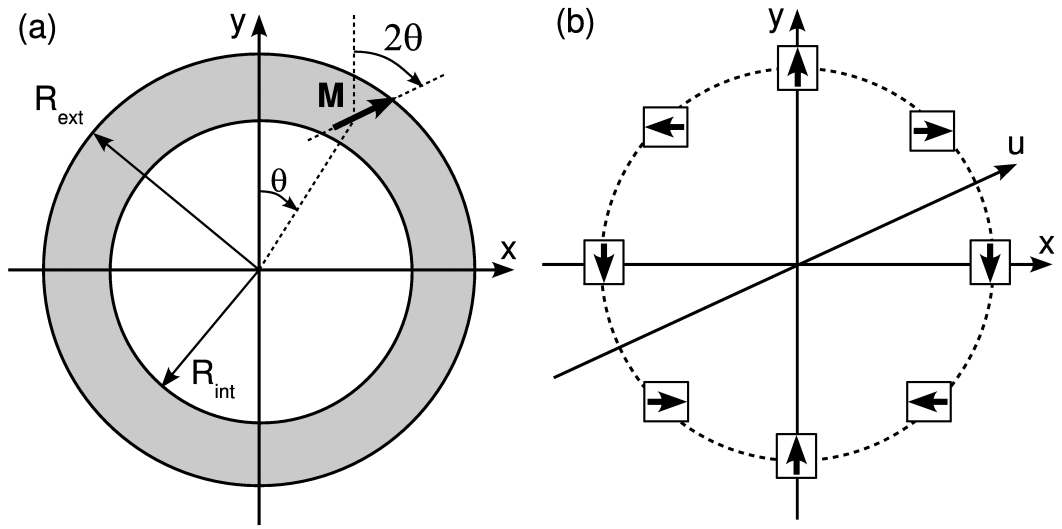

Figure 7.12: *(a) Notations du cylindre de Halbach. (b) Section transverse montrant l'approximation octupolaire de la configuration de Halbach.*

laquelle les aimants sont positionnés tout autour de l'axe. Le cas idéal du cylindre de Halbach correspond à un anneau infini dans la direction z et où, en un point de l'anneau qui fait un angle θ avec l'axe y, la magnétisation $\boldsymbol{M}$ forme un angle 2θ (voir FIG. 7.12 (a)). Le champ produit est alors transverse et homogène à l'intérieur de l'anneau et nul en dehors avec:

$$\boldsymbol{B}_{\mathrm{Hal}}(\boldsymbol{r}) = \begin{cases} \mathbf{0} & \text{for} \quad r > R_{\mathrm{ext}}, \\ B_{\mathrm{R}} \ln\left(\dfrac{R_{\mathrm{ext}}}{R_{\mathrm{int}}}\right) \hat{\boldsymbol{y}} & \text{for} \quad r < R_{\mathrm{int}}, \end{cases}$$

où B_{R} est le champ rémanent du matériau magnétique, et R_{int} et R_{ext} sont les dimensions du cylindre de Halbach.

Notre configuration correspond à une approximation octupolaire du cylindre de Halbach constitué de 8 aimants positionnés sur un cercle de rayon variable d autour du jet atomique et dont l'axe tourne conformément à la prescription de Halbach(voir FIG. 7.12 (b)). Nous utilisons des aimants allongés $6 \times 6 \times 148$ mm^3 dont la magnétisation est orthogonale au grand axe. Afin de varier longitudinalement l'amplitude du champ magnétique, la distance à l'axe d diminue progressivement. Pour garder une construction très simple, nous avons choisi de faire varier la distance à l'axe linéairement. Il est alors possible de trouver un pente qui produit un champ magnétique très proche du profil idéal.

Le montage mécanique est le suivant: (voir FIG. 7.13) les aimants sont insérés dans 8 longs profils en aluminium en forme de U, chaque profil glisse dans un des trous disposés en cercle de neuf montures ayant un rayon du cercle décroissant. Chaque monture peut être séparée en deux pour être montée autour du tube du

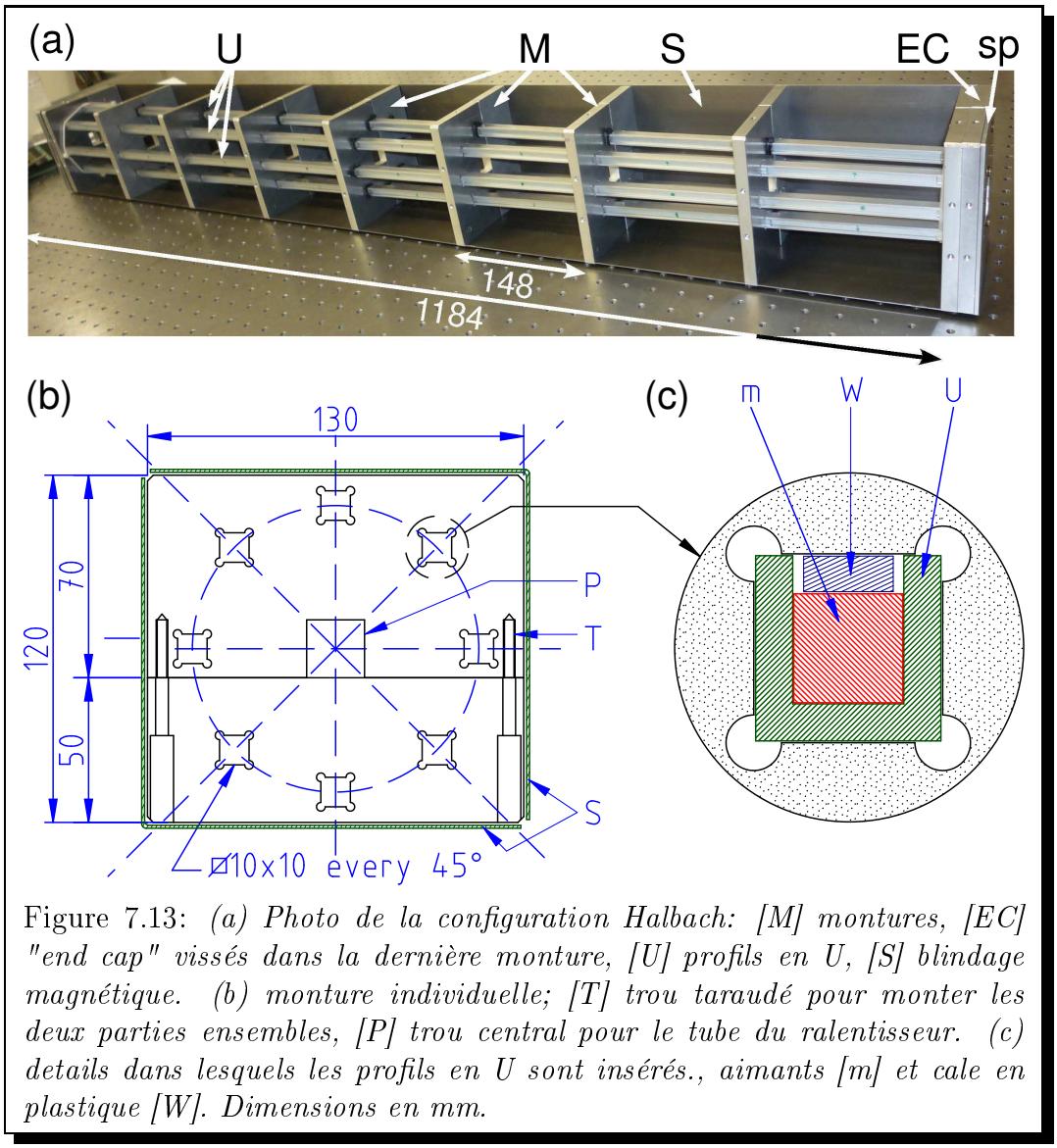

Figure 7.13: *(a) Photo de la configuration Halbach: [M] montures, [EC] "end cap" vissés dans la dernière monture, [U] profils en U, [S] blindage magnétique. (b) monture individuelle; [T] trou taraudé pour monter les deux parties ensembles, [P] trou central pour le tube du ralentisseur. (c) details dans lesquels les profils en U sont insérés., aimants [m] et cale en plastique [W]. Dimensions en mm.*

ralentisseur. Le résultat est à la fois robuste et léger.

Un blindage magnétique est ajouté autour de la structure pour réduire le champ de fuite, comme le champ à l'extérieur d'un cylindre de Halbach est nul, le blindage magnétique a cette fois très peu d'effet sur le profil de champ à l'intérieur du ralentisseur.

La mesure du champ magnétique produit montre que celui-ci varie de moins de 1 G sur une section transverse et est très lisse longitudinalement. Le champ résiduel au niveau de la chambre du PMO est trop faible pout être mesurable avec notre sonde à effet Hall.

Performances et puissances laser

Ce ralentisseur offre des performances très similaires au premier,*i.e*, un flux atomique $\Phi = 3 \times 10^{10}$ atomes/s à 30 m/s.

Une différence importante des ralentisseurs présentés ici par rapport aux ralentisseurs Zeeman conventionnels est que le champ magnétique est orthogonal au jet atomique. La polarisation de la lumière de refroidissement possède alors nécessairement une composante σ^+ dont l'effet est de dépomper les atomes vers l'état fondamental $F = 1$. Il est donc indispensable d'utiliser un deuxième laser repompeur sur la transition $F = 1 \rightarrow F' = 2$.

On peut néanmoins s'attendre à avoir besoin d'une puissance très limitée, or plusieurs dizaines de mW de puissance repompeur, correspondant à une intensité de 24 mW/cm^2 bien supérieure à l'intensité de saturation de la transition repompeur, sont nécessaires pour obtenir un flux maximal. Pour en comprendre l'origine, nous avons étudié l'efficacité du ralentisseur en fonction de la fréquence et de la polarisation du laser repompeur. Nous observons en fonction de la polarisation du repompeur différents spectres faisant apparaître plusieurs résonances. Ceci signifie que plusieurs chemin de dépompage sont impliqués, probablement à différentes positions dans le ralentisseur. A cause du grand nombre d'états internes impliqués (24 au total), il n'est pas aisé d'avoir une description simple des mécanismes de dépompage. Néanmoins, en balayant rapidement la fréquence du repompeur autour de la transition $F = 1 \rightarrow F' = 2$, il est possible d'obtenir un flux atomique légèrement plus important qu'avec une fréquence fixe en utilisant moins de 10 mW de puissance repompeur.

Finalement, nous démontrons l'efficacité du ralentisseur en chargeant un PMO d'environ 3×10^{10} atomes en moins d'une seconde.

Ce ralentisseur à effet Zeeman possède un certain nombre d'avantages comparé à un ralentisseur conventionnel:

- il ne nécessite pas de courant électrique ni de refroidissement à eau,
- il est facile à assembler sans ouvrir l'enceinte à vide,
- il est léger et facile à construire,
- il produit un champ très lisse sans champ de fuite.

Production de condensats de Rubidium

La condensation de Bose-Einstein se produit lorsque les longueurs d'onde de de Broglie des différents atomes d'un gaz se recouvrent. Ceci correspond à une densité dans l'espace des phases $\rho = n\lambda_T^3$ de l'ordre de 1. Pour atteindre la condensation, il est donc nécessaire d'augmenter la densité et de réduire la température du gaz atomique. Un nuage de Rubidium est d'abord capturé dans un piège magnéto-optique; la

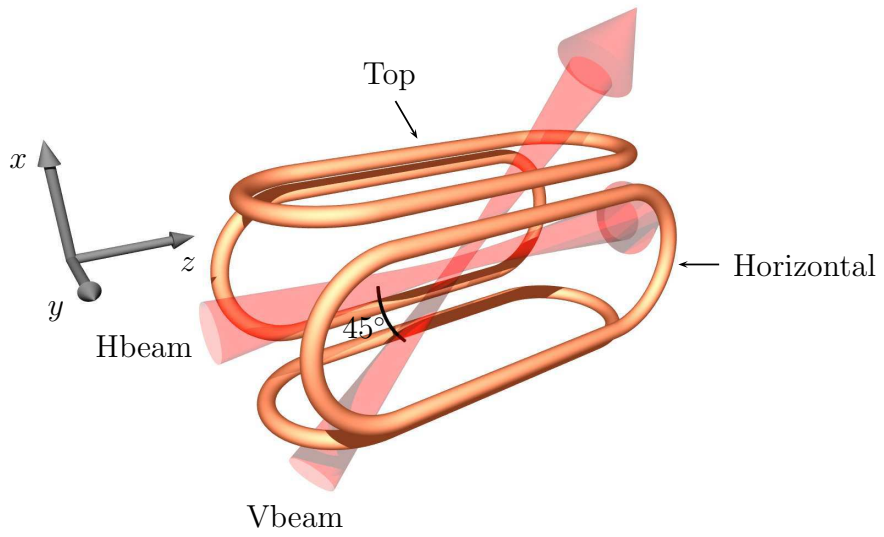

Figure 7.14: *Schéma du piège dipolaire croisé et des faisceaux PMO. Une des bobines du PMO (la bobine "Top" ou la bobine "Horizontal") est aussi utilisée pour effectuer la distillation de spin.*

température dans le PMO est typiquement de l'ordre de la centaine de μK, et la densité, limitée par la diffusion multiple des photons est de l'ordre de 10^{10} atomes/cm^3. La densité dans l'espace des phases est alors de l'ordre de $\rho \sim 10^{-7}$, loin de la limite de condensation. Le nuage est ensuite transféré dans un piège dipolaire croisé produit par deux faisceaux lasers désacordés vers le rouge à 1064 nm, un faisceau *guide* horizontal et un faisceau dit vertical à 45° (voir FIG. 7.14). L'augmentation de la densité dans le piège conservatif amène la densité dans l'espace des phase dans le domaine $\rho \sim 10^{-3}$. Pour gagner les trois ordres de grandeur qui séparent de la condensation, le nuage atomique est refroidi par évaporation forcée: la profondeur du piège est réduite progressivement en diminuant l'intensité du faisceau dipolaire *guide*.

Piege dipolaire et évaporation

L'allure du piège croisé varie au cours de l'évaporation. Initialement, le faisceau horizontal domine, le piège, et donc le nuage atomique sont très allongé dans la direction du guide. En l'absence de faisceau vertical, la fréquence du piège selon l'axe du guide est très faible et ne permet pas de mener l'évaporation à terme. A mesure que l'évaporation progresse, la contribution du faisceau vertical devient de plus en plus importante et, la température diminuant, les atomes sont piégés à l'intersection des deux faisceaux. Le nuage est alors beaucoup plus isotrope. A la fin de l'évaporation, les fréquences du piège sont de l'ordre de 100 Hz dans la direction du faisceau vertical et 200 Hz dans les deux autres directions.

Afin de réaliser l'évaporation forcée de manière efficace, il convient de réduire la

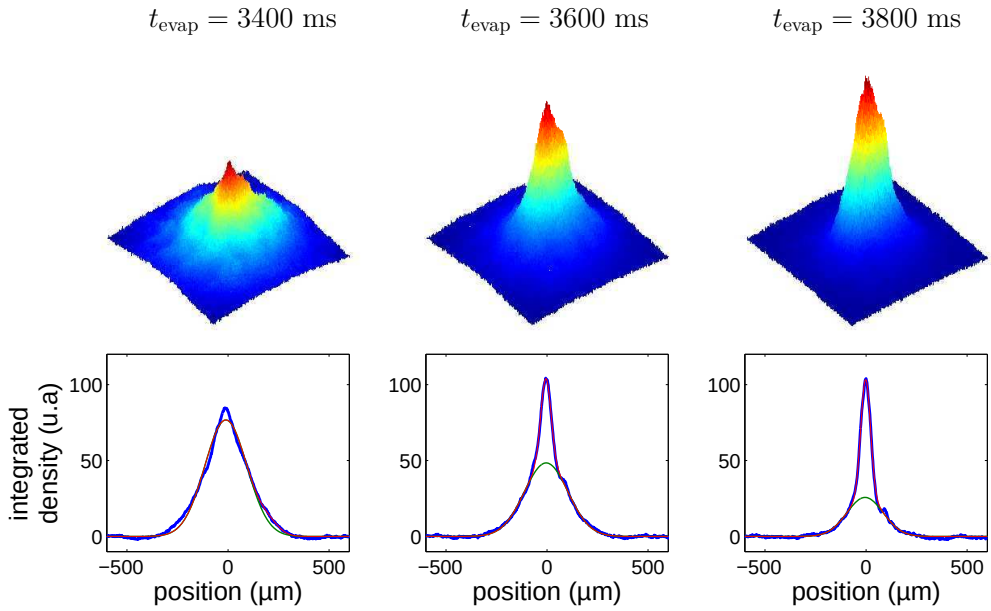

Figure 7.15: *Haut: densité atomique après un temps de vol de 15 ms pour différents temps d'évaporation autour de la condensation; un pic étroit apparaît à la limite de condensation. Bas: densité intégrée selon une direction, le profil de densité est ajusté par une double Gaussienne. La largeur de la Gaussienne la plus large est une mesure de la température du gaz tandis que le poids relatif des Gaussiennes indique la fraction condensée.*

profondeur du puits de potentiel suffisamment lentement par rapport au temps de thermalisation du gaz mais suffisamment rapidement par rapport au temps caractéristique des pertes atomiques. Dans notre piège, les pertes sont dominées par des pertes assistées par la lumière qui sont donc plus importantes en début d'évaporation lorsque l'intensité des faisceaux dipolaires est la plus importante. Le temps de vie dans le piège varie selon l'intensité de une seconde au début de l'évaporation à une dizaine de secondes à la fin de la rampe d'évaporation. Nous diminuons donc initialement rapidement la profondeur du piège pour éviter des pertes trop importantes, puis moins rapidement à la fin de l'évaporation afin de bénéficier d'une meilleure thermalisation. La puissance du faisceau guide est ainsi diminuée de la manière suivante:

$$P_{\mathrm{h}}(t) = P_0 \left(1 + t/\tau_{\mathrm{evap}}\right)^{-4}, \tag{7.17}$$

avec un temps caractéristique $\tau_{\mathrm{evap}} = 1300$ ms. Après environ 3.5 s d'évaporation, un condensat apparaît pour des températures de l'ordre de 150 nK.

Condensation

La condensation de Bose-Einstein est facilement identifiable par deux signaux caractéristiques. (i) La dispersion des vitesses du nuage possède une double structure; la

fraction d'atomes condensée forme un pic étroit entouré d'un nuage thermique plus large. (ii) La partie condensée subit une inversion d'ellipticité lors d'un temps de vol. En effet, la distribution des vitesses de la partie condensée dépend directement des caractéristiques du piège et reflète ici son anisotropie.

Le piège dipolaire n'étant pas sensible à l'état magnétique, les condensats obtenus sont *a priori* des condensats de spineurs. Pour pouvoir choisir l'état magnétique dans lequel les atomes condensent, nous utilisons la technique de distillation de spin qui consiste à ajouter un gradient de champ magnétique à l'aide d'une bobine du PMO. La forme du piège dépend alors du sous-état Zeeman, les atomes qui ressentent un puits de potentiel moins profond sont évaporés préférentiellement. En thermalisant avec les autres atomes, le gaz est refroidi par refroidissement sympathique. Il est alors possible d'obtenir des condensats presque purs de typiquement 50000 atomes dans un état de spin arbitraire.

Mise en place et caractérisation du réseau optique

Un réseau optique est formé par le croisement dans une région de l'espace de deux faisceaux optique cohérents. Si les lasers utilisés sont désaccordés par rapport à une transition atomique, l'onde stationnaire qui en résulte produit un potentiel dipolaire qui varie sur des distances de l'ordre de la longueur d'onde optique. Les réseaux optiques sont largement utilisés dans la communauté des atomes froids. Ils permettent de créer des potentiels très flexibles:

- En terme de dimensionnalité : en superposant des ondes stationnaires selon différentes directions de l'espace, il est possible de créer des réseaux à 1, 2 ou 3 dimensions. La dimensionnalité d'un problème peut alors être réduite si le mouvement atomique est gelé selon une direction.
- La géométrie est également modifiable en faisant varier la direction, l'intensité ou la phase des faisceaux qui interfèrent.
- Les potentiels dipolaire sont modulables dans le temps rapidement et facilement.

Les réseaux optiques sont utilisés d'une part dans des expériences visant à simuler des problèmes de matière condensée, la périodicité du potentiel reproduit alors le potentiel périodique produit par les ions d'un cristal, et d'autre part pour étudier des questions de transport quantique comme dans notre cas.

Mise en place

Le réseau optique est issue d'un laser à 850 nm installé sur une table indépendante sur laquelle la puissance du faisceau est controllé. Le faisceau est ensuite divisé en deux et mis en forme sur la table principale. Les deux faisceaux sont croisés

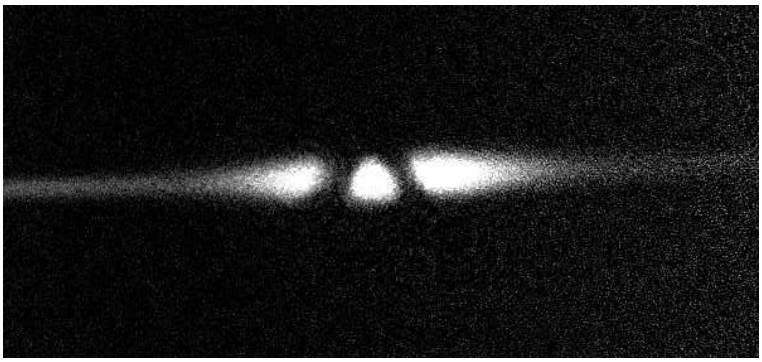

Figure 7.16: *Image par absorption des atomes dans le piège dipolaire. Avant de prendre une image, un faisceau dépompeur, superposé aux bras du réseau, est allumé pendant 1 ms pour dépomper localement les atomes. Les bras du réseau apparaissent alors comme des trous dans la distribution atomique.*

au niveau du nuage atomique avec un angle de 80°. Le profil d'intensité obtenue correspond à un potentiel périodique de période $d = 650$ nm dans la direction du guide et qui possède une envelope Gaussienne ayant un waist de 150 μm. Afin de bénéficier d'un contrôle fin sur le croisement des deux faisceaux, nous avons installé après les lentilles de collimation, des lames de verre épaisses qui dévient légèrement chaque faisceau d'une distance qui dépend de l'angle entre le faisceau incident et la lame. La précision obtenue par cette méthode est plus importante d'un facteur cent par rapport à la précision obtenue en faisant varier l'angle du dernier miroir.

Lors de la procédure de croisement, nous utilisons une séquence d'imagerie particulière afin de visualiser la position des faisceaux. Un faisceau résonant à 780 nm est superposé aux faisceaux du réseau, sa fréquence est stabilisée sur une transition dépompeur $F = 2 \rightarrow F' = 2$. Nous lanÃ§ons une séquence d'évaporation typique en l'arrêtant très tôt à 100 ms d'évaporation. Le nuage atomique est alors très allongé et marque la position du guide. Le laser dépompeur superposé au bras du réseau est allumé pendant 1 ms pour dépomper localement les atomes juste avant de prendre une image par absorption. La position des bras du réseau apparaît alors sur l'image par absorption comme un trou dans le nuage atomique (voir FIG. 7.16). Ceci permet de croiser précisément les deux bras du réseau avec le guide.

Calibration

Il est important de calibrer la profondeur du réseau obtenue grâce à une mesure directe sur les atomes. Nous utilisons pour cela la technique de diffraction de Kapitza-Dirac. Cette technique consiste à allumer pendant un temps très court le réseau optique sur le nuage atomique. Les atomes redistribuent alors les photons entre les deux modes laser par des processus d'absoprtion/emission stimulé. Ce faisant, l'impulsion est modifiée d'une quantité liée à la périodicité du réseau. La figure de

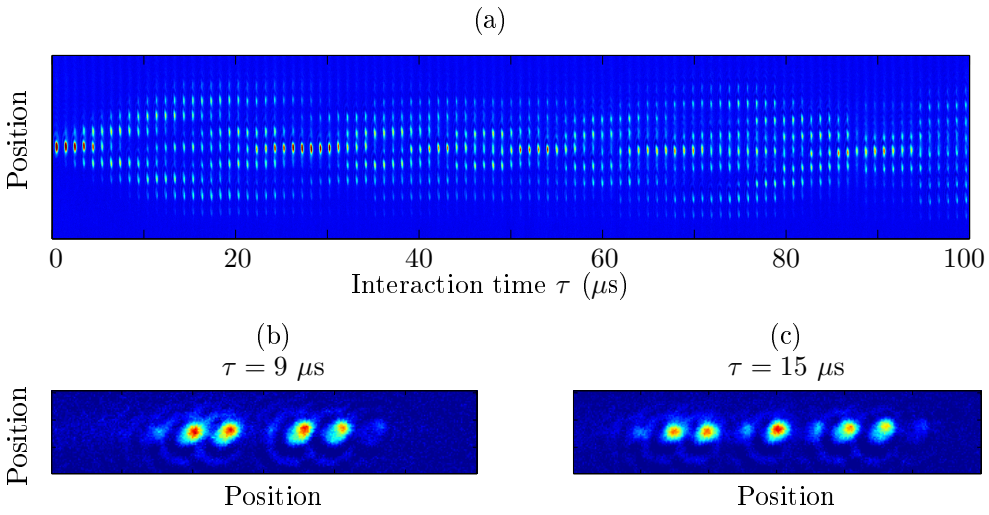

Figure 7.17: *Motifs de diffraction avec 48 mW par bras du réseau. (a) Motifs de diffraction concaténés pour différents temps d'interaction τ. (b) et (c) Motifs de diffraction à $\tau = 9$ et 15 μs respectivement.*

diffraction qui en résulte renseigne directement sur la profondeur du réseau optique (voir FIG. 7.17).

Dans le régime de temps d'interaction court dit de Raman-Nath, il est possible de calculer exactement le poids des différents ordres de diffraction en fonction de la profondeur du réseau et du temps d'interaction. Les poids relatifs correspondent aux carrés des fonctions de Bessel successives. En mesurant en fonction du temps d'interaction, le poids relatif des ordres de diffraction, il est alors possible de déduire précisément la profondeur du réseau optique.

Nous parvenons ainsi à réaliser et à calibrer des réseaux optique d'une profondeur maximale $U_0 = 17E_\mathrm{L}$, limitée par la puissance disponible du laser à 850 nm.

Outils théoriques pour les réseaux

Ce chapitre rappelle quelques outils utiles pour décrire le comportement d'une particule quantique dans un potentiel périodique: le théorème de Bloch et les résultats sur l'équation de Mathieu. Les solutions de l'équation de Mathieu sont ensuite utilisées pour analyser la diffusion d'une particule sur un réseau semi-infini.

Théorème de Bloch

Le théorème de Bloch donne la forme des solutions de l'équation de Schrödinger stationnaire pour un potentiel périodique. Les solutions peuvent être écrites comme

le produit d'une onde plane et d'une fonction périodique

$$\psi_{n,k}(x) = e^{ikz} u_{n,k}(z) \qquad \text{avec} \qquad u_{n,k}(z+d) = u_{n,k}(z), \tag{7.18}$$

où n est l'indice de bande et k la pseudo-impulsion. Les énergies sont regroupées en bandes indexées par n. Entre chaque bande, un gap est ouvert. La périodicité du potentiel et des fonctions de Bloch $u_{n,k}(z)$ rend la recherche des états et énergies propres facile. En développant, pour chaque pseudo-impulsion, l'équation de Schrödinger sur la base de Fourier, l'équation de Schrödinger se réécrit comme un problème d'inversion d'une matrice diagonale facile à résoudre numériquement. La détermination des états propres associés à chaque bande montre que ceux-ci sont reliés aux états liés dans un site isolé du réseau.

Equation de Mathieu

Le théorème de Bloch ne s'intéresse qu'aux états propres de l'Hamiltonien périodique. Cependant, ces états ne sont pas les seuls états utiles pour décrire par exemple les problèmes de diffusion sur un réseau. Considérons des solutions de l'équation de Schrödinger dépendante du temps du type

$$\psi(x,t) = e^{-iEt/\hbar} \phi(x), \tag{7.19}$$

où E est une énergie *choisie* (qui correspond à l'énergie d'une particule incidente dans le cas d'une diffusion). La fonction ϕ n'est ici pas nécessairement normée de sorte que ψ ne représente pas toujours un état propre de l'Hamiltonien. En injectant ces solutions dans l'équation de Schrödinger, on retrouve l'équation stationnaire, cependant celle-ci a un sens différent. Ce n'est plus une équation aux valeurs propres mais une simple équation différentielle où E correspond à une condition aux limites. Cette équation peut être mise sous la forme d'une équation de Mathieu

$$\frac{\mathrm{d}^2\phi}{\mathrm{d}\tilde{z}^2} + (a - 2q\cos(2\tilde{z}))\,\phi = 0, \tag{7.20}$$

dont les solutions sont bien connues et s'écrivent comme une superposition linéaire de deux états du type

$$f(z) = e^{ikz} p(z), \tag{7.21}$$

où $p(z)$ est une fonction périodique et où l'exposant caractéristique k est éventuellement imaginaire (alors que k est toujours réel dans le cadre du théorème de Bloch).

Les solutions de l'équation de Mathieu sont de deux types, les solutions stables pour lesquelles k est réel et qui correspondent exactement aux états de Bloch, et les solutions instables pour lesquelles k a une partie imaginaire. Les solutions sont stables (instables) si l'énergie *choisie* se situe dans une bande autorisée (un

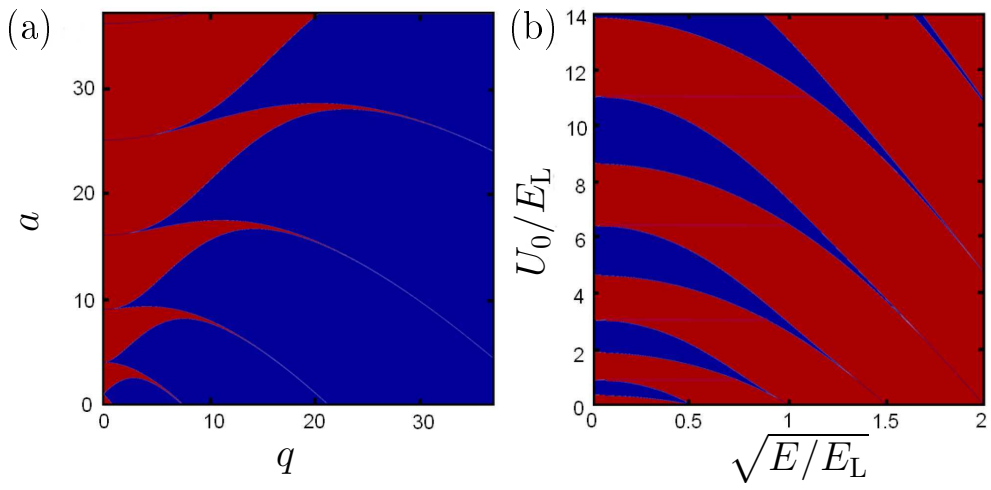

Figure 7.18: *Diagramme de stabilité de l'équation de Mathieu. Les régions stables (instables) sont indiquées en rouge (bleu). (a) diagramme en fonction des paramètres canoniques de l'équation de Mathieu. (b) Diagramme en fonction des paramètres pertinents dans l'équation de Schrödinger dans un réseau.*

gap) du diagramme de bande. Les solutions instables sont des ondes évanescentes qui s'atténuent sur une distance fixée par la partie imaginaire de k. La figure 7.18 présente les régions de stabilité en fonction des paramètres (a, q) et (E, U_0) qui interviennent respectivement dans l'équation de Mathieu et dans l'équation de Schrödinger.

Il est possible de trouver une solution analytique de l'exposant caractéristique en utilisant une méthode développé par Whittaker et s'appuyant sur l'analyse complexe. On trouve pour un réseau sinusoidal de profondeur U_0:

$$\cos(2\pi k/k_L) = 1 - \Delta(0)(1 - \cos(2\pi\sqrt{\kappa})), \tag{7.22}$$

où $\kappa = (U_0/2 + E)/E_L$.

Interprétation pour une expérience de diffusion

Considérons le cas d'une particule qui diffuse sur un réseau semi-infini de profondeur homogène. Dans l'espace libre, les états propres sont des ondes planes, dans le réseau les solutions de l'équation de Schrödinger sont les solutions de Mathieu. Pour connecter les fonctions d'onde à l'interface, les énergie dans le réseau et l'espace libre doivent être égales. L'exposant caractéristique de Mathieu est alors déterminé de manière univoque par l'énergie incidente. Si l'exposant de Mathieu possède une partie imaginaire non nulle, les solutions sont des ondes évanescentes et la transmission est nulle. Une onde plane ne peut se propager que si l'énergie incidente est dans une bande autorisée. Lorsque k est réel, les solutions de Mathieu sont les états propres de l'Hamiltonien périodique. Les conditions de continuité de la fonction d'onde et

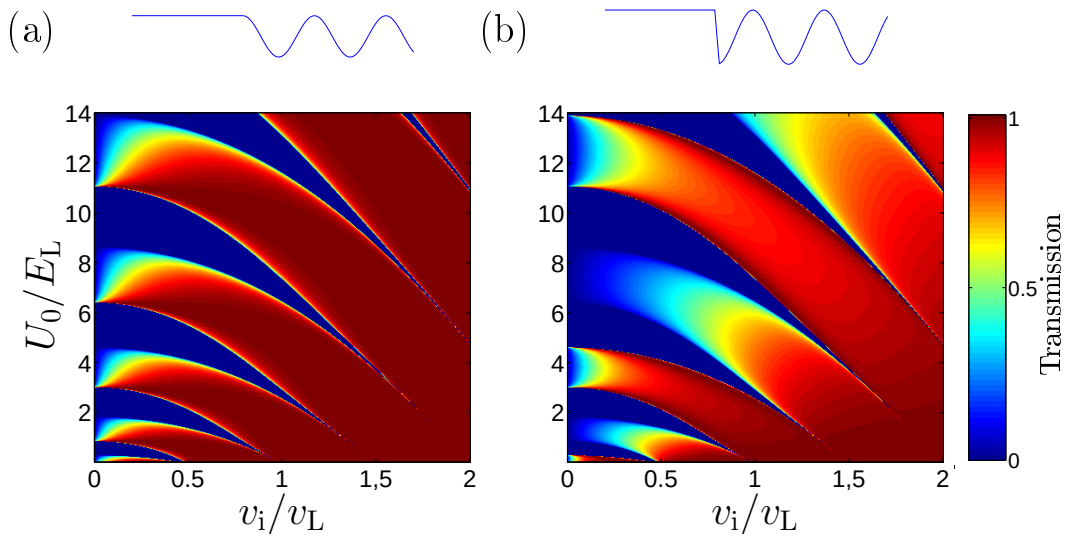

Figure 7.19: *Coefficient de transmission T à travers un réseau semi-infini. (a) L'interface est situé sur le bord d'un site du réseau, le potentiel n'a pas de discontinuité. (b) L'interface est situé au centre d'un site du réseau, le potentiel a alors une dicontinuité maximale. La réflection quantique est plus importante dans ce cas.*

de sa dérivé permettent alors de calculer un taux de transmission. Ici une réflection peut se produire essentiellement à cause de la réflection quantique sur les premiers puits. Le diagramme de transmission dépend donc fortement de la phase du réseau périodique à l'interface (voir FIG. 7.19).

Réflection de Bragg sur un réseau de taille fini

La réflection sur des structures diélectriques périodiques est un ingrédient omniprésent en optique. Elle permet par exemple la fabrication de miroirs de très haute réflectivité ou la fabrication de lasers en cavité étendue. En optique guidée, les réseaux de Bragg intégrés dans des fibres optiques servent à réaliser par exemple des multiplexeurs dans l'industrie des télécommunications ainsi que des coupleurs de sortie pour lasers à fibre de haute puissance. En analogie avec l'optique, ce chapitre décrit la réalisation d'un réflecteur de Bragg pour atomes en environnement guidé réalisé en envoyant des ondes de matière sur un réseau optique ayant une enveloppe Gaussienne.

Effet de l'enveloppe

A cause de l'enveloppe finie du réseau, lors de sa propagation, un atome d'énergie incidente E ressent des potentiels périodiques dont la profondeur varie de 0 loin du réseau à la profondeur maximale U_0 au centre. Il est possible d'analyser simplement la réflection; si à une certaine position dans le réseau, un atome pénètre dans une

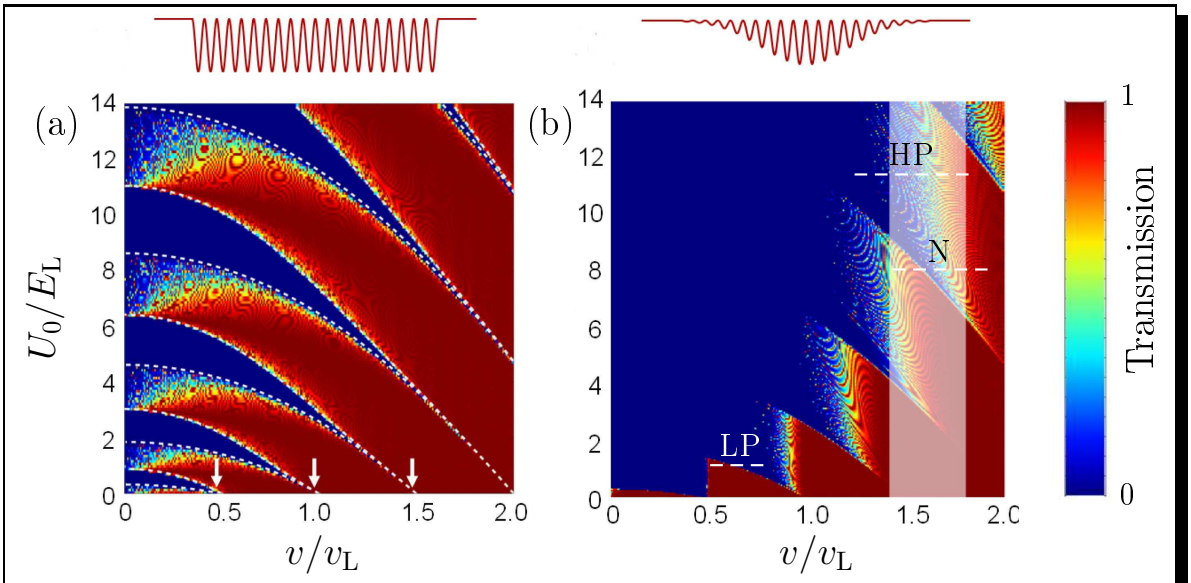

Figure 7.20: *Coefficient de transmission d'une onde plane à travers le réseau optique obtenue en intégrant l'équation de Schrödinger stationnaire. (a) Cas d'une enveloppe carrée. (b) Cas d'une enveloppe Gaussienne, U_0 est la profondeur maximale du réseau.LP, HP et N indiquent les régions de paramètres pour lesquelles le réseau agit comme un filtre respectivement passe-bas (LP), passe-haut (HP) et passe-bande (N).*

région instable de l'équation de Mathieu, il sera réfléchi à cette position particulière qui constitue un miroir de Bragg. En utilisant cet argument, le diagramme de transmission en fonction de la vitesse incidente et de la profondeur du réseau se déduit facilement du diagramme de stabilité de l'équation de Mathieu. Un atome est réfléchie si, pour une énergie donnée, il existe une profondeur inférieure à U_0 qui correspond à une région instable. Les domaines de réflection s'obtiennent alors en étendant vers le haut les régions instables du diagramme de stabilité. Dans cette image simple, le diagramme de transmission a alors une allure en dents de scie.

Le calcul du diagramme de transmission en intégrant l'équation de Schrödinger stationnaire confirme partiellement cette image. La transmission présente bien une structure en dents de scie, cependant, les zones de transmissions sont plus étendues que prévu (voir FIG. 7.20). Ceci est la conséquence de la taille finie de l'enveloppe du réseau, les régions instables de l'équation de Mathieu ont une extension spatiale finie; si la taille de ce gap est plus petite que la distance sur laquelle l'onde évanescente de Mathieu s'atténue, un atome peut traverser la zone interdite. La taille des zones de transmission augmente alors dans les régions de vitesse incidente élevé pour lesquelles un particule rencontre des zones interdites petites.

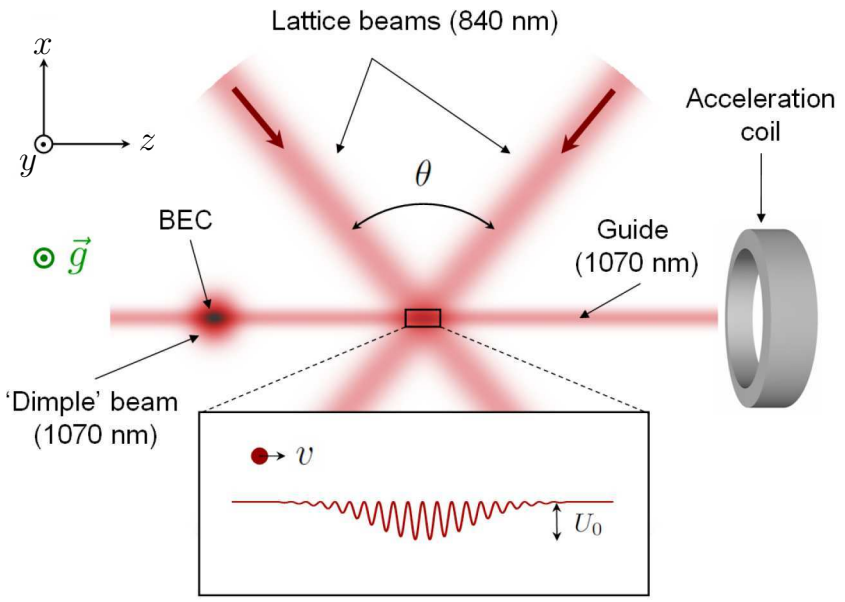

Figure 7.21: *Schéma du dispositif expérimental.*

Preparation du paquet d'onde

La première étape de l'expérience consiste à découpler un condensat de Bose-Einstein dans le guide et à l'accélérer jusqu'à la vitesse désirée. Afin de minimiser la dispersion des vitesses, de l'onde de matière produite, nous effectuons une décompression adiabatique du piège en diminuant progressivement l'intensité du faisceau vertical. Ceci permet de réduire le potentiel chimique du condensat qui est à l'origine de l'essentiel de la dispersion des vitesses de l'onde de matière. Cette technique a des limites, en effet en dessous d'une certaine intensité, des atomes quittent le piège et se propagent dans le guide. Le découplage est donc divisé en deux étapes, pendant 80 ms, l'intensité du faisceau verticale est diminuée de manière adiabatique puis, le faisceau est coupé instantanément pour libérer les atomes dans le guide. Avec cette technique, des dispersions de vitesses $\Delta v \sim 1.3 - 1.7$ mm/s sont obtenues.

Les atomes sont ensuite accélérés en utilisant un gradient de champ magnétique. Dans cette expérience, nous utilisons des condensats dans l'état $F = 1, m_F = 0$ qui ne sont sensibles au champ magnétique qu'au deuxième ordre. Nous avons donc besoin d'utiliser des courants assez élevés de 320 A pendant 15 ms dans une bobine dont l'axe coincide avec l'axe du guide (voir FIG. 7.21). De cette manière, le paquet d'onde a une vitesse moyenne $\bar{v} = 11$ mm/s

Résultats expérimentaux

L'onde de matière est préparée à 500 μm du réseau et se propage vers celui-ci. En prenant des images à des temps variables et pour une profondeur de réseau fixé $U_0 = 11E_L$, on observe une séparation du paquet en deux parties, une partie transmise

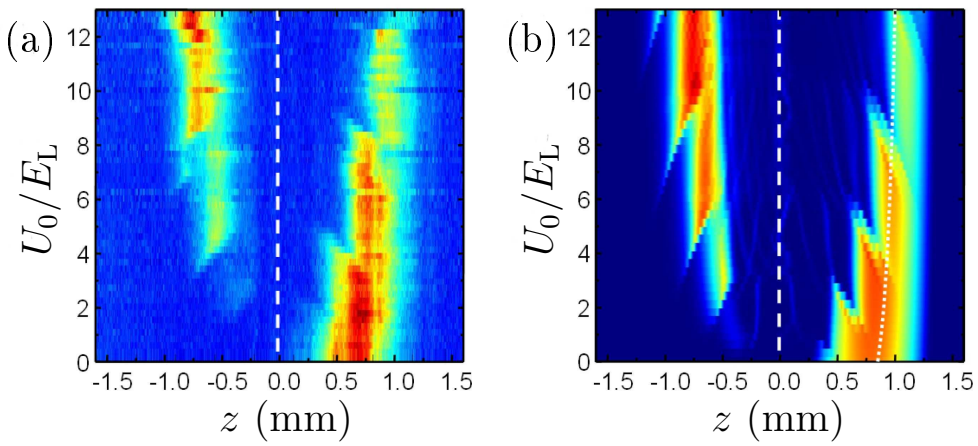

Figure 7.22: *(a) Expérience et (b) simulation numérique de la densité atomique en fonction de la position et de la profondeur du réseau après un temps de propagation de* 100 ms. *La ligne blanche indique la position du centre du réseau.*

qui correspond aux classes de vitesse les plus élevées, et une partie réfléchie. Afin de sonder le diagramme de transmission, nous laissons maintenant les atomes se propager pendant un temps long $t_{\text{prop}} = 100$ ms pour lequel tous les atomes ont fini d'interagir avec le réseau, et nous faisons varier la profondeur du réseau. Pour chaque profondeur, l'image est moyennée dans la direction transverse et les profils pour chaque profondeur sont ensuite regroupés. Le diagramme ainsi obtenu est séparé en une partie transmise (à droite) et une partie réfléchie (à gauche) (voir FIG. 7.22). La partie transmise présente un structure en dents de scie, et la partie réfléchie est son complémentaire. Ceci peut se comprendre facilement, en effet, pour un temps de propagation long, et en supposant que l'on peut négliger les effets de retard associés à la diffusion, il est possible d'associer chaque position dans la partie transmise du diagramme à une classe de vitesse de l'onde de matière initiale. La densité observée est alors la convolution de la transmission à travers le réseau par la distribution des vitesses initiale représentée en gris sur la figure 7.20. Selon les paramètres du réseau et du paquet d'onde initial, ce système peut donc réaliser différents types de filtres en vitesse, passe-haut, passe-bas ou passe-bande (voir FIG. 7.20).

Effets cavité

Pour expliquer l'essentiel des effets présentés ici, il n'est nécessaire de considérer qu'un miroir de Bragg. Cependant comme l'enveloppe du réseau est symétrique, il existe toujours deux miroirs de Bragg à des positions symétriques autour du centre du réseau. Ces miroirs peuvent alors former alors une cavité de Bragg. Les effets associés à cette cavité ne sont pas visibles dans l'expérience de diffusion. Cependant il est possible d'observer grâce aux simulations que lors d'une diffusion, un faible nombre d'atomes effectue des oscillations entre deux positions symétriques corre-

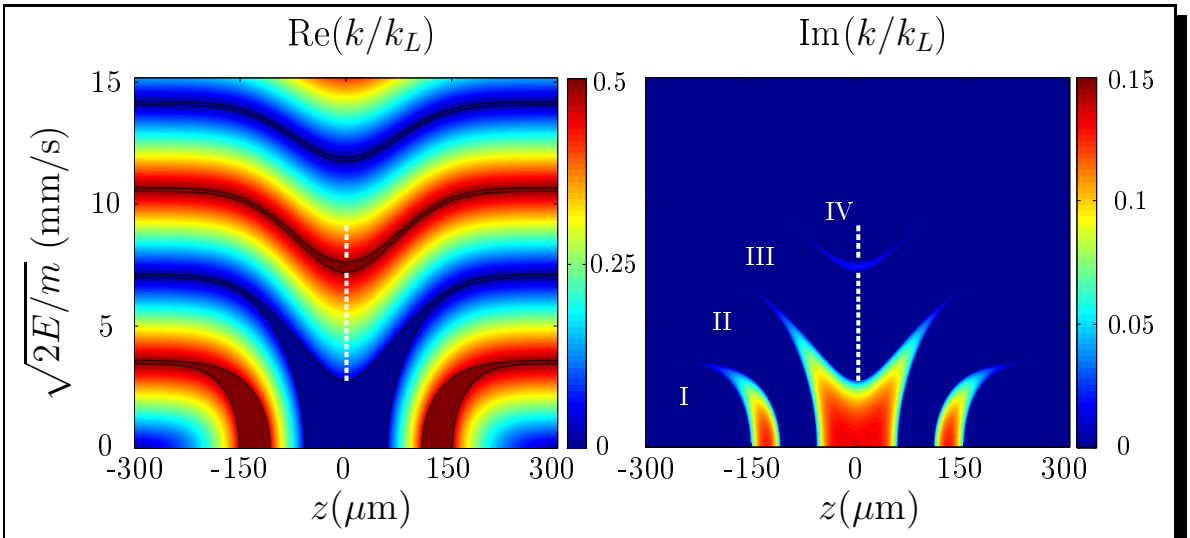

Figure 7.23: *Parties réelle et imaginaire de k avec $U_0/E_\mathrm{L} = 2.5$. Les régions où $\mathrm{Im}(k) \neq 0$ sont les gaps spatiaux qui correspondent à des solutions évanescentes. Les chiffres romains indiquent l'indice de bande. La ligne blanche représente la distribution initiale d'énergie (95 % des atomes).*

spondants aux miroirs de Bragg. A chaque réflection sur un des miroirs, une portion des atomes traverse le miroir et est découplée.

Réalisation d'une barrière tunnel à l'aide de gaps spatiaux

Structure de bande locale

Afin de comprendre la dynamique dans la cavité de Bragg, il est utile de présenter la structure de bande locale du réseau. A chaque position est associée une profondeur locale du réseau. L'exposant caractéristique des solutions de Mathieu dépend alors de l'énergie et de la position dans le réseau (voir FIG. 7.23). Cette structure fait apparaître des régions symétriques autour du centre du réseau où la partie imaginaire de l'exposant caractéristique est non nulle. Ces *gaps spatiaux* de taille finie séparent les différentes bandes autorisées. Certaines régions autorisées de ce diagramme sont entourées de deux gaps spatiaux et constituent alors des cavités de Bragg. Pour le diagramme présenté ici ($U_0 = 2.5E_\mathrm{L}$), ces régions correspondent aux bas de la troisième et de la quatrième bande.

A l'aide du modèle de gaps spatiaux, il est possible de calculer la probabilité de transmission à travers un gap d'une particule d'énergie E en intégrant l'exposant caractéristique:

$$T(E) = \exp\left(\int -2\mathrm{Im}[k(z,E)]\mathrm{d}z\right). \tag{7.23}$$

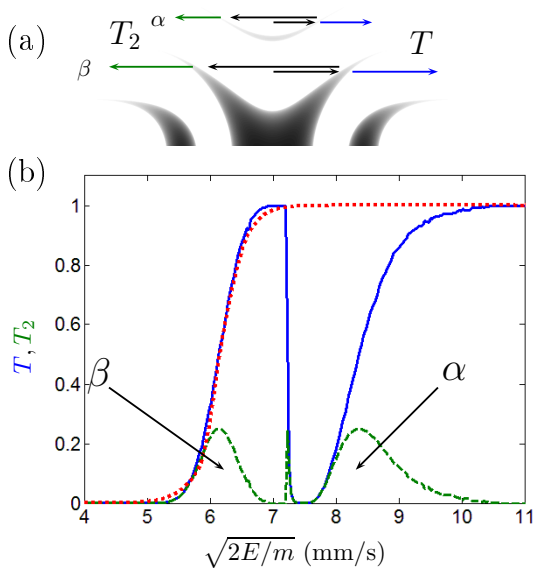

Figure 7.24: *(a) Schéma de l'évolution d'un paquet d'onde à l'intérieur du réseau et définition de T et T_2. (b) Probabilités de transmission. Ligne bleue continue: transmission à travers la moitié du réseau, les régions de réflection correspondent à des gaps spatiaux larges. Ligne rouge pointillé: Transmission à travers une barrière Gaussienne de variance $\sigma = 387$ nm. Tirets verts: probabilité de traverser par effet tunnel après une oscillation.*

La probabilité de transmission à travers la moitié du réseau présente en fonction de l'énergie une allure en forme de dents (voir FIG. 7.24). La transmission diminue lorsqu'un nouveau gap apparaît au centre du réseau. Il est aussi possible de calculer la probabilité pour une particule d'être réfléchie par un miroir de Bragg puis de traverser le miroir symétrique, $T_2 = T(E)(1-T(E))$. Cette probabilité présente des pics à chacune des marches de la transmission simple.

Il est intéressant de comparer les barrières tunnel obtenues grâce aux gaps spatiaux avec des barrières tunnel répulsives. Pour cela, on peut comparer la largeur des marches de transmission qui caractérise l'effet tunnel. Ici, la largeur de la première marche est équivalente à celle produites par une barrière répulsive de déviation standard $\sigma = 387$ nm. Une barrière si petite est complexe à mettre en place expérimentalement par exemple par des moyens optiques. Une barrière tunnel dans l'espace des position qui résulte d'une variation de l'enveloppe du réseau peut donc fournir une bonne alternative aux barrières répulsives.

Expérience

Afin d'obtenir un paquet d'onde initial dans un cavité de Bragg, il est nécessaire de charger les atomes sur une bande élevée du réseau. Pour la profondeur de réseau choisie $U_0 = 2.5E_\mathrm{L}$, les atomes doivent être chargés dans la troisième et la quatrième bande. Le condensat est préparé à la position du centre du réseau dans l'état magnétique $m_F = +1$. Les atomes sont ensuite découplés puis accélérés en 4 ms dans le guide jusqu'à $\bar{v} = 9.4$ mm/s en l'absence de réseau. Puis, le réseau est allumé adiabatiquement de faÃ§on à conserver l'indice de bande et la pseudo-impulsion. Les atomes se propagent ensuite pendant un temps variable.

La figure 7.25 montre la densité atomique le long du guide en fonction du temps de propagation. Les atomes sont dirigés initialement vers la droite du réseau. Une

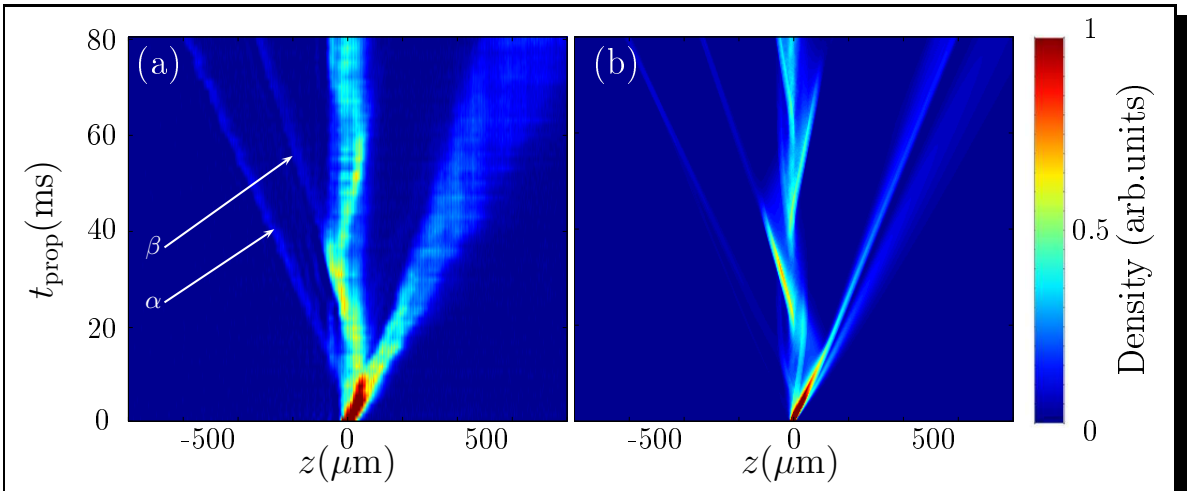

Figure 7.25: *(a) Profil de densité mesuré en fonction du temps de propagation. Chaque ligne est la moyenne de 4 images intégrées selon la direction transverse. (b) Intégration numérique de l'équation de Schrödinger pour les paramètres expérimentaux.*

partie des atomes, ceux qui ne rencontrent jamais de gap, quittent immédiatement le réseau. A l'intérieur du réseau, on observe ensuite des oscillations en forme "d'épines". Après quelques cycles, ces oscillations sont brouillées. Des paquets d'un petit nombre d'atomes correspondant à des classes de vitesse bien déterminées sont émis à chaque fois que les atomes sont réfléchis sur un miroir de Bragg. Deux paquets α et β qui correspondent à des atomes initialement sur la quatrième et la troisième bande respectivement sont successivement découplés.

Les paquets d'atomes découplés correspondent aux atomes qui ont été réfléchis par le premier miroir de Bragg puis sont passés par effet tunnel à travers le second. Les vitesses mesurées de ces paquets correspondent aux pics de la probabilité T_2 prédits par le modèle de bandes locales (voir FIG. 7.24).

Déphasage des différentes composantes de vitesse

Les différentes composantes de vitesse ne se déplacent pas à la même vitesse à l'intérieur du réseau, les composantes d'énergie plus élevés se propageant plus vite. De plus, la taille de la cavité de Bragg augmente avec l'énergie. Pour une envelope Gaussienne, le second effet est plus important, de sorte que la période d'oscillation augmente avec l'énergie. Cet effet dispersif limite le nombre d'oscillations visibles. Comme les deux effets sont opposés, il est néanmoins théoriquement possible de modifier l'envelope du réseau de faÃ§on à ce que la variation avec l'énergie de la taille de la cavité compense exactement la variation de vitesse de groupe. Une

envelope modifiée du type:

$$U(z) = -U_0 \exp(-2z^2/w^2) \left(1 + \frac{z^2}{D^2}\right), \tag{7.24}$$

avec $D = 112$ μm, permet ainsi d'annuler les effets de dispersion au premier ordre. Une telle envelope peut être obtenue par exemple grâce à des plaques holographiques. Ceci permettraient d'observer plus d'oscillations à l'intérieur de la cavité et de mieux localiser les paquets d'onde émis.

Diffusion sur un réseau modulé en amplitude

La diffusion d'ondes de matière sur un réseau optique permet de réaliser différents types de filtres en vitesse. Cependant, les caractéristiques de ces filtres sont directement liées à la taille d'un site du réseau, et sont donc peu modifiables. Nous allons voir qu'il est possible d'apporter beaucoup de flexibilité en modulant l'amplitude du réseau.

L'expérience

De faÃ§on similaire à l'expérience de la section 7.7, les atomes sont accélérés vers un réseau d'envelope Gaussienne. L'amplitude du réseau est cette fois modulée à des fréquences de l'ordre de la dizaine de kHz. Nous étudions ici la transmission à travers le réseau en fonction de la fréquence de modulation, pour une profondeur moyenne fixée $U_0 = 2E_\mathrm{L}$. De nouveau, le temps de propagation, $t_\mathrm{prop} = 78$ ms est tel que tous les atomes ont fini d'interagir avec le réseau et qu'il est possible d'associer position finale et vitesse initiale. La figure 7.26 présente les profils de densité obtenus en fonction de la fréquence de modulation.

On observe dans la partie transmise différentes déplétions dont la position varie en fonction de la fréquence de modulation. Certaines de ces lignes de déplétion ont un symétrique dans la partie réfléchie et correspondent à la réflection de certaines classes de vitesse. La ligne rouge (voir Fig. 7.26) n'as pas de symétrique, elle correspond à des classes de vitesse accélérées par la modulation.

Modèle de transitions interbandes

Afin de comprendre l'origine des lignes de déplétion, nous présentons d'abord un modèle simple basé sur des transitions interbandes dans la limite d'un réseau d'amplitude nulle. Une particule incidente entre sur une bande donnée avec une pseudo-impulsion fixée par son énergie. Supposons maintenant que la modulation d'amplitude provoque des transitions interbandes. A cause des symétries du potentiel périodique, ces transitions conservent la pseudo-impulsion et sont donc verticales dans le diagramme de bande. Dans la limite de profondeur nulle, la structure de bande n'est rien d'autre

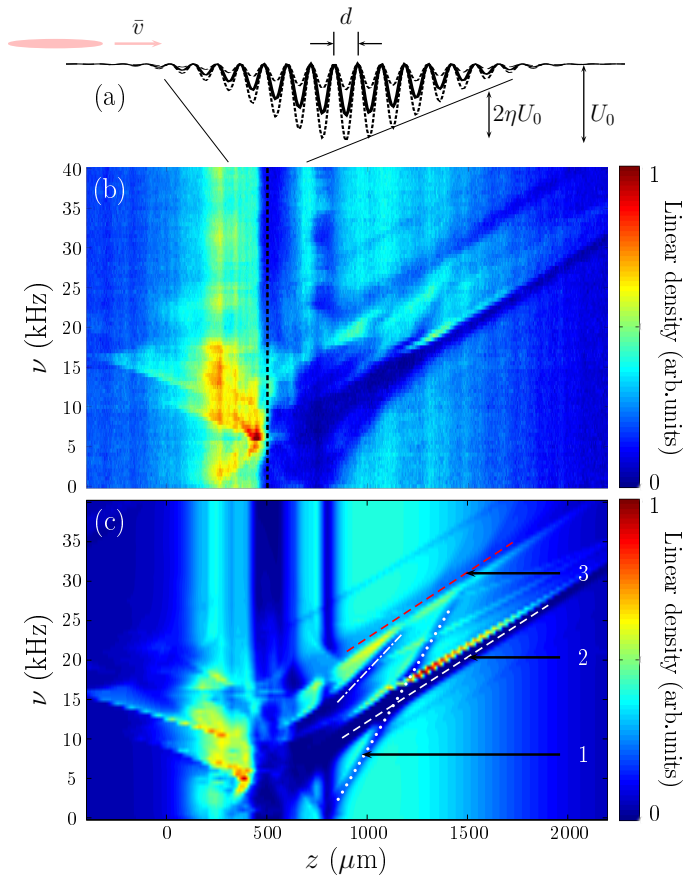

Figure 7.26: *(a) Schéma de l'expérience. (b) Profils de densité mesurés* $n(z, t_{\mathrm{acc}}+t_{\mathrm{prop}})$ *après un temps de propagation* $t_{\mathrm{prop}} =$ 78 ms *en fonction de la fréquence de modulation. L'amplitude de modulation est* $\eta = 30\%$*, et la position du réseau est représentée par la ligne pointillé. (c) Simulation numérique pour les même paramètres que l'expérience. On observe des déplétions dont la position dépend de la fréquence.*

qu'une parabole repliée, il est alors aisé de calculer la différence d'énergie entre la bande initiale et les différentes bandes sur lesquelles la particule peut être transférée. Les fréquences associées aux différentes transitions dépendent de la vitesse incidente v_0:

$$\pm\nu_{n\to n'} = \frac{E_n - E_{n'}}{h} = -(n-n')^2\nu_{\mathrm{L}} + \frac{n'-n}{d}v_0, \tag{7.25}$$

où n et n' sont des entiers. Les fréquences des différentes transitions interbandes varient linéairement avec la vitesse incidente, leurs pentes et positions correspondent précisément aux lignes de déplétion observées dans l'expérience. Chaque réflection induite par la modulation correspond donc à une transition interbande. Pour avoir une compréhension plus complète des phénomènes en terme de processus élémentaires, nous utilisons ci-après le formalisme de Floquet-Bloch.

Analyse à l'aide des états de Floquet-Bloch

Dans le cas d'un Hamiltonien périodique à la fois en espace et en temps, il est possible d'étendre le théorème de Bloch. Les solutions de l'équation de Schrödinger ont alors la forme d'un état de Floquet-Bloch:

$$\psi_{n,k}(z,t) = e^{i(kz-\varepsilon_n(k)t/\hbar)}u_{n,k}(z,t), \tag{7.26}$$

où $\varepsilon_n(k)$ sont les quasi-énergies et les fonctions $u_{n,k}$ sont bi-périodiques. A l'aide de ces états, nous construisons un nouveau diagramme de bande. Ce diagramme est la superposition de diagrammes de Bloch décalés de multiples de la fréquence de modulation. A chaque croisement entre deux diagrammes de Bloch, le couplage introduit par la modulation produit un anticroisement.

La trajectoire d'une particule dans le diagramme de Floquet-Bloch peut alors être simulée par un modèle semi-classique. Ce modèle décrit la trajectoire d'une particule sur une bande donnée via l'évolution couplée de sa position et de sa pseudo-impulsion, et prend en compte la possibilité de changer de bande via une transition Landau-Zener. Le modèle semi-classique reproduit bien les résultats expérimentaux et permet d'analyser la dynamique d'une particle isolée. La figure 7.27 présente les trajectoires de particules correspondants à certaines lignes de déplétion observées dans l'expérience notées 1, 2 et 3 (voir Fig. 7.26).

Dans chaque cas, le phénomène clef est l'absorption adiabatique d'une excitation du réseau. La particule subit ensuite une réflection de Bragg en bord de la zone de Brillouin. Les trajectoires dans l'espace réel peuvent alors être très complexe comme par exemple dans le cas de la trajectoire (1) où la vitesse de la particule change trois fois de signe.

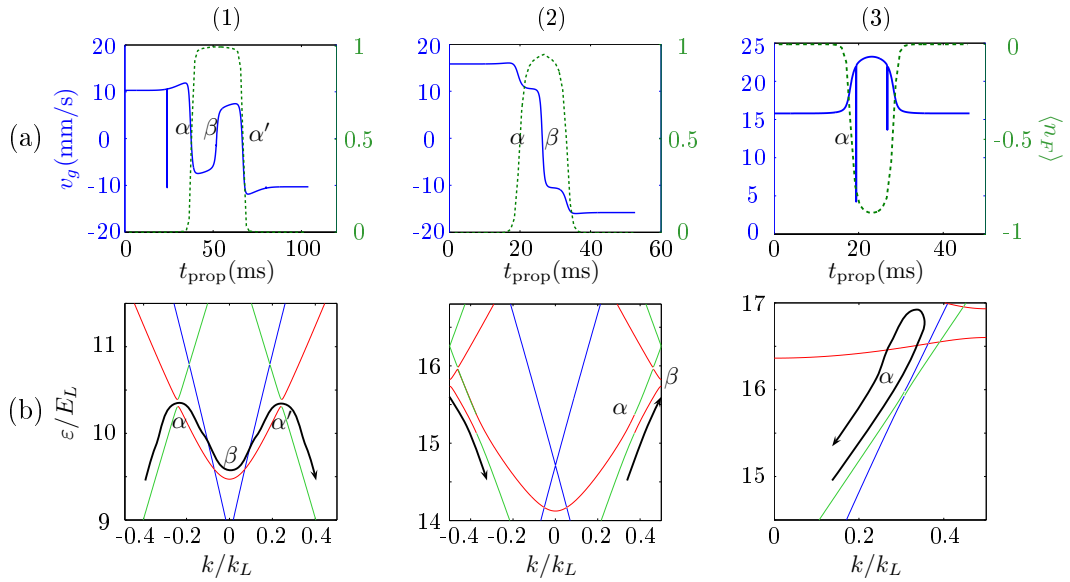

Figure 7.27: *(a) Vitesse et nombre moyen d'excitations de Floquet $\langle n_F \rangle$ en fonction du temps de propagation pour des paramètres correspondant à trois lignes de déplétion différentes (voir* FIG. *7.26). (b) Diagramme de Floquet-Bloch à la position pertinente. Les fléches indiquent les trajectoires des particules dans le diagramme de bande. (1) Réflection sur un gap ouvert par la modulation, $v = 10.3$ mm/s, $\nu = 8$ kHz. (2) Réflection sur un anticroisement suivi d'une réflection de Bragg. (3) accélération transitoire par absorption d'une excitation de Floquet. α indique l'absorption ou émission d'une excitation de Floquet et β une réflection de type Bragg.*

Application: filtre en vitesse

Il est possible d'utiliser simultanément différentes fréquences de modulation afin de créer un filtre en vitesse accordable. Par exemple, en combinant les déplétions induites par deux fréquences de modulation proches l'une de l'autre, nous pouvons créer entre des classes de vitesse rejetées un filtre passe-bande. Nous parvenons ainsi à filtrer une classe de vitesse de dispersion $\Delta v \simeq 450$ μm/s. Cette technique à l'avantage de ne pas reposer sur une structure interne particulière et est donc transposable à tous les types d'atomes.

Appendices

Appendix A

Published papers

This appendix presents the papers written during this thesis along with the abstracts.

A.1 Zeeman slowers made simple with permanent magnets in a Halbach configuration

P. Cheiney, O. Carraz, D. Bartoszek-Bober, S. Faure, F. Vermersch, C. M. Fabre, G. L. Gattobigio, T. Lahaye, D. Guéry-Odelin, & R. Mathevet
Review of Scientific Instruments, **82**, 063115 (2011)

We describe a simple Zeeman slower design using permanent magnets. Contrary to common wire-wound setups no electric power and water cooling are required. In addition, the whole system can be assembled and disassembled at will. The magnetic field is however transverse to the atomic motion and an extra repumper laser is necessary. A Halbach configuration of the magnets produces a high quality magnetic field and no further adjustment is needed. After optimization of the laser parameters, the apparatus produces an intense beam of slow and cold 87Rb atoms. With typical fluxes of 1 to 5×10^{10} atoms at 30 m/s, our apparatus efficiently loads a large magneto-optical trap with more than 10^{10} atoms in one second, which is an ideal starting point for degenerate quantum gases experiments.

A.2 Realization of a distributed Bragg reflector for propagating guided matter waves

C. M. Fabre, P. Cheiney, G. L. Gattobigio, F. Vermersch, S. Faure, R. Mathevet, T. Lahaye & D. Guéry-Odelin
Phys. Rev. Lett., **107**, 230401 (2011)

We report on the experimental realization of a Bragg reflector for guided matter waves. A Bose-Einstein condensate with controlled velocity distribution impinges onto an attractive optical lattice of finite length and directly probes its band structure. We study the dynamics of the scattering by this potential and compare the results with simple one-dimensional models. We emphasize the importance of taking into account the gaussian envelope of the optical lattice which gives rise to Bragg cavity effects. Our results are a further step towards integrated atom optics setups for quasi-cw matter waves.

A.3 Guided atom laser: transverse mode quality and longitudinal momentum distribution

F. Vermersch, C. M. Fabre, P. Cheiney, G. L. Gattobigio, R. Mathevet & D. Guéry-Odelin.
Phys. Rev. A, **84**, 043618 (2011)

We analyze the outcoupling of a matter wave into a guide by a time-dependent spilling of the atoms from an initially trapped Bose-Einstein condensate. This process yields intrinsically a breakdown of the adiabatic condition that triggers the outcoupling of the wave function. Our analysis of the time-dependent engineering and manipulation of condensates in momentum space in this context enables to work out the limits due to interactions in the mode quality of a guided atom laser. This study is consistent with recent experimental observations of low transverse excitations of guided atom lasers and suggests (i) an optimal strategy to realize such quasi-monomode guided atom lasers with, in addition, the lowest possible longitudinal velocity dispersion, or alternatively (ii) a strategy for engineering the atomic flux of the atom laser.

A.4 Matter wave scattering on an amplitude-modulated optical lattice

P. Cheiney, C. M. Fabre, F. Vermersch, G. L. Gattobigio, R. Mathevet, T. Lahaye & D. Guéry-Odelin.
Phys. Rev. A, **87**, 013623 (2013)

We experimentally study the scattering of guided matter waves on an amplitude-modulated optical lattice. We observe different types of frequency-dependent dips in the asymptotic output density distribution. Their positions are compared quantitatively with numerical simulations. A semiclassical model that combines local Floquet-Bloch bands analysis and Landau-Zener transitions provides a simple pic-

ture of the observed phenomena in terms of elementary Floquet photon absorption/emission processes and envelope-induced reflections. Finally, we propose and demonstrate the use of this technique with a bichromatic modulation to design a tunable sub-recoil velocity filter. Such a filter can be transposed to all species since it does not rely on a specific internal level configuration of the atoms.

A.5 Realization of tunnel barriers for matter waves using spatial gaps

P. Cheiney, F. Damon, G. Condon, B. Georgeot & D. Guéry-Odelin
arXiv:1302.1811 (2013)

We experimentally demonstrate the trapping of a propagating Bose-Einstein Condensate in a Bragg cavity produced by an attractive optical lattice with a smooth envelope. As a consequence of the envelope, the band gaps become position-dependent and act as mirrors of finite and velocity-dependent reflectivity. We directly observe both the oscillations of the wave packet bouncing in the cavity provided by these spatial gaps and the tunneling out for narrow classes of velocity. Synchronization of different classes of velocity can be achieved by proper shaping of the envelope. This technique can generate single or multiple tunnel barriers for matter waves with a tunable transmission probability, equivalent to a standard barrier of submicron size.

Appendix B

More on the outcoupling dynamics

In this appendix, we wish to adress a few questions motivated by the experimental observations. In particular, the output velocity does not vary as a function of the laser detuning as expected by the naive model presented at the beginning of chapter 1. A linear relation with $\mathrm{d}v_\mathrm{f}/\mathrm{d}\delta_0 = -0.78$ m.s^{-1}/MHz is expected, while, a slope close to 1 m.s^{-1}/MHz is observed experimentally. This discrepancy is related to some questions: under which conditions does the atom follow the resonance condition during the slowing? What happens during the extraction of the atoms at the output of the ZS?

Approximations to the equation of motion

The acceleration resulting from the radiation pressure (1.2) reads:

$$a = -a_0 \frac{s_0}{1 + 4\left(\delta_0 + kv(z) - \mu B(z)/\hbar\right)^2/\Gamma^2 + s_0}. \tag{B.1}$$

This equation cannot be solved analytically because of the non-linear terms in v and z. It is instructive, however, to develope the equation of motion around the resonance condition ideally followed by the atoms. Let us therefore define $v' = v - v_R$ where $v_R = v_c\sqrt{1 - z/\ell}$, is the velocity of an atom that is constantly decelerated at $a = -\eta a_0$ ($\eta < 1$), and is at rest at the output of the ZS. For a given trajectory, the acceleration is $a = v\mathrm{d}v/\mathrm{d}z$. The change of variables permits to cancel out the terms that depend on z in the detuning. The equation of motion becomes:

$$(v' + v_R)\frac{d(v' + v_R)}{dz} = -a_0 \frac{s_0}{1 + s_0 + 4(\delta_0' + kv')^2/\Gamma^2}, \tag{B.2}$$

where $\delta_0' = \delta_0 - \mu B_\mathrm{b}/\hbar$. If $v' \ll v_R$, (*i.e* we are close from the expected trajectory), it is possible to solve equation (B.2) at different orders in v'/v_R. At the zero-th order, we obtain:

$$a_0\left(\frac{s_0}{1 + s_0 + 4(\delta_0' + kv')^2/\Gamma^2} - \eta\right) = 0. \tag{B.3}$$

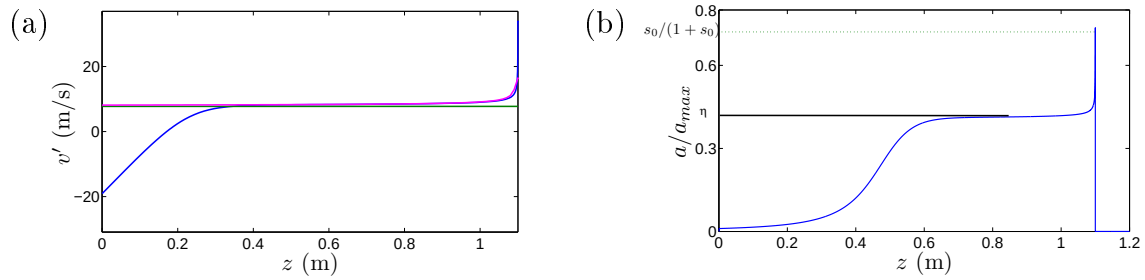

Figure B.1: *(a) An atom reaches an equilibrium velocity $v'_{\rm eq}$ for which the acceleration is $a = \eta a_0$. Blue: direct numerical integration of the non-linear equation of motion. Green (violet): solution at the zero-th (first) order in v'/v_R. (b) At the output of the ZS, the acceleration increases until it reaches a_0, the atoms are then outcoupled.*

The atom reaches in the decelerated frame a stationary velocity such that the detuning stay constant but non zero:[1]

$$kv_{stat} = -\delta'_0 - \frac{\Gamma}{2}\sqrt{\left(\frac{1-\eta}{\eta}\right)s_0 - 1}. \tag{B.4}$$

The atom trajectory is then set on one edge of the resonance profile. The trajectory gets closer to the center of the resonance profile as η gets closer to 1. Figure B.1 (a) shows the velocity in the decelerated frame calculated by integrating numerically the Eq. B.2 along with the calculated stationary velocity, we see that inside the ZS, the atom, clings to the expected stationary velocity.

Besides being slowed down, the atomic beam is also cooled. Indeed, at the first order in v'/v_R, the equation (B.2) becomes:

$$\frac{dv'}{dz} = \frac{-a_0}{v_R}\left(\frac{s_0}{1+s_0+4(\delta'_0+kv')^2/\Gamma^2} - \eta\right) + \frac{v_c^2}{lv'}. \tag{B.5}$$

It is then possible to expand the terms on the right around the stationary velocity $v_{\rm stat}$. We see then that the difference to the stationary velocity $v' - v_{\rm stat}$ is damped ($d(v' - v'_{\rm eq})/dz = -\gamma(v' - v'_{\rm eq})$), with a damping

$$\gamma = \frac{8\gamma_D\eta^2}{s_0}\sqrt{\left(\frac{1-\eta}{\eta} - 1\right)}, \tag{B.6}$$

where we introduced the parameter $\gamma_D = \hbar k^2/4m$ that corresponds to the maximum damping for a two-level atom. The cooling of the atomic beam in a ZS and in an optical molasse have the same origin (without considering the internal structure), however, in practice, the velocity dispersion in a ZS is generally much higher than

[1] The solution with the + sign is unstable.

in a molasse because it is ultimately dictated by the outcoupling mechanism at the output of the ZS.[2]

Outcoupling

The condition $v' \ll v_R$ is not fulfilled when:

- v' is too high, this occurs at the entrance of the ZS, when the atom has not yet reached the resonance condition.
- v_R tends to zero at the output.

In these two cases, it is necessary to integrate numerically the Eq. (B.2). In the first case, we see that v' reaches its equilibrium value in an overdamped regime without oscillation (see FIG. B.1 (a)). The second case is more interesting and explain the fact that the output velocity does not vary with the detuning δ_0 as simply as suggested by the naive model. The magnetic field has been calculated to induce a constant acceleration. However, this is not necessarily fulfilled everywhere inside the ZS even in the case of the ideal magnetic field. Indeed, if we take the derivative of the resonance condition

$$kv - \mu B/\hbar = cst, \tag{B.7}$$

we find that the acceleration is not constant and equal to

$$a = -\eta a_0 \left(1 - \frac{\delta_0'}{\mu \Delta B/\hbar \sqrt{1 - z/\ell}}\right). \tag{B.8}$$

The acceleration is strictly constant only if $\delta_0' = 0$, *i.e* if the atoms are extracted exactly at rest. This is not possible experimentally since the atomic beam would then become very divergent. In all other cases, because of the term $1/\sqrt{1 - z/\ell}$, the acceleration required to follow the resonance condition will eventually become larger than the maximum acceleration before the output of the ZS. At this location, the atom is outcoupled and will not fully benefit from the slowing in the last part of the ZS.

The atoms are outcoupled when a becomes larger than $a_0 s_0/(1 + s_0)$, it occurs at a location:

$$z_{\text{out}} = \ell \left(1 - \left(\frac{\hbar \delta_0'}{\mu \Delta B}(1 + s_0)\right)^2\right) \tag{B.9}$$

In normal conditions of operation, $\hbar\delta_0' \ll \mu\Delta B$), therefore, the outcoupling position is located only a few millimeters before the end of the ZS. This does not compromise the working out of the ZS, however, it has an important effect on the output velocity.

Using Eqs. (B.4) and (B.9), and assuming that the atoms are not decelerated anymore after the outcoupling, it is now possible to compute the variation of the

[2] An important transverse inhomogeneity can also result in an increase of the velocity dispersion.

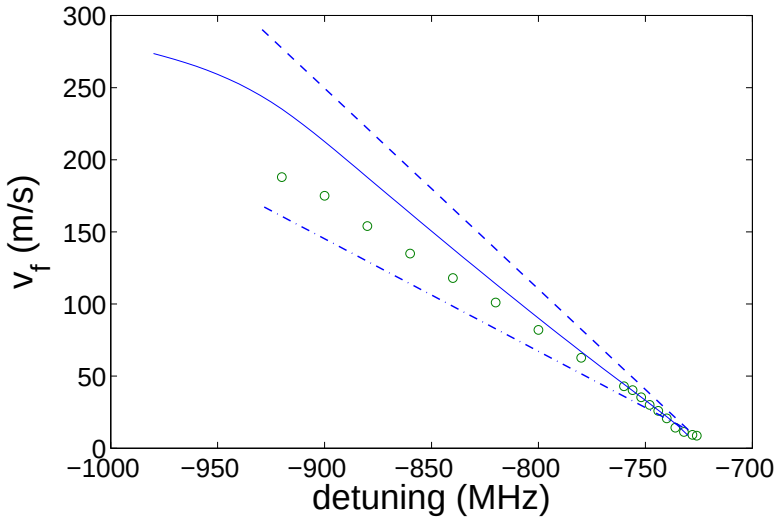

Figure B.2: *Output velocity as a function of the detuning: experimental (circle), with the naive model (Dash-dotted line), the model with premature outcoupling (dashed line) and using a full numerical resolution (plain line).*

final velocity. The final velocity does not vary as a function of the detuning as simply as expected using a simple approach.

$$kv_{\mathrm{f}} = -\delta_0' \left(1 + \frac{1+s_0}{s_0 \left(\frac{1-\eta}{\eta} \right) - 1} \right) - \frac{\Gamma}{2} \sqrt{\left(\frac{1-\eta}{\eta} \right) s_0 - 1}. \tag{B.10}$$

Figure B.2 presents the measured final velocity as a function of the detuning along with the result from the three calculations: the naive model presented in the beginning of the chapter, the calculation in which we take into account the outcoupling position, and the result of the numerical integration of the dynamics. The output velocity roughly varies linearly with the detuning. As outlined before, the slope predicted by the naive model (dash-dotted line) is too small. On the contrary, the slope obtained with our second model (dashed line) is too large and does not reproduce the experimental results. This means that atoms are still significantly slowed even after the outcoupling. The complete numerical integration (plain line) that takes this effect into account provides the best agreement.

Appendix C

Magnetic material characterization

Because in our magnet configurations, magnets are going to be close to one another, it is important to know to which extent their contributions to the total magnetic field can be added independently. Besides, the geometry of a magnetic material has *a priori* an influence on its magnetization. The values of magnetization found in the datasheet are measured on materials in a torus geometry. It is important to know if the magnetization changes significantly for our cuboid magnets. To answer these questions, we use the material characteristic $M(H)$ (see FIG. C.1). For "hard" magnetic materials, the characteristics has the shape of a large rectangle. Schematically, we can consider that the magnetization switches between to values $\pm M_{\text{sat}}$. The half-width of the rectangle is the intrinsic coercive field $H_{\text{ci}} \simeq 1,1$ kA/mm for our magnets. It represents the external magnetic field one has to apply to reverse the polarity of the magnet. The total magnetic field experienced by a magnet is the sum of the field produced by the other magnets and of its own magnetic field also called demagnetizing field H_{dem}. Computing the demagnetizing field is in general a very complex task and strongly depends on the geometry of the magnet. However, there is a simple solution if we suppose that the magnetization is homogeneous. In this case, thanks to the linearity of Maxwell's equations, the demagnetizing field is proportional to the magnetization $H_{\text{dem}} = -N_{\text{d}} M$, where N_{d} is the demagnetizing factor that depends only on the geometry. In the two realizations, the magnet geometries are such that $N_{\text{d}} \sim 0.75$ and 0.5 respectively. This leads to quite strong demagnetizing fields $H_{\text{dem}} = -0.75$ kA/mm and -0.5 kA/mm (see FIG. C.1). However, thanks to the high flatness of the characteristic, these effect remain very small in our case. The magnetization is reduced in the two setups of 2% and 0.5% respectively. This effect was not taken into account in the following where we suppose that the magnetization is constant and equals to $M = M_{\text{sat}} = 0.95$ kA/mm. The field produced by the other magnets, on the order of $H_{\text{ext}} \sim 25$ A/mm is very small compared to the demagnetization field. As a consequence, it is completely negligible.

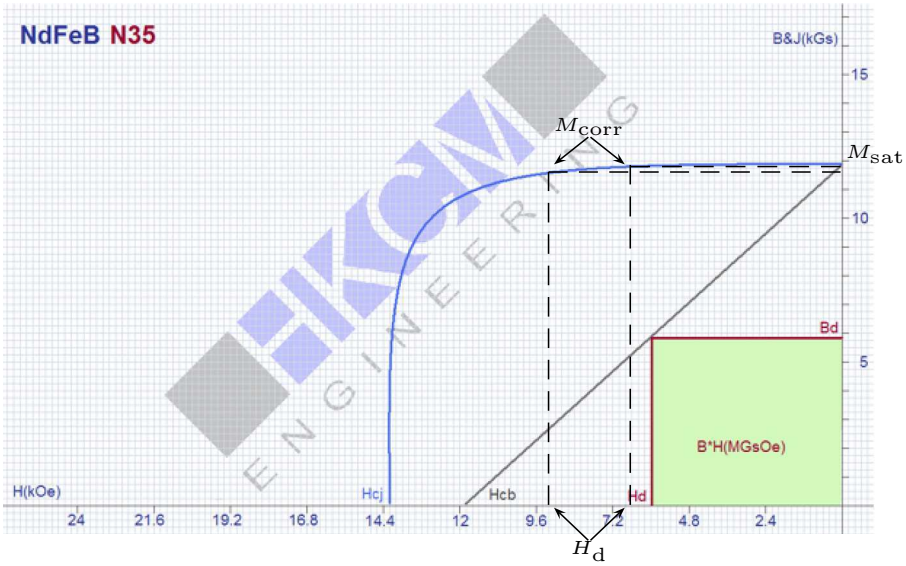

Figure C.1: *The caracteristic $M(H)$ has a rectangular shape, correlatively $B(H)$ is almost a straight line. The coercive field for the N35 grade is $H_{\mathrm{ci}} \simeq 1,1$ kA/mm and the residual induction $B_{\mathrm{r}} = 12$ kG ($M_{\mathrm{sat}} = B_{\mathrm{r}}/\mu_0 = 0.95$ kA/mm). The demagnetizing field though important only leads to 0.5 and 2 % changes in the magnetization.*

Appendix D

Atomic flux from absorption measurements

In this appendix, we develop the calculations to extract the atomic flux from the absorption measurements.

Let us assume that the atomic beam has a cylindrical symmetry and that the probe is small compared to the size of the atomic beam. Let $n(\rho)$ denote the beam density at a distance ρ from the center and $f(v)$ the atomic velocity distribution. The atom flux is:

$$\Phi = \int_0^{+\infty} 2\pi\rho \mathrm{d}\rho \; n(\rho) \int_0^{+\infty} \mathrm{d}v \; v f(v). \tag{D.1}$$

For a probe beam at an angle θ from the atomic beam, the absorption signal $A(\Delta)$ is:

$$A(\Delta) = \int_{-\infty}^{+\infty} \frac{\mathrm{d}\rho}{\sin\theta} \; n(r) \int_0^{+\infty} \mathrm{d}v \; f(v)\sigma(v,\Delta), \tag{D.2}$$

where $\sigma(v,\Delta) = \sigma_0/(1+4\Delta'^2/\Gamma^2)$ with $\Delta' = \Delta + kv\cos\theta$ is the absorption cross section. In the limit where the Doppler broadening is much larger than the natural

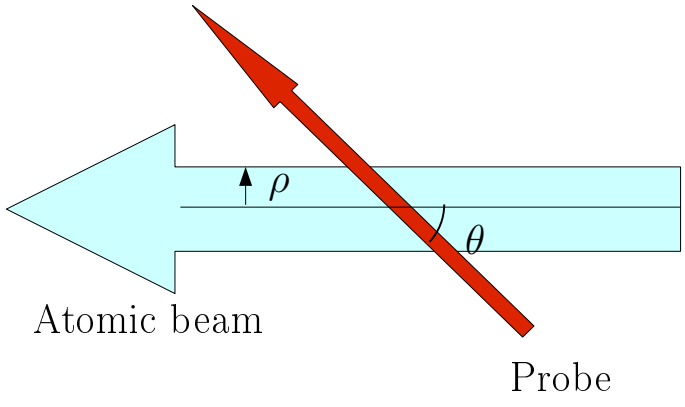

Figure D.1: *Sketch of the atomic beam detection scheme by an absorption probe.*

linewidth, $k\,\delta v\cos\theta \ll \Gamma$, we can approximate the absorption cross section by a δ-function:

$$\sigma(v,\Delta) \approx \frac{2}{\pi}\sigma_0\delta\left(\frac{\Delta}{\Gamma} - \frac{v\cos\theta}{\lambda\Gamma}\right).$$

In that case Eq. (D.2) simplifies:

$$A(\Delta) = \frac{2}{\pi}\sigma_0\frac{\lambda\Gamma}{\cos\theta}f\left(\frac{\lambda\Delta}{\cos\theta}\right)\int_{-\infty}^{+\infty}\frac{\mathrm{d}\rho}{\sin\theta}\,n(\rho)$$

and Eq. (D.1) is

$$\Phi = C\,D\frac{\lambda\tan\theta}{\sigma_0\Gamma}\int_{-\infty}^{+\infty}\mathrm{d}\Delta\;\Delta A(\Delta), \tag{D.3}$$

where D is the typical atom beam diameter and C a constant near unity defined according to:

$$C = \frac{\pi}{2}\frac{1}{D}\frac{\int_0^{+\infty}2\pi\rho\mathrm{d}\rho\;n(\rho)}{\int_{-\infty}^{+\infty}\mathrm{d}\rho\;n(\rho)}.$$

For a homogeneous cylindrical beam $C = \pi^2/8$. The atom flux is thus measured from the absorption signal by numerical integration following Eq. (D.3).

Appendix E

Recirculating oven

The atomic beam is created by an effusive oven loaded with 15 g of rubidium. In order to maximise the oven lifetime, we use a recirculating design. As compared to the so-called 'candlestick' designs,[138, 139] our oven, inspired in part by [140] is very simple and easy to operate. We have built several versions of the oven over the last five years, with minor variations between them, and observed comparable performances. The same design has been used also for a sodium BEC setup producing extremely large condensates [141] but no detailed description is given there.

A general view of the oven, made of standard CF-16 and CF-40 ultra-high vacuum fittings, is shown on Fig. E.1. A first chamber contains, at the bottom, molten rubidium kept at temperature T_1, in equilibrium with rubidium vapor, which effuses through a circular aperture of diameter $d_1 = 8$ mm drilled in the center of a blank CF-16 copper gasket. The other parts of the chamber are kept at $T_2 = T_3 = T_4 \sim T_1 + 30$ K in order to avoid the accumulation of rubidium on a cold spot and possible clogging of the oven aperture. The temperatures T_1 to T_4 are actively stabilized by means of four PID controllers, thermocouples as temperature sensors, and heating bands as actuators. The recirculation tube may also be heated just above the melting temperature of Rubidium to prevent it to be from

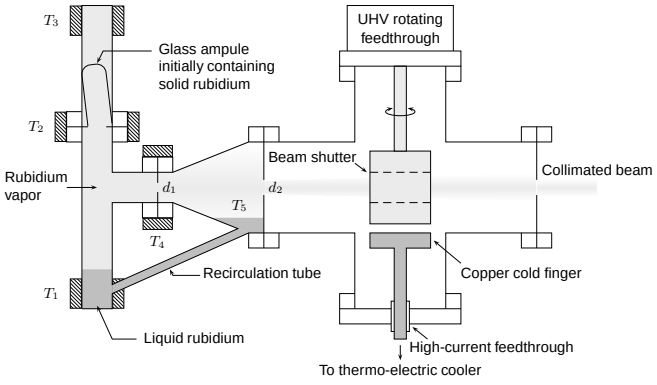

Figure E.1: *Sketch of the recirculating oven. Hatched rectangles represent heaters.*

being blocked by solid Rubidium. To achieve a good thermal insulation, the oven is covered with two layers of alkaline earth silicate wool and an external foil of metal coated Mylar. In steady state, the average power consumption is a few tens of watts. A second chamber (made of a conical CF-16 to CF-40 adapter) is used to collimate the beam by means of a second aperture (diameter $d_2 = 4$ mm) located 80 mm downstream.

The rubidium not used in the collimated beam accumulates into this chamber. Liquid rubidium at temperature $T_5 < T_1$ flows back by gravity to the first chamber through a 6 mm inner diameter stainless steel tube. A piece of gold-plated stainless steel mesh (Alfa-Aeser ref. 42011) covers the inside of the recirculating chamber to ease the accumulation of rubidium in its lower part.[1]

The loading of the oven is made in a very simple way: we cool down the rubidium ampule(s) in liquid nitrogen, break the glass with pliers, and insert the ampules upside down into the first oven chamber. We then close this chamber with a blank CF-16 flange, and pump down the oven to $\sim 10^{-6}$ mbar with a turbomolecular pump. When heating the oven, the rubidium melts and drips to the bottom of the first chamber.

[1] In some versions of the oven we rolled a small quantity of this mesh into a 'wick' that was inserted into the recirculation tube, in order to help recirculation by capillary action. However the ovens without this wick showed similar performance and the presence of the mesh is probably not necessary at all.

Appendix F

Ideal Halbach cylinder

In this appendix, we develop the magnetic field calculations produced by magnets in the ideal Halbach cylinder configuration depicted in FIG. F.1. Using polar coordinate, the magnetization reads:

$$\boldsymbol{M} = M_0(\cos\theta \boldsymbol{u_r} + \sin\theta \boldsymbol{u_\theta}) \tag{F.1}$$

Let us show that the resulting magnetic field $\boldsymbol{B}$:

- vanishes for $r > R_{\text{ext}}$,
- is uniform for $r < R_{\text{int}}$,

with inside the rim:

$$\boldsymbol{B} = \mu_0 M_0 \ln \frac{R_{\text{ext}}}{R_{\text{int}}} \boldsymbol{u_y}. \tag{F.2}$$

The magnetization distribution is equivalent to the following distribution of (i) surface current $\boldsymbol{j_s} = \boldsymbol{M} \times \boldsymbol{n}$, (ii) volume current $\boldsymbol{j} = \nabla \times \boldsymbol{M}$.

- internal surface $r = R_{\text{int}}$: $\boldsymbol{j_s} = M_0 \sin\theta \boldsymbol{u_z}$.
- external surface $r = R_{\text{ext}}$: $\boldsymbol{j_s} = -M_0 \sin\theta \boldsymbol{u_z}$.
- volume current: $\boldsymbol{j} = \frac{M_0}{r}\left(\partial_r(r\sin\theta) - \partial_\theta \cos\theta\right)\boldsymbol{u_z} = 2M_0 \sin\theta / r \boldsymbol{u_z}$.

Let us first work out the contribution of the surface currents. To do that, let us remark that the current distribution $\boldsymbol{j_s} = j_{s_0} \sin\theta \boldsymbol{u_z}$ is equivalent to the volume current distribution of two plain cylindrical conductors with radius r and current in opposite direction shifted in the x direction by a small distance ε (see FIG. F.2). The magnetic field produced at the point M by one cylindrical conductor is well known and reads $\boldsymbol{B}(\boldsymbol{M_{\text{int}}}) = \frac{\mu_0 j}{2} \boldsymbol{u_z} \times \boldsymbol{O_i M}$. It follows by linearity of the Maxwell equation that the magnetic field produced by the surface current distribution reads:

$$\boldsymbol{B}(\boldsymbol{M}) = \frac{\mu_0 j}{2} \boldsymbol{u_z} \times (\boldsymbol{O_2 M} - \boldsymbol{O_2 M}) = \frac{\mu_0 j \varepsilon}{2} \boldsymbol{u_z} \times \boldsymbol{u_x} \tag{F.3}$$

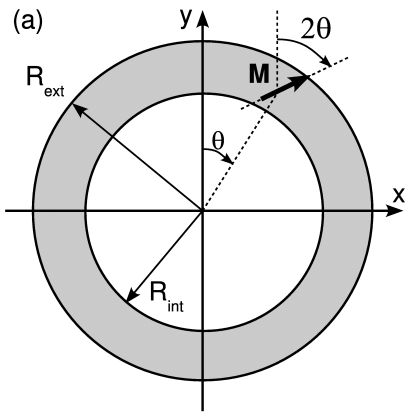

Figure F.1: *Ideal Halbach cylinder magnetic configuration, the magnetization at an angle θ from the y axis form an angle 2θ with the same axis.*

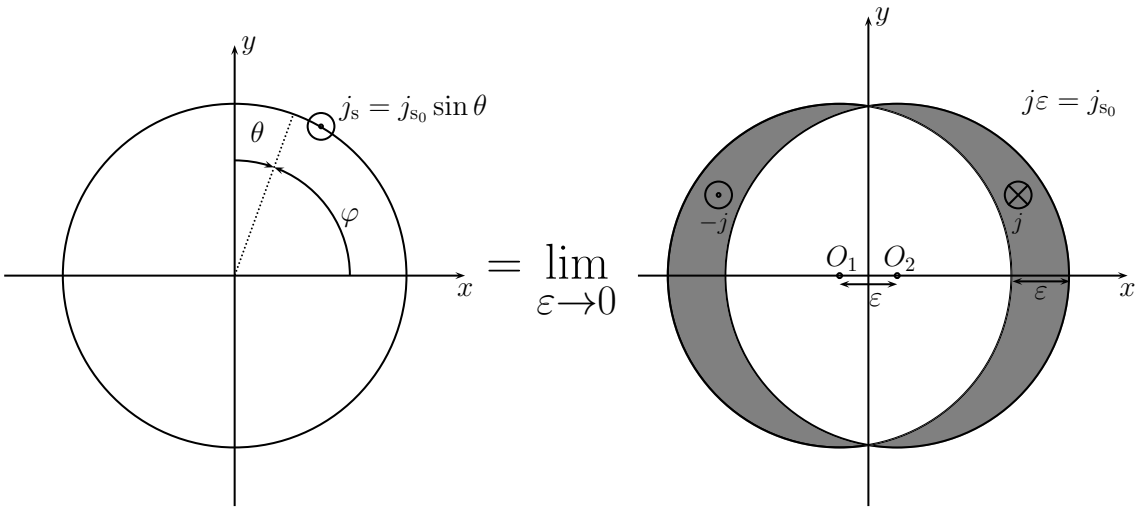

Figure F.2: *Equivalence between a surface current of the type $j_s = j_{s_0} \sin\theta$ and two plain conductor shifted by a small distance ε and carrying currents $j = \pm j_{s_0}/\varepsilon$.*

$$\boldsymbol{B}(\boldsymbol{M}) = \frac{\mu_0}{2} j_{s_0} \boldsymbol{u_y} \tag{F.4}$$

interestingly, this does not depend on the radius of the cylinder that support the surface current. The contributions of the internal and external surfaces thus compensate each other.

Let us now work out the contribution of the volume currents. Because the problem is in two dimensions, it is useful here to use the following complex notations:

$$\underline{z} = x + iy = re^{i\varphi}, \tag{F.5}$$

and

$$\underline{B} = B_x + iB_y. \tag{F.6}$$

With these notation, the magnetic field produced at location $\underline{z_0}$ generated by a current filament I infinite in the z direction, at location $\underline{z}$ reads:

$$\underline{B} = \frac{\mu_0 I}{2i\pi} \frac{1}{\underline{z_0} - \underline{z}}. \tag{F.7}$$

We can now integrate the contributions of the elementary volume current j. The total magnetic field reads:

$$\underline{B} = \frac{\mu_0}{2i\pi} \iint \frac{j}{\underline{z_0} - \underline{z}} r \mathrm{d}r\mathrm{d}\varphi. \tag{F.8}$$

let us use the Taylor expansion of the term $1/(\underline{z_0} - \underline{z})$, inside the rim ($|\underline{z_0}| < |\underline{z}|$):

$$\frac{1}{\underline{z_0} - \underline{z}} = -\sum_{n=1}^{\infty} \frac{\underline{z_0}^{n-1}}{\underline{z}^n} \tag{F.9}$$

In this way, we easily express the magnetic field as a Taylor expansion too:

$$\underline{B} = \sum_{n=0}^{\infty} \underline{b}_n, \tag{F.10}$$

with

$$\underline{b}_n = -\frac{\mu_0}{2i\pi} \iint \frac{j e^{-i(n+1)\varphi}}{r^n} \mathrm{d}r\mathrm{d}\varphi. \tag{F.11}$$

In our case, the volume current is $j = \frac{2\cos\varphi}{r} M_0 = \frac{e^{i\varphi} + e^{-i\varphi}}{r} M_0$. Because of the angular integral, the multipolar development (F.11) is exactly zero for $n \neq 0$. The magnetic field inside the rim is thus homogeneous and

$$\underline{B} = \underline{b}_0 = -\frac{\mu_0}{2i\pi} \iint \frac{M_0}{r} \mathrm{d}r\mathrm{d}\varphi, \tag{F.12}$$

$$\underline{B} = i\mu_0 M_0 \ln \frac{R_{\text{ext}}}{R_{\text{int}}}. \tag{F.13}$$

The magnetic field is homogeneous and along the direction y. Let us remark that if one chooses a magnetization that makes an angle $2N\theta$ with the y axis, a different term of the multipolar development (F.11) is priviledged so that this recipe can be used to obtain ideal multipolar fields.

Outside the magnetic rim ($|\underline{z_0}| > |\underline{z}|$), the Taylor expansion of $1/(\underline{z_0} - \underline{z})$ becomes:

$$\frac{1}{\underline{z_0} - \underline{z}} = \sum_{n=0}^{-\infty} \frac{\underline{z_0}^{n-1}}{\underline{z}^n} \tag{F.14}$$

In this case, all terms of the sum are identically zero and the field outside of the rim vanishes.

Appendix G

Development of the Floquet-Bloch band eigenvalue problem

We start with the hamiltonian:

$$H = -\frac{\hbar^2}{2m}\frac{\mathrm{d}^2}{\mathrm{d}z^2} + \frac{U_0}{2}(1+\eta\cos(\omega t))(1+\cos(k_{\mathrm{L}}x)) \tag{G.1}$$

The Floquet-Bloch states can be written:

$$\psi_{n,k}(z,t) = e^{i(kz-\varepsilon_n(k)t/\hbar)}u_{n,k}(z,t), \tag{G.2}$$

where $\varepsilon_n(k)$ are the quasi-energies and the functions $u_{n,k}(z,t)$ are biperiodic in space and time and therefore can be Fourier expanded:

$$\begin{aligned} u_{n,k}(z,t) = u_{n,k}(z+d,t) &= u_{n,k}(z,t+T) \\ &= \sum_l \sum_{n_{\mathrm{F}}} \phi^{n_F,l} e^{i(lk_L z - n_F\omega t)}. \end{aligned} \tag{G.3}$$

Let us expand each term of the Schrödinger equation on the Fourier basis:

$$i\hbar\frac{\partial\psi}{\partial t} = i\hbar\sum_{n_{\mathrm{F}}}(in_{\mathrm{F}}\omega - i\varepsilon_n(k)t/\hbar)\exp\left(i(n_{\mathrm{F}}\omega t - \varepsilon_n(k)t/\hbar)\right)\sum_l \phi^{n_{\mathrm{F}},l} \tag{G.4}$$

The kinetic energy term shall be expanded:

$$-\frac{\hbar^2}{2m}\frac{\mathrm{d}^2\psi}{\mathrm{d}z^2} = \sum_l\sum_{n_F}\frac{\hbar^2}{2m}(k+lk_{\mathrm{L}})^2\phi^{n_{\mathrm{F}},l}\exp\left[i((k+lk_{\mathrm{L}})z - (n_{\mathrm{F}}\omega + \varepsilon_n(k)/\hbar)t)\right]. \tag{G.5}$$

The time-dependent potential is expanded

$$U(z,t) = \frac{U_0}{2}\left(1+\eta\frac{e^{i\omega t}+e^{-i\omega t}}{2}\right)\left(1+\frac{e^{ik_{\mathrm{L}}z}+e^{-ik_{\mathrm{L}}z}}{2}\right). \tag{G.6}$$

$$U(z,t)\psi = \frac{U_0}{2}\sum_l\sum_{n_\mathrm{F}}((\phi^{n_\mathrm{F},l} + \frac{1}{2}(\phi^{n_\mathrm{F},l+1} + \phi^{n_\mathrm{F},l-1}) + \frac{\eta}{2}(\phi^{n_\mathrm{F}+1,l} + \phi^{n_\mathrm{F}-1,l}) + \frac{\eta}{4}(\phi^{n_\mathrm{F}+1,l+1} + \phi^{n_\mathrm{F}+1,l-1} + \phi^{n_\mathrm{F}-1,l+1} + \phi^{n_\mathrm{F}-1,l-1})) \tag{G.7}$$

combining Eqs. (G.4) to (G.7) into the Schrödinger equation and identifying each term of the Fourier expansion, one gets the following development:

$$\left[n_\mathrm{F}\zeta + q/2 + (k/k_\mathrm{L} + l)^2\right]\phi^{n_\mathrm{F},l} + \eta q/4(\phi^{n_\mathrm{F}+1,l} + \phi^{n_\mathrm{F}-1,l}) - q/4(\phi^{n_\mathrm{F},l+1} + \phi^{n_\mathrm{F},l-1}) - q/8(\phi^{n_\mathrm{F}+1,l+1} + \phi^{n_\mathrm{F}+1,l-1} + \phi^{n_\mathrm{F}-1,l+1} + \phi^{n_\mathrm{F}-1,l-1}) = \varepsilon\phi^{n_\mathrm{F},l}. \tag{G.8}$$

where $q = U_0/E_\mathrm{L}$ and $\zeta = \hbar\omega/E_\mathrm{L}$ are the normalized lattice depth and modulation frequency.

Bibliography

[1] L. de Broglie. *Recherches sur la théorie des quanta.* Ph.D. thesis, Paris (1924).

[2] C. Davisson and L. H. Germer. Diffraction of electrons by a crystal of nickel. *Phys. Rev.*, **30**, 705 (1927).

[3] O. Stern. Beugung von molekularstrahlen. *Zeitschrift fiir Physik*, **61** (1930).

[4] E. Fermi and L. Marshall. Interference phenomena of slow neutrons. *Phys. Rev.*, **71**, 666 (1947).

[5] D. W. Keith, M. L. Schattenburg, H. I. Smith, and D. E. Pritchard. Diffraction of atoms by a transmission grating. *Phys. Rev. Lett.*, **61**, 1580 (1988).

[6] O. Carnal and J. Mlynek. Young's double-slit experiment with atoms: A simple atom interferometer. *Phys. Rev. Lett.*, **66**, 2689 (1991).

[7] W. D. Phillips. Nobel lecture: Laser cooling and trapping of neutral atoms. *Rev. Mod. Phys.*, **70**, 3, 721 (1998).

[8] S. Chu. Nobel lecture : The manipulation of neutral particles. *Nobel Lecture : The manipulation of neutral particles*, **70**, 685 (1998).

[9] C. Cohen-Tannoudji. Nobel lecture : Manipulating atoms with photons. *Nobel Lecture : Manipulating atoms with photons*, **70**, 707 (1998).

[10] K. B. Davis, M. O. Mewes, M. R. Andrews, N. J. van Druten, D. S. Durfee, D. M. Kurn, and W. Ketterle. Bose-einstein condensation in a gas of sodium atoms. *Phys. Rev. Lett.*, **75**, 3969 (1995).

[11] M. H. Anderson, J. R. Ensher, M. R. Matthews, C. E. Wieman, and E. A. Cornell. Observation of bose-einstein condensation in a dilute atomic vapor. *Science*, **269**, 5221, 198 (1995).

[12] M. R. Andrews, C. G. Townsend, H.-J. Miesner, D. S. Durfee, D. M. Kurn, and W. Ketterle. Observation of interference between two bose condensates. *Science*, **275**, 637 (1997).

[13] J. Klaers, J. Schmitt, F. Vewinger, and M. Weitz. Bose einstein condensation of photons in an optical microcavity. *Nature*, **468**, 545 (2010).

[14] I. Bloch, T. W. Hänsch, and T. Esslinger. Atom laser with a cw output coupler. *Phys. Rev. Lett.*, **82**, 3008 (1999).

[15] E. W. Hagley, L. Deng, M. Kozuma, J. Wen, K. Helmerson, S. L. Rolston, and W. D. Phillips. A well-collimated quasi-continuous atom laser. *Science*, **283**, 1706 (1999).

[16] G. Cennini, G. Ritt, C. Geckeler, and M. Weitz. All-optical realization of an atom laser. *Phys. Rev. Lett.*, **91**, 240408 (2003).

[17] A. Couvert, M. Jeppesen, T. Kawalec, G. Reinaudi, R.Mathevet, and D. Guéry-Odelin. A quasi-monomode guided atom laser from an all-optical bose-einstein condensate. *EPL (Europhysics Letters)*, **83**, 5, 50001 (2008).

[18] M. Köhl, T. W. Hänsch, and T. Esslinger. Measuring the temporal coherence of an atom laser beam. *Phys. Rev. Lett.*, **87**, 160404 (2001).

[19] V. I. Balykin, V. S. Letokhov, Y. B. Ovchinnikov, and A. I. Sidorov. Quantum-state-selective mirror reflection of atoms by laser light. *Phys. Rev. Lett.*, **60**, 2137 (1988).

[20] M. Kasevich, W. A., S. David, and S. Chu. Normal-incidence reflection of slow atoms from an optical evanescent wave. *Optics Letters,*, **15**, 607 (1990).

[21] I. Bloch, M. Köhl, M. Greiner, T. W. Hänsch, and T. Esslinger. Optics with an atom laser beam. *Phys. Rev. Lett.*, **87**, 030401 (2001).

[22] A. Bell, B. Brezger, U. Drodofsky, S. Nowak, T. Pfau, and J. M. Stuhler, J. Th. Schulze. Nano-lithography with atoms. *Surface Science*, **433**, 40 (1999).

[23] G. Timp, R. E. Behringer, D. M. Tennant, J. E. Cunningham, M. Prentiss, and K. K. Berggren. Using light as a lens for submicron, neutral-atom lithography. *Phys. Rev. Lett.*, **69**, 1636 (1992).

[24] P. L. Kapitza and P. A. M. Dirac. The reflection of electrons from standing light waves. *Mathematical Proceedings of the Cambridge Philosophical Society*, **29**, 02, 297 (1933).

[25] H. Schwarz, H. A. Tourtellotte, and G. W. W. *Bull. Am. Phys. Soc.*, **10**, 1129 (1965).

[26] L. S. Bartell, R. R. Roskos, and H. B. Thompson. Reflection of electrons by standing light waves: Experimental study. *Phys. Rev.*, **166**, 1494 (1968).

[27] P. E. Moskowitz, P. L. Gould, S. R. Atlas, and D. E. Pritchard. Diffraction of an atomic beam by standing-wave radiation. *Phys. Rev. Lett.*, **51**, 370 (1983).

[28] C. Keller, J. Schmiedmayer, A. Zeilinger, T. Nonn, S. Dürr, and G. Rempe. Adiabatic following in standing-wave diffraction of atoms. *Applied Physics B: Lasers and Optics*, **69**, 303 (1999).

[29] W. L. Bragg. *Proc. Cambridge Philos. Soc.*, **17**, 43 (1912).

[30] S. Lepoutre, A. Gauguet, G. Trénec, M. Büchner, and J. Vigué. He-mckellar-wilkens topological phase in atom interferometry. *Phys. Rev. Lett.*, **109**, 120404 (2012).

[31] E. M. Rasel, M. K. Oberthaler, H. Batelaan, J. Schmiedmayer, and A. Zeilinger. Atom wave interferometry with diffraction gratings of light. *Phys. Rev. Lett.*, **75**, 2633 (1995).

[32] D. M. Giltner, R. W. McGowan, and S. A. Lee. Atom interferometer based on bragg scattering from standing light waves. *Phys. Rev. Lett.*, **75**, 2638 (1995).

[33] A. E. Leanhardt, A. P. Chikkatur, D. Kielpinski, Y. Shin, T. L. Gustavson, W. Ketterle, and D. E. Pritchard. Propagation of bose-einstein condensates in a magnetic waveguide. *Phys. Rev. Lett.*, **89**, 040401 (2002).

[34] M. J. Renn, D. Montgomery, O. Vdovin, D. Z. Anderson, C. E. Wieman, and E. A. Cornell. Laser-guided atoms in hollow-core optical fibers. *Phys. Rev. Lett.*, **75**, 3253 (1995).

[35] D. Cassettari, B. Hessmo, R. Folman, T. Maier, and J. Schmiedmayer. Beam splitter for guided atoms. *Phys. Rev. Lett.*, **85**, 5483 (2000).

[36] R. Dumke, T. Müther, M. Volk, W. Ertmer, and G. Birkl. Interferometer-type structures for guided atoms. *Phys. Rev. Lett.*, **89**, 220402 (2002).

[37] O. Houde, D. Kadio, and L. Pruvost. Cold atom beam splitter realized with two crossing dipole guides. *Phys. Rev. Lett.*, **85**, 5543 (2000).

[38] D. Müller, E. A. Cornell, M. Prevedelli, P. D. D. Schwindt, Y.-J. Wang, and D. Z. Anderson. Magnetic switch for integrated atom optics. *Phys. Rev. A*, **63**, 041602 (2001).

[39] G. L. Gattobigio, A. Couvert, G. Reinaudi, B. Georgeot, and D. Guéry-Odelin. Optically guided beam splitter for propagating matter waves. *Phys. Rev. Lett.*, **109**, 030403 (2012).

[40] T. Erdogan. Fiber grating spectra. *Journal of lightwave technology.*, **15**, 1277 (1997).

[41] P. Cheiney, O. Carraz, D. Bartoszek-Bober, S. Faure, F. Vermersch, C. M. Fabre, G. L. Gattobigio, T. Lahaye, D. Guery-Odelin, and R. Mathevet. A zeeman slower design with permanent magnets in a halbach configuration. *Review of Scientific Instruments*, **82**, 6, 063115 (2011).

[42] C. M. Fabre, P. Cheiney, G. L. Gattobigio, F. Vermersch, S. Faure, R. Mathevet, T. Lahaye, and D. Guéry-Odelin. Realization of a distributed bragg reflector for propagating guided matter waves. *Phys. Rev. Lett.*, **107**, 230401 (2011).

[43] P. Cheiney, F. Damon, C. G, G. B. G. L., and D. Guéry-Odelin. Realization of tunnel barriers for matter waves using spatial gaps. *arXiv*, **1302.1811** (2013).

[44] P. Cheiney, C. M. Fabre, F. Vermersch, G. L. Gattobigio, R. Mathevet, T. Lahaye, and D. Guéry-Odelin. Matter-wave scattering on an amplitude-modulated optical lattice. *Phys. Rev. A*, **87**, 013623 (2013).

[45] W. D. Phillips and J. V. Prodan. Laser-cooled and trapped atoms. *Natl. Bur. Stand.* (1983).

[46] O. Morsch, D. Campini, and E. Arimondo. Controlling atomic matter waves by shaking. *Europhysics News*, **41**, 3, 21 (2010).

[47] J. Schoser, A. Batär, R. Löw, V. Schweikhard, A. Grabowski, Y. B. Ovchinnikov, and T. Pfau. Intense source of cold Rb atoms from a pure two-dimensional magneto-optical trap. *Phys. Rev. A*, **66**, 023410 (2002).

[48] W. D. Phillips and H. Metcalf. Laser deceleration of an atomic beam. *Phys. Rev. Lett.*, **48**, 596 (1982).

[49] Y. B. Ovchinnikov. A Zeeman slower based on magnetic dipoles. *Opt. Comm.*, **276**, 2, 261 (2007).

[50] G. Reinaudi, C. B. Osborn, K. Bega, and T. Zelevinsky. Dynamically configurable and optimizable Zeeman slower using permanent magnets and servomotors. *J. Opt. Soc. Am. B*, **29**, 4, 729 (2012).

[51] D. Steck. Rubidium 87 d line data. Technical report, Available online at http://steck.us/alkalidata (2009).

[52] T. E. Barrett, S. W. Dapore-Schwartz, M. D. Ray, and G. P. Lafyatis. Slowing atoms with σ^- polarized light. *Phys. Rev. Lett.*, **67**, 3483 (1991).

[53] A. A. G. Grynberg and C. Fabre. *Introduction to Quantum Optics, From the Semi-classical Approach to Quantized Light*, (Cambridge University Press 2010).

[54] W. G. Kaenders, F. Lison, I. Müller, A. Richter, R. Wynands, and D. Meschede. Refractive components for magnetic atom optics. *Phys. Rev. A*, **54**, 6, 5067 (1996).

[55] K. Halbach. Design of permanent multipole magnets with oriented rare-earth cobalt material. *Nuc. Inst. Meth.*, **169**, 1, 1 (1980).

[56] W. Ketterle, K. B. Davis, M. A. Joffe, A. Martin, and D. E. Pritchard. High densities of cold atoms in a *dark* spontaneous-force optical trap. *Phys. Rev. Lett.*, **70**, 2253 (1993).

[57] D. J. Wineland and W. M. Itano. Laser cooling of atoms. *Phys. Rev. A*, **20**, 1521 (1979).

[58] W. D. Ketterle, S. Durfee, and D. M. Stamper-Kurn. Making, probing and understanding bose-einstein condensates in proceedings of the international school of physics "enrico fermi". In *Bose-Einstein Condensation in Atomic Gases* (1999).

[59] C. S. Adams, H. J. Lee, N. Davidson, M. Kasevich, and S. Chu. Evaporative cooling in a crossed dipole trap. *Phys. Rev. Lett.*, **74**, 3577 (1995).

[60] A. Couvert. *Production et étude de lasers à atomes guidés, et de leur interaction avec des défauts contrôlés.* Ph.D. thesis, Université Paris VI - Pierre et Marie Curie (2009).

[61] C. M. Fabre. *Miroirs de Bragg pour ondes de matière et apport de la supersymétrie aux potentiels exponentiels.* Ph.D. thesis, Université Toulouse 3 Paul Sabatier (2012).

[62] L. Pitaevskii and S. Stringari. *Bose-Einstein Condensation*, (Oxford science publications 2003).

[63] T. Lahaye. *Refroidissement par évaporation d'un jet atomique guidé magnétiquement.* Ph.D. thesis, Université Paris VI - Pierre et Marie Curie (2005).

[64] K. Dieckmann, R. J. C. Spreeuw, M. Weidemüller, and J. T. M. Walraven. Two-dimensional magneto-optical trap as a source of slow atoms. *Phys. Rev. A*, **58**, 3891 (1998).

[65] R. Grimm, M. Weidemüller, and Y. B. Ovchinnikov. Optical dipole traps for neutral atoms. *Advances in Atomic, Molecular and Optical Physics*, **42**, 95 (2000).

[66] T. Lauber, J. Küber, O. Wille, and G. Birkl. Optimized bose-einstein-condensate production in a dipole trap based on a 1070-nm multifrequency laser: Influence of enhanced two-body loss on the evaporation process. *Phys. Rev. A*, **84**, 043641 (2011).

[67] K. M. O'Hara, M. E. Gehm, S. R. Granade, and J. E. Thomas. Scaling laws for evaporative cooling in time-dependent optical traps. *Phys. Rev. A*, **64**, 051403 (2001).

[68] K. J. Arnold and M. D. Barrett. All-optical bose-einstein condensation in a 1.06 μm dipole trap. *Optics Communications*, **284**, 13, 3288 (2011).

[69] G. Grynberg, B. Lounis, P. Verkerk, J.-Y. Courtois, and C. Salomon. Quantized motion of cold cesium atoms in two- and three-dimensional optical potentials. *Phys. Rev. Lett.*, **70**, 2249 (1993).

[70] L. Tarruell, D. Greif, T. Uehlinger, G. Jotzu, and T. Esslinger. Creating, moving and merging dirac points with a fermi gas in a tunable honeycomb lattice. *Nature*, **483**, 302 (2012).

[71] M. Greiner, O. Mandel, T. Esslinger, T. W. Hansch, and I. Bloch. Quantum phase transition from a superfluid to a Mott insulator in a gas of ultracold atoms. *Nature*, **415**, 39 (2002).

[72] J. Struck, C. Ölschläger, R. Le Targat, P. Soltan-Panahi, A. Eckardt, M. Lewenstein, P. Windpassinger, and K. Sengstock. Quantum simulation of frustrated classical magnetism in triangular optical lattices. *Science*, **333**, 6045, 996 (2011).

[73] D. Greif, T. Uehlinger, G. Jotzu, L. Tarruell, and T. Esslinger. Quantum magnetism of ultracold fermions in an optical lattice. *arXiv*, **1212.2634v1** (2012).

[74] E. Riis, D. S. Weiss, K. A. Moler, and S. Chu. Atom funnel for the production of a slow, high-density atomic beam. *Phys. Rev. Lett.*, **64**, 1658 (1990).

[75] G. Roati, C. D'Errico, L. Fallani, M. Fattori, C. Fort, M. Zaccanti, G. Modugno, M. Modugno, and M. Inguscio. Anderson localization of a non-interacting bose-einstein condensate. *Nature*, **453**, 895 (2008).

[76] M. Albert and P. Leboeuf. Localization by bichromatic potentials versus anderson localization. *Phys. Rev. A*, **81**, 013614 (2010).

[77] C. Mennerat-Robilliard, D. Lucas, S. Guibal, J. Tabosa, C. Jurczak, J.-Y. Courtois, and G. Grynberg. Ratchet for cold rubidium atoms: The asymmetric optical lattice. *Phys. Rev. Lett.*, **82**, 851 (1999).

[78] H. Haffner, A. Browaeys, N. R. Heckenberg, K. Helmerson, C. McKenzie, G. J. Milburn, W. D. Phillips, S. L. Rolston, H. Rubinsztein-Dunlop, and B. Upcroft. Dynamical tunnelling of ultracold atoms. *Nature*, **412**, 52 (2001).

[79] C. V. Raman and N. S. N. Nath. *Proc. Indian Acad. Sci.*, **2**, 406 (1936).

[80] J. H. Huckans, I. B. Spielman, B. L. Tolra, W. D. Phillips, and J. V. Porto. Quantum and classical dynamics of a bose-einstein condensate in a large-period optical lattice. *Phys. Rev. A*, **80**, 043609 (2009).

[81] N. W. Ashcroft and N. D. Mermin. *Solid state physics*, (W. B. Saunders Co., Philadelphia 1976).

[82] E. Mathieu. Mémoire sur le mouvement vibratoire d'une membrane de forme elliptique. *Journal des Mathématiques Pures et Appliquées*, pp. 137–203 (1868).

[83] E. T. Whittaker and G. N. Watson. *A course of modern analysis*, (Cambridge University Press 1962).

[84] J. E. Sträng. On the characteristic exponents of floquet solutins to the mathieu equation. *Acad. Roy. Belg. Bull. Cl. Sci.*, **6**, 269 (2005).

[85] N. W. McLachlan. *Theory and application of Mathieu functions*, (Dever Publications 1964).

[86] L. Santos and L. Roso. A band-like reflection spectrum of an atomic beam on a periodic laser profile. *J. Phys. B: At. Mol. Opt. Phys*, **30**, 5169 (1997).

[87] L. Santos and L. Roso. Multilayer "dielectric" mirror for atoms. *Phys. Rev. A*, **58**, 2407 (1998).

[88] I. Carusotto and G. C. La Rocca. Modulated optical lattice as an atomic fabry-perot interferometer. *Phys. Rev. Lett.*, **84**, 399 (2000).

[89] R. O. N. Friedman and N. Davidson. Quantum reflection of atoms from a periodic dipole potential. *J. Opt. Soc. Am. B*, **15**, 1749 (1998).

[90] C. Zener. Non-adiabatic crossing of energy levels. *Proceedings of the Royal Society of London. Series A*, **137**, 833, 696 (1932).

[91] T. Lauber, P. Massignan, G. Birkl, and A. Sanpera. Atomic wave packet dynamics in finite time-dependent optical lattices. *Journal of Physics B: Atomic, Molecular and Optical Physics*, **44**, 6, 065301 (2011).

[92] F. Vermersch, C. M. Fabre, P. Cheiney, G. L. Gattobogio, R. Mathevet, and D. Guéry-Odelin. Guided-atom laser: Transverse mode quality and longitudinal momentum distribution. *Phys. Rev. A*, **84**, 043618 (2011).

[93] G. L. Gattobigio, A. Couvert, B. Georgeot, and D. Guéry-Odelin. Exploring classically chaotic potentials with a matter wave quantum probe. *Phys. Rev. Lett.*, **107**, 254104 (2011).

[94] M. D. Feit, J. A. Fleck, and A. Steiger. Solution of the schrodinger equation by a spectral method. *Journal of Computational Physics*, **47**, 412 (1982).

[95] J. R. Bryce Gadway, Daniel Pertot and D. Schneble. Probing an ultracold-atom crystal with matter waves. *Nature Physics*, **8**, 544 (2012).

[96] B. Eiermann, T. Anker, M. Albiez, M. Taglieber, P. Treutlein, K.-P. Marzlin, and M. K. Oberthaler. Bright bose-einstein gap solitons of atoms with repulsive interaction. *Phys. Rev. Lett.*, **92**, 230401 (2004).

[97] C. Weiss and Y. Castin. Elastic scattering of a quantum matter-wave bright soliton on a barrier. *J. Phys. A: Math. Theor*, **45**, 455306 (2012).

[98] T. P. Billam, S. L. Cornish, and S. A. Gardiner. Realizing bright-matter-wave-soliton collisions with controlled relative phase. *Phys. Rev. A*, **83**, 041602 (2011).

[99] A. L. Marchant, T. P. Billam, T. P. Wiles, M. M. H. Yu, S. A. Gardiner, and C. S. L. Controlled formation and reflection of a bright solitary matter-wave. *arXiv*, **1301.5759v1** (2013).

[100] G. Gamow. Zur quantentheorie des atomkernes. *Zeitschrift für Physik*, **51**, 204 (1928).

[101] R. W. Gurney and E. U. Condon. Quantum mechanics and radioactive disintegration. *Phys. Rev.*, **33**, 127 (1929).

[102] L. Esaki. New phenomenon in narrow germanium $p-n$ junctions. *Phys. Rev.*, **109**, 603 (1958).

[103] L. Esaki. Long journey into tunneling. *Rev. Mod. Phys.*, **46**, 237 (1974).

[104] G. Binnig and H. Rohrer. Scanning tunneling microscopy—from birth to adolescence. *Rev. Mod. Phys.*, **59**, 615 (1987).

[105] F. Krausz and M. Ivanov. Attosecond physics. *Rev. Mod. Phys.*, **81**, 163 (2009).

[106] C. Cohen-Tannoudji and D. Guéry-Odelin. *Advances in atomic physics - An overview*, (World Scientific 2011).

[107] B. Josephson. Possible new effects in superconductive tunnelling. *Physics Letters*, **1**, 7, 251 (1962).

[108] O. V. Astafiev, L. B. Ioffe, S. Kafanov, Y. A. Pashkin, K. Y. Arutyunov, D. Shahar, O. Cohen, and J. S. Tsai. Coherent quantum phase slip. *Nature*, **484**, 355 (2012).

[109] M. Albiez, R. Gati, J. Fölling, S. Hunsmann, M. Cristiani, and M. K. Oberthaler. Direct observation of tunneling and nonlinear self-trapping in a single bosonic josephson junction. *Phys. Rev. Lett.*, **95**, 010402 (2005).

[110] S. Levy, E. Lahoud, I. Shomroni, and J. Steinhauer. The a.c. and d.c. josephson effects in a bose-einstein condensate. *Nature*, **449**, 579 (2007).

[111] T. Betz, S. Manz, R. Bücker, T. Berrada, C. Koller, G. Kazakov, I. E. Mazets, H.-P. Stimming, A. Perrin, T. Schumm, and J. Schmiedmayer. Two-point phase correlations of a one-dimensional bosonic josephson junction. *Phys. Rev. Lett.*, **106**, 020407 (2011).

[112] O. Morsch and M. Oberthaler. Dynamics of bose-einstein condensates in optical lattices. *Rev. Mod. Phys.*, **78**, 179 (2006).

[113] M. J. Davis and E. J. Heller. Quantum dynamical tunneling in bound states. *J. Chem. Phys.*, **75**, 246 (1981).

[114] L. Santos and L. Roso. Bloch-like quantum multiple reflections of atoms. *Phys. Rev. A*, **60**, 2312 (1999).

[115] I. Carusotto, D. Embriaco, and G. C. La Rocca. Nonlinear atom optics and bright-gap-soliton generation in finite optical lattices. *Phys. Rev. A*, **65**, 053611 (2002).

[116] H. Denschlag, J. E. Simsarian, H. Haffner, C. McKenzie, A. Browaeys, D. Cho, K. Helmerson, S. L. Rolston, and W. D. Phillips. A bose-einstein condensate in an optical lattice. *Journal of Physics B: Atomic, Molecular and Optical Physics*, **35**, 3095 (2002).

[117] L. Schiff. *Quantum Mechanics*, (New York: McGraw Hill1968).

[118] M. Kasevich and S. Chu. Laser cooling below a photon recoil with three-level atoms. *Phys. Rev. Lett.*, **69**, 1741 (1992).

[119] D. A. Steck, W. H. Oskay, and M. G. Raizen. Observation of chaos-assisted tunneling between islands of stability. *Science*, **293**, 5528, 274 (2001).

[120] A. del Campo, F. Delgado, G. Garcia-Calderon, J. G. Muga, and M. G. Raizen. Decay by tunneling of bosonic and fermionic tonks-girardeau gases. *Phys. Rev. A*, **74**, 013605 (2006).

[121] V. Ahufinger, B. A. Malomed, G. Birkl, R. Corbalán, and A. Sanpera. Double-barrier potentials for matter-wave gap solitons. *Phys. Rev. A*, **78**, 013608 (2008).

[122] S. D. Hansen, N. Nygaard, and K. Molmer. Scattering of matter wave solitons on localized potentials. *arXiv:1210.1681* (2012).

[123] J. Billy, V. Josse, Z. Zuo, A. Bernard, B. Hambrecht, P. Lugan, D. Clement, L. Sanchez-Palencia, P. Bouyer, and A. Aspect. Direct observation of anderson localization of matter-waves in a controlled disorder. *Nature*, **453**, 891 (2008).

[124] S. Keshavamurthy and P. Schlagheck. *Dynamical Tunneling: Theory and Experiment*, (CRC Press, Singapore 2011).

[125] B. G. Klappauf, W. H. Oskay, D. A. Steck, and M. G. Raizen. Observation of noise and dissipation effects on dynamical localization. *Phys. Rev. Lett.*, **81**, 1203 (1998).

[126] J. Ringot, P. Szriftgiser, J. C. Garreau, and D. Delande. Experimental evidence of dynamical localization and delocalization in a quasiperiodic driven system. *Phys. Rev. Lett.*, **85**, 2741 (2000).

[127] J. Chabé, G. Lemarié, B. Grémaud, D. Delande, P. Szriftgiser, and J. C. Garreau. Experimental observation of the anderson metal-insulator transition with atomic matter waves. *Phys. Rev. Lett.*, **101**, 255702 (2008).

[128] H. Lignier, C. Sias, D. Ciampini, Y. Singh, A. Zenesini, O. Morsch, and E. Arimondo. Dynamical control of matter-wave tunneling in periodic potentials. *Phys. Rev. Lett.*, **99**, 220403 (2007).

[129] E. Kierig, U. Schnorrberger, A. Schietinger, J. Tomkovic, and M. K. Oberthaler. Single-particle tunneling in strongly driven double-well potentials. *Phys. Rev. Lett.*, **100**, 190405 (2008).

[130] Y.-A. Chen, S. Nascimbène, M. Aidelsburger, M. Atala, S. Trotzky, and I. Bloch. Controlling correlated tunneling and superexchange interactions with ac-driven optical lattices. *Phys. Rev. Lett.*, **107**, 210405 (2011).

[131] A. Alberti, G. Ferrari, V. V. Ivanov, M. L. Chiofalo, and G. M. Tino. Atomic wave packets in amplitude-modulated vertical optical lattices. *New Journal of Physics*, **12**, 6, 065037 (2010).

[132] S. Arlinghaus and M. Holthaus. Controlled wave-packet manipulation with driven optical lattices. *Phys. Rev. A*, **84**, 063617 (2011).

[133] C. E. Creffield and F. Sols. Directed transport in driven optical lattices by gauge generation. *Phys. Rev. A*, **84**, 023630 (2011).

[134] J. F. Sherson, S. J. Park, P. L. Pedersen, N. Winter, M. Gajdacz, S. Mai, and J. Arlt. The pump probe coupling of matter wave packets to remote lattice states. *New J. Phys.*, **14**, 083013 (2012).

[135] J. H. Shirley. Solution of the schrödinger equation with a hamiltonian periodic in time. *Phys. Rev.*, **138**, B979 (1965).

[136] R. Battesti, P. Cladé, S. Guellati-Khélifa, C. Schwob, B. Grémaud, F. Nez, L. Julien, and F. Biraben. Bloch oscillations of ultracold atoms: A tool for a metrological determination of h/m_{rb}. *Phys. Rev. Lett.*, **92**, 253001 (2004).

[137] C. Weiss and Y. Castin. Creation and detection of a mesoscopic gas in a nonlocal quantum superposition. *Phys. Rev. Lett.*, **102**, 010403 (2009).

[138] L. V. Hau, J. A. Golovchenko, and M. M. Burns. A new atomic beam source: The "candlestick". *Rev. Sci. Inst.*, **65**, 12, 3746 (1994).

[139] M. R. Walkiewicz, P. J. Fox, and R. E. Scholten. Candlestick rubidium beam source. *Rev. Sci. Inst.*, **71**, 3342 (2000).

[140] G. M. Carter and D. E. Pritchard. Recirculating atomic beam oven. *Rev. Sci. Inst.*, **49**, 120 (1978).

[141] K. M. R. van der Stam, E. D. van Ooijen, R. Meppelink, J. M. Vogels, and P. van der Straten. Large atom number bose-einstein condensate of sodium. *Rev. Sci. Inst.*, **78**, 013102 (2007).